A novel optical bio-chemical sensor based on hybrid nanostructures of Bowtie nanoantennas and Fabry-Perot Interferometer

Huanhuan Liu

N° d'ordre 2013-41 Année 2013

Thèse

A novel optical bio-chemical sensor based on Hybrid nanostructures of Bowtie Nanoantennas and Fabry-Perot Interferometer

Présentée devant

L'Ecole Centrale de Lyon

Pour obtenir

Le grade de docteur

École doctorale : Electronique, Electrotechnique et Automatisme de Lyon

Par

Huanhuan LIU

Soutenue le 20 novembre 2013

Jury

Rapporteur	Gilles LERONDEL	Professeur des Universités
Rapporteur	Ralf B. WEHRSPOHN	Professeur des Universités
Examinateur	Thierry GROSJEAN	Chargé de Recherche CNRS
Examinateur	Pascal PERRIAT	Professeur - INSA de Lyon
Directeur de Thèse	Xavier LETARTRE	Directeur de recherche CNRS
Co-directeur de Thèse	Cécile JAMOIS	Chargée de recherche CNRS
Invité	Ali BELAROUCI	Chargé de recherche CNRS
Invité	Emmanuel COTTANCIN	Maître de conférences UCBL

Institut des Nanotechnologies de Lyon (INL) – CNRS UMR 5270

ÉCOLE CENTRALE LYON **Direction de la recherche**

Liste des personnes Habilitées à Diriger des Recherches en poste à l'Ecole Centrale de Lyon

Nom-Prénom	*Corps grade*	Laboratoire ou à défaut département ECL	Etablissement
BEROUAL Abderrahmane	*professeur*	AMPERE	ECL
BURET François	*professeur*	AMPERE	ECL
JAFFREZIC-RENAULT Nicole	*directeur de recherche*	AMPERE	CNRS/ECL
KRÄHENBÜHL Laurent	*directeur de recherche*	AMPERE	CNRS/ECL
NICOLAS Alain	*professeur*	AMPERE	ECL
NICOLAS Laurent	*directeur de recherche*	AMPERE	CNRS/ECL
SCORLETTI Gérard	*professeur*	AMPERE	ECL
SIMONET Pascal	*directeur de recherche*	AMPERE	CNRS/ECL
VOLLAIRE Christian	*professeur*	AMPERE	ECL

Nbre Ampère 9

HELLOUIN Yves	*maître de conférences*	DER EEA	ECL

Nbre DER EEA 1

GUIRALDENQ Pierre	*professeur émérite*	DER STMS	ECL
VINCENT Léo	*professeur*	DER STMS	ECL

Nbre DER STMS 2

LOHEAC Jean-Pierre	*maître de conférences*	ICJ	ECL
MAITRE Jean-François	*professeur émérite*	ICJ	ECL
MARION Martine	*professeur*	ICJ	ECL
MIRONESCU Elisabeth	*professeur*	ICJ	ECL
MOUSSAOUI Mohand	*professeur*	ICJ	ECL
MUSY François	*maître de conférences*	ICJ	ECL
ZINE Abdel-Malek	*maître de conférences*	ICJ	ECL

Nbre ICJ 7

CALLARD Anne-Ségolène	*professeur*	INL	ECL
CLOAREC Jean-Pierre	*maître de conférences*	INL	ECL
GAFFIOT Frédéric	*professeur*	INL	ECL
GAGNAIRE Alain	*maître de conférences*	INL	ECL
GARRIGUES Michel	*directeur de recherche*	INL	CNRS/ECL
GENDRY Michel	*directeur de recherche*	INL	CNRS/ECL
GRENET Geneviève	*directeur de recherche*	INL	CNRS/ECL
HOLLINGER Guy	*directeur de recherche*	INL	CNRS/ECL
KRAWCZYK Stanislas	*directeur de recherche*	INL	CNRS/ECL
LETARTRE Xavier	*chargé de recherche*	INL	CNRS/ECL
O'CONNOR Ian	*professeur*	INL	ECL
PHANER-GOUTORBE Magali	*professeur*	INL	ECL
ROBACH Yves	*professeur*	INL	ECL
SAINT-GIRONS Guillaume	*chargé de recherche*	INL	CNRS/ECL
SEASSAL Christian	*directeur de recherche*	INL	CNRS/ECL

SOUTEYRAND Eliane	directeur de recherche	INL	CNRS/ECL
TARDY Jacques	directeur de recherche	INL	CNRS/ECL
VIKTOROVITCH Pierre	directeur de recherche	INL	CNRS/ECL

Nbre INL 18

CHEN Liming	professeur	LIRIS	ECL
DAVID Bertrand	professeur	ICTT	ECL

Nbre LIRIS 2

BAILLY Christophe	professeur	LMFA	ECL
BERTOGLIO Jean-Pierre	directeur de recherche	LMFA	CNRS/ECL
BLANC-BENON Philippe	directeur de recherche	LMFA	CNRS/ECL
BOGEY Christophe	chargé de recherche	LMFA	CNRS/ECL
CAMBON Claude	directeur de recherche	LMFA	CNRS/ECL
CARRIERE Philippe	directeur de recherche	LMFA	CNRS/ECL
CHAMPOUSSIN J-Claude	professeur émérite	LMFA	ECL
COMTE-BELLOT geneviève	professeur émérite	LMFA	ECL
FERRAND Pascal	directeur de recherche	LMFA	CNRS/ECL
GALLAND Marie-Annick	professeur	LMFA	ECL
GODEFERD Fabien	directeur de recherche	LMFA	CNRS/ECL
GOROKHOVSKI Mikhail	professeur	LMFA	ECL
HENRY Daniel	directeur de recherche	LMFA	CNRS/ECL
JEANDEL Denis	professeur	LMFA	ECL
JUVE Daniel	professeur	LMFA	ECL
LE RIBAULT Catherine	chargée de recherche	LMFA	CNRS/ECL
LEBOEUF Francis	professeur	LMFA	ECL
PERKINS Richard	professeur	LMFA	ECL
ROGER Michel	professeur	LMFA	ECL
SCOTT Julian	professeur	LMFA	ECL
SHAO Liang	directeur de recherche	LMFA	CNRS/ECL
SIMOENS Serge	chargé de recherche	LMFA	CNRS/ECL
TREBINJAC Isabelle	maître de conférences	LMFA	ECL

Nbre LMFA 23

BENAYOUN Stéphane	professeur	LTDS	ECL
CAMBOU Bernard	professeur	LTDS	ECL
COQUILLET Bernard	maître de conférences	LTDS	ECL
DANESCU Alexandre	maître de conférences	LTDS	ECL
FOUVRY Siegfrid	chargé de recherche	LTDS	CNRS/ECL
GEORGES Jean-Marie	professeur émérite	LTDS	ECL
GUERRET Chrystelle	chargé de recherche	LTDS	CNRS/ECL
HERTZ Dominique	past	LTDS	ECL
ICHCHOU Mohamed	professeur	LTDS	ECL
JEZEQUEL Louis	professeur	LTDS	ECL
JUVE Denyse	ingénieur de recherche	LTDS	ECL
KAPSA Philippe	directeur de recherche	LTDS	CNRS/ECL
LE BOT Alain	directeur de recherche	LTDS	CNRS/ECL
LOUBET Jean-Luc	directeur de recherche	LTDS	CNRS/ECL
MARTIN Jean-Michel	professeur	LTDS	ECL
MATHIA Thomas	directeur de recherche	LTDS	CNRS/ECL
MAZUYER Denis	professeur	LTDS	ECL
PERRET-LIAUDET Joël	maître de conférences	LTDS	ECL
SALVIA Michelle	maître de conférences	LTDS	ECL
SIDOROFF François	professeur	LTDS	ECL
SINOU Jean-Jacques	professeur	LTDS	ECL
STREMSDOERFER Guy	professeur	LTDS	ECL

THOUVEREZ Fabrice	*professeur*	LTDS	ECL
TREHEUX Daniel	*professeur*	LTDS	ECL
VINCENS Eric	*maître de conférences*	LTDS	ECL
		Nbre LTDS 25	
	Total HdR ECL	91	

Acknowledgments

It is a great pleasure to sincerely thank the program “Groups of Five Ecoles Centrales” between China Scholarship Council (CSC) and Lyon Institute of Nanotechnologies (INL, CNRS UMR 5270) which provided me this opportunity to do my PhD study in INL.

I would like to express my deep and sincere appreciation to my PhD supervisors: Professor Xavier LETARTRE, Cécile JAMOIS and Ali BELAROUCI, for supporting me during the past three years. Without their guidance and persistent help, this dissertation would not have been possible. Xavier was supportive and gave me the illuminating advices to complete my studies. His wide knowledge, logical ways of thinking, understanding and encouraging provided me an example to be followed in my future research career. It is a great pleasure to sincerely thank Cécile for her theoretical & experimental advices. From amount of discussions and communications with her, I learnt the way to do the research and to be a proper researcher. She was my primary resource for getting my questions and was instrumental in modifying the thesis. I want also thank Ali who gave me key advices and helps in the structures design, as well as the correction of the thesis. His passion and serious attitude on the science research inspired my interest in this domain. Three of them gave me enough freedom and motivated greatly my self-confidence in the research work. I would like to thank Prof. Gilles LERONDEL, Prof. Ralf B. WEHRSPOHN, Mr. Thierry GROSJEAN, Mr. Pascal PERRIAT and Mr. Emmanuel COTTANCIN as accepted to be my committee and for insightful comments and discussions.

I will forever be thankful to my former college research advisor: Professor Xiaodong ZENG, who was helpful in providing advice many times during my graduate school career. He is my role model for a scientist, mentor, and teacher.

I also thank Abdelmounaim HAROURI for his help during the sensing experiments, thank Emmanuel GERELLI and Laurent MILORD for their helps during optical characterization of my structures, thank Mohsen EROUEL for his help and discussion during the fabrication of porous silicon structures, thank Taha BENYATTOU and Régis OROBTCHOUK for fruitful discussions about PSi characterization, thank Taiping ZhANG for his help in learning the e-beam lithography and lift-off procedures. I would also thank Brice DEVIF and Radoslaw MAZURCZYK who helped us to deposit silica layer several times, and thank all members of

NanoLyon Platform: Khaled AYADI, Jöelle GREGOIRE, Philippe GIRARD, Robert PERRIN, Céline CHEVALIER, Pierre CREMILLIEU and Jean-Louis LECLERQ, who provided me a healthy environment to complete the fabrication of my samples. I would thank all members of Photonics team.

My sincere thanks are due to all the secretaries and other stuff: Nicole DURAND, Patricia DUFAUT, especially, Sylvie GONCALVES for their kindly and nicely helps on official papers. I also thank Xianqin MENG, Zhen LIN and Cédric BLANCHARD to give me a fruitful discussion about the detailed issues. I would also thank my colleagues Roman ANUFRIEV, Mouhannad MASSOUD, Xuan HU, Yao ZHU, Shi YIN, Nanhao ZHU, Zhenfu FENG, Zhen LI, He DING and so on, you always make me feel that I am not alone in France.

Last but not the least, I am grateful to my parents who share my worries, frustrations and happiness during my whole life.

Résumé

Aujourd'hui, la préoccupation croissante pour l'analyse environnementale et le contrôle de la qualité des aliments, ainsi que les besoins médicaux tels que le diagnostic rapide en cas de situations d'urgence, entraîne un besoin croissant de nouvelles générations de capteurs chimiques et biologiques. Ces dispositifs doivent avoir une haute sensibilité et fiabilité, ils doivent permettre une détection spécifique de molécules et une détection parallèle de différentes molécules, tout en étant bas coût, portables, rapides et faciles à utiliser. Ainsi, une tendance générale se porte sur les capteurs biochimiques intégrés sur puce, sans marqueur, et compatibles avec les procédés standard des micro-technologies. Les dispositifs diélectriques photoniques à base de silicium poreux et les nanostructures métalliques à résonances plasmoniques sont de bons candidats pour répondre aux exigences ci-dessus. Le silicium poreux est un matériau biocompatible, avec une énorme surface spécifique entrainant un gain de la sensibilité de plusieurs ordres de grandeur par rapport aux matériaux massifs ; en outre, son indice de réfraction et son épaisseur peuvent être facilement ajustés, permettant la réalisation d'une grande variété de dispositifs photoniques. Les nanostructures métalliques offrent un fort confinement et une forte amplification du champ électromagnétique dans des régions sub-longueur d'onde, ce qui conduit à des sensibilités élevées ; combinées avec d'autres mécanismes de détection comme la fluorescence, le Raman ou la spectroscopie IR, elles ont déjà démontré un gain important du potentiel pour la détection. La réalisation d'un dispositif hybride combinant ces deux éléments est très intéressant, car il peut offrir les avantages des deux éléments ; la structure photonique pourrait aussi façonner la résonance plasmonique pour le développement de dispositifs ultrasensibles à largeur de raie de résonance étroite tout en ayant une profondeur de détection accrue. Dans ce contexte, l'objectif de cette thèse est d'explorer les défis de cette solution en considérant la conception, la réalisation, la caractérisation et le potentiel de dispositifs hybrides photoniques/plasmoniques qui exploitent le couplage entre la résonance plasmonique de surface localisée d'un réseau d'antennes papillon et les modes photoniques d'un interféromètre en silicium poreux.

Les mots clés : nano-antenne papillon, silicium poreux, interféromètre, dispositifs hybrides photoniques/plasmoniques, capteurs

Abstract

Nowadays, the increasing concern for environmental analysis and food quality control, as well as medical needs such as fast diagnosis in case of emergency events, leads to a growing need for new generations of chemical and biological sensors. These devices should have high sensitivity and reliability, perform specific detection of molecules and enable multiple parallel sensing, while being cheap, portable, fast and easy to use. Thus, a general trend tends towards bio-chemical sensors which are on-chip integrated, label-free, and compatible with standard micro-technologies. Photonic dielectric devices based on porous silicon and metallic nanostructures based on plasmon resonances are good candidates to fulfill the above requirements. Porous silicon is a biocompatible material, with a huge specific surface providing a sensitivity enhancement by several orders of magnitude compared to bulk materials; furthermore, its refractive index and thickness can be easily tuned, enabling for the realization of a large variety of photonic designs. Metallic nanostructures provide high confinement and strong field enhancement in sub-wavelength regions, leading to high sensitivities; combined with fluorescence or other sensing mechanisms such as Raman or IR spectroscopy, they have already demonstrated increased sensing potential. The realization of a hybrid device combining both elements would be highly interesting, since it could yield the advantages of both elements, and the photonic structure could shape the plasmonic resonance to develop ultrasensitive devices with narrow resonance linewidth and increased sensing depth. In this context, we realized and studied a novel hybrid photonic / plasmonic device exploiting the coupling between the surface plasmon resonance of a bowtie nano - antenna (NAs) array and the photonic modes of porous silicon (PSi) interferometer.

We designed and fabricated a NAs array with resonance wavelength ~ 1.3µm on a homogeneous PSi interferometer. A thin spacing silica layer with controllable density protects the pores of PSi layer and provides a smooth surface for the fabrication of NAs. The coupling mechanisms of two elements - NA array and interferometer, are studied with 2 models, which are interferometer approach and resonator approach. The interferometer approach is focused on studying the influence of NAs array as a homogeneous layer on the fringes shift of the interferometer. For resonator approach, the coupled mode theory is applied. With these models, strong coupling between both elements are discovered: splitting. In the case of

smaller environment variation, the hybrid device gains 5-10 fold sensitivity enhancement vs. 2 elements alone. The controllable SiO_2 layer allows us to sense the index variation within PSi interferometer. This opens a route towards double parallel sensing. The development of the theoretical models under different environment is ongoing, which is expected to utilize the strong coupling for the sensing. A further investigation of the sensing potential of the hybrid device would be expected. And the 2 elements constituting the hybrid structure – the interferometer and the NA array – could be modified in order to enlarge the study to a wider family of devices with greater properties and performances.

This work was performed within the framework of the program “Groups of Five Ecoles Centrales” between China Scholarship Council (CSC) and Lyon Institute of Nanotechnologies (INL, CNRS UMR 5270). The project has been supported by the Nanolyon technology platform at INL.

Key words: bowtie nano-antenna, porous silicon, interferometer, plasmonic/photonic hybrid device, sensing

Table of content

PART I. RESUME DETAILLE DU CONTENU DU MANUSCRIT 1

CHAPITRE 1 INTRODUCTION 5

1.1 Elément photonique : Dispositif en Si poreux 6

1.2 Elément plasmonique: Nano-antenne optique 11

1.3 Objectifs de ce travail 15

CHAPITRE 2 METHODES EXPERIMENTALES 19

2.1 Fabrication 20

2.2 Caractérisation optique 23

CHAPITRE 3 ETUDE DU COUPLAGE OPTIQUE ENTRE INTERFEROMETRE F-P ET NANO-ANTENNES 27

3.1 Approche interférentielle 28

3.2 Approche résonante: modes couplés 37

CHAPITRE 4 APPLICATION AUX CAPTEURS 41

4.1 Détection de larges variations d'indice 42

4.2 Détection de faibles variations d'indice 45

CHAPITRE 5 CONCLUSIONS ET PERSPECTIVES 49

CHAPITRE 6 REFERENCES 51

PART II. MAIN MANUSCRIPT 59

CHAPTER 1 INTRODUCTION 63

1.1 Introduction 65

1.2 Photonic element: Porous silicon device 67

1.3 Plasmonic element: optical nano-antenna 81

1.4 Design, Objectives and Organization of this work 95

1.5 References 102

CHAPTER 2 DEVICE FABRICATION AND OPTICAL CHARACTERIZATION 117

2.1 Introduction 119

2.2 Fabrication 121

2.3 Optical Characterization 141

2.4 Conclusion 156

2.5 References 157

CHAPTER 3 INVESTIGATION OF OPTICAL INTERACTION BETWEEN F-P INTERFEROMETER AND BOWTIE NAS 159
3.1 Introduction *161*
3.2 Study of bowtie NA resonance *163*
3.3 Hybrid device: Interferometer approach *168*
3.4 Hybrid device: Resonator approach *199*
3.5 Conclusion *209*
3.6 References *211*
CHAPTER 4 SENSING INVESTIGATION 213
4.1 Introduction *215*
4.2 Large refractive index variation Δn *216*
4.3 Small refractive index variation Δn *226*
4.4 Conclusion *237*
4.5 References *238*
CHAPTER 5 CONCLUSIONS AND PERSPECTIVES 239
5.1 Conclusions *239*
5.2 Perspectives *241*
5.3 References *244*
PART III. APPENDICES 245
APPENDIX A: 247
MULTI-LAYER THIN FILM INTERFERENCE 247
A-1 Single layer-PSi/Si *247*
A-2 Two-layer interferometer - SiO_2/PSi/Si *251*
A-3 Three-layer interferometer – Absorbing layer/SiO_2/PSi/Si *255*
APPENDIX B: 260
FIT OF MACRO-REFLECTIVITY SPECTRUM FOR PSI LAYER CHARACTERIZATION 260
APPENDIX C: 261
ATTENUATION IN THE OPTICAL FIBERS AT 1.4 µM 261
REFERENCES 262

Part I. Résumé détaillé du contenu du manuscrit

Introduction générale

Aujourd'hui, la préoccupation croissante pour l'analyse environnementale et le contrôle de la qualité des aliments, ainsi que les besoins médicaux tels que le diagnostic rapide en cas de situations d'urgence, entraînent un besoin croissant de nouvelles générations de capteurs chimiques et biologiques. Ces dispositifs doivent avoir une haute sensibilité et fiabilité, ils doivent permettre une détection spécifique de molécules et une détection parallèle de différentes molécules, tout en étant bas coût, portables, rapides et faciles à utiliser. Ainsi, une tendance générale se porte sur les capteurs (bio)chimiques intégrés sur puce, sans marqueur, et compatibles avec les procédés standard des micro-technologies.

Les dispositifs diélectriques photoniques à base de silicium poreux et les nanostructures métalliques à résonances plasmoniques sont de bons candidats pour répondre aux exigences ci-dessus. Le silicium poreux est un matériau biocompatible, avec une énorme surface spécifique entrainant un gain de sensibilité de plusieurs ordres de grandeur par rapport aux matériaux massifs ; en outre, son indice de réfraction et son épaisseur peuvent être facilement ajustés, permettant la réalisation d'une grande variété de dispositifs photoniques. Les nanostructures métalliques offrent un fort confinement et une forte amplification du champ électromagnétique dans des régions sub-longueur d'onde, ce qui conduit à des sensibilités élevées ; combinées à d’autres mécanismes de détection comme la fluorescence, le Raman ou la spectroscopie IR, elles ont déjà démontré un gain important du potentiel pour la détection.

La réalisation d'un dispositif hybride couplant ces deux éléments est très intéressante, car il pourrait combiner les avantages des deux éléments ; de plus la structure photonique pourrait façonner la résonance plasmonique pour le développement de dispositifs ultrasensibles à largeur spectrale de résonance étroite, tout en ayant une profondeur de détection accrue.

Dans ce contexte, l'objectif de cette thèse est d'explorer les défis de cette solution en considérant la conception, la réalisation, la caractérisation et le potentiel de dispositifs hybrides photoniques/plasmoniques qui exploitent le couplage entre la résonance plasmonique de surface localisée d'un réseau de nano-antennes papillon (NA) et les modes photoniques d'un interféromètre en silicium poreux.

Le manuscrit débute par une introduction au monde des capteurs optiques, avec une attention particulière sur les propriétés du Si poreux et les dispositifs basés sur ce matériau, ainsi que

sur les nanostructures plasmoniques ; cet état de l'art permettra d'acquérir les bases nécessaires à la compréhension des objectifs et des challenges de ce travail de thèse. La partie suivante est consacrée aux méthodes expérimentales, en particulier les techniques de fabrication et de caractérisation des dispositifs. Puis le cœur du travail est présenté : l'étude des mécanismes de couplage entre les 2 éléments – le réseau de NAs et l'interféromètre, à travers le développement de 2 modèles et leur confrontation avec les résultats expérimentaux. Enfin, le potentiel de tels dispositifs pour l'application à la détection est discuté à travers des exemples spécifiques très différents.

Ce travail a été réalisé dans le cadre du programme des « groupes de cinq Écoles Centrales » entre le China Scholarship Council (CSC) et l'Institut des Nanotechnologies de Lyon (INL, CNRS UMR 5270). Le projet a été soutenu par la plateforme technologique Nanolyon à l'INL.

Chapitre 1 Introduction

D'après Peter Hauptmann [1] « un capteur convertit l'élément physique à mesurer en un signal électrique qui peut être traité ou transmis sous forme électronique ». Au-delà de cette définition générale, le transducteur peut également être magnétique, thermique, mécanique, chimique, ou bien sûr optique. Les capteurs optiques, rencontrent un intérêt croissant car ils peuvent être ultra-sensibles, permettre une détection spécifique et non-destructive d'une grande diversité de molécules, avec possibilité de lecture à distance, et d'analyse multiple parallèle sur puce [2-3]. Parmi les principes à la base des capteurs optiques reportés dans la littérature, on trouve la fluorescence [4], le Raman [5], l'interférométrie [6-8], ou encore la plasmonique [9-11]. Une des tendances actuelles est de s'orienter vers des capteurs sans marqueur, intégrés sur puce, et compatibles avec des procédés standard de fabrication, afin d'augmenter la flexibilité et la simplicité d'utilisation de ces dispositifs, tout en diminuant les coûts. Dans ce contexte, les dispositifs diélectriques à base de silicium, ainsi que les structures plasmoniques, sont deux candidats présentant un grand potentiel. La conception de dispositifs hybrides combinant ces deux éléments permettrait de faire émerger une nouvelle famille de capteurs intégrés, sans marqueur, très sensibles, avec des bandes passantes très étroites et des profondeurs de détection importantes.

L'objectif de cette thèse est d'explorer ces systèmes hybrides, en choisissant un exemple spécifique constitué d'un interféromètre en Si poreux couplé à un réseau de nano-antennes papillons. Cette exploration se fera d'abord du point de vue fondamental, puis applicatif, et les phénomènes qui seront mis en évidence se laissent facilement généraliser à une large diversité de systèmes hybrides. Cette première partie, présentée ci-dessous, est consacrée aux propriétés du Si poreux et des dispositifs de détection basés sur ce matériau, ainsi que sur les nanostructures plasmoniques ; cet état de l'art permettra d'acquérir les bases nécessaires à la compréhension des objectifs et des challenges de ce travail de thèse.

1.1 Elément photonique : Dispositif en Si poreux

Le dispositif photonique proposé dans ce travail est un interféromètre constitué d'une couche simple de Si mésoporeux, comme illustré dans la Fig. 1.1.1.

Les raisons de ce choix sont multiples :

- Le Si mésoporeux est un matériau intéressant pour les études fondamentales, car il est relativement rapide à fabriquer et son indice de réfraction de même que l'épaisseur de la couche peuvent être facilement variés pour la réalisation d'interféromètres avec des paramètres variés [12].
- Le Si mésoporeux est également un matériau intéressant du point de vue applicatif, grâce à sa porosité et sa large surface spécifique qui permettent la détection d'une grande quantité de molécules dans le volume, à sa chimie de surface bien maitrisée, sa biocompatibilité et sa compatibilité avec les procédés standard des micro-technologies, et la large diversité de propriétés exploitables pour la détection, telles que chimiques, optiques, électroniques, mécaniques ou encore thermiques [13].

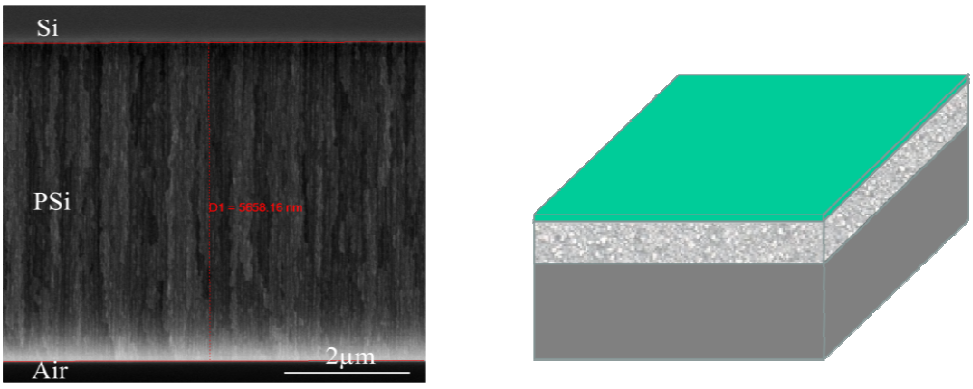

(a) *(b)*

Fig 1.1.1 L'interféromètre en Si poreux considéré dans cette étude : (a) Vue en profil au microscope électronique à balayage (MEB), (b) Vue schématique.

1.1.1 Propriétés du Si poreux

Le Si poreux est un matériau artificiel découvert par hasard dans les années 1950. La grande diversité de morphologies de ce matériau donne lieu à une grande variété de propriétés et d'applications. La technique la plus répandue pour sa fabrication est une gravure électrochimique de Si cristallin en présence d'une solution d'acide fluorhydrique (HF) généralement diluée dans de l'eau et/ou un alcool comme l'éthanol [14-16].

Comme présenté dans la Fig. 1.1.2, cette « anodisation » repose sur les diffusions ioniques et des porteurs de charges induites par le courant circulant entre 2 électrodes, l'une immergée dans la solution, l'autre en face arrière du substrat. Les trous générés dans le substrat cristallin ainsi que les ions fluor présents dans l'électrolyte convergent vers l'interface Si/électrolyte entrainant la dissolution locale des atomes de Si.

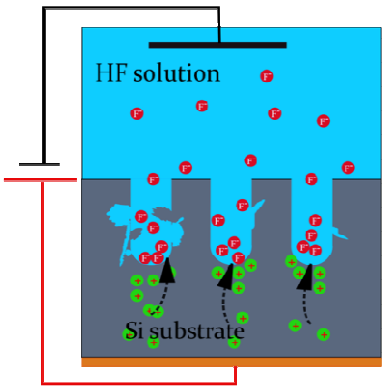

Fig 1.1.2 Vue schématique d'une anodisation

Différents paramètres peuvent influencer la cinétique d'anodisation et la morphologie du Si poreux [17] :

- Le dopage du substrat : c'est un des paramètres primordiaux pour contrôler la morphologie. On divise en général le Si poreux en 3 catégories : le Si nanoporeux (taille des pores < 2 nm), obtenu à partir de substrats de type p faiblement dopés ; le Si macroporeux (taille des pores > 50 nm), obtenu à partir de substrats de type n faiblement dopés, en général sous éclairement ; et le Si mésoporeux (taille des pores 2 – 50 nm), obtenu à partir de substrats de type p ou n fortement dopés. Dans ce travail nous nous intéresserons au Si mésoporeux obtenu avec des substrats p+.

- La concentration et la composition de l'électrolyte de HF : ce paramètre influence également la morphologie du Si poreux, et principalement la porosité (le volume d'air dans le matériau), qui diminue quand la concentration de HF augmente.
- La densité de courant appliquée : elle influence également la porosité qui augmente avec la densité de courant.
- La température : ce paramètre contrôle la diffusion des ions qui participent à la gravure. Une faible température permet d'obtenir des porosités plus importantes, mais également des interfaces beaucoup plus planes de meilleure qualité, ce qui est essentiel pour les applications à la photonique où la rugosité d'interface peut entrainer des pertes par diffraction de la lumière.

La surface spécifique du Si poreux est un autre paramètre morphologique important, notamment pour les applications aux capteurs. Elle est liée à la porosité, comme illustré dans la figure 1.1.3.

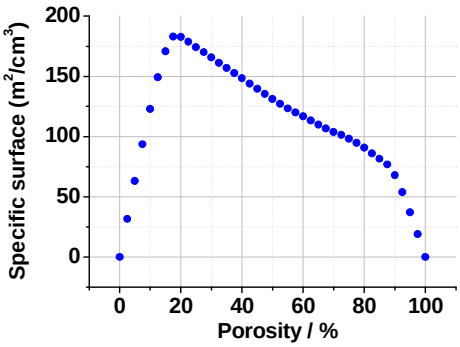

Fig 1.1.3 Variation de la surface spécifique du Si mésoporeux en fonction de la porosité [18]

L'indice de réfaction du Si poreux est également directement lié à la porosité. Plusieurs modèles de milieux effectifs ont été proposés pour décrire l'indice de réfraction de ce matériau [17]. Dans le cas de notre Si mésoporeux, le modèle le mieux adapté est celui de Landau-Lifshitz-Looyenga (LLL) [19] :

$$n^{2/3} = \sum_i f_i n_i^{2/3} \qquad \text{(EQ-1-1)}$$

où n_i et f_i représentent respectivement l'indice de réfraction et la fraction volumique du matériau i constituant le Si poreux – dans le cas le plus simple d'une couche fraichement

préparée *i* = air, Si. La figure 1.1.4 illustre les variations de l'indice de réfraction dans notre matériau [20].

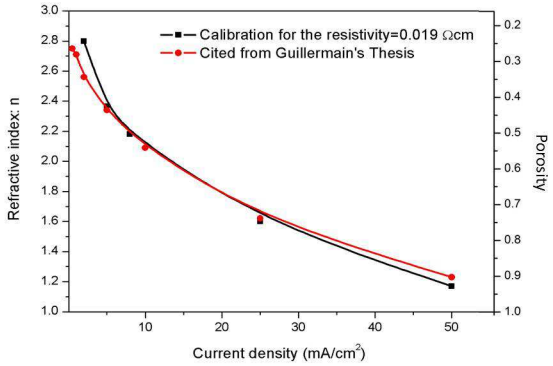

Fig 1.1.4 Variation de l'indice de réfraction du Si mésoporeux à la longueur d'onde 1500 nm [20]

1.1.2 Les capteurs optiques à base de Si poreux

Les capteurs optiques basés sur Si poreux utilisent deux propriétés principales du matériau :

- La porosité qui permet d'infiltrer des espèces à l'intérieur des pores, et qui offre une surface spécifique très grande pour le greffage et l'interaction des molécules à détecter sur les parois
- L'indice de réfraction qui varie fortement avec la présence de molécules dans les pores, comme l'indique l'équation EQ-1-1 ci-dessus.

Parmi les dispositifs en Si poreux proposés pour la détection, nous pouvons citer :

- Les interféromètres Fabry-Perot, qui consistent en une couche simple de Si poreux généralement excitée par un faisceau en incidence normale. L'observation des franges d'interférence et de leur décalage en présence des molécules cibles permet de mettre en évidence la présence de ces molécules [21-23].
- Les miroirs de Bragg, qui sont des multicouches périodiques constitués d'une alternance de 2 couches de porosités différentes – et donc d'indices de réfraction différents. Ces dispositifs sont en général également excités en incidence normale, et ils présentent des plateaux de forte réflectivité dont la position spectrale est directement liée à l'indice des couches, donc qui permettent de monitorer la présence de molécules cibles dans les pores [24-26]. Les microcavités constituent une variante des miroirs de Bragg, dans lesquels une couche supplémentaire introduite dans le miroir se comporte comme un

défaut résonnant, dont la résonnance positionnée sur le plateau de réflectivité du Bragg est également très sensible à l'indice de la couche [27-28].

- Les dispositifs de type guide d'onde sont une autre famille de dispositifs proposés comme capteurs. En particulier les guides d'ondes plans [29-30], qui sont constitués d'une couche mince de porosité moyenne sur un substrat poreux de forte porosité – indice de réfraction plus faible – sont intéressants car la couche sensible est de faible épaisseur et directement accessible à la surface, ce qui limite les problèmes éventuels de diffusion des espèces à détecter dans les pores.
- Les dispositifs à cristaux photoniques présentant soit des modes guidés [31-32], soit des résonnances excitées à incidence normale [32-33] permettent d'exploiter les mêmes avantages que les guides d'ondes plans dans des structures beaucoup plus performantes et plus simples d'utilisation et d'intégration car pouvant être directement excitées à incidence normale.

1.2 Elément plasmonique: Nano-antenne optique

Le dispositif plasmonique proposé dans ce travail est un réseau de nano-antennes optiques « papillons », qui sont constituées chacune de deux triangles d'or placés face à face et séparés par un gap nanométrique, comme illustré dans la figure 1.2.1.

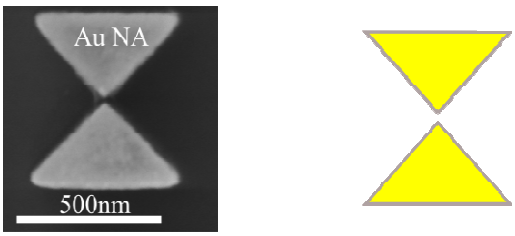

(a) *(b)*

Fig 1.2.1 Illustration d'une nano-antenne papillon : (a) Image MEB, (b) vue schématique

Les nano-antennes optiques sont l'équivalent pour le spectre visible des antennes radiofréquence. Elles permettent en particulier de manipuler et de localiser le champ électromagnétique à des dimensions sub-longueur d'onde [34-38], pour une large variété d'applications, notamment dans le domaine des capteurs. La conception et la fabrication de telles nanostructures, ainsi que leurs propriétés optiques et leur couplage avec d'autres dispositifs, sont encore le sujet de recherches intensives.

Dans ce contexte, les nano-antennes papillons offrent les avantages suivants :

- Un design robuste permettant une bonne reproductibilité de fabrication, notamment l'obtention de gaps nanométriques (~ 10 nm) entre les deux triangles
- Une forte localisation et une forte amplification du champ électromagnétique dans le gap nanométrique
- Une longueur d'onde de résonnance pouvant être ajustée sur une large gamme spectrale, en particulier dans le proche infrarouge aux longueurs d'ondes des télécoms.

1.2.1 Introduction aux structures plasmoniques

Un plasmon est une oscillation cohérente des électrons d'un matériau soumis à une excitation électrique ou optique. On distingue les plasmons de volume (3D), les plasmons de surface (surface plasmon polaritons, SPP) qui se propagent à l'interface entre un métal et un

diélectrique (2D ou 1D) et qui sont évanescents à la fois dans le métal et dans le diélectrique, et les plasmons localisés (localized surface plasmon, LSP), par exemple dans les nanoparticules (0D) [39].

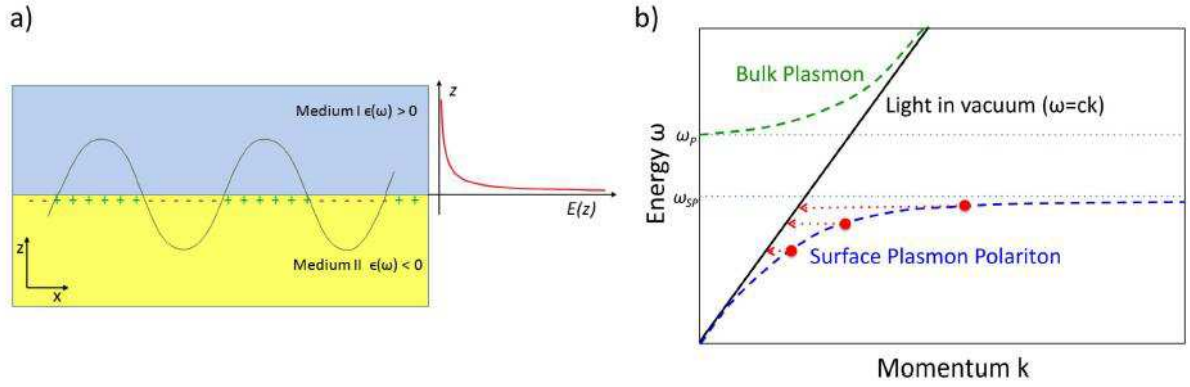

Fig 1.2.2: a) Illustration schématique d'un SPP à l'interface entre deux régions semi-infinies ayant des fonctions diélectriques de signes opposés. b) Courbe de dispersion de l'énergie (ω) versus momentum (k) pour le SPP propagatif (bleu) et le plasmon de volume (vert). Les fréquences plasmons sont notées par des lignes horizontales [40].

Les propriétés des plasmons sont illustrées dans la figure 1.2.2 et peuvent être décrites suivant le modèle de Drude, qui sera détaillé dans le chapitre 3. La fréquence de résonnance d'un plasmon de volume est $\omega_p = \sqrt{\frac{4\pi ne^2}{m_e}}$, celle d'un plasmon de surface est $\omega_{sp} = \omega_p / \sqrt{2}$, où m_e et e sont respectivement la masse effective et la charge élémentaire d'un electron, et n est la densité électronique.

Les plasmons de volume et de surface requièrent des techniques d'excitation par prisme, réseau ou guide d'onde. Les plasmons localisés, en revanche, présentent l'avantage de pouvoir être excités directement en espace libre. D'autres avantages les rendent très prometteurs du point de vue applicatif, comme illustrés dans la figure 1.2.3 :

- La forte localisation du champ électromagnétique
- La forte amplification du champ dans ces espaces de dimensions nanométriques
- Une large variété de géométries
- L'accordabilité, qui résulte de la flexibilité des géométries et du couplage entre différentes nanoparticules
- La sensibilité à l'environnement et en particulier à sa fonction diélectrique.

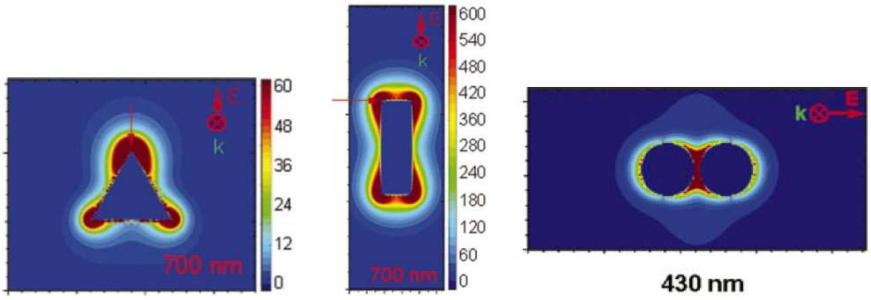

(a) *(b)* *(c)*

Fig 1.2.3 Amplification du champ électrique de différentes nanostructures plasmoniques: (a) prisme triangulaire, (b) nanofil cylindrique, (c) Dimère de nanoparticules sphériques d'Ag séparées d'une distance de 2 nm. [41]

Les nanoparticules plasmoniques peuvent être fabriquées suivant deux voies principales :

- Par voie chimique (bottom-up) [42, 43], généralement obtenue par réduction de sels métalliques. Une large variété de formes et de compositions peut être obtenue.
- Par voie physique (top-down) [41, 44, 45], généralement par une technique de lithographie suivie d'un dépôt métallique. C'est la voie choisie dans ce travail.

Le couplage entre nanoparticules [45-48], qui dépend de la polarisation et qui est d'autant plus fort que la distance entre particules est faible, permet d'obtenir de fortes amplifications de champ dans le gap, comme illustré dans la figure 1.2.3c, et de modifier la longueur d'onde de résonnance. La nano-antenne papillon qui est étudiée dans ce travail est un autre exemple de particules couplées, de forme triangulaire. Elle combine les propriétés de pointes métalliques à celles de nanoparticules couplées à résonnance plasmonique.

1.2.2 Les capteurs optiques à base de structures plasmoniques

Les capteurs optiques à base de nanostructures plasmoniques exploitent la forte sensibilité des plasmons à leur environnement immédiat, et en particulier à la fonction diélectrique de l'environnement.

On distingue 2 grandes familles de dispositifs suivant les mécanismes qui sont exploités :

- Les capteurs basés sur une lecture directe des variations de la résonnance plasmon : ce principe est utilisé en colorimétrie [49, 50] où la présence des espèces à détecter induit un changement de couleur (shift de la résonnance plasmon) dû à une variation de la distance inter-particule et/ou l'interaction entre particules et espèces chimiques. Une autre

configuration très répandue est celle de nanoparticules sur substrat (par exemple fabriquées par lithographie électronique), qui permet de détecter de fines couches de biomolécules en interaction avec la nanostructure plasmonique [51, 52]. En jouant sur l'amplification de champ induit pat le couplage entre particules très proches, une forte augmentation de la sensibilité peut être obtenue [53, 54].

- Les capteurs basés sur l'amplification d'un autre mécanisme optique via la résonnance plasmon : c'est le cas de capteurs basés sur la détection de fluorescence (Plasmon-Enhanced Fluorescence [55-57]) ou encore sur la spectroscopie Raman (Surface Enhanced Raman Scattering, SERS [58-60]), pour lesquels la détection de molécule unique a été démontrée.

Un autre principe de détection est actuellement étudié, basé sur le couplage entre une structure plasmonique et une structure photonique. Parmi le peu de dispositifs hybrides déjà proposés, on peut citer :

- Un interféromètre Fabry-Perot couplé à une résonance plasmon de surface obtenue dans une couche d'or rugueux [61] : ces travaux pionniers dans le domaine ont mis en évidence le gain de sensibilité du dispositif plasmonique apporté par la présence de l'interféromètre.
- Une microcavité couplée à des nanofils plasmoniques : ces travaux plus récents ont porté sur l'interaction entre une microcavité et des nanofils d'or fabriqués par lithographie et positionnés à la surface ou à l'intérieur de la cavité ; l'étude a révélé, non seulement un gain de sensibilité [62], mais également des mécanismes de couplage entre dispositif plasmonique et photonique, en particulier la mise en évidence d'un dédoublement de mode en régime de couplage fort [63].
- Une cavité Fabry-Perot couplée à une nanoparticule [64], où l'expérience de détection a constitué à varier l'indice de l'interféromètre, au lieu de l'indice de l'environnement comme dans les travaux précédents.

1.3 Objectifs de ce travail

L'objectif de ce travail est d'étudier un nouveau type de dispositif hybride plasmonique/photonique, constitué d'un interféromètre de Si poreux et d'un réseau de nano-antennes papillon à sa surface (Fig. 1.3.1) :

- Le Si poreux combine les avantages d'une fabrication rapide, d'une grande versatilité en termes d'indice de réfraction et d'épaisseur, et de la porosité permettant l'infiltration d'espèces dans le dispositif ;
- Les nano-antennes papillon ont un design robuste qui permet la réalisation de gaps petits avec une bonne reproductibilité pour l'obtention de fortes amplifications de champ ; elles permettent également l'obtention de résonnances sur une grande gamme spectrale, notamment dans le proche infrarouge vers 1300 nm où les pertes dues au Si poreux sont fortement réduites.

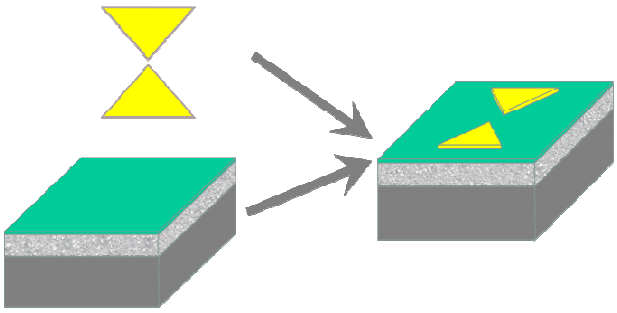

Fig 1.3.1 Vue schématique de la structure hybride considérée dans ce travail

1.3.1 Notre choix de dispositif

Le dispositif visé est composé des éléments suivants :

- Une monocouche de Si poreux d'environ 5 µm d'épaisseur et d'indice ~ 1.5 sur son substrat de Si ;
- Une fine couche d'espacement/protection en silice ;
- Un réseau périodique de nano-antennes papillon en or, avec une période de 800 nm, dont les paramètres et la réponse optique sont présentés dans la figure 1.3.2.

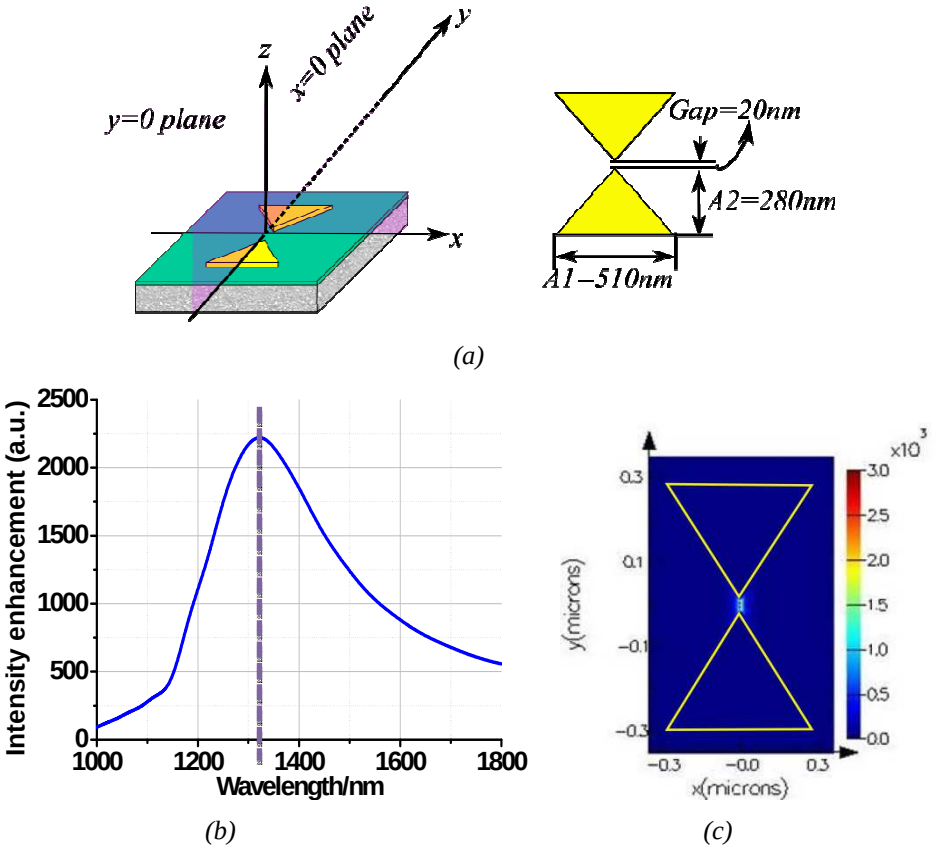

Fig 1.3.2: (a) Vue schématique de la nano-antenne papillon après optimisation sur substrat semi-infini d'indice 1.5; (b) Intensité de champ correspondante, calculée par FDTD (finite-difference time domain) et mettant en évidence la résonnance vers 1300 nm, et (c) distribution de champ à 1300 nm montrant la forte localisation d'énergie dans le gap. La structure est excitée en incidence normale par une onde plane polarisée suivant l'axe de la nano-antenne.

Quand la nano-antenne est placée sur l'interféromètre en Si poreux, la réponse optique est fortement modifiée, comme illustré dans la figure 1.3.3 :

- Le spectre de réflectivité présente à la fois la résonnance de la nano-antenne à 1300 nm, et les oscillations Fabry-Perot dus à l'interféromètre, qui sont fortement perturbées à la résonnance ;
- Les distributions de champs mettent en évidence les variations d'intensité dues aux interférences dans l'interféromètre, ainsi que la forte concentration de champ dans le gap de la nano-antenne.

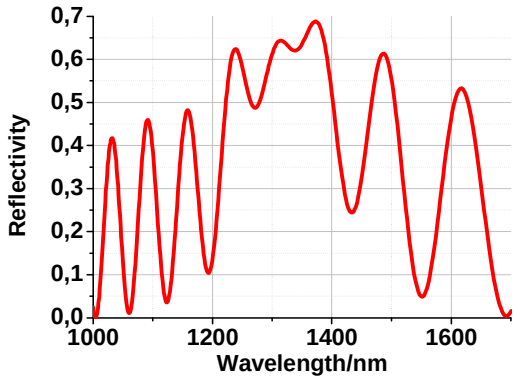

(a)

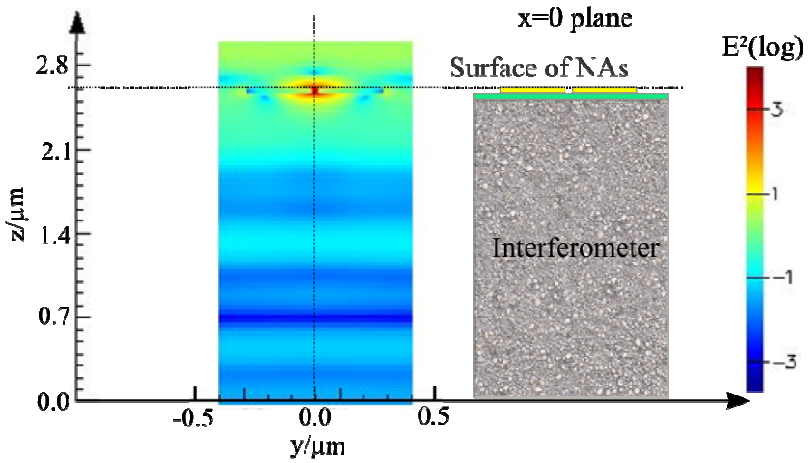

(b)

Fig 1.3.3: (a) Réflectivité du dispositif hybride excité par une onde plane polarisée suivant l'axe de la nano-antenne; (b) Distribution du champ électrique correspondant

Ces deux observations confirment la nature hybride du dispositif.

1.3.2 Objectifs de ce travail

Après l'optimisation des techniques expérimentales pour la fabrication et la caractérisation des dispositifs (chapitre 2), deux études successives seront menées :

- L'étude du couplage entre l'interféromètre et les nano-antennes (chapitre 3) : l'approche développée est basée sur des modèles phénoménologiques permettant une compréhension fondamentale des mécanismes optiques, et sur leur comparaison systématique avec des études expérimentales.
- L'étude du potentiel d'un tel dispositif hybride pour les applications capteurs (chapitre 4), via une variété d'expériences permettant d'évaluer, dans chaque cas, le gain de

sensibilité du dispositif hybride par rapport aux nano-antennes et à l'interféromètre considérés séparément.

Chapitre 2 Méthodes expérimentales

Afin d'étudier l'interaction entre le réseau de NA et l'interféromètre Fabry-Perot, les 3 systèmes présentés dans la figure 2.0.1 sont fabriqués et leurs réponses optiques comparées.

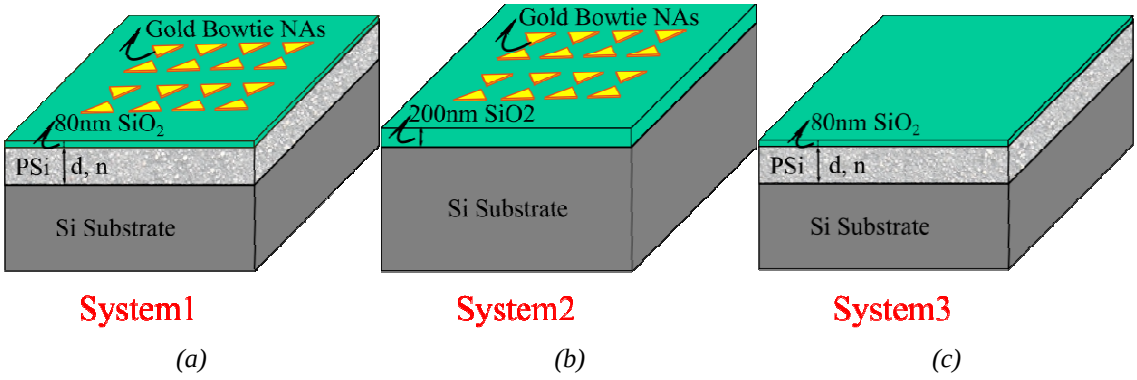

Fig 2.0.1 Vue schématique des 3 systèmes : (a) Structure hybride constituée de l'interféromètre, du spacer de silice et du réseau de NA ; (b) Réseau de NA seules sur substrat d'indice équivalent à la structure hybride : (c) interféromètre seul avec le spacer de silice.

Dans ce chapitre, les différentes techniques de fabrication et de caractérisation de ces 3 systèmes sont présentés, en particulier :

- Fabrication
  - Formation des couches de Si poreux par anodisation ;
  - Dépôt des couches de SiO_2 (par pulvérisation cathodique ou PECVD) ;
  - Fabrication des NA par lithographie électronique et lift-off ;
- Caractérisation optique
  - Caractérisation des couches de Si poreux par macro-réflectivité (détermination de l'indice de réfraction et de l'épaisseur) ;
  - Etude des propriétés optiques des 3 systèmes par micro-réflectivité/transmission.
  - Système micro-fluidique utilisé pour les expériences en milieu liquide, en particulier pour les études de détection.

2.1 Fabrication

2.1.1 Anodisation de Si poreux

L'anodisation de Si pour la fabrication des couches de Si poreux s'effectue dans la cellule électrochimique présentée dans la figure 2.1.1, suivant le principe détaillé dans la partie 1.1. Le substrat de silicium (100), fortement dopé (p+), est placé sur l'anode de cuivre en bas de la cellule. La cathode est une électrode en spirale en platine (inerte chimiquement) et est placée dans l'électrolyte en haut de la cellule. La cellule est remplie d'acide fluorhydrique à 35% (HF : eau : éthanol 35% : 35% : 30%). La densité du courant qui circule entre les deux électrodes est contrôlée de manière à contrôler la porosité du Si poreux. L'anodisation a été optimisée à basse température (-40°C) afin d'obtenir des couches de qualité bien maitrisée et des interfaces très planes.

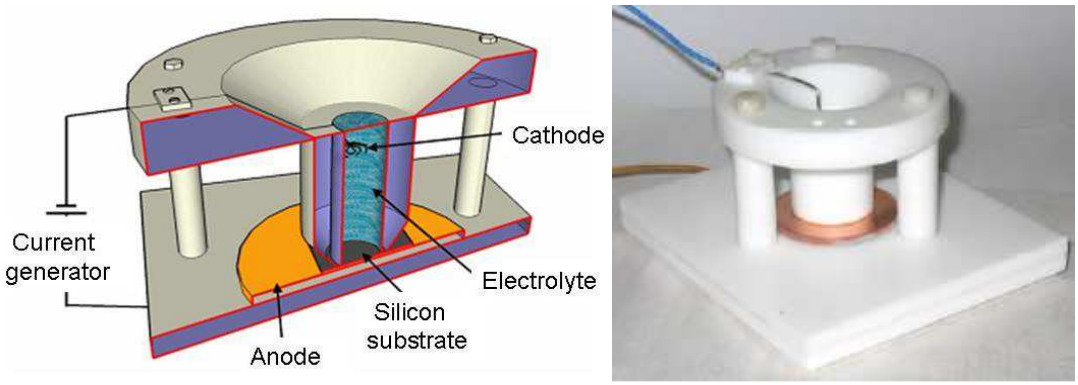

(a) *(b)*

Fig 2.1.1 (a) Vue schématique de la cellule d'anodisation; (b) Photo de la cellule [19,21]

2.1.2 Dépôt des couches de silice

Un spacer de silice de 80nm est inséré entre le Si poreux et le réseau de NA pour améliorer l'homogénéité et la qualité de fabrication des nanostructures d'or sur le Si poreux. La silice a été choisie pour son indice proche de l'indice souhaité pour le Si poreux (1.5) ainsi que pour sa compatibilité chimique avec les procédés de fabrication.

Dans le cas du Système 2 (NA seules) l'épaisseur de la couche de silice a été optimisée pour garantir une bonne isolation optique des NA vis-à-vis du substrat de Si.

Différentes techniques de dépôt de la silice ont été testées dans le cadre de ce travail, par PECVD et pulvérisation cathodique, dans des conditions variées, afin d'identifier les

conditions permettant d'obtenir la qualité de silice souhaitée. En particulier, la porosité de la silice peut ainsi être contrôlée, ce qui permet la fabrication de couches perméables ou imperméables suivant l'application souhaitée. Cette particularité sera exploitée dans le chapitre 4.

2.1.3 Fabrication des nano-antennes

La fabrication des NA se base sur des travaux antérieurs [40] et a été optimisée dans le cadre de cette thèse pour la fabrication de réseaux sur substrat de Si poreux. Le design souhaité des NA est présenté dans la figure 2.1.2. Les NA sont disposées périodiquement (période 800 nm) sur des champs de 50 x 50 µm. La base et la hauteur de chaque triangle constituant les NA font respectivement A1 = 540 nm et A2 = 280 nm. Le gap interstitiel de chaque NA fait 20 nm.

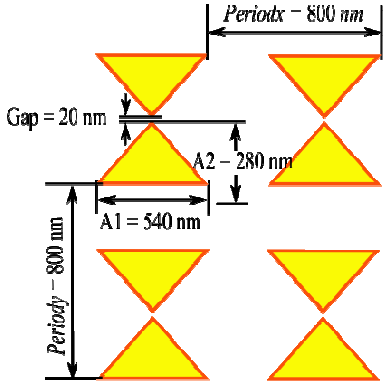

Fig 2.1.2 Design des NA

La fabrication des NA s'effectue par lithographie électronique, dépôt métallique puis lift-off suivant le procédé présenté dans la figure 2.1.3. La lithographie s'effectue avec une double-couche de résine (MMA/PMMA C2) afin de garantir les bons profils de résine souhaités pour le lift-off. Sur chaque substrat différents réseaux sont fabriqués en variant légèrement les designs de NA ainsi que les doses de lithographie, afin de compenser les fluctuations expérimentales et d'obtenir systématiquement un réseau présentant les paramètres et les propriétés souhaitées. Pour assurer une bonne adhérence de la couche d'or sur la silice, une couche d'accroche de titane est utilisée. Le lift-off est effectué en deux temps, tout d'abord une amorce dans une solution de trichloroéthylène chaud (60°C) puis le lift-off dans une solution d'acétone chaud (60°C).

La figure 2.1.3 illustre un exemple de réseau de NA fabriqué sur interféromètre de Si poreux.

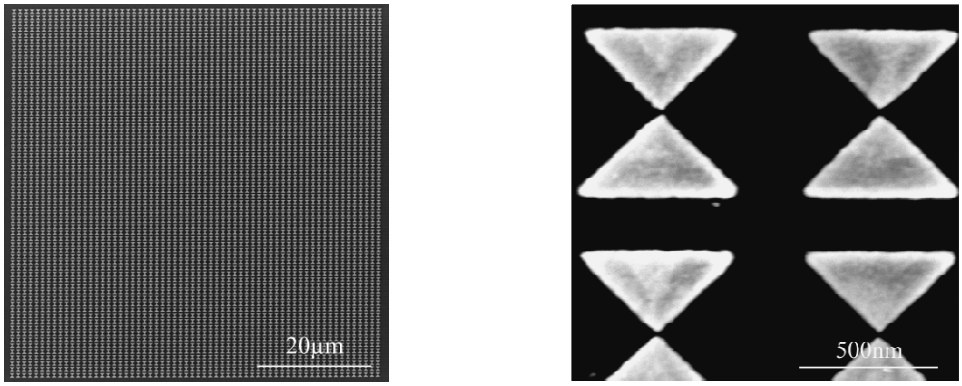

(a) *(b)*

Fig 2.1.3 Images MEB d'un réseau de NA: (a) réseau complet, (b) details.

2.2 Caractérisation optique

2.2.1 Caractérisation de Si poreux par macro-réflectivité

Le principe de la caractérisation des couches de poreux en macro-réflectivité est illustré dans la figure 2.2.1. Il consiste à mesurer puis analyser les interférences dans la couche de Si poreux excitée à incidence normale par une lampe blanche. Le chemin optique est directement lié à la distance inter-frange de la courbe de réflectivité, suivant l'expression :

$$nd = \frac{k/2}{\lambda_{m+k}^{-1} - \lambda_m^{-1}} \qquad \text{(EQ-2-1)}$$

Où n et d sont respectivement l'indice de réfraction et l'épaisseur de la couche, □m la longueur d'onde du maximum d'ordre m et k un entier.

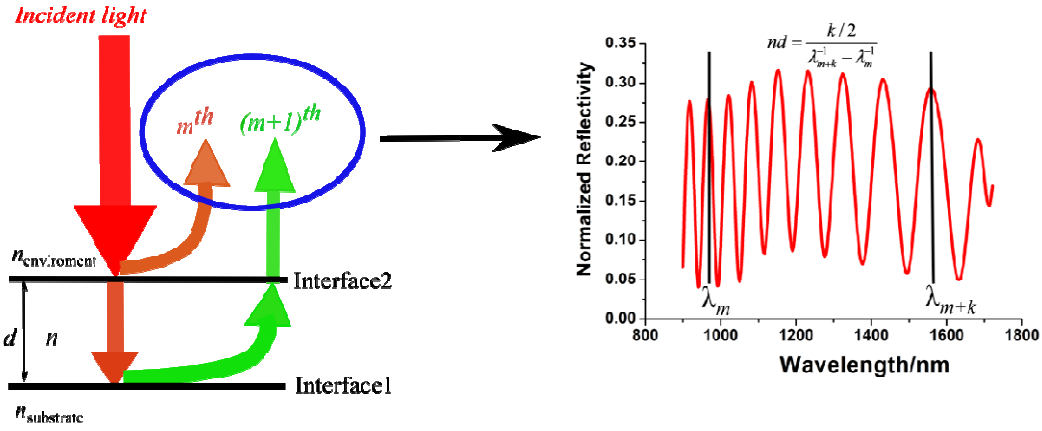

(a) *(b)*

Fig 2.2.1 (a) Principe de la caractérisation en macro-réflectivité ; (b) exemple de spectre

Différents programmes de fit ont été mis au point pour déduire les valeurs de n et d à partir des spectres de réflectivité.

Dans le cas d'une couche de Si poreux l'indice effectif est fonction des différents matériaux qui constituent le matériau. Comme présenté dans le chapitre 1, le modèle utilisé pour décrire notre matériau est celui de Landau-Lifshitz-Looyenga (LLL) (EQ-1-1).

Grâce à la détermination des valeurs de n et d, différentes informations sont déduites, en particulier l'homogénéité de chaque couche de Si poreux (en effectuant une cartographie par macro-réflectivité), ou encore le vieillissement des échantillons qui se traduit par une

diminution de l'indice avec le temps du fait de la formation d'une fine couche de silice à l'intérieur des pores du matériau. La fraction de silice formée PSiO2 peut également être déterminée par le modèle LLL et a été implémentée dans notre programme de fit. En connaissant la surface spécifique S du matériau (100 m2/cm3 dans le cas de notre Si mésoporeux d'indice 1.5), l'épaisseur de la couche de silice dSiO2 peut être extrapolée :

$$d_{SiO_2} = P_{SiO_2} / S \qquad \text{(EQ-2-2)}$$

2.2.2 Caractérisation des dispositifs par micro-réflectivité

La micro-réflectivité/transmission en incidence normale est utilisée pour l'étude en champ lointain du signal réfléchi ou transmis par les systèmes de dimensions microscopiques. Le principe du montage optique est présenté dans la figure 2.2.2. L'excitation est effectuée par une lampe blanche halogène, la détection par un spectromètre NIRQuest512. Le signal émis par la lampe est d'abord injecté dans une fibre multimode (105 µm de cœur) connectée à une lentille (focale 30 mm) pour une excitation en espace libre. Avec une focalisation via un objectif x20 d'ouverture numérique 0.4 la taille de faisceau incident sur l'échantillon est 30 µm, qui correspond à la zone d'homogénéité des réseaux de NA. Un contrôle de la polarisation est effectué à l'aide d'un polariseur IR (1200-1600 nm) pour assurer une excitation parallèle à l'axe des NA (E//) et des beam splitters sont insérés sur le trajet du faisceau pour séparer le signal incident du signal réfléchi vers le spectromètre, ainsi que le signal visible qui sert au positionnement de l'échantillon.

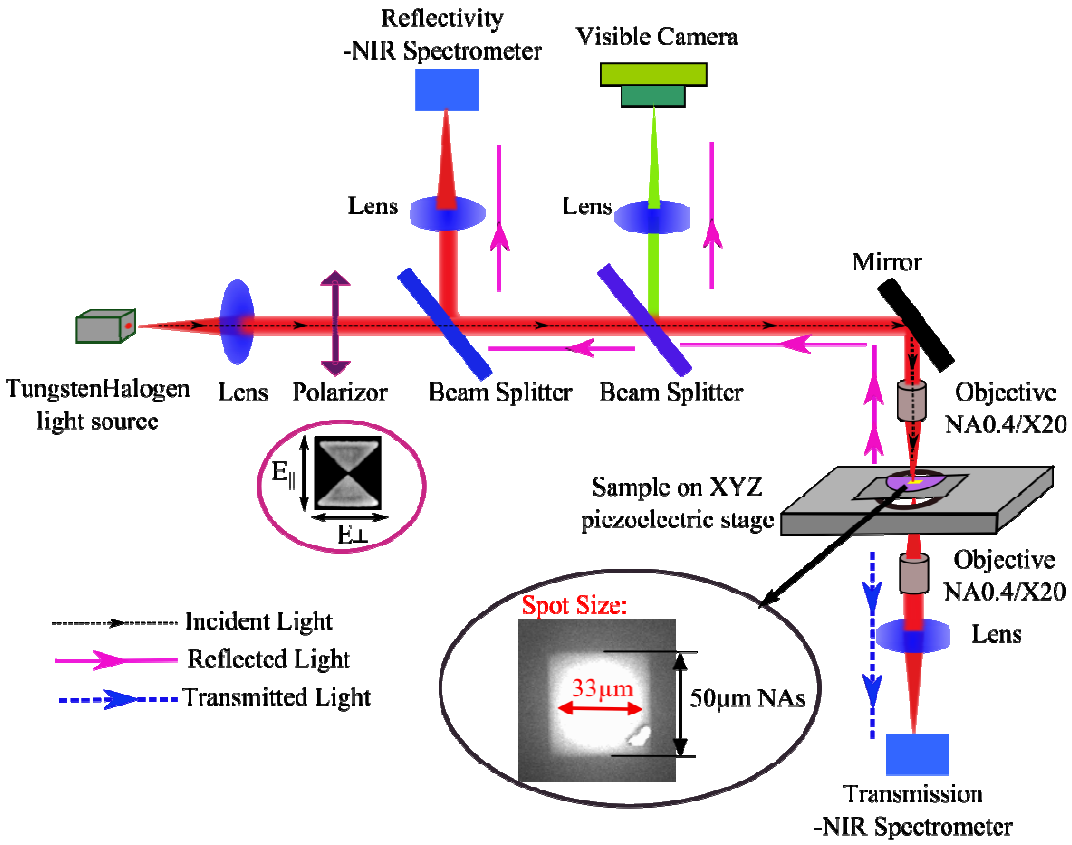

Fig 2.2.2 Schéma du montage optique utilisé en micro-réflectivité/transmission.

L'exploitation des spectres de réflectivité requière la normalisation par des spectres de référence. Deux types de références sont utilisés dans ce travail :

- la référence « absolue » mesurée sur un miroir d'Ag dans le cas de la réflectivité, et à travers une lame de verre dans le cas de la transmission ; l'inconvénient de cette normalisation est la variation de plan focal entre la référence et l'échantillon, qui introduit des artefacts sur la courbe normalisée.
- la référence « relative » par rapport au substrat, qui permet d'éviter ces artefacts ; c'est la solution préférée dans ce travail, sauf indication contraire dans els résultats qui seront présentés dans la suite.

Lors des expériences de détection réalisées au cours de cette thèse, la cellule fluidique présentée dans la figure 2.2.3 a été utilisée [65]. Elle est constituée de deux lames de verre séparée par un joint étanche, à l'intérieur duquel l'échantillon est positionné. Le maintien mécanique est assuré par deux cadres en aluminium assemblés par des vis, et la circulation des liquides se fait par des tubes flexibles qui traversent la lame de verre supérieure.

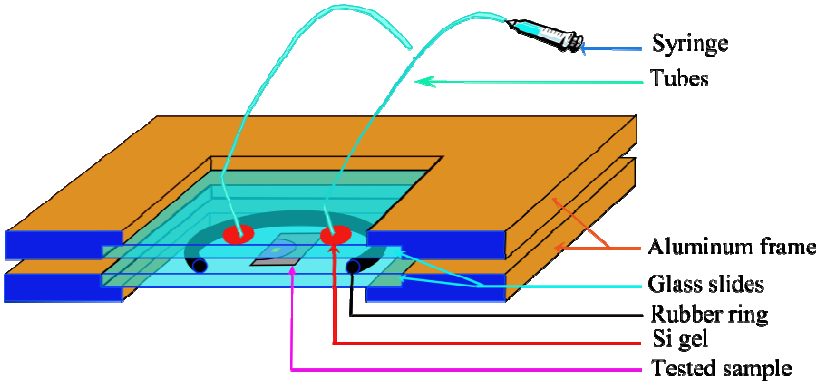

(a)

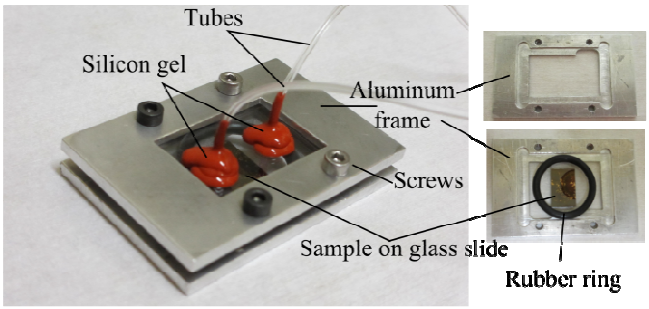

(b) *(c)*

Fig 2.2.3 Cellule fluidique utilisée pour les expériences en milieu liquide : (a) vue schématique, (b) photos.

Chapitre 3 Etude du couplage optique entre interféromètre et nano-antennes

Le but de ce chapitre est une étude fondamentale des interactions entre NA et interféromètre, notamment l'influence de l'interféromètre sur la réponse des NA, et l'influence du réseau de NA sur celle de l'interféromètre, à la résonance et hors résonance. Deux approches complémentaires ont été développées :

- Approche interférométrique : dans ce modèle le réseau de NA est considéré équivalent à une couche homogène de même épaisseur et même fonction diélectrique, celle-ci étant déterminée grâce à une généralisation du modèle de Drude (Fig. 3.0.1). L'influence du réseau de NA sur la réponse optique de l'interféromètre peut ainsi être étudiée par le développement d'un modèle basé sur les accords de phase dans la structure multicouche (phase matching model, PMM).

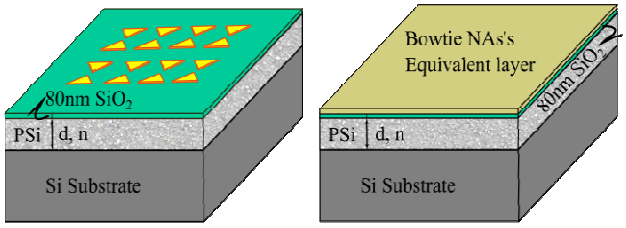

(a) *(b)*

Fig 3.0.1 Principe de la première approche : le système (a) est considéré comme une structure multicouche dans laquelle le réseau de NA est équivalent à une couche homogène de mêmes épaisseur et fonction diélectrique.

- Approche résonante : dans ce modèle le réseau de NA est considéré comme un oscillateur harmonique (Fig. 3.0.2), et le couplage entre NA et interféromètre est étudié par la théorie des modes couplés.

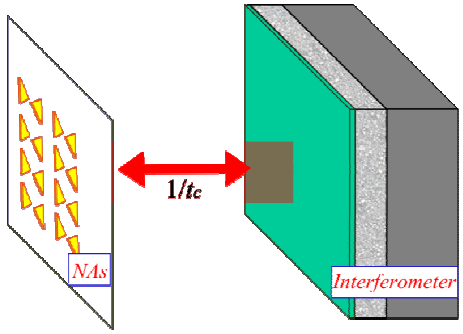

Fig 3.0.2 Approche résonante : le réseau de NA est vu comme un oscillateur couplé à l'interféromètre

3.1 Approche interférentielle

Dans cette partie le modèle pour l'étude des interactions dans le système multicouche est développé pas à pas. Après un rappel sur les bases des accords de phase dans un système interférométrique monocouche (modèle PMM), la structure est généralisée au cas d'un système bicouche, puis tricouche, et les fonctions diélectriques des structures métalliques sont introduites.

A chaque étape le modèle théorique développé est confronté aux résultats expérimentaux.

3.1.1 Modèle interférométrique

- Système monocouche :

Le principe du système interférentiel a été présenté au chapitre 2 dans la caractérisation par macro-réflectivité (Fig. 2.2.1). D'une manière générale, la différence de phase $\Delta\varphi 1$ entre les faisceaux réfléchis aux deux interfaces d'une couche interférométrique est :

$$\Delta\varphi_1 = \frac{4\pi}{\lambda} n_2 d \qquad \text{(EQ-3-1-1)}$$

avec n_2 et d l'indice et l'épaisseur de la couche. L'interféromètre considéré ici est la monocouche de Si poreux ($n_2 = n_{PSi}$) sur son substrat de Si cristallin (n_{Si}) dans un environnement extérieur d'air ($1 < n_{PSi} < n_{Si}$). Les conditions d'accord de phase (PMM) qui indiquent que la réflectivité R du système est maximale (Rmax) pour la frange d'ordre m à la longueur d'onde $\lambda max1$ s'expriment de la manière suivante [66]:

$$R = R_{\max} \quad \Delta\varphi_1 = 2m\pi, \quad m = 0, \pm 1, \pm 2, \ldots \quad \lambda_{\max 1} = \frac{4n_{PSi}d}{2m} \qquad \text{(EQ-3-1-2)}$$

Les spectres de réflectivité de nos structures sont simulés par la méthode des matrices de transfert (TMM) [67]. Les paramètres des structures sont déterminés par les fits des courbes de réflectivité expérimentales, dans lesquelles les fractions volumiques des différents matériaux constituant le Si poreux (air, Si et oxyde natif) sont calculées en considérant que les indices de ces matériaux suivent une loi de Cauchy dans le domaine spectral considéré [33].

Un exemple est donné dans la figure 3.1.1. La parfaite adéquation sur la position des maxima entre résultats expérimentaux et résultats déterminés par simulation est une validation des modèles de fit et de la simulation TMM.

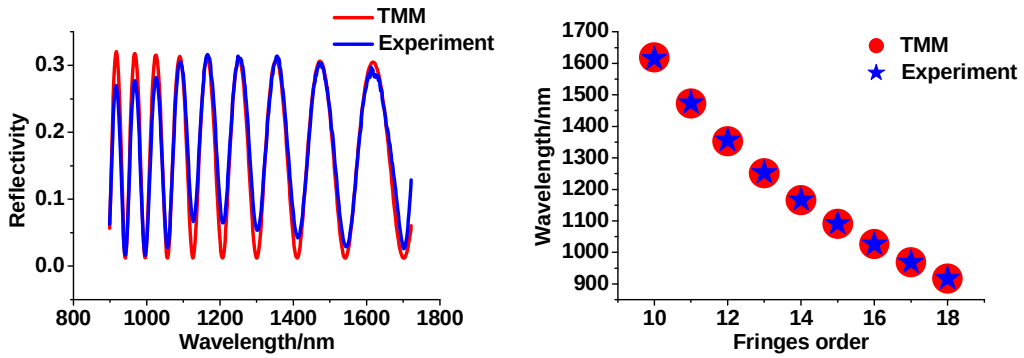

(a) *(b)*

Fig 3.1.1. Comparaison entre les résultats expérimentaux et la simulation TMM utilisant les paramètres déduits des fits pour une couche de Si poreux d'épaisseur 4.85 µm, et de fractions volumiques 53% pour l'air et 19% pour l'oxide natif, respectivement: (a) spectres de réflectivité, (b) position des maximas, l'ordre des frange est déduit des conditions PMM (EQ-3-1-2).

- Système bicouche :

Les conditions PMM dans le cas d'un système multicouche deviennent beaucoup plus complexes et sont décrites en détail en annexe (Appendix A). Dans le cas présent, on considère que la deuxième couche (le spacer de silice) est extrêmement fine, d'absorption faible et d'indice proche de celui de l'interféromètre, ce qui permet de déduire l'approximation suivante :

$$\frac{4\pi(n_{PSi}d_{PSi} + n_{SiO_2}d_{SiO_2})}{\lambda_{2\max}} = 2m\pi \qquad \text{avec} \quad \lambda_{2\max} > \lambda_{1\max} \qquad \text{(EQ-3-1-3)}$$

Cette condition indique que pour un ordre m donné, la présence de la couche de silice devrait conduire à un shift vers le rouge des franges par rapport au système monocouche initial.

La structure expérimentale considérée correspond au système 3 (Fig. 2.0.1), avec 80 nm de silice dont l'indice est à nouveau déterminé grâce à une loi de Cauchy. Les résultats expérimentaux sont confrontés aux simulations TMM et illustrés dans la Fig. 3.1.2 pour la même structure que celle présentée dans la Fig. 3.1.1. La comparaison avec le système monocouche initial (Fig. 3.1.2b) met en évidence le shift vers le rouge des franges.

Afin de valider les approximations effectuées dans le modèle PMM, les positions des maximas déduits des spectres expérimentaux et simulés sont comparées à celles prédites par l'équation EQ-3-1-3. On voit que l'écart obtenu □2 est négligeable et comparable aux erreurs dues aux imperfections expérimentales.

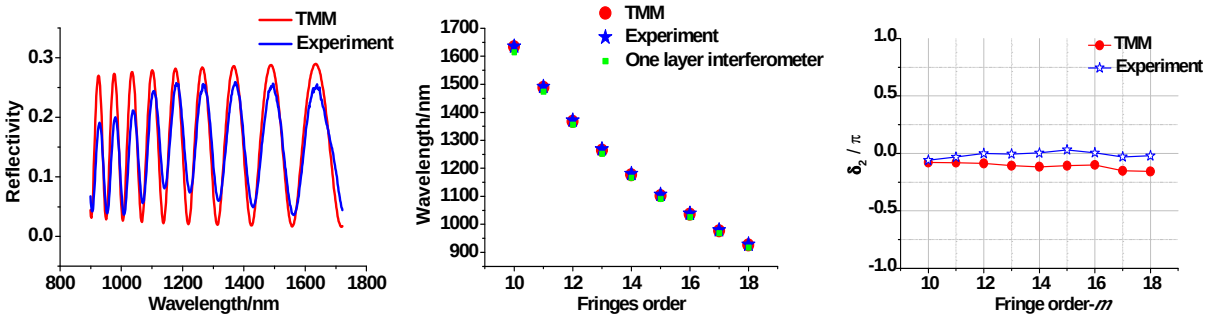

(a) *(b)* *(c)*

Fig 3.1.2 Comparaison entre les résultats expérimentaux et la simulation TMM pour le système bicouche (l'interféromètre est le même que dans la figure 3.1.1): (a) spectres de réflectivité, (b) position des maximas, (c) écart entre la position des maximas et la prédiction du modèle PMM (EQ-3-1-3).

- Système tricouche avec couche homogène métallique :

Ce sytème est un cas limite de notre structure hybride hors résonance des NA. A nouveau le développement exact du modèle est détaillé dans l'annexe (Appendix A). Dans le cas présent on peut faire l'approximation d'une couche d'or extrêmement fine, dont l'indice va avoir deux influences, d'une part la partie réelle Re (n_{Au}) entraine des variations de chemin optique (comme dans le cas du spacer de silice), et d'autre part la partie imaginaire non-nulle due à l'absorption entraine un déphasage additionnel aux interfaces de la couche de métal $\Delta\varphi_{interface}$. Dans cette approximation, le modèle PMM devient :

$$\frac{4\pi\left[n_{PSi}d_{PSi}+n_{SiO_2}d_{SiO_2}\right]}{\lambda_{3\max}}+\Delta\varphi_{tot}=2m\pi \quad \text{avec} \quad \Delta\varphi_{tot}=4\pi\frac{\mathrm{Re}\left(n_{Au}\right)}{\lambda_3}d_{Au}+\Delta\varphi_{interface} \qquad \text{(EQ-3-1-4)}$$

On peut montrer (cf. Appendix A) que pour une couche homogène métallique on a $\Delta\varphi_{tot}<0$ Le décalage des franges induit par la présence de la couche d'or sur le système bicouche Si/SiO_2 est donné par :

$$\frac{n_{PSi}d_{PSi}+n_{SiO_2}d_{SiO_2}}{\lambda_{2\max}}=\frac{n_{PSi}d_{PSi}+n_{SiO_2}d_{SiO_2}}{\lambda_{3\max}}+\frac{\Delta\varphi_{tot}}{4\pi} \qquad \text{d'où } \lambda_{3\max}<\lambda_{2\max} \qquad \text{(EQ-3-1-5)}$$

Dans ce cas on s'attend à un shift vers le bleu des franges d'interférence, qui est vérifié expérimentalement, comme illustré dans la Fig. 3.1.3. En supposant que l'écart entre le modèle présenté dans l'équation EQ-3-1-4 et les valeurs des maximas déduites des spectres est négligeable (comme démontré précédemment pour le cas du bicouche), on peut déduire la valeur de $\Delta\varphi_{tot}$. On voit dans la Fig. 3.1.3c que cette valeur est quasi constante (aux fluctuations expérimentales près) et d'environ -0.75π, ce qui est très proche de la prédiction théorique démontrée dans l'Appendix A et qui est également reportée dans la figure pour comparaison.

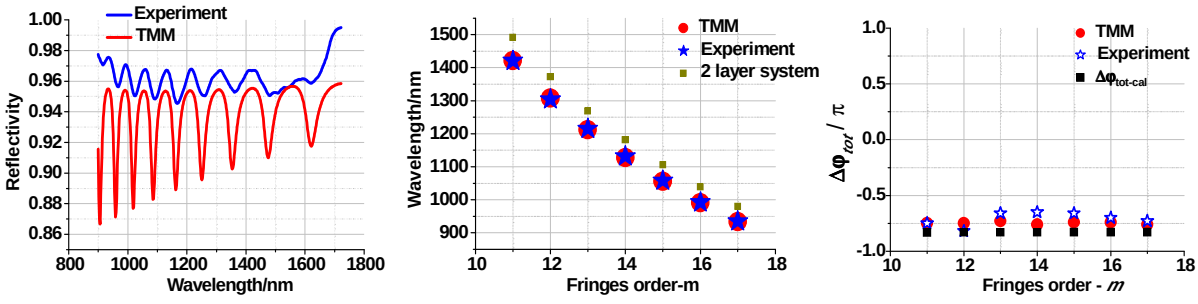

(a) *(b)* *(c)*

Fig 3.1.3 Comparaison entre les résultats expérimentaux et la simulation TMM pour le système tricouche avec couche homogène d'or : (a) spectres de réflectivité, (b) position des maximas, (c) valeur de $\Delta\varphi_{tot}$ déduite du modèle (EQ-3-1-4).

3.1.2 Interféromètre avec couche de nano-antennes

- Modèle de Drude généralisé aux NA :

Il a été démontré [68] qu'il existe une analogie entre les déplacements électroniques dans le gap entre les deux triangles d'une NA papillon et les transitions inter-bandes d'électrons liés dans un métal sous rayonnement électromagnétique. On peut donc décrire les propriétés optiques d'une NA en adaptant le modèle de Drude-Sommerfeld [69] :

$$\varepsilon(\omega)=\varepsilon_{\infty}+\frac{\tilde{\omega}_p^2}{\omega_0^2-\omega^2-i\gamma\omega};\quad \mu=1\quad ;\ \tilde{\omega}_p=\sqrt{\tilde{n}e^2/m\varepsilon_0}\quad ;\ \omega_0=\sqrt{\alpha/m} \qquad \text{(EQ-3-1-6)}$$

où ε_∞ est la constante diélectrique aux grandes énergies, γ est l'atténuation, $\tilde{\omega}_p$ est la fréquence plasma équivalente, $\tilde{n}$ la densité et m la masse effective des électrons liés, et α la raideur.

Dans le cas de nos réseaux de NA, les valeurs de $\varepsilon_\infty, \omega_p$ et γ ont été déterminées par un fit des spectres expérimentaux obtenus pour le système 2 (NA seules sur substrat), en confrontant ces spectres à ceux obtenus par simulation TMM utilisant l'équation EQ-3-1-6 pour décrire la fonction diélectrique du réseau de NA. Le meilleur accord a été obtenu pour les valeurs suivantes : $\varepsilon_\infty = 3$ [70], $\omega_p = 2\times10^{15}/s$, $\gamma = 4\times10^{13}/s$, pour la longueur d'onde λ_0 = 1300 *nm* (correspondant à $\omega_0 = 1.43\times10^{15}/s$). Les variations de la fonction diélectrique sont présentées dans la Fig. 3.1.4. Elles sont très similaires à celles décrites par le modèle de Drude, en particulier à la résonance (1300 nm) on observe de fortes variations des parties réelles et imaginaires.

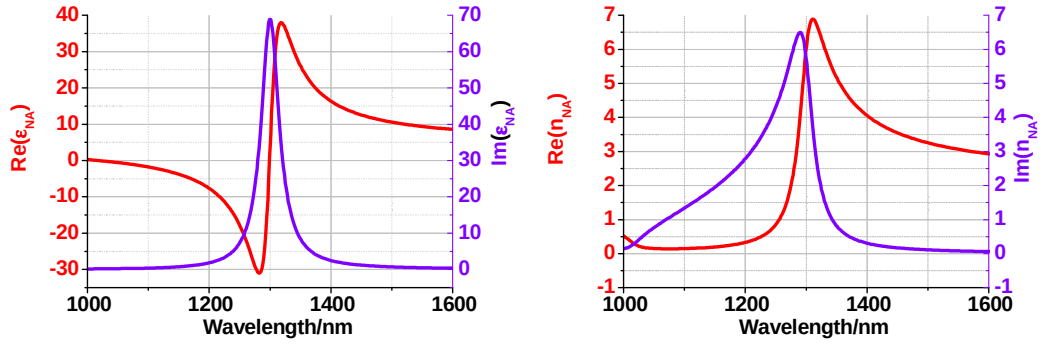

(a) *(b)*

Fig 3.1.4 Fonction diélectrique du réseau de NA : (a) constante diélectrique effective, (b) indice de réfraction effectif

- Modèle PMM pour le système tricouche PSi/SiO_2/NA :

Il est très similaire à celui déduit dans le cas de la couche d'or homogène :

$$\frac{4\pi\left[n_{PSi}d_{PSi} + n_{SiO2}d_{SiO2} + \mathrm{Re}(n_{NA})d_{NA}\right]}{\lambda_{3\max}} + \Delta\varphi_{\mathrm{int}\,erface} = 2m\pi \qquad \text{(EQ-3-1-7)}$$

La comparaison avec le système bicouche Si/SiO_2 permet de prédire le comportement des franges :

$$4\pi\left(n_{PSi}d_{PSi}+n_{SiO_2}d_{SiO_2}\right)\left(\frac{1}{\lambda_2}-\frac{1}{\lambda_3}\right)=\Delta\varphi_{tot} \quad \text{avec } \Delta\varphi_{tot}=4\pi\frac{\mathrm{Re}\left(n_{NA}\right)}{\lambda_3}d_{NA}+\Delta\varphi_{interface} \text{ (EQ-3-1-8)}$$

On en déduit :

→ Un shift vers le bleu ($\lambda_3<\lambda_2$), si $\Delta\varphi_{tot}<0$

→ Un shift vers le rouge ($\lambda_3>\lambda_2$), si $\Delta\varphi_{tot}>0$

Le comportement des franges dépend donc des variations respectives de $\Delta\varphi_{interface}$ et Re(n_{NA}). Comme démontré dans l'Appendix A, la valeur de $\Delta\varphi_{tot}$ peut être déduite de la fonction diélectrique des NA en utilisant les équations de Fresnel. On obtient les variations présentées dans la Fig. 3.1.5

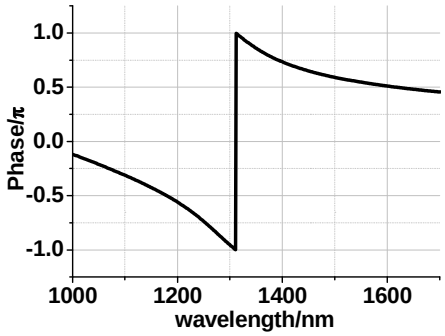

Fig 3.1.5 Variations de $\Delta\varphi_{tot}=4\pi\frac{\mathrm{Re}\left(n_{NA}\right)}{\lambda_3}d_{NA}+\Delta\varphi_{interface}$ *déduites de la fonction diélectrique du réseau de NA présentée dans la Fig. 3.1.4.*

Ces variations montrent clairement plusieurs comportements différents suivant la gamme spectrale considérée :

→ Avant la résonance (λ < 1300 nm): $\Delta\varphi_{tot}<0$. Dans cette région, on attend un shift vers le bleu des franges.

→ A la résonance (λ ≈ 1300 nm), $\Delta\varphi_{tot}$ varie abruptement de –π à +π.

→ Après la résonance (λ > 1300 nm): $\Delta\varphi_{tot}>0$. Dans cette région, on attend un shift vers le rouge des franges.

- Simulation du spectre de réflectivité du système tricouche PSi/SiO_2/NA :

Afin de vérifier le comportement déduit de la Fig. 3.1.5, des simulations TMM ont été effectuées en utilisant la fonction diélectrique de la Fig. 3.1.4, et sont illustrées dans la Fig. 3.1.6.

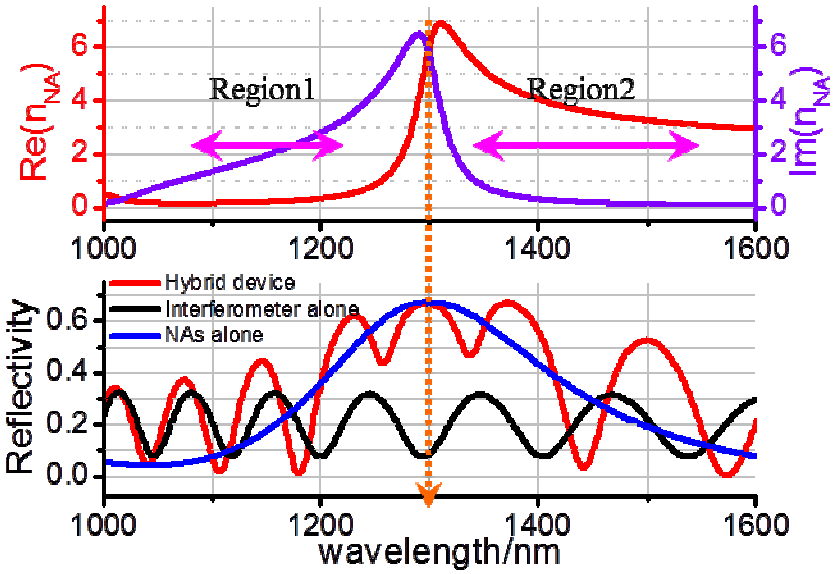

Fig 3.1.6 Résultats des simulations TMM pour le système 1 (PSi/SiO_2/NA) effectuées en utilisant la fonction diélectrique présentée à nouveau en haut de la figure, et comparées aux systèmes 2 (NA seules) et 3 (PSi/SiO_2).

On observe notamment :

→ Une augmentation de l'intensité des franges qui coïncide bien avec la résonance des NA

→ Une plus grande amplitude des franges pour le système 1 que pour le système 3, qui peut être relié à l'indice effectif plus élevé de la couche de NA

→ Un décalage des franges différent suivant la gamme spectrale : avant résonance (région 1), décalage vers le bleu des franges du système 1 par rapport au système 3 ; après résonance (région 2), décalage vers le rouge. Ces comportements sont en accord avec les prédictions déduites du modèle PMM.

→ A la résonance, apparition d'une frange supplémentaire due à une dégénérescence attribuée aux fortes variations de la fonction diélectrique. Cette dégénérescence est confirmée par la détermination des ordres des franges déduite du modèle

PMM : deux franges successives d'ordre identique sont obtenues à la résonance. Ce phénomène a également été observé dans la littérature pour des systèmes hybrides photoniques/plasmoniques et attribués à un couplage fort entre le plasmon et le mode de cavité [63].

- Influence de l'interféromètre sur le splitting:

Si le phénomène de splitting résulte bien d'un couplage fort entre l'interféromètre et les NA, l'amplitude du splitting doit pouvoir être variée en fonction de la force de ce couplage, donc en variant les paramètres de l'interféromètre.

Ceci est illustré dans la Fig. 3.1.7, qui montre l'évolution du splitting en fonction de l'indice de l'interféromètre (pour une épaisseur de PSi constante).

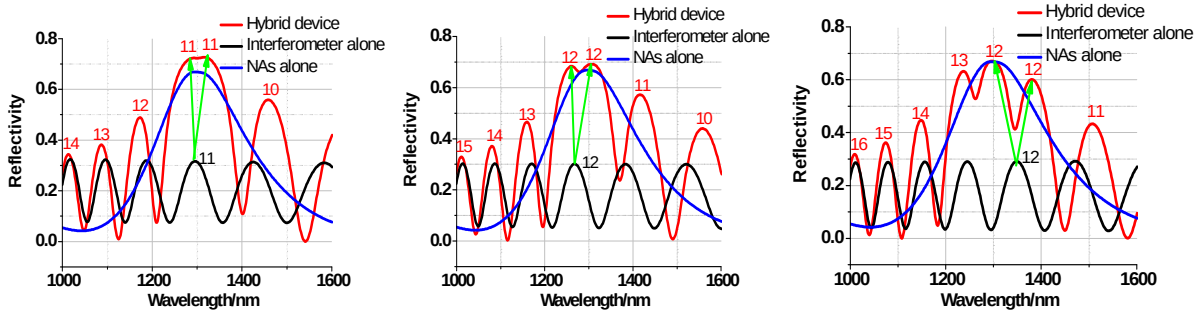

(a) $n_{PSi}=1.4$, $d_{PSi}=5\mu m$ *(b)* $n_{PSi}=1.5$, $d_{PSi}=5\mu m$ *(c)* $n_{PSi}=1.6$, $d_{PSi}=5\mu m$

Fig 3.1.7 Simulations TMM montrant l'évolution du splitting en fonction de l'indice de l'interféromètre.

On voit que suivant la valeur de l'indice, donc suivant le chemin optique dans l'interféromètre, l'ordre des franges dégénérées varie et ces franges sont plus ou moins rapprochées : 23 nm, 47 nm et 84 nm, respectivement, pour l'indice 1.4, 1.5 et 1.6. Ceci indique un couplage plus ou moins fort entre l'interféromètre et les NA. Des résultats similaires sont obtenus en variant l'épaisseur de l'interféromètre à indice constant, et ces résultats sont parfaitement reproduits dans les spectres expérimentaux.

Un couplage fort entre NA et interféromètre n'est possible que si les maximas de champs des modes plasmoniques et photoniques coïncident. Afin d'expliquer l'origine de la différence de couplage en fonction du chemin optique, on considère donc les distributions de champs dans l'interféromètre. Dans la Fig. 3.1.8, on observe qu'un maximum de réflectivité (λ = 1341 nm) correspond à un minimum de champ à la surface de l'interféromètre : dans ce cas défavorable

qui correspond à celui de la Fig. 3.1.7a, le couplage entre NA et interféromètre doit être faible. C'est en effet le cas : dans la Fig. 3.1.7a, les franges sont très proches, le splitting est faible. Dans l'autre cas correspondant à un minimum de réflectivité (λ = 1292 nm) similaire à celui de la Fig. 3.1.7c, le champ est maximal à la surface, donc on est dans les conditions pour un bon recouvrement des champs de l'interféromètre et des NA ; un couplage plus fort est attendu avec un écartement des franges, qui est confirmé dans la Fig. 3.1.7c.

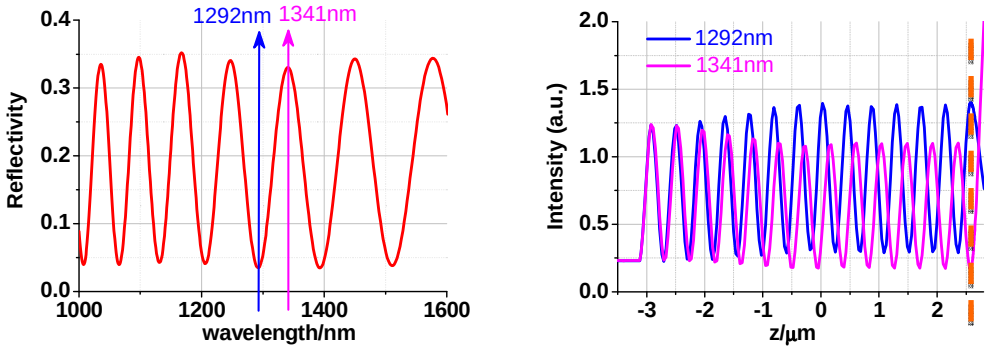

Fig 3.1.8 Correspondance entre intensité réfléchie (gauche) et distribution de champ E^2 dans l'interféromètre (droite).La ligne en pointillés orange indique la position de la surface.

3.2 Approche résonante: modes couplés

Dans cette seconde approche illustrée dans la Fig. 3.2.1, le réseau de NA est considéré comme un oscillateur harmonique en interaction avec une onde plane.

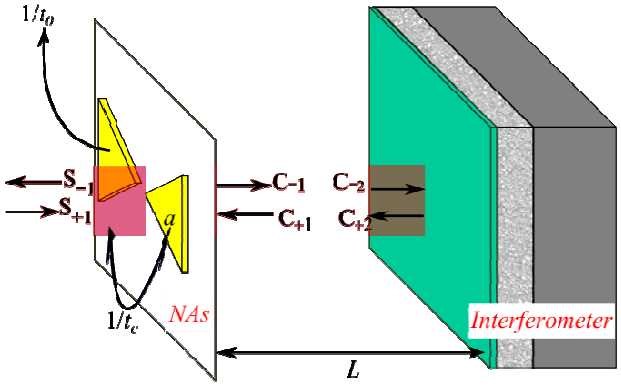

Fig 3.2.1 Illutration de l'approche résonante : a est l'amplitude complexe du mode résonant, $S_{\pm i}$ et $C_{\pm i}$ sont les amplitudes des ondes planes se propageant dans le système dans les directions directes et inverses, L est la distance entre le plan des NA et l'interféromètre, $1/\tau_0$ est le taux de pertes optiques intrinsèques des NA et $1/\tau_c$ est le taux de couplage entre les NA et les modes propagatifs.

- Théorie des modes couplés :

La théorie des modes couplés (CMT) décrit la cinétique des interactions entre NA et interféromètre par l'équation suivante :

$$\frac{da}{dt} = (j\omega_0 - 1/\tau_c - 1/\tau_0)a + KS_{+1} + KC_{+1} \qquad \text{(EQ-3-2-1)}$$

Avec ω_0 la pulsation de résonance des NA et K le coefficient de couplage entre les ondes planes et le résonateur. Selon la loi de conservation de l'énergie, on a les relations suivantes :

$$S_{-1} = C_{+1} - K^* a \qquad C_{-1} = S_{+1} - K^* a \qquad K = \sqrt{\frac{1}{\tau_c}} e^{j\theta} \qquad \text{(EQ-3-2-2)}$$

Après transformation de Fourier, il est possible de déduire la matrice de transfert entre les composantes $\begin{bmatrix} S_{+1} \\ S_{-1} \end{bmatrix}$ et $\begin{bmatrix} C_{-1} \\ C_{+1} \end{bmatrix}$:

$$M_r = \begin{bmatrix} 1-\dfrac{C}{1-C} & \dfrac{-C}{1-C} \\ \dfrac{C}{1-C} & \dfrac{1}{1-C} \end{bmatrix} \quad \text{avec} \quad C = \frac{|K|^2}{j\omega - j\omega_0 + \dfrac{1}{\tau_0} + \dfrac{1}{\tau_c}} \qquad \text{(EQ-3-2-3)}$$

Avec ω la pulsation du signal d'entrée.

Cette matrice de transfert *Mr* peut ensuite être injectée dans la simulation TMM pour déterminer les caractéristiques spectrales des systèmes étudiés. On définit les facteurs de qualité de couplage Q_c et de pertes intrinsèques Q_0 : $Q_c = \omega_0 \tau_c / 2$, $Q_0 = \omega_0 \tau_0 / 2$, et le facteur de qualité total $Q = \left(Q_c^{-1} + Q_0^{-1}\right)^{-1}$. Ces facteurs de qualité Q_0 et Q_c ainsi que la pulsation de résonance ω_0 sont les 3 paramètres influençant le comportement du système. En particulier, on peut réécrire l'équation EQ-3-2-3 de la manière suivante :

$$C = \frac{1}{1+\dfrac{Q_c}{Q_0}} \frac{1}{1+ j2Q\dfrac{\omega-\omega_0}{\omega_0}} \qquad \text{(EQ-3-2-4)}$$

- Influence des facteurs de qualité sur la réponse des NA :

On considère dans un premier temps le réseau des NA seules pour étudier l'influence des facteurs de qualité sur le couplage des NA avec le mode propagatif. La longueur d'onde de résonance étant fixée à λ_0 = 1325 nm, le facteur de qualité *Q* est d'abord varié à Q_c/Q_0 fixe (Fig. 3.2.2a), puis le rapport Q_c/Q_0 est varié à *Q* fixe (Fig. 3.2.2b).

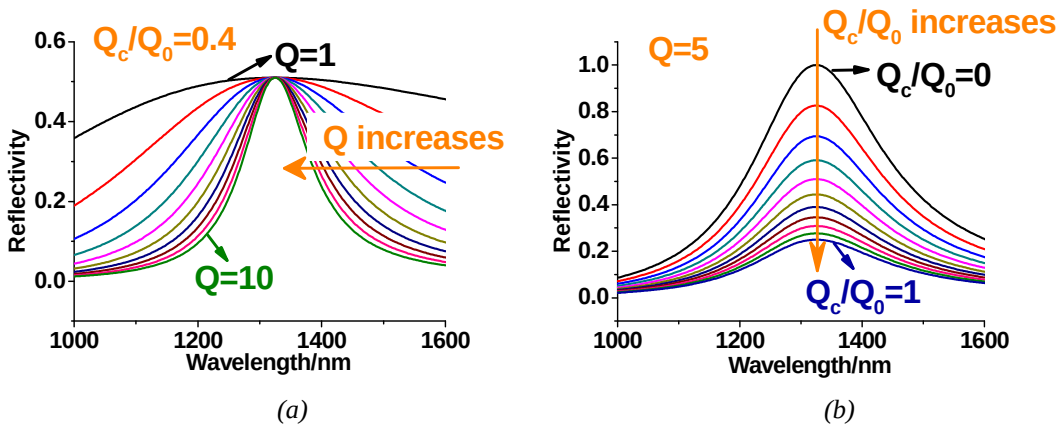

(a) *(b)*

Fig. 3.2.2 Réflectivité des NA à la longueur d'onde 1325 nm : (a) pour Qc/Q0 = 0.4, et Q variable, (b) pour Q = 5 et Qc/Q0 variable.

On déduit de la Fig. 3.2.2 que la bande passante de la résonance est entièrement déterminée par $1/Q$, qui représente les pertes totales des NA. A Q fixé, l'amplitude de la résonance dépend du rapport Q_c/Q_0 : si $Q_c << Q_0$, l'onde incidente est entièrement réfléchie à la résonance et aucune absorption ne se produit, indiquant un mauvais couplage avec la NA ; si $Q_c = Q_0$, le couplage est « critique » et optimal, on a 25% de la puissance incidente qui est réfléchie, 25% transmise et 50% absorbée ou diffusée.

Afin de déterminer le régime dans lequel se trouve les dispositifs expérimentaux, des fits des spectres de résonance ont été effectués en variant les valeurs des facteurs de qualité dans les simulations CMT et en les comparant aux spectres expérimentaux. Le meilleur accord est trouvé pour $Q = 2.2$ et $Q_c/Q_0 = 0.3$. A noter que ces valeurs sont similaires pour les NA seules et le système hybride, et que le splitting des franges à la résonance observé avec les simulations CMT reproduit également les résultats expérimentaux.

- Influence de la fréquence de résonance sur la réponse du système hybride :

La longueur d'onde de résonance λ_{NA} est un paramètre crucial qui va influencer la position respective des franges et de la résonance, et donc la force du couplage entre NA et interféromètre. En variant cette longueur d'onde de résonance on s'attend à observer un comportement du splitting similaire à celui discuté dans le paragraphe 3.1.2. C'est en effet le cas, comme illustré dans la Fig. 3.2.3 : le splitting est faible (couplage faible) lorsque la longueur d'onde de résonance coïncide avec un maximum de réflectivité de l'interféromètre, et il est fort (couplage fort) lorsque λ_{NA} coïncide avec un minimum de réflectivité de l'interféromètre.

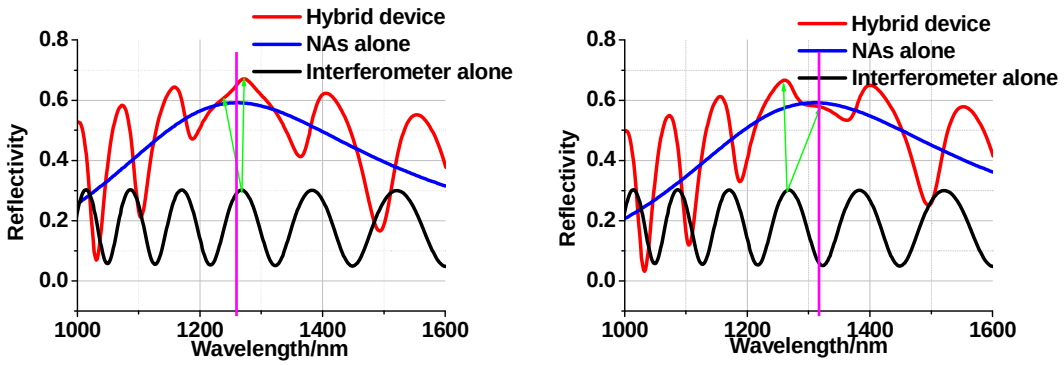

(a) λ_{NA} = 1260 nm *(b) λ_{NA} = 1310 nm*

Fig. 3.2.3 Variations du splitting en fonction de la fréquence de résonance pour un interféromètre donné ($n_{Psi} = 1.5$ et $d_{PSi} = 5\ \mu m$)

Ces résultats sont également en accord avec les résultats expérimentaux.

Chapitre 4 Application aux capteurs

Il a été démontré au chapitre 3 que le couplage entre NA et interféromètre induit une structuration de la résonance plasmon par les franges d'interférence, avec une augmentation de l'amplitude de ces franges par rapport à celles de l'interféromètre. De plus un décalage spectral des franges ainsi qu'un splitting ont été mis en évidence. Le but de ce chapitre est d'étudier le potentiel de ces caractéristiques optiques pour des applications à la détection en comparant avec les deux systèmes pris séparément (l'interféromètre seul et les NA sur substrat).

Les expériences de détection envisagées visent à détecter des variations du milieu environnant : faibles/fortes variations d'indice, détection de vapeur.

4.1 Détection de larges variations d'indice

Plusieurs expériences ont été effectuées pour étudier la détection de larges variations d'indice du milieu environnant : détection de liquide et détection d'une couche additionnelle sur la structure.

Nous présentons ici la détection d'une couche de résine PMMA déposée sur la surface de l'interféromètre/des NA.

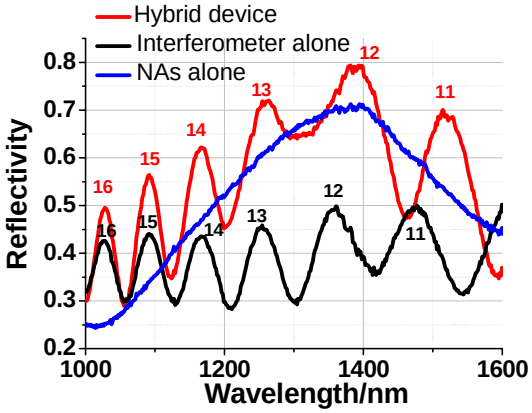

Fig. 4.1.1 Réflectivité initiale des 3 systèmes dans l'air

Les 3 systèmes sont d'abord étudiés à l'air, puis la couche de PMMA est déposée. Les spectres initiaux mesurés avant dépôt de PMMA sont présentés dans la Fig. 4.1.1. La résonance plasmon des NA se situe vers 1350 nm avec une bande passante de 470 nm. Le splitting se produit pour la frange d'ordre 12 sous la forme d'une frange élargie (couplage faible dans ce cas).

Après dépôt de 240 nm de 950 PMMA C2, les spectres présentés dans la Fig. 4.1.2 sont obtenus.

On remarque que la présence de PMMA induit un décalage très important de la résonance plasmon de 1350 nm à 1600 nm, ce qui démontre la forte sensibilité des NA à leur environnement ; Le shift vers le rouge s'explique par l'augmentation d'indice de la couche par rapport à l'air initial. Un shift est également observé dans le cas de l'interféromètre, de 1370 nm à 1410 nm pour la frange d'ordre 12. A nouveau le shift vers le rouge s'explique par l'augmentation d'indice de la couche, en accord avec le modèle développé dans le chapitre 3.

Les décalages vers le rouge sont également observés dans le cas du système hybride, à la fois pour la résonance plasmon (décalage du pic et des régions autour de la résonance où les franges sont amplifiées) et pour les franges hors résonance. A la résonance, les décalages de franges sont différents, d'une part à cause du splitting qui intervient pour un ordre différent dans les deux cas (ordre 12 à l'air et ordre 11 avec PMMA) et d'autre part à cause de la variation abrupte de fonction diélectrique des NA.

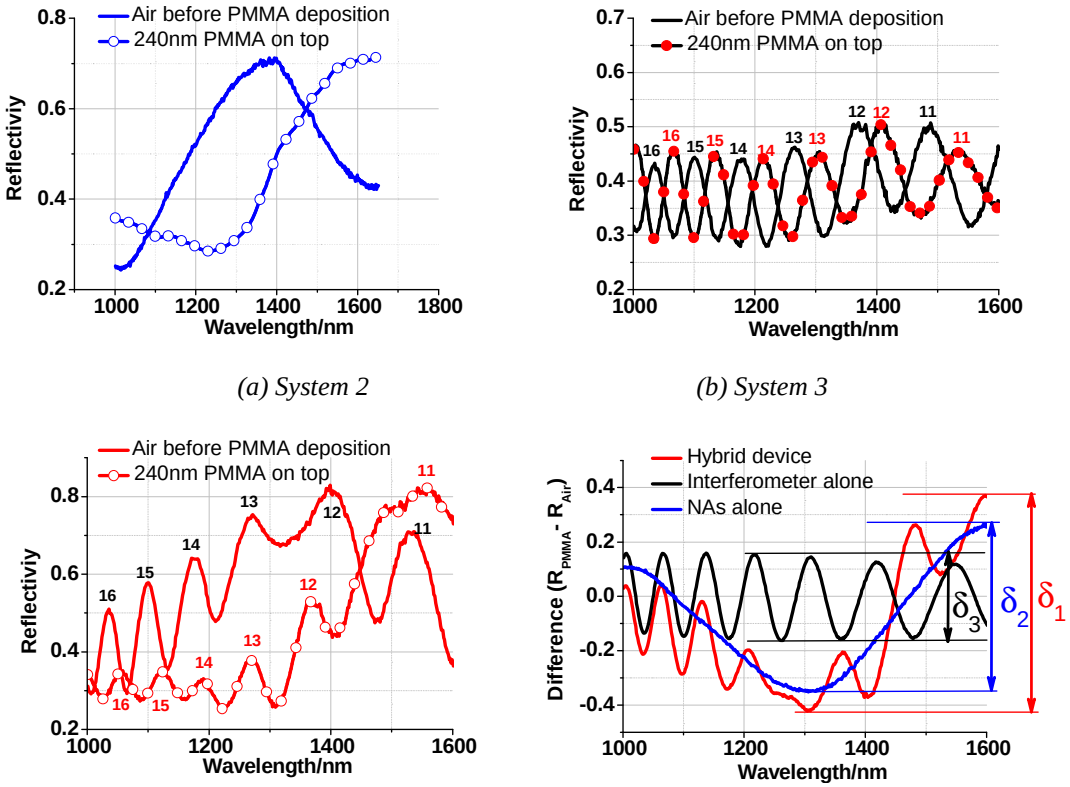

(a) System 2 *(b) System 3*

(c) System 1 *(d) Différence R_{PMMA} - R_{Air}*

Fig. 4.1.2. Comparaison entre la réflectivité des 3 systèmes avant et après dépôt de PMMA.

Afin de comparer les sensibilités des différents systèmes, on considère le signal de différence :

$$\Delta R = R_{with\ PMMA} - R_{Air}$$

Deux indicateurs sont introduits, la valeur absolue maximale du signal de différence ($|\Delta R|_{max}$) qui est appropriée dans le cas de détection à longueur d'onde fixe, et l'amplitude totale du signal de différence ($\delta = \Delta R_{\max} - \Delta R_{\min}$) sur toute la gamme spectrale considérée, qui est

appropriée dans le cas de mesures spectrales. On introduit également la sensibilité relative à la variation d'indice : $\delta_n = \delta/\Delta n$. Ces indicateurs sont mis en évidence dans la Fig. 4.1.2d.

Les conclusions sont les suivantes : pour les deux indicateurs considérés ($|\Delta R|_{max}$ et δ) on obtient un gain en sensibilité de 150% du système hybride par rapport à l'interféromètre, mais seulement de 20% par rapport aux NA sur substrat. Le facteur δ_n correspondant est 0.5.

Des expériences effectuées en milieu liquide viennent conforter ces conclusions. D'autres expériences visant à détecter une variation d'épaisseur de la couche de PMMA ont démontré d'une part que les sensibilités des systèmes avec NA (seules ou structures hybrides) dépendent peu de l'épaisseur contrairement à celle de l'interféromètre qui est très sensible au chemin optique dans la PMMA, et d'autre part que les optima de sensibilité sont différents s'il s'agit de détecter la présence d'une couche ou une variation de son épaisseur : la détection doit donc être optimisée pour chaque système en fonction du paramètre à détecter.

4.2 Détection de faibles variations d'indice

On vient de voir que le système hybride apporte peu de gain par rapport aux NA seules dans le cas d'une détection de larges variations d'indice. Deux cas sont proposés pour l'étude des faibles variations d'indice : la détection de concentrations de liquides (mélanges eau/éthanol) et la détection de vapeur d'eau.

4.2.1 Mélanges eau/ethanol

L'indice de réfraction du mélange eau/éthanol est connu et varie entre 1.33 (eau pure) et 1.365 en fonction du pourcentage d'éthanol dans la solution. Nous avons d'abord varié ce pourcentage par simulation entre 0 et 100% afin de nous affranchir des problèmes d'absorption du liquide. Les résultats pour 10, 20 et 30% sont présentés dans la Fig. 4.2.1.

Dans la Fig. 4.2.1, on voit clairement que les variations de réponse optique sont largement amplifiées à la résonance (vers 1500 nm) pour le système hybride, induisant un fort signal différentiel. Les deux indicateurs considérés ($|R|_{max}$ et δ) donnent un gain en sensibilité de 2.5 du système hybride par rapport aux NA sur substrat, et d'un ordre de grandeur par rapport à l'interféromètre. Le facteur δ_n correspondant est 4.

Les études expérimentales effectuées donnent des gains en sensibilité similaires à ceux obtenus par simulation. Ces résultats démontrent que la sensibilité du système hybride augmente largement par rapport à celle des NA ou de l'interféromètre dans le cas des faibles variations d'indice. Un ordre de grandeur de gain en sensibilité peut ainsi être obtenu dans le cas d'une variation de 10% de la concentration d'éthanol, ce qui correspond à une vraition d'indice de l'ordre de 10^{-4}.

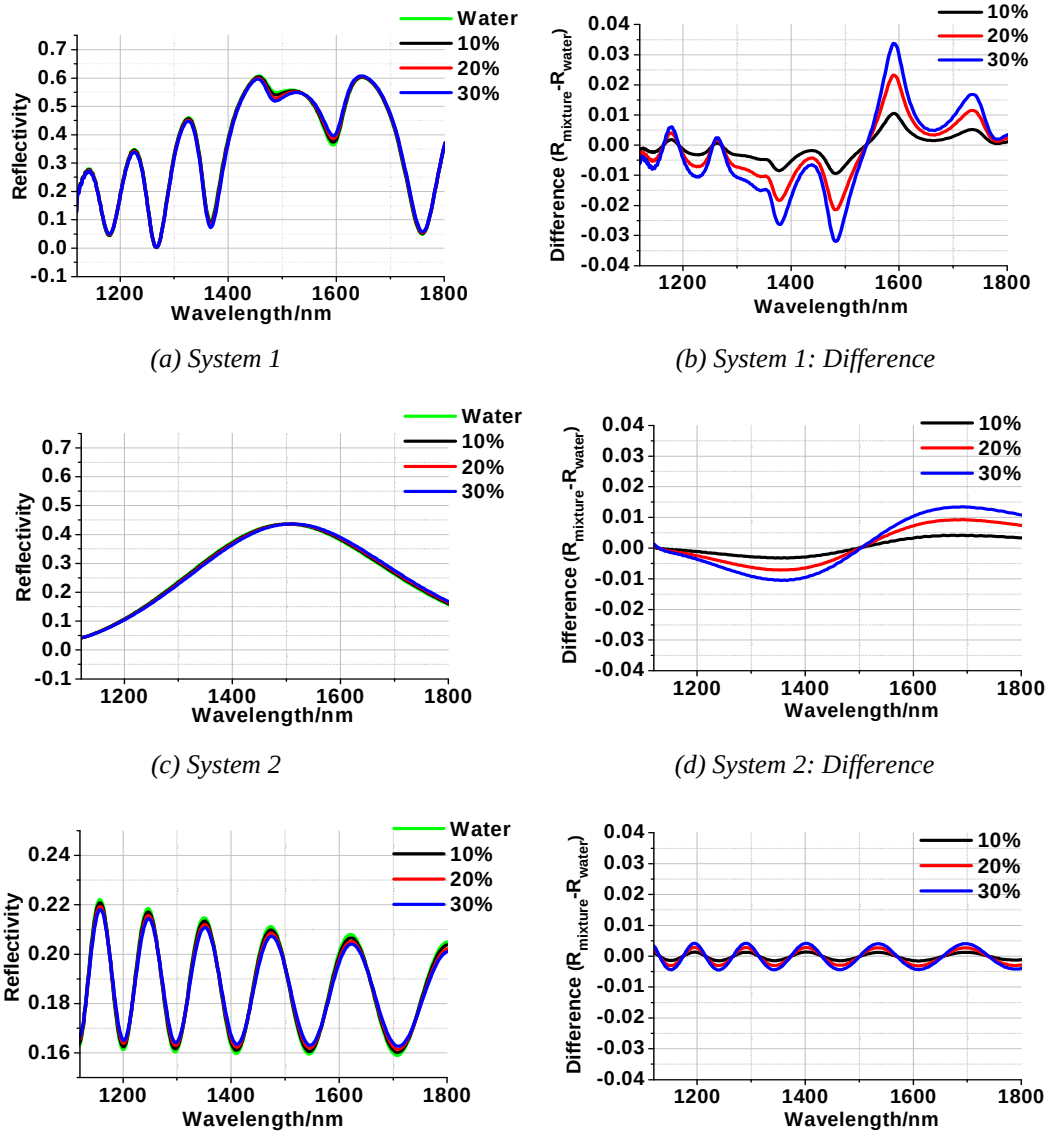

(a) System 1 *(b) System 1: Difference*

(c) System 2 *(d) System 2: Difference*

(e) System 3 *(f) System 3: Difference*

Fig. 4.2.1 Réflectivité (gauche) et signal de différence par rapport à l'eau pure (droite) pour les 3 systèmes dans le cas d'une détection de faibles pourcentages d'éthanol dans l'eau ; (a)-(b) : Système 1 : structure hybride ; (c)-(d) : Système 2 : NA sur substrat ; (e)-(f) : Système 3 : interféromètre.

4.2.2 Humidité

Dans les études précédentes, nous avons varié l'indice de l'environnement des dispositifs. L'objectif de cette étude est d'évaluer le potentiel du système hybride pour la détection de faibles variations d'indice dans la couche de Si poreux constituant l'interféromètre. Pour cela nous exploitons la porosité du spacer de silice afin de laisser pénétrer des molécules d'eau en provenance du milieu environnant saturé en vapeur d'eau, qui viennent ensuite condenser sur la surface interne du Si poreux et modifier son indice. Le modèle de LLL présenté dans les

chapitres 1 et 2 est utilisé pour déduire la fraction et l'épaisseur de la couche d'eau condensée dans le matériau.

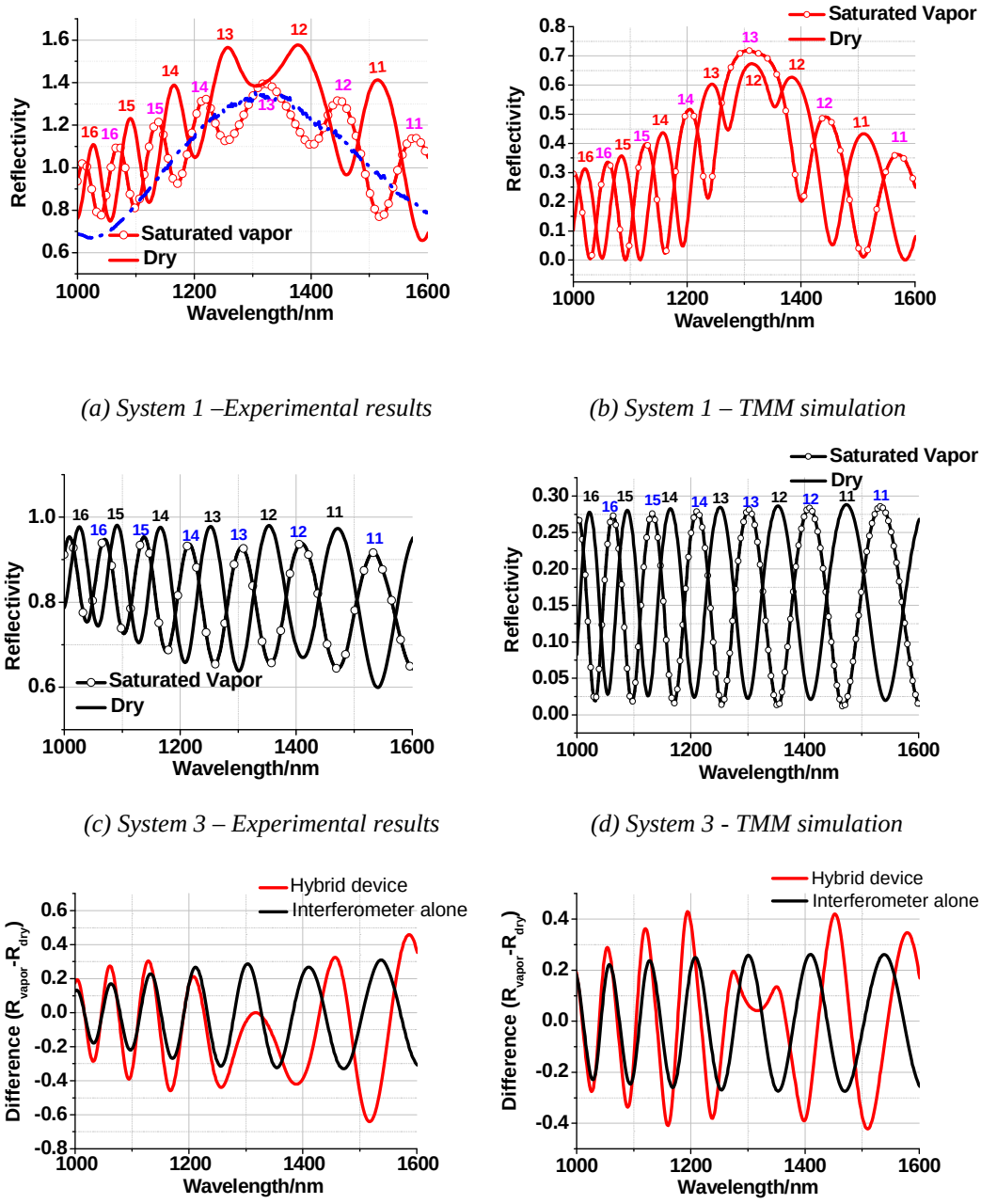

(a) System 1 –Experimental results *(b) System 1 – TMM simulation*

(c) System 3 – Experimental results *(d) System 3 - TMM simulation*

(e) Difference signals – Experimental results *(f) Difference signals – TMM simulation*

Fig. 4.2.2 Réflectivité expérimentale (gauche) et simulée (TMM – droite) pour les systèmes 1 (système hybride) et 3 (interféromètre) dans le cas d'une saturation en vapeur d'eau.

Les NA sur substrat n'ayant montré aucune sensibilité à ce type de détection, le système hybride est uniquement comparé à l'interféromètre. Des mesures résolues en temps sont effectuées pour visualiser la réponse des dispositifs entre le moment d'exposition avec la vapeur et la saturation dans les pores, puis le retour à l'état initial par séchage progressif. Les

résultats expérimentaux sont en parfait accord avec les simulations et sont présentés dans la Fig. 4.2.2.

L'augmentation d'indice dans la couche de Si poreux due à la condensation de l'eau conduit à un décalage vers le rouge des franges d'interférence. L'indice initial de la couche est 1.66, celui déduit des spectres présentés dans la Fig. 4.2.2c à saturation est neff-vapor ~ 1.73. En appliquant le modèle de LLL à ces résultats, on obtient une fraction d'eau condensée de 21%, qui correspond à une épaisseur de 1.6 nm pour une surface spécifique de 100 m^2/cm^3. Ces résultats sont parfaitement reproduits par les simulations TMM.

Le décalage vers le rouge des franges est également visible pour le système hybride. Par contre la position de la résonance plasmon reste constante, ce qui confirme l'absence de sensibilité des NA à la condensation d'eau. Le shift relatif des franges par rapport à la résonance induit donc un changement de la force du splitting, qui est mis en évidence par la simulation présentée dans la Fig. 4.2.2b.

Les sensibilités déduites des signaux interférentiels indiquent un gain d'un facteur 2 pour le dispositif hybride par rapport à l'interféromètre. Ce gain pourrait certainement être optimisé par optimisation de la force du splitting à la résonance.

Chapitre 5 Conclusions et perspectives

Dans le cadre de cette thèse, un dispositif hybride plasmonique/photonique constitué d'un réseau de NA papillons sur un interféromètre de Si poreux a été étudié. Après optimisation du design puis des procédés de fabrication et des outils de caractérisation, une étude d'abord fondamentale a été effectuée pour mettre en évidence les mécanismes de couplage entre les NA et l'interféromètre. Deux approches complémentaires ont été développées et confrontées aux résultats expérimentaux, un modèle interférométrique puis un modèle résonant. En particulier, ces modèles ont permis de mettre en évidence un splitting des franges d'interférence dû au couplage avec les NA à la résonance. La force de ce splitting dépend de la position respective des franges et de la résonance, qui influence le recouvrement des champs des deux dispositifs.

Le potentiel du système hybride pour la détection a ensuite été étudié, dans le cas de variations de l'indice de l'environnement puis de l'indice de l'interféromètre. Il a été démontré que le dispositif hybride apporte un fort gain en sensibilité (un ordre de grandeur) par rapport aux NA seules ou à l'interféromètre seul dans le cas de faibles variations d'indice obtenues en modifiant la teneur en éthanol d'un mélange eau/éthanol. Les variations de l'indice de l'interféromètre ont été obtenues par saturation de vapeur d'eau à l'intérieur des pores du Si poreux, et ont montré un gain en sensibilité d'un facteur 2 pour le dispositif hybride, qui pourrait certainement être optimisé.

Les perspectives de ce travail sont nombreuses. L'étape suivante dans l'application à la détection est d'effectuer des expériences de biodétection, en exploitant la chimie orthogonale des nanostructures métalliques et du Si poreux pour greffer des biomolécules soit sur les NA, soit dans le Si poreux, soit différentes biomolécules sur les deux matériaux pour une détection double.

Les dispositifs étudiés dans ce travail sont un cas d'école destiné à mettre en évidence les mécanismes intervenant dans le couplage photonique/plasmonique et dans le gain de sensibilité pour l'application à la détection. Basés sur ces travaux préliminaires, de nombreux dispositifs hybrides peuvent être optimisés pour obtenir des sensibilités beaucoup plus importantes : NA avec d'autres designs, nanorods, ou un autre métal pour le dispositif

plasmonique ; microcavité ou cristal photonique présentant des résonances spectrales fines pour le dispositif photonique.

Chapitre 6 Références

[1] Hauptmann, Peter (1993). Sensors : principles and applications. C. Hanser ; Hemel Hempstead ; Englewood Cliffs, NJ : Prentice Hall, Munich

[2] C. Jamois, C. Li, E. Gerelli, Y. Chevolot, V. Monnier, R. Skryshevskyi, R. Orobtchouk, E. Souteyrand, and T. Benyattou. "Porous-Silicon-Based Photonic Crystals for Sensing Applications." 2010.

[3] Fan, Xudong, Ian M White, Siyka I Shopova, Hongying Zhu, Jonathan D Suter, and Yuze Sun. "Sensitive Optical Biosensors for Unlabeled Targets: A Review." analytica chimica acta 620, no. 1 (2008): 8-26.

[4] James, Tony D, KRA Sandanayake, and Seiji Shinkai. "A Glucose - Selective Molecular Fluorescence Sensor." Angewandte Chemie International Edition in English 33, no. 21 (1994): 2207-09.

[5] Talley, Chad E, Leonard Jusinski, Christopher W Hollars, Stephen M Lane, and Thomas Huser. "Intracellular Ph Sensors Based on Surface-Enhanced Raman Scattering." Analytical chemistry 76, no. 23 (2004): 7064-68.

[6] Wijaya, Edy, Cédric Lenaerts, Sophie Maricot, Juriy Hastanin, Serge Habraken, Jean-Pierre Vilcot, Rabah Boukherroub, and Sabine Szunerits. "Surface Plasmon Resonance-Based Biosensors: From the Development of Different Spr Structures to Novel Surface Functionalization Strategies." Current Opinion in Solid State and Materials Science 15, no. 5 (2011): 208-24.

[7] Sepúlveda, B, Laura G Carrascosa, D Regatos, Marinus A Otte, D Farina, and Laura M Lechuga. "Surface Plasmon Resonance Biosensors for Highly Sensitive Detection in Real Samples." Paper presented at the SPIE NanoScience+ Engineering, 2009.

[8] Subramanian, Anand, Joseph Irudayaraj, and Thomas Ryan. "A Mixed Self-Assembled Monolayer-Based Surface Plasmon Immunosensor for Detection of< I> E. Coli</I> O157: H7." Biosensors and Bioelectronics 21, no. 7 (2006): 998-1006.

[9] Schultz, Sheldon, David R Smith, Jack J Mock, and David A Schultz. "Single-Target Molecule Detection with Nonbleaching Multicolor Optical Immunolabels." Proceedings of the National Academy of Sciences 97, no. 3 (2000): 996-1001.

[10] Zhao, Jing, Xiaoyu Zhang, Chanda Ranjit Yonzon, Amanda J Haes, and Richard P Van Duyne. "Localized Surface Plasmon Resonance Biosensors." (2006).

[11] Enoch, Stefan, Romain Quidant, and Gonçal Badenes. "Optical Sensing Based on Plasmon Coupling in Nanoparticle Arrays." Opt. Express 12, no. 15 (2004): 3422-27.

[12] Sailor, Michael J. "Fundamentals of Porous Silicon Preparation." Porous Silicon in Practice: Preparation, Characterization and Applications. Wiley (2011): 1-42.

[13] Jane, Andrew, Roman Dronov, Alastair Hodges, and Nicolas H Voelcker. "Porous Silicon Biosensors on the Advance." Trends in biotechnology 27, no. 4 (2009): 230-39.

[14] Dennis R. Turner, “Electropolishing Silicon in Hydrofluoric Acid Solutions,” Journal of The Electrochemical Society 105, no. 7 (July 1, 1958): 402–408, doi:10.1149/1.2428873.

[15] Takashi Unagami, “Formation Mechanism of Porous Silicon Layer by Anodization in HF Solution,” Journal of The Electrochemical Society 127, no. 2 (February 1, 1980): 476–483, doi:10.1149/1.2129690.

[16] V. Lehmann and U. Gosele, “Porous Silicon Formation: A Quantum Wire Effect,” Applied Physics Letters 58, no. 8 (1991): 856–858, doi:10.1063/1.104512.

[17] Kochergin, Vladimir, and Helmut Fèoll. Porous Semiconductors: Optical Properties and Applications. Springer, 2009.

[18] Guillermain, Elisa. "Dispositifs Nanophotoniques Ondes De Surface En Silicium Poreux: Technologie et Application La Bio-Détection." PhD Thesis, Institut National des Sciences Appliquées de Lyon, France, 142p, 2007.

[19] Looyenga, H. "Dielectric Constants of Heterogeneous Mixtures." Physica 31, no. 3 (1965): 401-06.

[20] Cheng, LI. "Nouvelle filière nanotechnologique sur silicium poreux: Application à des dispositifs photoniques." PhD diss., Institut National des Sciences Appliquées de Lyon, 2010.

[21] Lin, Victor S-Y, Kianoush Motesharei, Keiki-Pua S Dancil, Michael J Sailor, and M Reza Ghadiri. "A Porous Silicon-Based Optical Interferometric Biosensor." Science 278, no. 5339 (1997): 840-43.

[22] De Stefano, Luca, Paolo Arcari, Annalisa Lamberti, Carmen Sanges, Lucia Rotiroti, Ilaria Rea, and Ivo Rendina. "DNA Optical Detection Based on Porous Silicon Technology: From Biosensors to Biochips." Sensors 7, no. 2 (2007): 214-21.

[23] Gao, Jun, Ting Gao, and Michael J Sailor. "Porous-Silicon Vapor Sensor Based on Laser Interferometry." Applied Physics Letters 77, no. 6 (2000): 901-03.

[24] Vincent, G. "Optical Properties of Porous Silicon Superlattices." Applied physics letters 64, no. 18 (1994): 2367-69.

[25] Snow, PA, EK Squire, P St J Russell, and LT Canham. "Vapor Sensing Using the Optical Properties of Porous Silicon Bragg Mirrors." Journal of Applied Physics 86, no. 4 (1999): 1781-84.

[26] Rea, Ilaria, Annalisa Lamberti, Ivo Rendina, Giuseppe Coppola, Mariano Gioffrè, Mario Iodice, Maurizio Casalino, Edoardo De Tommasi, and Luca De Stefano. "Fabrication and Characterization of a Porous Silicon Based Microarray for Label-Free Optical Monitoring of Biomolecular Interactions." Journal of Applied Physics 107, no. 1 (2010): 014513-13-4.

[27] Reece, PJ, G Lerondel, WH Zheng, and M Gal. "Optical Microcavities with Subnanometer Linewidths Based on Porous Silicon." Applied physics letters 81, no. 26 (2002): 4895-97.

[28] Ouyang, Huimin, Christopher C Striemer, and Philippe M Fauchet. "Quantitative Analysis of the Sensitivity of Porous Silicon Optical Biosensors." Applied Physics Letters 88, no. 16 (2006): 163108-08-3.

[29] Rong, Guoguang, Ali Najmaie, John E Sipe, and Sharon M Weiss. "Nanoscale Porous Silicon Waveguide for Label-Free DNA Sensing." Biosensors and Bioelectronics 23, no. 10 (2008): 1572-76.

[30] Wei, Xing, and Sharon M Weiss. "Guided Mode Biosensor Based on Grating Coupled Porous Silicon Waveguide." Opt. Express 19, no. 12 (2011): 11330-39.

[31] Guillermain, E, V Lysenko, R Orobtchouk, T Benyattou, S Roux, A Pillonnet, and P Perriat. "Bragg Surface Wave Device Based on Porous Silicon and Its Application for Sensing." Applied physics letters 90, no. 24 (2007): 241116-16-3.

[33] Jamois, C., Li, C., Gerelli, E., Orobtchouk, R., Benyattou, T., Belarouci, A., Chevolot, Y., Monnier, V. and Souteyrand, E. (2011). New concepts of integrated photonic biosensors based on porous silicon, Biosensors - Emerging Materials and Applications. Ed. Pier Andrea Serra, Intech, pp. 265–290.

[33] Jamois, C., Li, C., Gerelli, E., Chevolot, Y., Monnier, V., Skryshevskyi, R., Orobtchouk, R., Souteyrand, E. and Benyattou, T. (2010a). Porous-silicon based planar photonic crystals for sensing applications, Proc. SPIE 7713, Conference on Photonic Crystal Materials and Devices IX, 7713OU, pp. 1–10

[34] N. J. Halas, “Connecting the dots: Reinventing optics for nanoscale dimensions,” PNAS 106 (10), 3643 (2009)

[35] L. Novotny and N. van Hulst, “Antennas for light,” Nature Photon. 5, 83 (2011)

[36] P. Muhlschlegel, H.-J. Eisler, O. J. F. Martin, B. Hecht, and D. W. Pohl, “Resonant optical antennas,” Science 308, 1607 (2005)

[37] A. Sundaramurthy, K. B. Crozier, and G. S. Kino, “Field enhancement and gap dependent resonance in a system of two opposing tip-to-tip Au nanotriangles,” Phys. Rev. B 72, 165409 (2005)

[38] W. L. Barnes, A. Dereux, and T. W. Ebbesen, “Surface plasmon subwavelength optics,” Nature 424, 824 (2003)

[39] STEFAN A. MAIER, PLASMONICS: FUNDAMENTALS AND APPLICATIONS, Springer, 2007.

[40] TP Zhang, Plasmonic-Photonic Hybrid Nano-device, Institut des Nanotechnologies de Lyon, Thesis defense on 22th November, 2012

[41] Maier, Stefan A., and Harry A. Atwater. "Plasmonics: Localization and guiding of electromagnetic energy in metal/dielectric structures." Journal of Applied Physics 98, no. 1 (2005): 011101-011101.

[42] Julien R G Navarro, Delphine Manchon, et al., Synthesis of PEGylated gold nanostars and bipyramids for intracellular uptake, Nanotechnology 23, pp. 465602, (2012)

[43] Carsten Sönnichsen, “Plasmons in metal nanostructures”, Ludwig-Maximilians-University of Munich, 20, June, 2001.

[44] Yun-Chorng Chang, Shih-Ming Wang, Hsin-Chan Chung, Chun g-Bin Tseng, Shih-Hui Chang, ‘Large-Area Bowtie Nanoantenna Arrays Fabricated with Economic Oxygen Plasma-Assisted Nanosp here Lithography’, Plasmonics (2011), Springer Science+Business Media, LLC 2011, 6:599– 604, DOI 10.1007/s11468-011-9240-5

[45] Kumar, Anil. Optical nano-antennas: Fabrication, characterization and applications. University of Illinois at Urbana Champaign, 2011

[46] A. Sundaramurthy, K. B. Crozier, G. S. Kino, D. P. Fromm, P. J. Schuck and W. E. Moerner, “Field enhancement and gap-dependent resonance in a system of two opposing tip-to-tip Au nanotriangles,” Phys. Rev. B 72, 165409 (2005)

[47] Grober, Robert D, Robert J Schoelkopf, and Daniel E Prober. "Optical Antenna: Towards a Unity Efficiency near-Field Optical Probe." Applied Physics Letters 70, no. 11 (1997): 1354-56.

[48] Crozier, K. B., A. Sundaramurthy, G. S. Kino, and C. F. Quate. "Optical antennas: Resonators for local field enhancement." Journal of Applied Physics 94, no. 7 (2003): 4632-4642

[49] Kim, Youngjin, Robert C Johnson, and Joseph T Hupp. "Gold Nanoparticle-Based Sensing of "Spectroscopically Silent" Heavy Metal Ions." Nano Letters 1, no. 4 (2001): 165-67

[50] Tsai, Charng-Sheng, Ting-Bin Yu, and Chao-Tsen Chen. "Gold Nanoparticle-Based Competitive Colorimetric Assay for Detection of Protein–Protein Interactions." Chemical communications, no. 34 (2005): 4273-75

[51] Greg Barbillon « Etude théorique et expérimentale de nanocapteurs d'espèces biochimiques à plasmons de surface localisés sur des nanoparticules métalliques », PhD thesis (2007)

[52] Cinel, Neval A, Serkan Bütün, and Ekmel Özbay. "Electron Beam Lithography Designed Silver Nano-Disks Used as Label Free Nano-Biosensors Based on Localized Surface Plasmon Resonance." Optics Express 20, no. 3 (2012): 2587-97

[53] Acimovic, S. S., Kreuzer, M. P., Gonzalez, M. U., et al., Acimovic, Srdjan S., et al. "Plasmon near-field coupling in metal dimers as a step toward single-molecule sensing." ACS nano 3.5 (2009): 1231-1237

[54] He L, Musick MD, Nicewarner SR, et al., He, Lin, et al. "Colloidal Au-enhanced surface plasmon resonance for ultrasensitive detection of DNA hybridization." Journal of the American Chemical Society 122.38 (2000): 9071-9077

[55] Lakowicz, Joseph R. "Plasmonics in biology and plasmon-controlled fluorescence." Plasmonics 1.1 (2006): 5-33

[56] Roux, Stéphane, et al. "Synthesis, characterization of dihydrolipoic acid capped gold nanoparticles, and functionalization by the electroluminescent luminol." Langmuir 21.6 (2005): 2526-2536

[57] Kinkhabwala, Anika, Zongfu Yu, Shanhui Fan, Yuri Avlasevich, Klaus Müllen, and W. E. Moerner. "Large single-molecule fluorescence enhancements produced by a bowtie nanoantenna." Nature Photonics 3, no. 11 (2009): 654-657

[58] Jeffrey N. Anker, W. Paige Hall, Olga Lyandres, et al. "Biosensing with plasmonic nanosensors." Nature materials 7.6 (2008): 442-453

[59] Fleischmann, M_, P. J. Hendra, and A. J. McQuillan. "Raman spectra of pyridine adsorbed at a silver electrode." Chemical Physics Letters 26.2 (1974): 163-166

[60] Fromm, David P., Arvind Sundaramurthy, Anika Kinkhabwala, P. James Schuck, Gordon S. Kino, and W. E. Moerner. "Exploring the chemical enhancement for surface-enhanced Raman scattering with Au bowtie nanoantennas." Journal of Chemical Physics 124, no. 6 (2006): 61101-64100

[61] Lu, Guowei, Bolin Cheng, Hong Shen, Yueliang Zhou, Zhenghao Chen, Guozhen Yang, Olivier Tillement, Stéphane Roux, and Pascal Perriat. "Fabry-Perot type sensor with surface plasmon resonance." Applied physics letters 89, no. 22 (2006): 223904-223904

[62] Ameling, Ralf, Lutz Langguth, Mario Hentschel, Martin Mesch, Paul V. Braun, and Harald Giessen. "Cavity-enhanced localized plasmon resonance sensing." Applied Physics Letters 97, no. 25 (2010): 253116-253116

[63] Ameling, Ralf, and Harald Giessen. "Cavity plasmonics: large normal mode splitting of electric and magnetic particle plasmons induced by a photonic microcavity." Nano letters 10, no. 11 (2010): 4394-4398

[64] Schmidt, Markus A., Dang Yuan Lei, Lothar Wondraczek, Virginie Nazabal, and Stefan A. Maier. "Hybrid nanoparticle - microcavity-based plasmonic nanosensors with improved detection resolution and extended remote-sensing ability." Nature communications 3 (2012): 1108

[65] Abdelmounaim Harouri, Biocapteurs photoniques : Réalisation d'une cellule fluidique pour une détection in-situ, Master thesis, INSA-Lyon (2011)

[66] M. Born and E. Wolf, “Principles of optics: electromagnetic theory of propagation, interference and diffraction of light”. Oxford, Pergamon Press, 1964.

[67] D. M. Topasna and G. A. Topasna, “Numerical modeling of thin film optical filters,” *Education and Training in Optics and Photonics*, EP5, 2009. (Conference paper)

[68] A. Sundaramurthy, K. Crozier, G. Kino, D. Fromm, P. Schuck and W. Moerner, “Field enhancement and gap-dependent resonance in a system of two opposing tip-to-tip Au nanotriangles,” *Physical Review B*, vol. 72, no. 16, p. 165409, Oct. 2005.

[69] L. Novotny and B. Hecht, “Principles of nano-optics”, Chapter 12, pp. 407–450, Printed in the United Kingdom at the university Press, Cambridge, 2012, ISBN 978-1-107-00546-4 Hardback-

[70] S. A. Maier, “Plasmonics: Fundamentals and applications”, Springer, XXV, 2007.

Part II. Main manuscript

General introduction

Nowadays, the increasing concern for environmental analysis and food quality control, as well as medical needs such as fast diagnosis in case of emergency events, leads to a growing need for new generations of chemical and biological sensors. These devices should have high sensitivity and reliability, perform specific detection of molecules and enable multiple parallel sensing, while being cheap, portable, fast and easy to use. Thus, a general trend tends towards bio - chemical sensors which are on - chip integrated, label - free, and compatible with standard micro - technologies.

Photonic dielectric devices based on porous silicon and metallic nanostructures based on plasmon resonances are good candidates to fulfill the above requirements. Porous silicon is a biocompatible material, with a huge specific surface providing a sensitivity enhancement by several orders of magnitude compared to bulk materials; furthermore, its refractive index and thickness can be easily tuned, enabling for the realization of a large variety of photonic designs. Metallic nanostructures provide high confinement and strong field enhancement in sub-wavelength regions, leading to high sensitivities; combined with fluorescence or other sensing mechanisms such as Raman or IR spectroscopy, they have already demonstrated increased sensing potential.

The realization of a hybrid device combining both elements would be highly interesting, since it could yield the advantages of both elements, and the photonic structure could shape the plasmonic resonance to develop ultrasensitive devices with narrow resonance linewidth and increased sensing depth.

In this context, the purpose of this PhD thesis is to explore this challenging solution by considering the design, realization, characterization and sensing potential of hybrid photonic / plasmonic devices that exploit the coupling between the localized surface plasmon resonance of a bowtie antenna array and the photonic modes of a porous silicon interferometer.

This thesis will start with an introduction to the world of optical sensors, with particular emphasis on the properties of porous silicon and optical devices based on this material, as well as plasmonic nanostructures; this will provide the necessary background to understand the objectives and challenges of this work (chapter 1). Next, the experimental tools optimized

during this PhD work will be presented and discussed, such as the technological processes for the device realization and the optical characterization setups (chapter 2). The next chapter will be dedicated to the investigation of the behavior of the optical elements constituting the device – NA array and interferometer – as well as the coupling mechanisms between them. This fundamental study is essential to gain understanding on the optical performances of the hybrid structure (chapter 3). Finally, the potential of the device for sensing applications will be explored by testing the device performance in different environments and different sensing experiments (chapter 4).

This work was performed within the framework of the program “Groups of Five Ecoles Centrales” between China Scholarship Council (CSC) and Lyon Institute of Nanotechnologies (INL, CNRS UMR 5270). The project has been supported by the Nanolyon technology platform at INL.

Chapter 1 Introduction

1.1 INTRODUCTION 65

1.2 PHOTONIC ELEMENT: POROUS SILICON DEVICE 67

1.2.1 Porous silicon formation 68

1.2.2 Structural properties of porous silicon 70

1.2.3 Specific surface area 72

1.2.4 Optical properties of porous silicon 73

1.2.5 Optical sensors based on porous silicon 75

1.3 PLASMONIC ELEMENT: OPTICAL NANO-ANTENNA 81

1.3.1 Introduction to plasmons 82

1.3.2 Metallic particles synthesis 86

1.3.3 Optical antenna 88

1.3.4 Optical sensors based on metallic nanostructures 89

1.4 DESIGN, OBJECTIVES AND ORGANIZATION OF THIS WORK 95

1.4.1 Our design 95

1.4.2 Objectives of the PhD work 100

1.4.3 Organization of the thesis 100

1.5 REFERENCES 102

1.1 Introduction

If the search “sensors” is entered in Google, within 0.3 seconds, 942000000 results will be given, which shows that sensors are really a hot topic nowadays. Then, what is a sensor?

In my view, a sensor is a tool designed to help people to recognize matter or events that are hard to be directly observed. Similar to the sense organs of the human body, it is an intelligent system that provides the desired information. Strictly speaking, we cite the definition given in ‘Sensors principles & applications’ by Peter Hauptmann [1.1]:

> *A sensor converts (changes in) the physical dimension which is to be measured into (changes in) an electrical dimension which can be processed or transmitted electronically.*

After this conversion, a complete sensor system would require as well a signal preparation stage (such as amplification, filtering, analog-digital conversion or simple correction circuits, etc) and a processing unit in the electrical dimension, as illustrated in Fig 1.1.

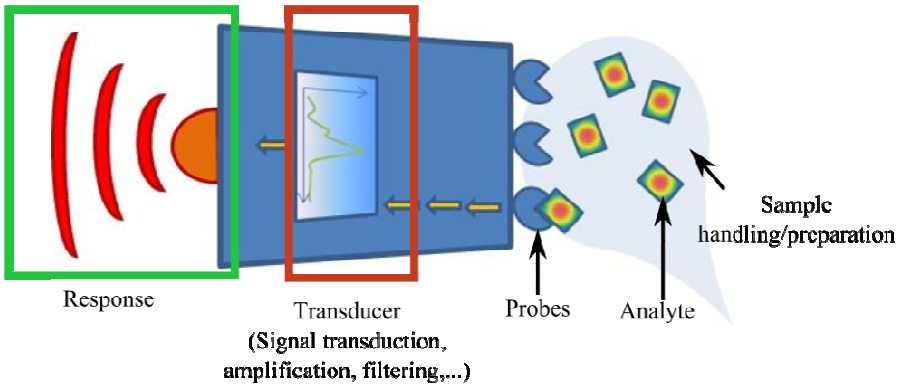

Fig 1.1 Schematic view of a sensor [1.2]

Generally, it is possible to classify approximately 2000 basic types of sensors which are available to measure more than 100 physical dimensions such as magnetic signals, chemical volumes, electro-magnetic radiation, mechanical signals, thermal signals etc. According to the transduction mode, sensors could be classified as optical sensors, electronic sensors, chemical sensors, pressure sensors, machinery vibration monitoring sensors, temperature sensors and so on. A good sensor should yield adequate sensitivity, high degree of accuracy and good reproducibility, insensitivity to interference and environmental influence, high stability and reliability; long life expectancy and problem-free replacement [1.1].

Among the wide diversity of available sensors, optical sensors are of high interest, as they are highly sensitive and allow for specific and non-destructive detection of a large variety of molecules, while being immune to electro-magnetic interference, capable of performing remote sensing and of providing multiplexed detection within a single device [1.3, 1.4]. Various optical sensors have been studied in the literature for biological and chemical detection, such as sensors based on fluorescence [1.5], surface-enhanced Raman scattering [1.6], chemiluminescence, colorimetry [1.7], interferometry [1.8 - 1.10], gratings [1.11 - 1.14], waveguides [1.15], surface-plasmon resonance [1.16 - 1.18], or nano-particles plasmonic resonances [1.19 - 1.21].

In order to answer the growing needs for rapid, simple and cost-effective monitoring or diagnosis, a new trend tends towards biological and chemical sensors which are on-chip integrated, label-free, and compatible with standard fabrication micro-processes. Photonic dielectric devices based on silicon and plasmonic devices based on metallic nanostructures are good candidates to fulfill these additional requirements. Hybrid devices combining the advantages of both worlds have recently emerged as a possible way to develop miniaturized, label-free and ultrasensitive devices with narrow linewidth and large sensing depth.

In this context, the purpose of this PhD thesis is to explore this challenging solution by considering the design, realization, characterization and sensing potential of a particular simple hybrid photonic / plasmonic device consisting of a bowtie antenna array yielding a localized surface plasmon resonance at the surface of a porous silicon interferometer.

Before starting the study of the properties and potential of our hybrid device, the aim of this first chapter is to give a review of the main properties of the two separate building blocks of this hybrid structure: the porous silicon photonic device and the nano-antenna array, as well as their applications in the sensing area, and a description of the few other hybrid devices that have already been proposed.

1.2 Photonic element: Porous silicon device

The photonic device proposed in this work is an interferometer consisting of a single layer of mesoporous silicon; Fig 1.2.0 gives an illustration of such a device.

The reasons for this choice are numerous:

- Mesoporous silicon is a very interesting material for fundamental studies, as it is cheap, rapid and simple to fabricate [1.22], and its refractive index and thickness can be easily tuned, yielding a large span of interferometer designs;
- Mesoporous silicon is also a very interesting material for applications to sensing [1.23], due to its porosity and large specific surface area enabling the volume detection of large quantities of molecules, its well-known surface chemistry and biocompatibility, its compatibility with silicon-based micro-technology, and its large diversity of complementary optical, electronic, chemical, mechanical or thermal properties, offering a huge choice of possible devices for sensing applications.

These properties are presented in more details in the following, as well as a few key examples of optical sensors based on porous silicon including the porous silicon interferometer.

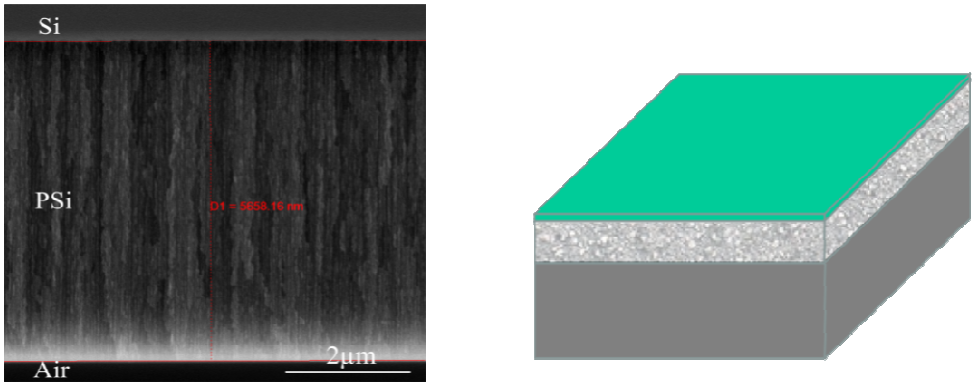

(a) *(b)*

Fig 1.2.0 Illustration of the porous silicon interferometer:
(a) Image from scanning-electron microscope, (b) artistic view

1.2.1 Porous silicon formation

Porous silicon (PSi) is a nano-crystalline artificial material accidentally discovered at the end of the 1950's. The great variety of properties of this material arising from its multitude of possible morphologies and porosities, such as huge specific surface, modulation of refractive index, luminescence, thermal and electrical insulation, have found interest in many applications like telecommunications, energy or sensing. The most standard technique to fabricate PSi is electro-chemical etching of crystalline silicon [1.24-1.25]. This "anodization" takes place in hydrofluoric acid (HF) - based electrolyte, generally diluted with water and / or an alcohol like ethanol.

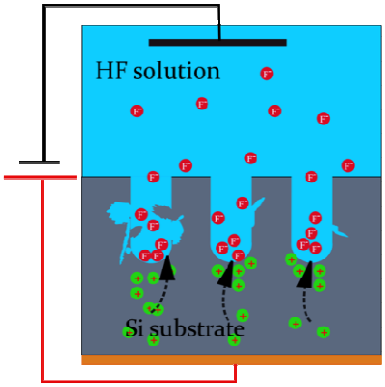

Fig 1.2.1 Schematic view of an anodization cell

As shown in Fig 1.2.1, the anodization usually requires two electrodes to enable the migration of charge carriers. The first one is immersed in the electrolyte and acts as the cathode to supply electrons to the solution; the second one is usually obtained via good electrical contact at the backside of the silicon wafer, which acts as an anode supplying the holes that are necessary for the etching. Both the ions and the holes converge towards the Si / electrolyte interface, where local dissolution of Si occurs.

During the anodization process, there are two reactions occurring at the same time at the Si / electrolyte interface:

- Oxidation: under the influence of the electric field, holes and fluoride ions are injected to the Si / electrolyte interface through the Si substrate and the electrolyte, respectively, and break the surface Si - H bonds of the material;
- Reduction: thanks to incoming electrons, the H^+ ions freed from the surface recombine to form hydrogen gas.

Among the variety of models proposed to explain the electro - chemical etching reactions, the mechanism proposed by Lehmann is the most acknowledged. As shown in Fig 1.2.2, the model assumes that the Si - Si and Si - H bonds are broken under the effect of the holes and fluoride ions, which produce SiF_6^{2-} ions and hydrogen gas [1.26].

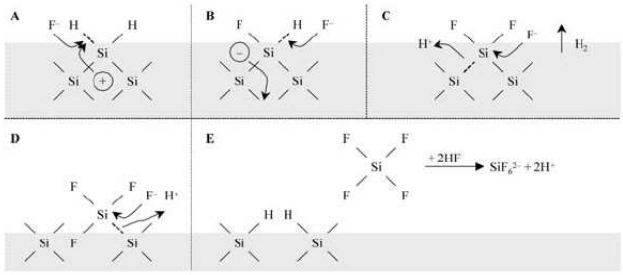

Fig 1.2.2 Principle of electrochemical dissolution of silicon proposed by Lehmann [1.26]

If the applied current density is lower than a critical value corresponding to the threshold of electro - polishing regime, the material is not completely dissolved and dissolution occurs on preferential sites. The initial sites where dissolution starts are the surface defects or irregularities, because their presence induces a perturbation of field lines leading to an accumulation of charge carriers at those points [1.27]. For the same reason, during anodization electro - chemical etching only takes place at the pores tips where the field intensity is maximum, while the pore walls are passivated. This leads to the formation of pores, that usually grow along the <100> crystalline direction [1.28, 1.22], that is the closest to the field lines: in the common case of <100> substrate and electrical field normal to the substrate surface, the main pore direction should be in the depth perpendicular to the surface.

Several parameters can influence the anodization kinetics and the pore morphology of porous silicon [1.29]:

- Substrate doping;
- Concentration and composition of HF electrolyte;
- Applied current density;
- Temperature.

As most properties of porous silicon are determined by the porosity and the pore morphology, the influence of these different anodization parameters is crucial and is discussed in the following.

1.2.2 Structural properties of porous silicon

1.2.2.1 Pore morphology

During PSi formation, the crystallinity of the Si substrate is usually preserved; depending on the pore size and on the size of interconnectivity of the crystallites, PSi can be classified into three categories:

- Nanoporous silicon, with pores smaller than ~ 2 nm, can be fabricated from p-doped substrates;
- Mesoporous silicon, with pore sizes between 2 nm and 50 nm, can be fabricated from highly-doped p^+ or n^+ substrates;
- Macroporous silicon, with pore sizes larger than 50nm, can be fabricated from n - doped substrates. Note that, due to the low concentration of holes in n - doped substrates, such anodization is usually performed under light illumination in order to create the necessary free carriers.

In this thesis, we will focus on mesoporous silicon obtained from highly p - doped <100> substrates. Hence, the properties discussed in the following are mainly focusing on this type of material.

1.2.2.2 Porosity and etching kinetics

The properties of porous silicon are principally determined by the porosity, which is defined as the ratio of air volume to the total volume of silicon and air:

$$porosity = \frac{V_{air}}{V_{air} + V_{silicon}} \qquad \text{(EQ-1-1)}$$

For a given silicon substrate, e.g., p^+ - doped in the case of mesoporous silicon, the porosity is dependent on external anodization parameters: in particular, current density, HF concentration in the electrolyte, and temperature. The same parameters strongly influence the etching kinetics as well, which represents the ratio of porous silicon thickness over etching time.

- Current density: when the other anodization conditions are constant, both porosity and etching velocity should increase with increasing current density (Fig 1.2.3); this can be

explained by the larger amount of free carriers reaching the Si / electrolyte interface and taking part to the Si dissolution.

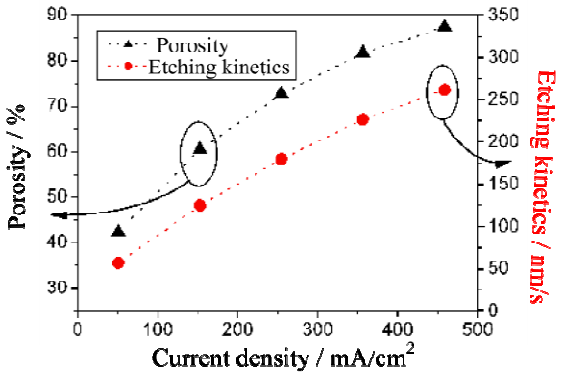

Fig 1.2.3 The evolution of porosity and etching kinetics versus the current density. The p+ type silicon is anodized at room temperature in 25% HF electrolyte [1.30].

- HF concentration: when the other anodization conditions are constant, the etching velocity should increase with increasing HF concentration, which can be attributed to the higher amount of F^- ions in the solution. At the same time, the porosity should decrease with increasing HF concentration; this phenomenon can find two explanations: the decrease of the free carriers to F^- ions ratio, and the decrease of the percentage of alcohol in the electrolyte which leads to a reduction of the wettability of the Si interface (Fig 1.2.4).

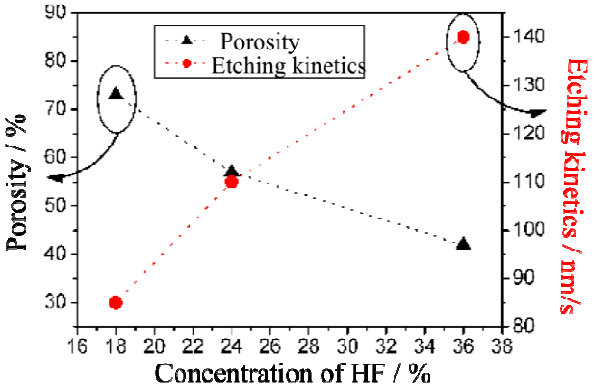

Fig 1.2.4: The evolution of porosity and etching kinetics versus the concentration of HF in the electrolyte. The electrochemical etching is carried out on p+ type silicon substrate at room temperature with a current density of 130 mA/cm^2 [1.31]

- Temperature: as illustrated in Fig 1.2.5, when the other anodization conditions are constant, the porosity should increase with decreasing temperature; this is related to the variation of electrolyte viscosity [1.32]. The lower the temperature is, the more

viscous the solution will be, which leads to an enhancement of wettability of the Si interface. At the same time, the etching velocity should decrease with decreasing temperature, as the reaction kinetics is slowed down.

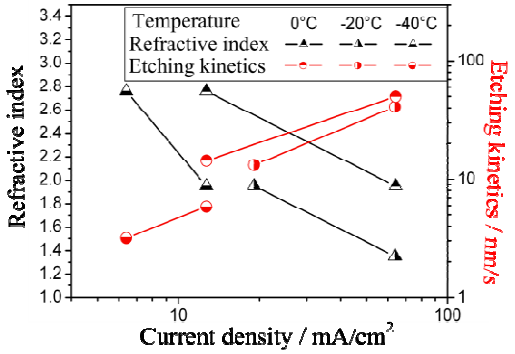

Fig 1.2.5 Influence of temperature on the porosity and etching kinetics for mesoporous silicon (on p+ type silicon wafer) [1.30]

1.2.3 Specific surface area

The porous nature of porous silicon induces a very large specific surface area. The specific surface area is usually defined as the accessible area of solid surface per unit volume or mass of material and expressed in units of m^2 / cm^3 or m^2 / g.

Experimentally, there are different methods to measure this value, such as hydrogen desorption [1.33], determination of crystallite dimension and quantity [1.34], or the widely used nitrogen adsorption on the material surface, following the BET principle (Brunauer – Emmett – Teller) [1.35]. The specific surface area is deduced from the amount of gas molecules adsorbed on the surface when saturation is reached. In the case of mesoporous silicon, the specific surface reaches about 50 - 100 m^2 / cm^3 for higher porosities and can be as high as 200 m^2 / cm^3 for lower porosities, as illustrated in Fig 1.2.6.

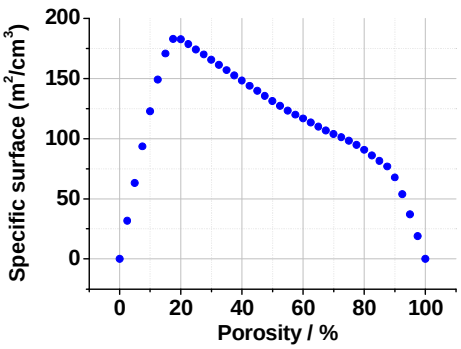

Fig 1.2.6 Specific surface vs. Porosity [1.30]

The very large specific surface of porous silicon is one of the key properties of this material leading to a range of applications from energy generation [1.33] to sensing [1.23, 1.36].

1.2.4 Optical properties of porous silicon

Porous silicon is a highly interesting material from the point of view of its very diverse properties, which arise mainly from its morphology and fabrication process. Mechanical properties [1.37], as well as thermal [1.38] and electrical conductivity [1.39, 1.40], have found applications in various micro-systems, in particular sensors.

Porous silicon luminescence has been first observed by Canham in 1990 [1.41]. It is the first optical property of porous silicon that has awoken interest, for its potential in the area of light emission and sensing [1.42-1.44]. In the following we will focus on the other optical properties of the material, which are of crucial importance for application to on-chip integrated optical sensors.

1.2.4.1 Modulation of refractive index

In the case of mesoporous silicon considered in the near-infrared optical range, the pore size is much smaller than the wavelength and the material can be considered homogeneous. Hence, the dielectric function of the material can be described by effective medium models [1.29]. In the approximation of an isotropic medium where the anisotropy of pore morphology is not taken into account, the main models used for the calculation of the effective dielectric function are those proposed by Bruggeman [1.45] and Landau-Lifshitz-Looyenga (LLL) [1.46]. The resulting description of refractive index is quite similar for these two models [1.47], although the LLL model tends to be more accurate for larger porosities. In this work, we will consider the LLL model to describe the dielectric function of our porous silicon structures:

$$n^{2/3} = \sum_i f_i n_i^{2/3} \qquad \text{(EQ-1-2)}$$

Where n_i and f_i represent the refractive index and filling fraction of material i, respectively. In the case of freshly prepared porous silicon where the only constituting materials are air and silicon, the refractive index can be expressed as:

$$n_{eff}^{2/3} = P + n_{Si}^{2/3}(1-P) \qquad \text{(EQ-1-3)}$$

with *P* the porosity of the material, which is equivalent to the air filling fraction. As demonstrated in the expressions above, the dielectric constant of porous silicon directly depends on the porosity. A broad range of refractive index values can be obtained by modulation of the porosity, as shown in Fig 1.2.7. Values as high as 2.8 can be obtained with low porosities (~25%) and as low as 1.2 with high porosities (~90%).

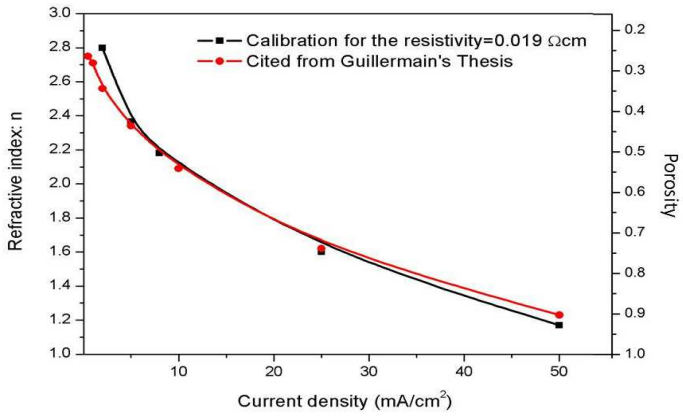

Fig 1.2.7 Refractive index of mesoporous silicon versus the porosity at the wavelength of 2000 nm [1.48]

As will be presented in section 1.2.4, the modulation of the refractive index is a key to the realization of a large variety of optical devices such as Fabry-Perot cavities, Bragg mirrors, waveguides, or photonic crystal structures.

1.2.4.2 Optical losses

Material losses are crucial issues for many optical applications and have been the focus of many early works on porous silicon. The main sources of optical losses in porous silicon are absorption and scattering losses.

Porous silicon absorption is quite high in the high-energy range. In the case of mesoporous silicon, it has been shown to be close to that of crystalline silicon [1.49]. However, in the near - IR range where the crystalline material becomes transparent, the residual absorption was shown to be almost negligible [1.50], and the main sources of optical losses are scattering - induced.

Scattering losses have two origins: the first one is Rayleigh scattering at the interfaces of porous silicon nanocrystallites, and the second one is induced by roughness at the dissolution interfaces of the material. It has been shown that two different kinds of roughness coexist [1.51]:

- 'Waviness' at a millimeter scale, is attributed to doping fluctuations of the silicon wafer that lead to fluctuations of the porous silicon microstructure and etching velocity;
- 'Roughness' at a microscopic scale is mainly attributed to the initial surface state of the substrate, where any inhomogeneity or ruggedness can induce local variations of current density leading to variations of etching velocity. Low temperature anodization helps reducing interface roughness [1.32], because the higher electrolyte viscosity slows down ion diffusion at the Si/electrolyte interface.

1.2.4.3 In-depth inhomogeneity

In-depth control of layer thickness and porosity is crucial for good optical quality [1.52]. Two competing mechanisms are responsible for undesired fluctuations of porosity and etching velocity with anodization time:

- Pure chemical etching by the HF solution induces an increase of porosity with time, leading to larger pores towards the top of the layer that has been exposed the longest to the electrolyte. This mechanism can usually be neglected, except in the case of very long anodization times.
- Decreasing ion concentration in the electrolyte with increasing pore depth, induced by insufficient electrolyte regeneration, can lead to strong increase of porosity in the depth of the porous silicon layer. Introducing pause times during anodization to help renew the electrolyte is a way to reduce in-depth variation of the porosity; another way is to slow down the anodization kinetics using a low-temperature process.

1.2.5 Optical sensors based on porous silicon

In the previous section, we have introduced the main properties of mesoporous silicon, in particular the properties of interest for optical sensor applications:

- The huge specific surface of mesoporous silicon offers a great potential for gas and bio-chemical sensing, because of the very large interaction area available for target molecules, enabling the sensing of a large quantity of molecules.

- The refractive index of the porous material is directly depending on the presence of molecules within the pores; hence, any adsorption events should lead to the modification of the effective refractive index, which should induce a variation of the optical properties of the device.

A few examples of optical sensors based on porous silicon are reviewed in the following.

1.2.5.1 Porous silicon monolayer: a Fabry-Perot interferometer

The most common photonic devices based on porous silicon are single layers and multi-layers consisting of stacks of layers with different porosities. The optical properties exploited in such devices usually rely on interference phenomena arising from multiple reflections at the layers interfaces. A single layer of mesoporous silicon constitutes the simplest of these interference devices.

Due to the refractive index contrast at the interfaces between the monolayer and its surrounding, incident light beams are partially reflected and interferences build up like in a Fabry-Perot interferometer. Hence, the reflectivity spectrum of a PSi monolayer exhibits Fabry-Perot fringes with maxima fulfilling the following condition at incidence angle θ:

$$m\lambda = \frac{2nd}{\cos\theta} \qquad \text{(EQ-1-4)}$$

where λ is the wavelength of incident light, n and d are the effective refractive index and the thickness of the monolayer, respectively, and m is an integer representing the order of each fringe.

When used as optical devices, Fabry-Perot interferometers based on porous silicon monolayer usually have a thickness of a few µm or less, in order to optimize the number of reflectivity maxima /minima in the spectral range of interest. In particular, they have been largely studied for their potential as sensors, based on the variation of effective refractive index of the porous silicon layer when the target species are coating the internal surface of the pores or chemically reacting with it. Such devices are either measuring the shift of the interference fringes in spectroscopic measurements, or monitoring the variation of reflectivity at fixed wavelength.

The first biosensor based on porous silicon monolayer was reported as early as 1997, for a variety of biomolecules such as DNA and proteins [1.53]. This early demonstration has shown detection sensitivities better than 1 pMol of analyte concentration, and is illustrated in Fig 1.2.8. Through appropriate pore size and surface chemistry tailoring [1.54] these devices could be optimized for the specific detection of a large variety of biomolecules, and great progress has been made towards the integration of these biosensors into biochips [1.55].

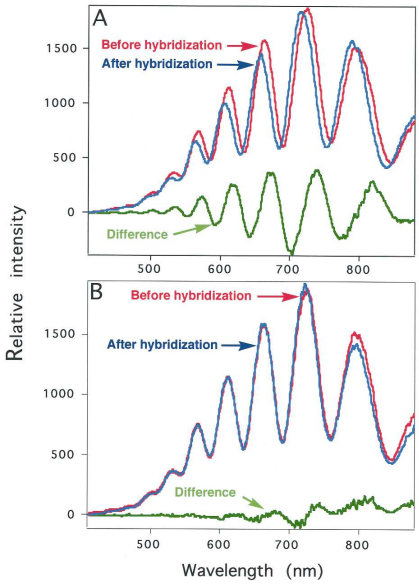

Fig 1.2.8 Example of DNA sensing extracted from [1.53]. The fringes experience a clear shift after exposure to the analyte containing the complementary DNA strand with concentration of 2.10^{-12}mol.

Interferometers based on porous silicon monolayer have also been widely studied as chemical sensors, for the detection of solvent concentrations in liquids [1.56], of dangerous gases such as HF [1.57], or more usually for the detection of solvent vapors. In particular, Gao *et al.* demonstrated a detection limit as low as 500 ppb and a dynamic range of nearly five orders of magnitude for the detection of 1.7% ethanol vapor in air [1.58].

1.2.5.2 Other interference-based devices

The refractive index of mesoporous silicon is directly related to its porosity, which means that a variation of porosity in the depth of the material leads to a variation of refractive index. By controlling the anodization parameters with time, any porosity – hence, refractive index – profile can be obtained, enabling for the fabrication of multilayer devices, such as Bragg mirror or micro-cavities.

A Bragg mirror is a multilayer structure which consists of stacks of layers with alternating porosity and thickness. In such a structure, the complex optical interferences lead to the creation of a “stop band”, a region of high reflectivity with a width increasing with the index contrast between the constituting layers. The first Bragg mirrors based on mesoporous silicon were realized in the 90’s [1.59]. With the improvement of the anodization conditions, very high-quality mirrors can now be fabricated, as illustrated in Fig 1.2.9.

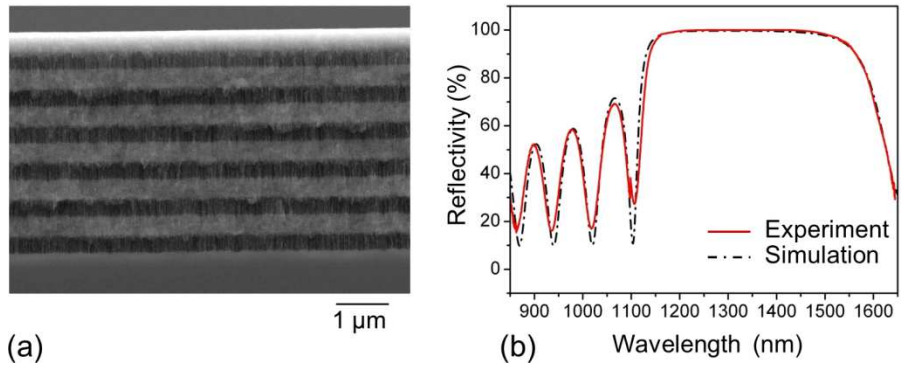

Fig 1.2.9 (a) Exemple of Bragg mirror in mesoporous silicon and (b) experimental and simulated reflectivity response; extracted from [1.30].

A large variety of work has been performed to demonstrate the potential of Bragg mirrors for optical sensing, ranging from chemical sensing like vapor sensing [1.60] to the detection of biomolecules [1.61]. Integration of such devices in micro-arrays has also been reported [1.62].

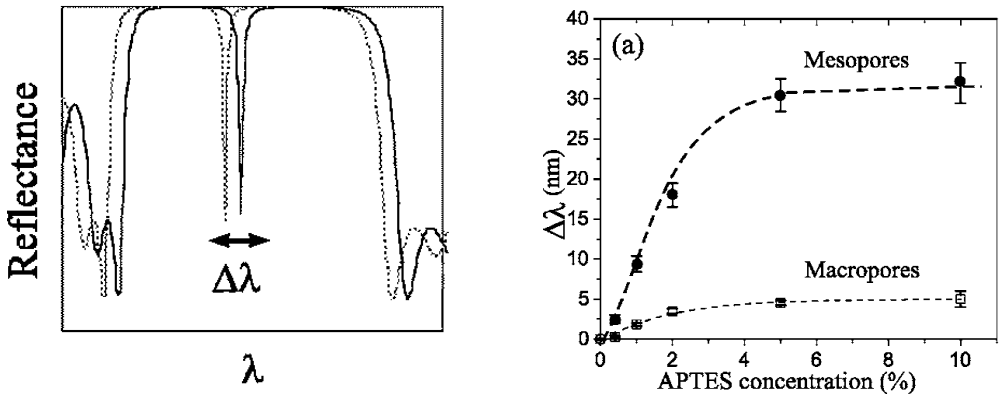

Fig 1.2.10 (a) Principle of sensing by monitoring the shift of microcavity resonance, (b) Example of resonance shift variation depending on the molecule concentration, for 2 different pore size; Extracted from [1.64]

When an extra layer is introduced inside the Bragg mirror, with a different width or a different porosity from the PSi layers constituting the multilayer, a microcavity is built. Such Fabry-Perot microcavities are very popular photonic devices based on porous silicon

multilayers, as they yield very sharp resonances on the high-reflectivity spectrum of the Bragg mirror [1.63]. By monitoring the shift of the resonance, high-sensitivity bio- and chemical sensing [1.64, 1.65] has been proposed. In particular, Ouyang et al. investigated the detection sensitivity of such microcavities depending on pore size and predicted a detection limit equivalent to a layer thickness below 0.01 nm. This work is illustrated in Fig 1.2.10.

1.2.5.3 Guided-waves devices

Guided-wave devices are another important family of photonic devices and present a good alternative to devices based on multilayers for biosensing applications, because the sensing layer can be a thin layer at the device surface, thus favoring efficient molecule infiltration [1.66].

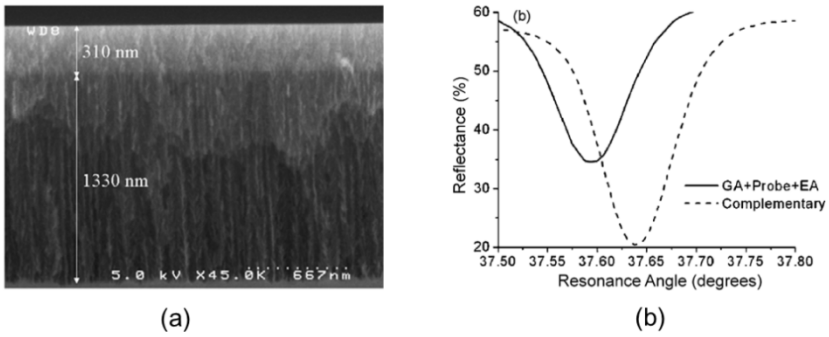

Fig 1.2.11 (a) Planar waveguide in mesoporous silicon; (b) its application as a biosensor for DNA sensing; A shift in coupling angle of 0.046° is observed after exposure to 50 µM of complementary DNA. Extracted from [1.68]

Among such devices, planar waveguides are the simplest structures, which usually consist of a bilayer with a thin guiding layer with medium porosity on top of a highly porous substrate. In these structures, light confinement and guiding is achieved by total internal reflection due to the index-contrast between the waveguide and its surrounding. Such structures can be seen as the dielectric equivalent of the surface plasmon resonance (SPR) structures introduced in the next section; similarly to SPR devices, there are several configurations to excite the modes of planar waveguides: in transmission, where light is injected directly through the cleaved edge of the waveguide [1.67]; or via surface excitation, either through a prism [1.68] or a grating [1.69]. Fig 1.2.11 shows an example of planar waveguide used as a biosensor for DNA detection by Rong *et al*. In this case the device is excited through a prism, i.e., light coupling into the waveguide mode occurs at very particular incidence angles, which can be

monitored. In the biosensor application presented here, DNA hybridization induces a variation of the waveguide refractive index, which leads to a variation of coupling angle.

If periodicity is introduced into the planar waveguide, e.g. via in-plane patterning and / or replacing the substrate by a Bragg mirror, a large variety of « photonic crystal » devices can be designed [1.70]. In particular, surface-waves devices can be realized, which consist of a periodic multilayer with a defect layer at its surface, in which a propagating mode can be excited [1.71]. Very high sensitivity of the surface wave to the surface layer optical thickness was demonstrated, hence leading to applications to biochemical [1.72] and gas sensing [1.73]. Compared to the planar waveguide, such devices yield a higher sensitivity and enable a wider range of refractive index for the guiding layer, hence enabling a larger range of sensing applications due to a larger choice of porosities.

Introducing lateral patterning into the waveguiding structure enables to gain control over properties of the propagating mode, such as its velocity. In particular, it has been demonstrated that a strong reduction of light velocity, obtained by etching a periodic array of air slits into the waveguiding layer of a surface wave device, could lead to an increase of the sensitivity by an order of magnitude [1.74]. Similarly, planar photonic crystal structures, obtained by lateral patterning of a periodic array of air slits into a planar waveguide, have shown high sensitivity for sensing applications [1.75], due to the high spectral finesse of the excited resonances. An example of such device is illustrated in Fig 1.2.12 (b). The current drawback of such devices is the experimental realization, as PSi patterning is quite difficult [1.48].

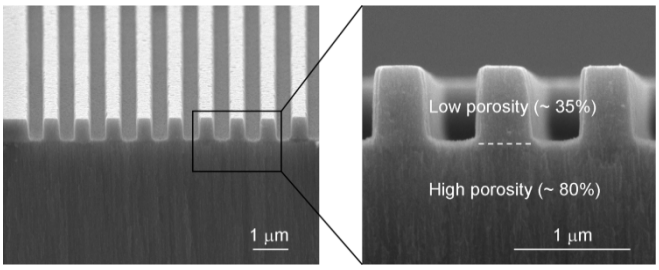

Fig 1.2.12 SEM images of fabricated planar photonic crystal in porous silicon; the period of the patterns is 900 nm, and the device has a total size of 100 µm x 100 µm (extracted from [1.75]).

1.3 Plasmonic element: optical nano-antenna

The plasmonic device proposed in this work is an array of optical bowtie nano-antennas, each of them consisting of two gold submicron-size triangles facing tip to tip, as illustrated in Fig 1.3.0.

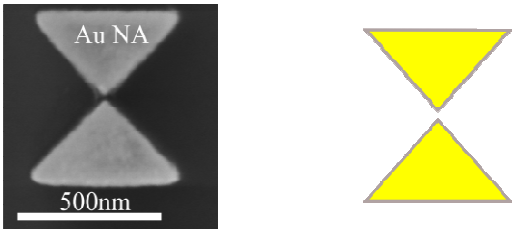

(a) *(b)*

Fig 1.3.0 Illustration of the bowtie nano-antenna:
(a)Image from scanning-electron microscope, (b) artistic view

Optical nano-antennas are the visible spectrum analogue of radio frequency (RF) antennas [1.76-1.78] (Fig 1.3.1). However, due to important losses in the visible-NIR spectrum and the presence of coherent electron oscillations (i.e. plasmonic resonance) [1.79], the optical response could be quite different. A striking feature of the optical antenna is its ability to manipulate and localize the electromagnetic field down to subwavelength dimensions [1.80], making them attractive for a wide range of applications including cloaking [1.81], biological and chemical sensing [1.82], sub-diffraction lithography [1.83], optical imaging [1.84], and energy harvesting [1.85].

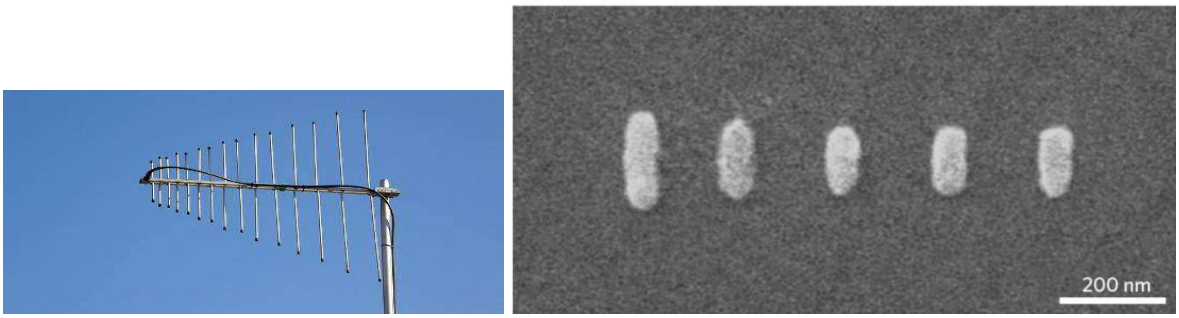

Fig 1.3.1 Examples of an RF antenna [1.86] (left, with characteristic dimensions of several centimeters) and its counterpart in the visible spectrum [1.78] (few hundreds of nanometers)

The area of biological and chemical sensing is one of the most important applications driving the current research in optical nano-antennas. Several hot issues are the object of intensive study: the design and fabrication of nanostructures with accurate geometries and good

repeatability in spite of their very small features, the understanding of their optical response, and the investigation of their interaction with photonic elements for ultrasensitive applications.

In this respect, bowtie nano-antennas offer the following advantages:

- their design is very robust, hence limiting experimental fluctuations and enabling fabrication via top-down techniques with a good control of the geometry and a good reproducibility;
- their design also enables the fabrication of very small gaps between the 2 triangle tips, hence yielding high field enhancement in very small and controlled space;
- their resonance wavelength can be tuned over a large spectral range.

In the following, we present a basic introduction to the area of plasmonics and nano-antennas, as well as a short review on the applications of metallic nanostructures for sensing, including their use in hybrid photonic / plasmonic devices.

1.3.1 Introduction to plasmons

Many of the fundamental electronic properties of the solid state can be described by the Drude model where single electrons are moving in an ionic lattice. In this model, the particle motion is well depicted by a classical dynamical equation. Upon electric or optical excitation, the negatively charged conduction electrons carry out a collective motion with respect to the fixed positive-ions in the lattice, creating an effective charge at the surface that result in a restoring force attracting the electron gas back to its original position. These two opposite forces lead to an oscillation motion of the electron gas at a frequency ω_p around the equilibrium position. The coherent electron oscillation, called plasmon, is harmonically bounded to the positive ionic lattice and is present in bulk materials (3D) as well as at the interface of planar metal-dielectric interfaces (2D) and within metallic nanoparticles (0D):

1.3.1.1 Bulk Plasmon

For volume plasmon, $\omega_p = \sqrt{\frac{4\pi n e^2}{m_e}}$, where e is the elementary charge, m_e is the effective mass of the electron, n is the electron density. The value of ω_p for most metals lies in the ultraviolet

region and it decides the appearance of the metal - they are shiny and glittering in the visible spectrum.

1.3.1.2 Surface Plasmon Polaritons (SPP)

Surface plasmon polaritons is an electromagnetic wave propagating at the interface between a dielectric medium and metal. These surface waves have transverse magnetic (TM) polarization, and are evanescent in both the dielectric and the metal, i.e. the field intensity, in both media, decays exponentially perpendicular to the interface (See Fig 1.3.2). The excitation requires an opposite sign of Re (ε) of two media at the interface, which is always met for the device formed by metals and a dielectric since the former is strongly absorbing. The frequency of surface plasma polaritons, ω_{sp} is $\omega_p / \sqrt{2}$.

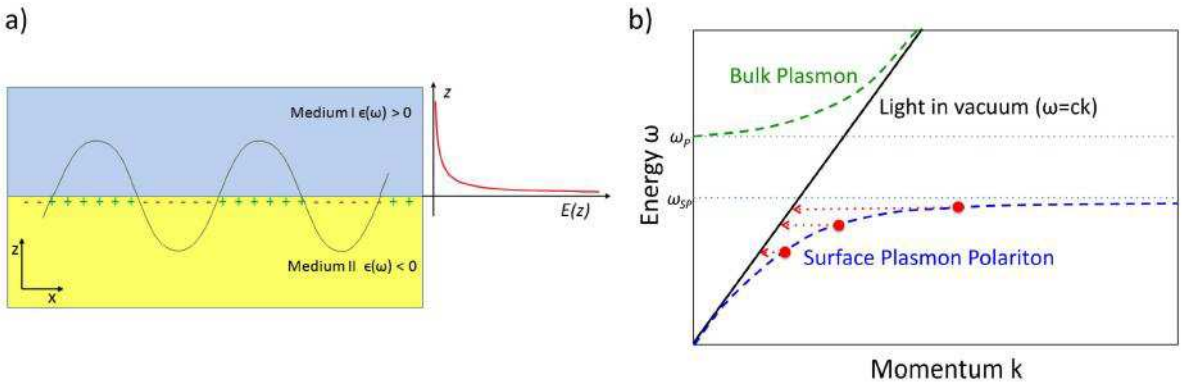

Fig 1.3.2: a) Schematics of SPP at an interface separating two semi-infinite regions with two dielectric functions of different sign, propagating along x direction and confined in z direction. b) Energy (ω) versus momentum (k) dispersion line of the propagating surface plasmon polariton (blue-dashed line). The bulk plasma frequency ω_p and the surface plasmon energy ω_{sp} are marked as dotted horizontal lines [1.87].

Experimentally, special phase - matching techniques such as prism coupling (e.g. Kretschmann or Otto configuration [1.88]), waveguide coupling [1.89], grating coupling [1.90] and so on need to be used [1.91]. As an example, a scheme of Otto configuration is shown in Fig 1.3.3. Like the excitation of waveguide based on PSi, the prism is placed on top of the metal film and both of them are separated by a thin air gap. At specific incident angle, total internal reflection (TIR) takes place at the prism / air interface and part of them are evanescently tunneled to the air / metal interface, which will induce a minimal intensity in the reflected beam through the prism. The plasmonic mode is ultra - sensitive to changes in the permittivity of the adjacent dielectric environment and any target molecules binding events or

small change of the local refractive index close to the interface will lead to a deviation of the wavelength of the Plasmon resonance. Research in this field is far advanced and sensors based on this concept on the effect of the surface plasmon resonance shift are commercially available.

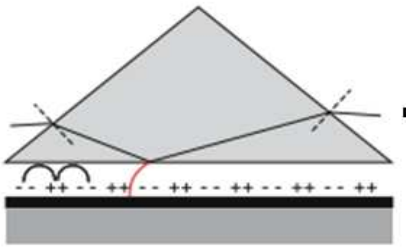

Fig 1.3.3 Prism coupling to SPPs with Otto configuration [1.88]

1.3.1.3 Localized surface plasmons (LSP)

Glass / metal nanoparticle composites have been in use for centuries as coloured glasses in church windows and other artistic works (Fig 1.3.4). Metal nanostructures show optical properties that are remarkably different from the properties of the bulk material. This optical effect is due to a strong interaction between light and the conduction electrons. For particles much smaller than the wavelength, the electron cloud starts oscillating in phase. A dipolar field outside the particle is formed, which leads to an enhanced absorption and scattering cross section, and also an enhancement of the local electromagnetic field. As opposed to 3D or 2D systems the LSP can be excited from free space.

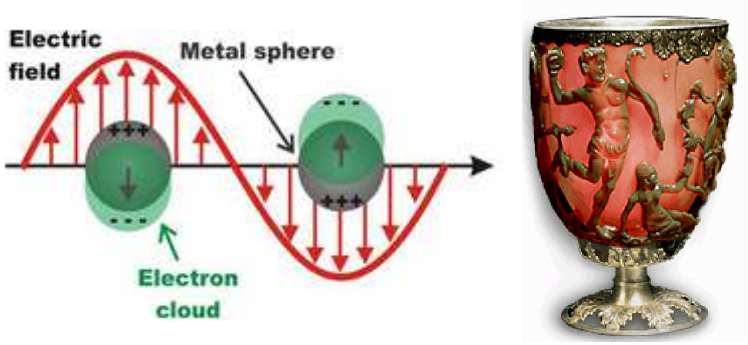

(a) *(b)*

Fig 1.3.4 (a) Schematic view of LSPR in nanoparticles, (b) Lycurgus cup (Extracted from [1.99])

In modern times metallic nanoparticles have found many new applications. The research on plasmonic materials has been the subject of a rapid growth in the past decade. This interest is founded on the progress and improved proficiency in fabrication methods to create metallic

structures of well-defined sizes & shapes and the potential to exploit these materials in important applications such as biomarkers for molecular imaging, light extraction of light-emitting diode, drug delivery and photo-thermal cancer treatment [1.92].

LSPR exhibits some distinct properties which have generated promising prospects in a variety of fields of science and technology. We summarize some of these properties:

- Localization of the electromagnetic fields: The fields induced by surface plasmons decay exponentially as we move away from the surfaces where they are excited. Thus, all the electromagnetic effects induced by those fields are reduced to a small region close to the surface (typically several nanometers). In addition, plasmons have shorter length compared to the wavelength of incoming source that excites them. As a result, it is possible to concentrate light on regions < the diffraction limit. Thanks to this property, for example greater resolution can be achieved if plasmons are used for imaging purposes. On the other hand, this feature is also essential for spectroscopic applications where a small amount of molecules located near a surface can be sufficient for the detection purpose.
- Field enhancement: according to Maxwell equations, the plasmonic resonances is the collective oscillation of free electron gas which leads to pile up of charges at the surface of the metals and those charges oscillate, which induces electromagnetic fields on the surroundings of the surface. Therefore, the fields around the surface are enhanced when they are compared to electromagnetic fields in free space (e.g. Fig 1.3.5). This field enhancement is a key property for many photonic applications, such as spectroscopy and sensing.

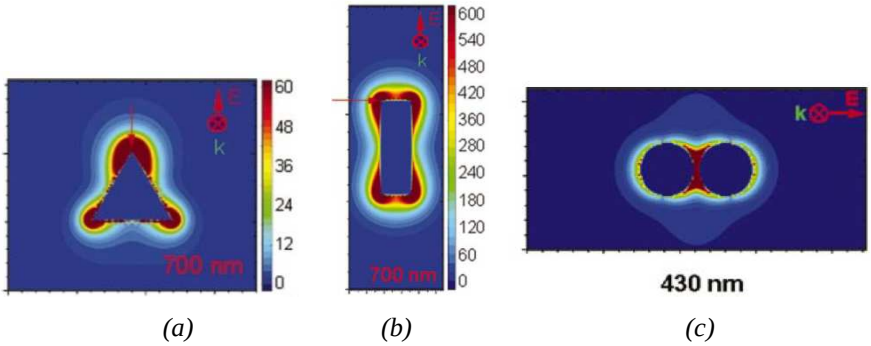

(a) *(b)* *(c)*

Fig 1.3.5 E-field enhancement contours external to monomers with different shapes. (a) and (b) are the E-field enhancement contours external to a triangular prism polarized along the one symmetry axes and a rod polarized along their long axes, respectively. The arrows show where the maximum of E-filed is. (c) A dimer of Ag nanoparticles separated by 2 nm, for a plane that is along the inter-particle axis. (Extracted from [1.96])

- Tunability: Plasmons exhibit also the tunability of their resonances via the modification of both the geometry and/or the coupling between different systems [1.93, 1.94, 1.95], e.g. 3 different geometrical nanoparticles shown in Fig 1.3.5. This opens up the door to engineer the optical spectral response in optically active systems to optimize the properties of plasmons for the requirements of a particular application.
- Sensitive to the environment: like SPPS, LSPR are extremely sensitive to the polarizability (e.g. the dielectric property, refractive index) of the surrounding medium. Thus, a small change on the dielectric function of the surrounding medium can produce large spectral shifts on the far - field radiation of the system. This feature is another key property of metal particles for sensing.

1.3.2 Metallic particles synthesis

The various applications require precisely defined antenna characteristic. Antenna should meet two important criteria: particle properties have to be well defined and the sample structure should allow easy localization and identification of individual particles. Metal nanoparticles can be produced either by thermal evaporation of metal onto pre-structured substrates (top-down process) or by wet-chemical synthesis (bottom-up route). Both methods have been extensively used in the literature and will be briefly presented in the following.

1.3.2.1 Nanoparticles synthesized by chemical methods:

Metallic nanoparticles, e.g. nanospheres and nanorods (Fig 1.3.6 (*a*) and (*b*)), could be prepared by chemical synthesis. The production mechanism is based on the reduction of the metal salt in solution with the presence of stabilizing agents that prevent the atoms agglomerating [1.97]. Between the benefits of chemical route are simplicity, reproducibility, and the possibility to synthesize a variety of well-controlled shapes ranging from simple spheres to more “exotic” shapes like nanostars or bipyramids [1.98]**.** Even though extremely monocrystalline nanoparticules can be produced, the size dispersion should not be underestimated. This point is highlighted in Fig 1.3.6 (*c*) where gold nanoparticles in aqueous suspensions are observed with a transmission electron microscope (TEM). The image clearly evidences deviations from the spherical shape due to facet formations.

The surface plasmon resonant spectra are determined by the sizes, shapes, and compositions which rely on the reaction conditions, like, temperature, pressure, types of solvents, PH value,

time, the method of excitation sources through the chemical synthesis (e.g. microwave, ultrasound process or x-ray), and so on [1.100]. Particularly, for Au and Ag nanoparticles, their LSPR happens within the ultra-visible (UV) range. The bigger the particles are, the smaller the plasmonic resonant wavelength will be (See Fig 1.3.6 (*c*)) [1.99]. Meanwhile, the gold surface provides the sites to realize the functionalization of biological targets via Au-S covalent binding. Both make Au nanoparticles to be perfect candidates for colorimetric biosensing applications [1.101].

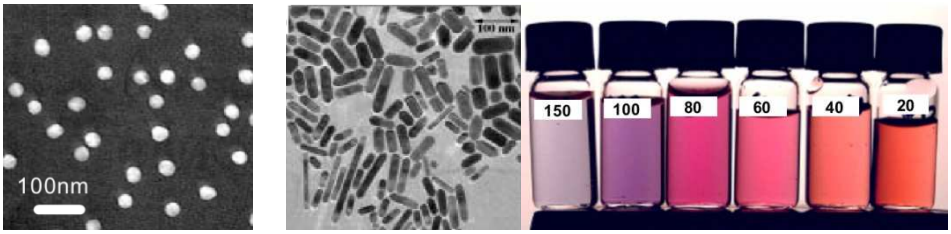

(a) *(b)* *(c)*

Fig 1.3.6 Example of nanoparticles (extracted from [1.99])

1.3.2.2 Nanoparticles fabricated by top-down methods

Precise control over nanoscale architecture is an essential aspect in relating new size-dependent material properties. Electron-beam lithography is a powerful tool for the fabrication of metal nanostructures. The ultimate resolution is better than 10 nm, and the technique is highly flexible over a wide range of materials. The flexibility originates from the fact that the electron-beam is scanned over the surface by a programmable pattern generator. The electron beam of a scanning electron microscope (SEM) is used to expose small areas in a positive resist on top of the sample. Additional processing steps are required for the fabrication of metal nanostructures, including a chemical development process, metal evaporation and resist lift-off. Other approaches based on nanosphere lithography (NSL, [1.102, 1.103]) and nanoimprint lithography (NIL, [1.104]) have been implemented with success (Fig 1.3.7).

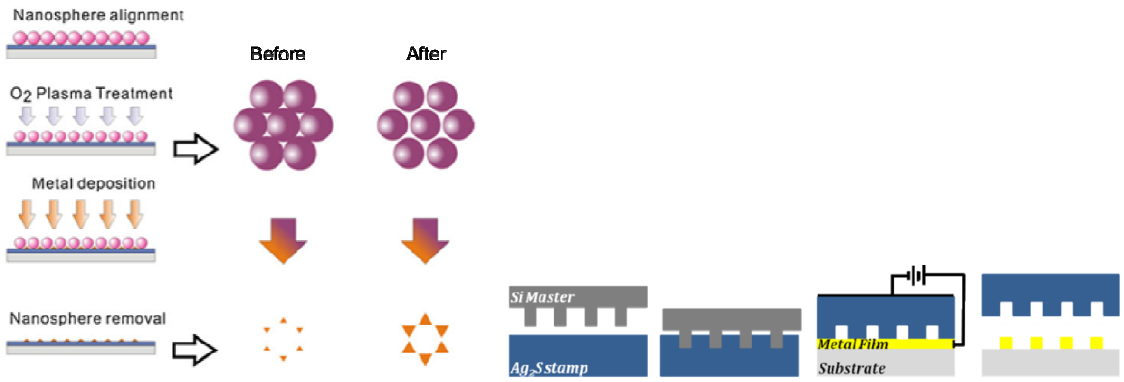

(a) *(b)*

Fig 1.3.7 Illustration of (a) NSL (extracted from [1.102]) (b) NIL (extracted from [1.104])

1.3.3 Optical antenna

In antenna theory, antenna parameters are directly related to the wavelength of the incident radiation. However at optical frequencies the extension of the antenna concept falls down because incident radiation is no longer perfectly reflected from the metal's surface and free-electron gas oscillation (surface plasmons) has to be taken into account. Radiation penetrates into the metal and gives rise to oscillations of the free-electron gas. Hence, at optical frequencies, the solution given by classical antenna theory is no longer valid and the antenna no longer responds to the external wavelength but to a shorter effective wavelength which depends on the material properties. Recent theoretical and experimental works have shown that the resonant length of optical dipole antennas is considerably shorter than one-half the wavelength of the incident light [1.78, 1.105, 1.106]. Control over the plasmon frequencies has been achieved by playing with particle shapes, as recently shown for nanoshells [1.107], nanorings [1.108], and nanorods [1.109]. Optical properties of ordered, interacting metal nanoparticles have recently come to the forefront in the merging field of plasmonic [1.102, 1.110, 1.111]. In particular, coupling particle dipole modes have been observed to induce a strongly red-shifted dipole-active mode for external fields oriented along the inter-particle axis and a blue shifted mode for perpendicular orientations [1.112]. As the gap between the two interacting particles is decreased, the coupling strength will increase and give rise to an enhanced electric field in the vicinity of the gap. The coupling effect has been studied between two interacting circles [1.112], ellipses [1.106], triangles [1.113], and rectangles [1.78] using far-field, polarization defined light. This work focuses on a particular type of dimer: the bowtie antenna (Fig 1.3.0) consisting of two metallic triangles facing tip to tip that are separated by a small gap. It combines the electromagnetic properties of sharp metal tips

with those of coupled plasmon resonant nanoparticle pairs. Bowties were first proposed in the microwave regime [1.114], and various antennas have been studied since in the mid-infrared wavelengths near 10 μm [1.115] and at the optical frequencies [1.116, 1.117]. Far-field measurements have demonstrated enhanced fields corresponding to proper resonant wavelengths and polarization of incident light [1.78, 1.113]. Antennae have been fabricated on NSOM tips [1.118] and laser diodes [1.105].

1.3.4 Optical sensors based on metallic nanostructures

1.3.4.1 Sensing via direct monitoring of the plasmon resonance

Gold nanoparticles are among the most fascinating objects for biological sensors in nanotechnology, because their localized surface plasmon resonance can be directly monitored by colorimetry. Owing to their surface plasmon resonance absorption which strongly depends on their size and inter-particle distance, solutions of nanoparticles generally exhibit a color change from red to blue when inter-particle distance is reduced towards the aggregated state, and inversely, from blue to red when inter-particle distance is enlarged and the particles are more dispersed. Based on this state-dependent (aggregation / dispersion) SPR absorption properties, gold nanoparticles can be used as a convenient tool for the sensing of metal ions [1.119], enzymes [1.120], or biomolecules like proteins [1.121, 1.122].

Plasmonic nanoparticles deposited or fabricated on top of a substrate have also been widely studied for sensing applications. Among the large variety of shapes and target molecules that have been proposed, silver or gold nanodisks fabricated by electron-beam lithography have been used to demonstrate successful sensing of species ranging from bacteria to proteins such as avidin, by monitoring the plasmon resonance shift ([1.123], [1.124]). It was shown that such nanoparticles yielded very short decay length of the field intensity from the nanoparticle surface into the analyte, thus enabling the detection of very thin molecule layers with good sensitivity [1.125]. Following this promising works based on single nanodisks sensing, dimers of nanoparticles have also been proposed for sensing applications of organic molecules and proteins, based on coupled gold nanodisks realized by electron-beam lithography. Depending on the inter-particle distance and the efficiency of particle functionalization, a sensitivity enhancement by a factor up to 6 has been demonstrated with respect to similar single nanodisks in the particular case of BSA sensing [1.126]. Replacing the second nanodisk in the dimer by a chemically-synthesized nanoparticle deposited onto the nanodisk enables to obtain

much smaller inter-particle gaps yielding very high sensitivities in highly localized spaces. A way to achieve reproducible gap sizes is via molecular grafting; in this configuration, the nanoparticle can also be used as a marker for the detection of the biomolecular recognition. A similar principle has been used for SPR substrates, where a 18-fold increase of sensitivity was demonstrated for DNA sensing already more than a decade ago [1.127].

1.3.4.2 Surface plasmon resonance-enhanced sensing

Another large application of nanoparticles or nanoantennas in sensing is via plasmon-resonance-enhanced mechanisms such as fluorescence [1.128] or Raman spectroscopy [1.129]. Enhancement of such mechanisms is mostly resulting from the increased cross section provided by the metallic structure and from the strong field intensities in the vicinity of the metal due to the plasmon resonance, yielding abilities for single molecule sensing when the conditions for strong coupling are obtained.

Plasmonic nanoparticles have been increasingly used in a wide variety of sensors based on luminescence mechanisms. As an example, Chen et al reported a new fluorescence sensor for the highly selective detection of Cu^{2+} ions based on the aggregation-induced fluorescence quenching of highly-fluorescent glutathione-capped gold nanoparticles [1.130]. In the case of chemiluminescence, it has been shown that gold nanoparticles functionalized with luminol yield an enhancement of chemiluminescence intensity by almost an order of magnitude with respect to luminol alone [1.131]**.** Nanoantennas have also been investigated for fluorescence enhancement, and single-molecule detection has been demonstrated thanks to the enhancement of molecule fluorescence by 3 orders of magnitude provided by a bowtie nanoantenna [1.132].

The first enhancement of Raman signal in the vicinity of a metallic surface was observed by Fleischmann in 1974, while studying pyridine on a rough silver electrode [1.133]. This exciting discovery gave birth to the field of Surface-Enhanced Raman Scattering, in which the initial metallic surfaces have been gradually replaced by metallic nanoparticles of various shapes and arrangements [1.134, 1.135] or nano-antennas, in order to optimize the optical properties and the sensitivity enhancement of the systems. In particular, single gold bowtie nanoantennas were used to provide a controllable environment for Surface-Enhanced Raman Scattering of adsorbed molecules, allowing for single molecule detection [1.136].

The coupling with plasmon resonance nanostructures is also a way to achieve sensitivity enhancement in integrated photonic devices such as Fabry-Perot cavities or interferometers, as presented in the following.

1.3.4.3 Hybrid structures:

Interferometer coupled with surface plasmon

The first Fabry-Perot surface plasmon resonance sensor was demonstrated by Lu *et al.* in 2006 [1.137]. This hybrid structure consisted of a Fabry-Perot (F-P) interferometer coupled to a localized surface plasmon resonance (LSPR) structure. As shown in Fig 1.3.8, the F-P interferometer was composed of a thick $BaTiO_3$ (BTO) layer on top of a smooth thin silver mirror; the top mirror was replaced by a thin gold layer with controlled roughness supporting LSPR, whose position could be controlled by the island morphology.

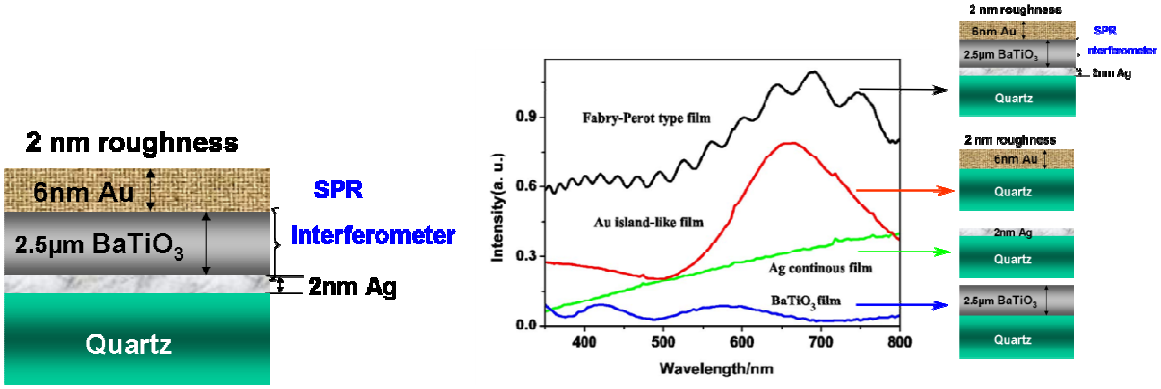

Fig 1.3.8 Fabry-Perot SPR sensor proposed by Lu et al. [1.137]

Comparing the optical response of the hybrid structure with the spectrum of each layer constituting the device (Fig 1.3.8), it was shown that the UV-vis spectrum of the Fabry-Perot SPR hybrid device (black curve) exhibited both Fabry-Perot interference fringe patterns (like the BTO layer alone – blue curve) and the strong increase of intensity around the plasmon resonance peak (like the rough Au layer alone – red curve). Upon functionalization of the gold thin film with thiols and subsequent immobilization of nanoparticles, it was demonstrated that the gain in sensitivity of the Fabry-Perot SPR sensor was highly interesting compared to the SPR system made of the same rough gold layer without interferometer.

Microcavity coupled to nanowires

More recently, Ameling *et al.* proposed to enhance the sensitivity of a localized plasmon resonance sensor made of a gold nanorod array via coupling with a microcavity [1.138]. The cavity consisted of a glass layer sandwiched between two mirrors placed at Bragg distance, the bottom mirror being a smooth gold layer, while the top mirror was replaced by the nanorod array (Fig 1.3.9 (*a*)).

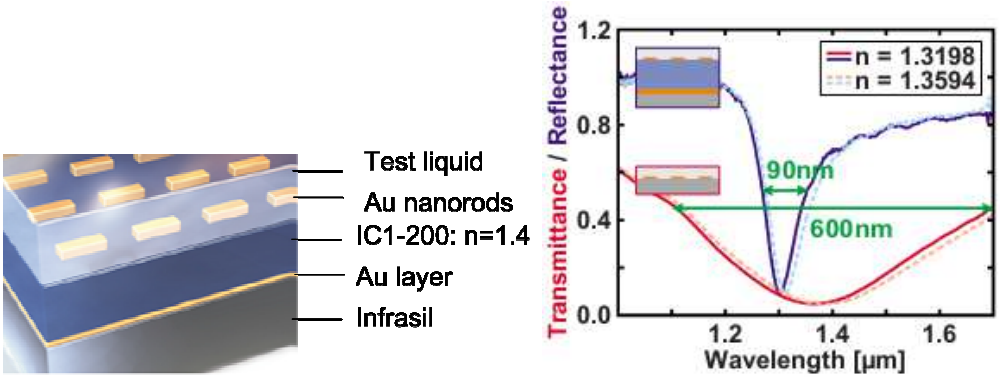

(a) *(b)*

Fig 1.3.9 Cavity – enhanced localized plasmon resonance sensor proposed by Ameling et al. (a) illustration view of the device; (b) sensing experiment showing a comparison between the hybrid device and the array of nanorods; extracted from [1.138]

Comparing the optical response of the hybrid device with the nanorod array, they showed that the coupling of the plasmon resonance with the high-finesse microcavity mode leads to a higher peak intensity and strong decrease of the resonance linewidth; this resulted in a strong increase of sensitivity by a factor of 3.7, which was demonstrated in a liquid sensing experiment comparing water (n = 1.3198) and a glucose solution (n = 1.3594), as illustrated in Fig 1.3.9 (*b*).

A more detailed study of the mechanisms of coupling between the plasmon resonance and the microcavity mode was performed by the same group, using a slightly different design where the nanorods were replaced by nanowires pairs and positioned inside the microcavity [1.139], as illustrated in Fig 1.3.10 (*a*). By varying the position of the nanowire pair with respect to the field distribution within the cavity, it was demonstrated that strong coupling could be obtained when the nanowires overlapped with a maximum of field intensity; moreover, a mode splitting was observed when the condition of strong coupling was fulfilled, as shown in Fig 1.3.10 (*b*).

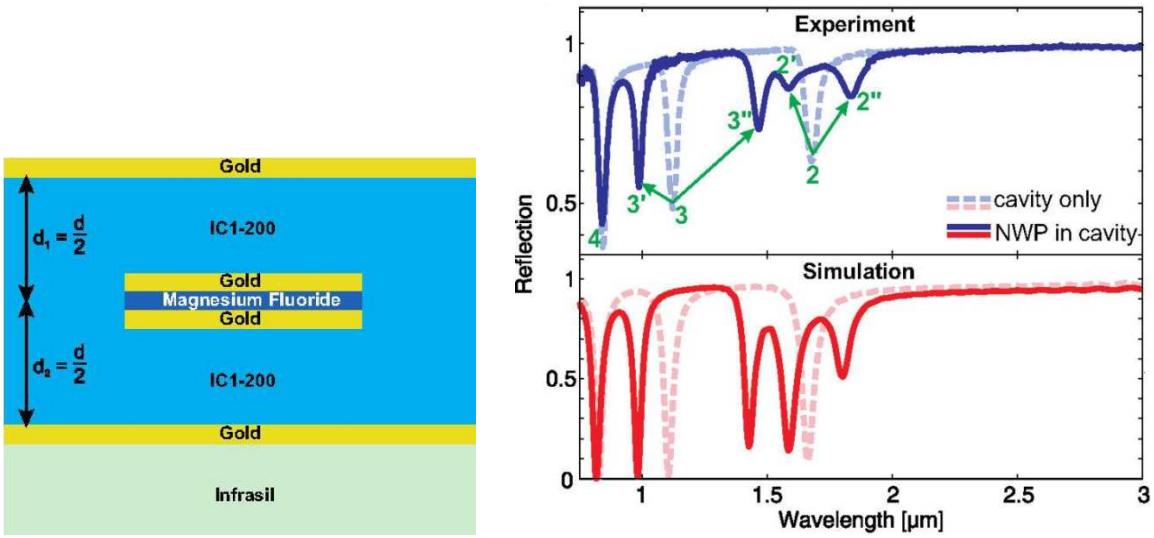

Fig 1.3.10 (a) Structure used for the study of the coupling between plasmonic nanostructure (gold nanowire pairs) and a microcavity; (b) Experimental and simulated reflectivity spectra showing mode splitting (extracted from [1.139])

Fabry-Perot cavity coupled with single nanoparticle

In 2012, Schmidt *et al.* proposed a hybrid nanoparticle - microcavity sensor, in which the photonic cavity is constituted by a high-refractive index film with a few µm thickness, on top of a lower refractive index substrate; the plasmonic nanostructure was a single gold nanoparticle with ~100 nm average diameter placed on top of the cavity, as illustrated in Fig 1.3.11 (*a*) [1.140].

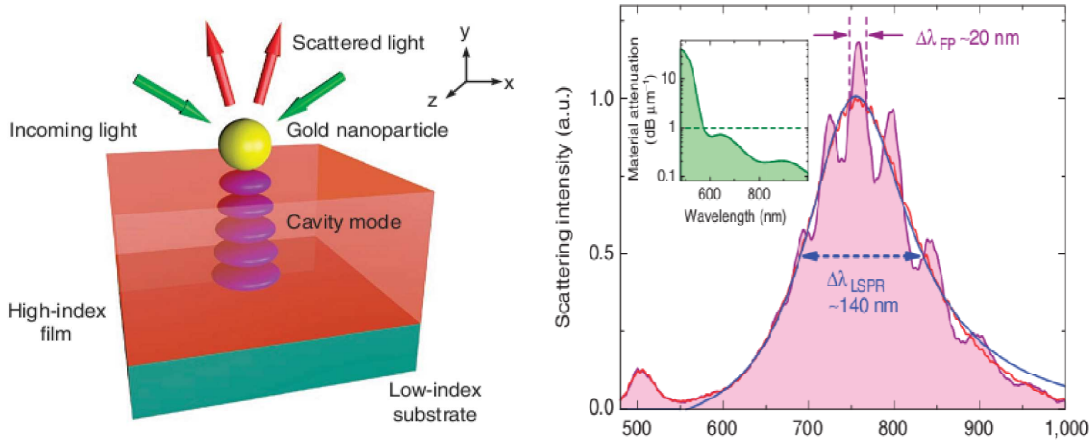

(a) *(b)*

Fig 1.3.11 Hybrid nanoparticle-microcavity sensor proposed by Schmidt et al. (a) Schematic view of the hybrid system; (b) Scattering spectra of the hybrid system (purple curve) and of the nanoparticle alone (red curve), and Fourier transformation spectrum of the hybrid system (blue curve); the insert is the absorption spectrum of BiYIG used as cavity material (extracted from [1.140])

Here again, the optical response of the hybrid structure (purple curve in the scattering spectra shown in Fig 1.3.11 (*b*)) exhibits both the broad peak of the nanoparticle alone (red curve) and the pronounced F-P interferometric oscillations from the cavity. Unfortunately, the related analysis discussing the influence of the nanoparticle on the interferometer was performed at a wavelength outside the plasmonic resonance of the nanoparticle.

A sensing experiment was reported, considering the case of a UV irradiation-induced variation of refractive index of a chalcogenide interferometer; unfortunately, the sensitivity was not evaluated and the comparison with the performances of the interferometer without nanoparticle was very unclear.

1.4 Design, Objectives and Organization of this work

1.4.1 Our design

The hybrid device proposed in this work is illustrated in Fig 1.4.0. It consists of the two following building blocks:

- PSi interferometer: as discussed in section 1.2, mesoporous silicon combines the advantage of an easy fabrication and high versatility in terms of refractive index and thickness; moreover, the porosity of the material offers a larger variety of sensing experiments, as the analyte can be either in the environment around the device, or infiltrated inside the PSi structure.
- Au bowtie NAs: as mentioned in section 1.3, bowtie NAs have a robust design enabling to obtain small inter-particle gaps with good reproducibility, with resulting high field enhancements; furthermore, their resonance can be tuned over a large wavelength range; here, we select the spectral range around 1300 nm, in order to be in the low-loss region of the PSi structure.

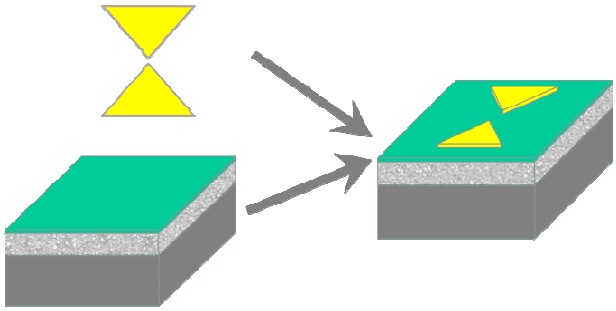

Fig 1.4.0 Schematic view of the hybrid structure proposed in this thesis: bowtie NAs coupled to a Fabry-Perot interferometer made of a PSi monolayer

1.4.1.1 Description of the device

The proposed hybrid device is presented in more details in Fig1.4.1. The interferometer is a monolayer of PSi on its Si substrate; a spacing layer of SiO_2 is deposited on top to protect the PSi layer and allow for NA fabrication. The PSi monolayer is about 5µm thick and its refractive index is ~1.5 similar to the index of silica. The bowtie NAs are fabricated on top of the silica layer and arranged in a periodic array with a period of 800 nm. This period is kept constant throughout this work in order to keep the collective response of the NA array always

the same and overcome the influence of coupling between the single NAs. The adherence of the gold structures on the silica surface will be ensured by a thin (4nm) titanium layer.

Similarly to the other hybrid structures presented above, we expect the coupling between the modes from the interferometer and the NA array to yield interesting phenomena, resulting in a sensitivity enhancement for sensing applications. In order to validate this choice of device, a preliminary demonstration of the NA/interferometer interaction is presented in the following.

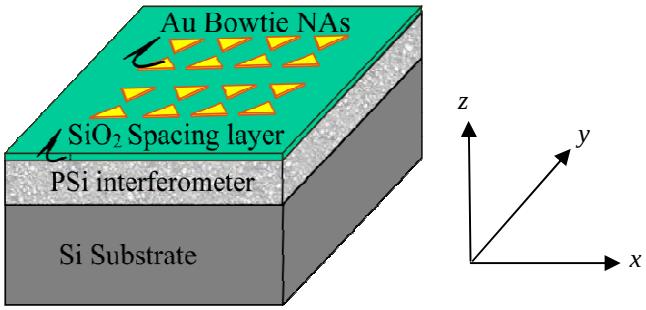

Fig 1.4.1 Description of the hybrid structure

1.4.1.2 Validation of the device choice

NA design

From the previous sections we gained some insight into classical antenna theory and the optical properties of metals. To predict in more detail the properties of a NA one has to perform computer simulations that take into account the antenna shape and the frequency dependant permittivity of the antenna material. The NA design was performed using the finite-difference time-domain (FDTD) method, for a gold bowtie geometry on a semi-infinite PSi based substrate. The dielectric functions for gold and for the titanium adhesion layer were given by the simulation software (Lumerical); the dielectric function of PSi was extracted from experimental measurements. The bowtie antenna is excited with a plane wave coming from the air and polarized in the *y* or *x* direction. A sketch of the geometry used for the simulation is shown in Fig 1.4.2.

The bowtie geometry has been optimized to yield a plasmonic resonance matching around 1300 nm wavelength. The following optimized parameters have been found: *A1* = 510 nm, *A2* = 280 nm, height = 30 nm, Gap = 20 nm, where "height" represents the thickness of the gold layer, and *A1*, *A2* and Gap are indicated in Fig 1.4.2 (*a*). The corresponding near-field

intensity enhancement factor ($=|E/E_0|^2$, monitored 20 nm above the antenna) is presented in Fig 1.4.2 (*b*) as a function of the wavelength. The plane wave is polarized in the *y* - direction along the antenna axis, and E_0 refers to the incident evanescent field in the absence of the antenna. The spectrum clearly shows a large field enhancement (few thousands) around 1300 nm in the *y* polarization. This resonance is broad and its quality factor is estimated to be close to unity.

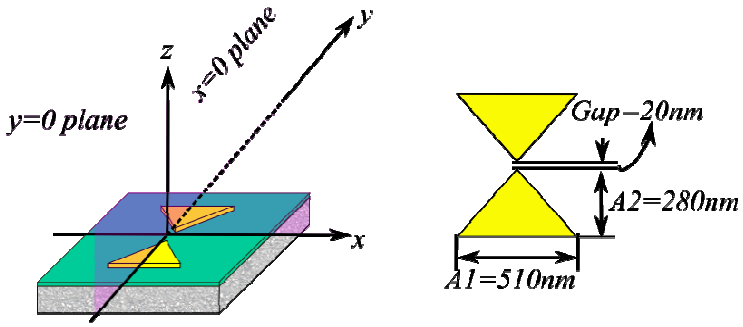

(a)

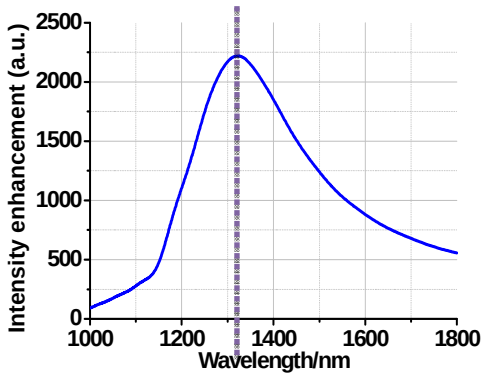

(b)

Fig 1.4.2: (a) Schematic view of the optimized bowtie geometry; (b) Corresponding near-field intensity enhancement factor versus wavelength for the optimized NAs on SiO_2 substrate

To understand the field confinement and enhancement in the bowtie NA, the electromagnetic field distribution was simulated for both *y* and *x*-direction polarization, presented in Fig 1.4.3.

The excitation with *y* - direction polarization enhances the field in the center of the bowtie gap while the *x* - direction polarization exhibits strong enhancement along the outside tips of the bowtie. The enhancement is about 1500 when the bowtie is excited with a *y* - polarization and 100 in the perpendicular direction. Hence, for the rest of the thesis the *y* - direction polarization will be considered.

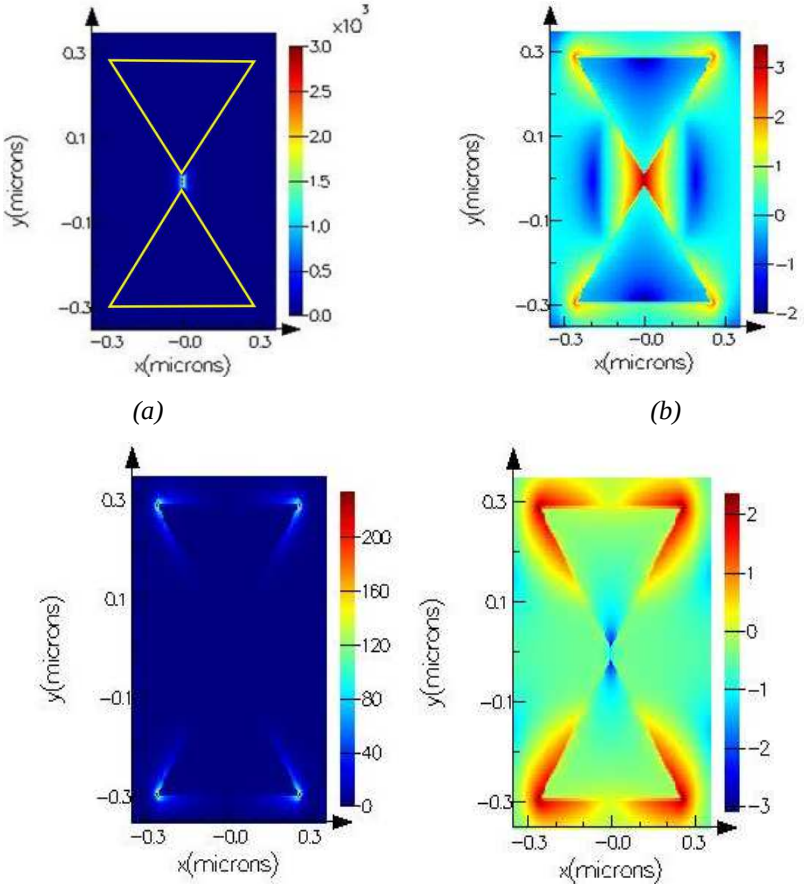

Fig 1.4.3 Electric field intensity (E^2) with y-polarization: (a) linear scale, (b) log scale; E^2 with x- polarization: (c) linear scale, (d) log scale.

Hybrid structure

When the semi-infinite substrate used in the simulations above is replaced by the interferometer structure, the reflectivity spectrum shown in Fig 1.4.4 is obtained. In this simulation, a plane wave polarized along *y* was used as excitation source. As can be observed, the spectrum exhibits both the Fabry-Perot oscillations of the interferometer and the amplification around 1300 nm of the NA resonance. Some additional features, like a strong variation of the fringe pattern around the resonance, indicate a clear signature of the optical coupling between the photonic and plasmonic modes.

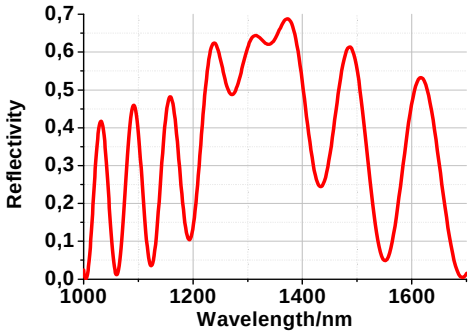

Fig 1.4.4 Optical response of the hybrid structure

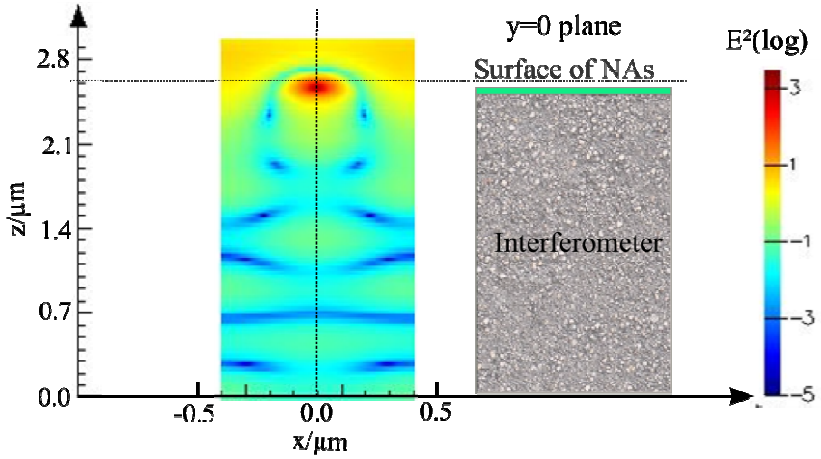

(a)

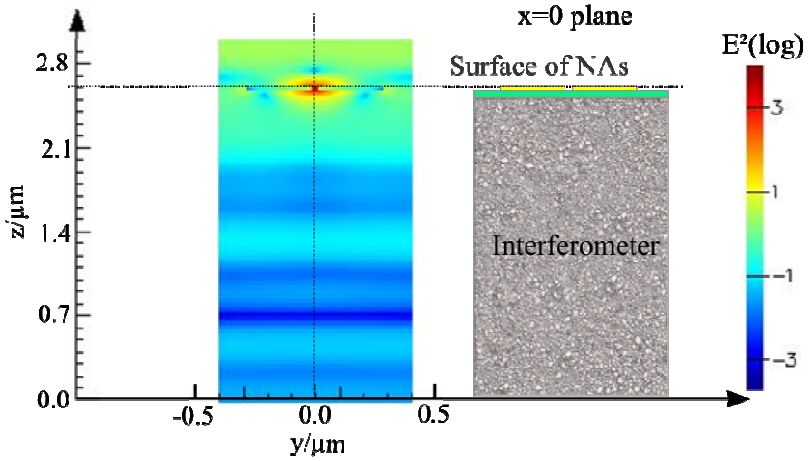

(b)

Fig 1.4.5 Electric field intensity (E^2 – log scale) in the 2 planes cutting through the middle of the NA: (a) xz plane (y=0) and (b) yz plane (x=0)

To further highlight the optical interaction between the metallic and dielectric building blocks, we have carried out optical mappings of the field distributions in the hybrid structure. They are presented in Fig 1.4.5 for the $y = 0$ and $x = 0$ planes, at 1300 nm wavelength. The figure confirms the hybrid nature of the mode.

1.4.2 Objectives of the PhD work

In this thesis, we will follow two successive objectives:

- The investigation of the coupling mechanisms between the bowtie NA array and the PSi interferometer: our approach will be the development of phenomenological models allowing for the description and the understanding of the optical mechanisms occurring within the device, as well as a systematical validation of the models by experimental results.
- The study of the potential of the hybrid device for sensing applications: a variety of sensing experiments will be performed in order to evaluate the gain in sensitivity yielded by the hybrid device with respect to the NA array and the interferometer considered separately.

1.4.3 Organization of the thesis

The next chapters of this thesis are organized as follows:

In Chapter 2, we will present the experimental fabrication and characterization techniques used in this work. The technological realization required intensive studies for the optimization of the different techniques: anodization for PSi layer fabrication, SiO_2 layer deposition, NA fabrication by electron-beam lithography and lift-off. Characterization of the devices was performed using structural (SEM) and optical techniques, such as macro-reflectivity for the characterization of PSi layers (determination of refractive index and thickness), and micro-reflectivity / transmission for the study of the optical properties of the devices; the opto-fluidic cell used for sensing experiments will also be presented.

In Chapter 3, we will study the coupling mechanisms between the 2 elements constituting the hybrid device, following 3 steps combining simulations and experimental results. First, a basic study will be performed in order to understand better the bowtie NA resonance, as well as the influence of the geometrical parameters on the resonance. Next, a phase matching model will be built to study the effect of the NA array on the interferometer; in this approach the NAs will be viewed as an equivalent layer having the same dielectric function, which will be derived from the Drude model. Finally, we will adopt a complementary point of view and

study the interaction between NAs and interferometer by coupled-mode theory, where the NA will be equivalent to a harmonic resonator.

In Chapter 4, we will present the a variety of sensing experiments with the hybrid device, to evaluate the potential of the device for sensing applications and the gain in sensitivity compared to the 2 systems constituting the hybrid structures: a bowtie NA array and a PSi interferometer. Different conditions for environmental sensing will be explored, ranging from large environment variations to small variations.

1.5 References

[1.1] Hauptmann, Peter (1993). Sensors: principles and applications. C. Hanser; Hemel Hempstead ; Englewood Cliffs, NJ : Prentice Hall, Munich

[1.2] http://www.realtimebiosensor.com/

[1.3] Jamois, C., C. Li, E. Gerelli, Y. Chevolot, V. Monnier, R. Skryshevskyi, R. Orobtchouk, E. Souteyrand, and T. Benyattou. "Porous-Silicon-Based Photonic Crystals for Sensing Applications." 2010.

[1.4] Fan, Xudong, Ian M White, Siyka I Shopova, Hongying Zhu, Jonathan D Suter, and Yuze Sun. "Sensitive Optical Biosensors for Unlabeled Targets: A Review." analytica chimica acta 620, no. 1 (2008): 8-26.

[1.5] James, Tony D, KRA Sandanayake, and Seiji Shinkai. "A Glucose - Selective Molecular Fluorescence Sensor." Angewandte Chemie International Edition in English 33, no. 21 (1994): 2207-09.

[1.6] Talley, Chad E, Leonard Jusinski, Christopher W Hollars, Stephen M Lane, and Thomas Huser. "Intracellular Ph Sensors Based on Surface-Enhanced Raman Scattering." Analytical chemistry 76, no. 23 (2004): 7064-68.

[1.7] Li, Tao, Erkang Wang, and Shaojun Dong. "Lead (Ii)-Induced Allosteric G-Quadruplex Dnazyme as a Colorimetric and Chemiluminescence Sensor for Highly Sensitive and Selective Pb^{2+} Detection." Analytical chemistry 82, no. 4 (2010): 1515-20.

[1.8] Swann, Marcus J, Louise L Peel, Simon Carrington, and Neville J Freeman. "Dual-Polarization Interferometry: An Analytical Technique to Measure Changes in Protein Structure in Real Time, to Determine the Stoichiometry of Binding Events, and to Differentiate between Specific and Nonspecific Interactions." Analytical biochemistry 329, no. 2 (2004): 190-98.

[1.9] Heideman, RG, RPH Kooyman, and J Greve. "Performance of a Highly Sensitive Optical Waveguide Mach-Zehnder Interferometer Immunosensor." Sensors and Actuators B: Chemical 10, no. 3 (1993): 209-17.

[1.10] Schmitt, Katrin, Bernd Schirmer, Christian Hoffmann, Albrecht Brandenburg, and Patrick Meyrueis. "Interferometric Biosensor Based on Planar Optical Waveguide Sensor Chips for Label-Free Detection of Surface Bound Bioreactions." Biosensors and Bioelectronics 22, no. 11 (2007): 2591-97.

[1.11] Rao, Yun-Jiang. "In-Fibre Bragg Grating Sensors." Measurement science and technology 8, no. 4 (1997): 355.

[1.12] Morey, William W, Gerald Meltz, and William H Glenn. "Fiber Optic Bragg Grating Sensors." Paper presented at the OE/FIBERS'89, 1990.

[1.13] Zangooie, S, R Bjorklund, and H Arwin. "Vapor Sensitivity of Thin Porous Silicon Layers." Sensors and Actuators B: Chemical 43, no. 1 (1997): 168-74.

[1.14] James, Stephen W, and Ralph P Tatam. "Optical Fibre Long-Period Grating Sensors: Characteristics and Application." Measurement Science and Technology 14, no. 5 (2003): R49-R61.

[1.15] MacCraith, BD, V Ruddy, C Potter, B O'kelly, and JF McGilp. "Optical Waveguide Sensor Using Evanescent Wave Excitation of Fluorescent Dye in Sol-Gel Glass." Electronics letters 27, no. 14 (1991): 1247-48.

[1.16] Wijaya, Edy, Cédric Lenaerts, Sophie Maricot, Juriy Hastanin, Serge Habraken, Jean-Pierre Vilcot, Rabah Boukherroub, and Sabine Szunerits. "Surface Plasmon Resonance-Based Biosensors: From the Development of Different Spr Structures to Novel Surface Functionalization Strategies." Current Opinion in Solid State and Materials Science 15, no. 5 (2011): 208-24.

[1.17] Sepúlveda, B, Laura G Carrascosa, D Regatos, Marinus A Otte, D Farina, and Laura M Lechuga. "Surface Plasmon Resonance Biosensors for Highly Sensitive Detection in Real Samples." Paper presented at the SPIE NanoScience+ Engineering, 2009.

[1.18] Subramanian, Anand, Joseph Irudayaraj, and Thomas Ryan. "A Mixed Self-Assembled Monolayer-Based Surface Plasmon Immunosensor for Detection of< I> E. Coli</I> O157: H7." Biosensors and Bioelectronics 21, no. 7 (2006): 998-1006.

[1.19] Schultz, Sheldon, David R Smith, Jack J Mock, and David A Schultz. "Single-Target Molecule Detection with Nonbleaching Multicolor Optical Immunolabels." Proceedings of the National Academy of Sciences 97, no. 3 (2000): 996-1001.

[1.20] Zhao, Jing, Xiaoyu Zhang, Chanda Ranjit Yonzon, Amanda J Haes, and Richard P Van Duyne. "Localized Surface Plasmon Resonance Biosensors." (2006).

[1.21] Enoch, Stefan, Romain Quidant, and Gonçal Badenes. "Optical Sensing Based on Plasmon Coupling in Nanoparticle Arrays." Opt. Express 12, no. 15 (2004): 3422-27.

[1.22] Sailor, Michael J. "Fundamentals of Porous Silicon Preparation." Porous Silicon in Practice: Preparation, Characterization and Applications. Wiley (2011): 1-42.

[1.23] Jane, Andrew, Roman Dronov, Alastair Hodges, and Nicolas H Voelcker. "Porous Silicon Biosensors on the Advance." Trends in biotechnology 27, no. 4 (2009): 230-39.

[1.24] Dennis R. Turner, “Electropolishing Silicon in Hydrofluoric Acid Solutions,” Journal of The Electrochemical Society 105, no. 7 (July 1, 1958): 402–408, doi:10.1149/1.2428873.

[1.25] Takashi Unagami, “Formation Mechanism of Porous Silicon Layer by Anodization in HF Solution,” Journal of The Electrochemical Society 127, no. 2 (February 1, 1980): 476–483, doi:10.1149/1.2129690.

[1.26] V. Lehmann and U. Gosele, “Porous Silicon Formation: A Quantum Wire Effect,” Applied Physics Letters 58, no. 8 (1991): 856–858, doi:10.1063/1.104512.

[1.27] M. Beale, N. Chew, M. Uren et al., Microstructure and formation mechanism of porous silicon, Applied Physics Letters, Vol. 46, (1985), pp. 86-88

[1.28] Bisi, Olmes, Stefano Ossicini, and Lorenzo Pavesi. "Porous Silicon: A Quantum Sponge Structure for Silicon Based Optoelectronics." Surface Science Reports 38, no. 1 (2000): 1-126.

[1.29] Kochergin, Vladimir, and Helmut Fèoll. Porous Semiconductors: Optical Properties and Applications. Springer, 2009.

[1.30] Guillermain, Elisa. "Dispositifs Nanophotoniques Ondes De Surface En Silicium Poreux: Technologie et Application La Bio-Détection." PhD Thesis, Institut National des Sciences Appliquées de Lyon, France, 142p, 2007.

[1.31] Nychyporuk, T., Nouvelles morphologies du silicium nanostructuré issues de l'anodisation electrochimiques: Elaboration,propriétés physico-chimiques et applications. Laboratoire de Physique de la Matière de lINSA de Lyon, 2006

[1.32] Setzu, S, G Lerondel, and R Romestain. "Temperature Effect on the Roughness of the Formation Interface of P-Type Porous Silicon." Journal of Applied Physics 84, no. 6 (1998): 3129-33.

[1.33] Lysenko, Vladimir, Fabrice Bidault, Sergei Alekseev, Vladimir Zaitsev, Daniel Barbier, Christophe Turpin, Francesco Geobaldo, Paola Rivolo, and Edoardo Garrone. "Study of Porous Silicon Nanostructures as Hydrogen Reservoirs." The journal of physical chemistry B 109, no. 42 (2005): 19711-18.

[1.34] Nychyporuk, T, V Lysenko, and D Barbier. "Fractal Nature of Porous Silicon Nanocrystallites." Physical Review B 71, no. 11 (2005): 115402.

[1.35] Brunauer, Stephen, Paul Hugh Emmett, and Edward Teller. "Adsorption of Gases in Multimolecular Layers." Journal of the American Chemical Society 60, no. 2 (1938): 309-19.

[1.36] Lewis, Stephen E., John R. DeBoer, James L. Gole, and Peter J. Hesketh. "Sensitive, selective, and analytical improvements to a porous silicon gas sensor." Sensors and Actuators B: Chemical 110, no. 1 (2005): 54-65.

[1.37] Populaire, Ch, B Remaki, V Lysenko, D Barbier, H Artmann, and T Pannek. "On Mechanical Properties of Nanostructured Meso-Porous Silicon." Applied physics letters 83, no. 7 (2003): 1370-72.

[1.38] Lysenko, V, S Perichon, B Remaki, and D Barbier. "Thermal Isolation in Microsystems with Porous Silicon." Sensors and Actuators A: Physical 99, no. 1 (2002): 13-24.

[1.39] Archer, M, and PM Fauchet. "Electrical Sensing of DNA Hybridization in Porous Silicon Layers." physica status solidi (a) 198, no. 2 (2003): 503-07.

[1.40] Song, Min-Jung, Dong-Hwa Yun, Nam-Ki Min, and Suk-In Hong. "Electrochemical Biosensor Array for Liver Diagnosis Using Silanization Technique on Nanoporous Silicon Electrode." Journal of bioscience and bioengineering 103, no. 1 (2007): 32-37.

[1.41] Canham, L_T. "Silicon Quantum Wire Array Fabrication by Electrochemical and Chemical Dissolution of Wafers." Applied Physics Letters 57 (1990): 1046.

[1.42] Halimaoui, A, C Oules, G Bomchil, A Bsiesy, F Gaspard, R Herino, M Ligeon, and F Muller. "Electroluminescence in the Visible Range During Anodic Oxidation of Porous Silicon Films." Applied physics letters 59, no. 3 (1991): 304-06.

[1.43] Komoda, Takuya, and N Koshida. "Nanocrystalline Silicon Ballistic Electron Emitter." In Device Applications of Silicon Nanocrystals and Nanostructures, 251-91: Springer, 2009.

[1.44] Wolkin, MV, J Jorne, PM Fauchet, G Allan, and C Delerue. "Electronic States and Luminescence in Porous Silicon Quantum Dots: The Role of Oxygen." Physical Review Letters 82, no. 1 (1999): 197.

[1.45] Bruggeman, D., Berechnung verschiedener physikalischer Konstanten von heterogenen Substanzen. Annalen der Physik, Vol. 416, (1935) pp. 665-679

[1.46] Looyenga, H. "Dielectric Constants of Heterogeneous Mixtures." Physica 31, no. 3 (1965): 401-06.

[1.47] Theiß, Wolfgang. "Optical Properties of Porous Silicon." Surface Science Reports 29, no. 3 (1997): 91-192.

[1.48] Cheng, LI. "Nouvelle filière nanotechnologique sur silicium poreux: Application à des dispositifs photoniques." PhD diss., Institut National des Sciences Appliquées de Lyon, 2010.

[1.49] Diesinger, Heinrich, Ahmad Bsiesy, and Roland Hérino. "In Situ Measurement of the Optical Absorption Coefficient of Porous Silicon." Journal of Applied Physics 89, no. 1 (2001): 221-25.

[1.50] Vincent, G, F Leblanc, I Sagnes, PA Badoz, and A Halimaoui. "Investigation of Optical Properties of Free-Standing Porous Silicon Films by Absorption and Mirage Effect." Journal of luminescence 57, no. 1 (1993): 217-21.

[1.51] Lérondel, G, R Romestain, and S Barret. "Roughness of the Porous Silicon Dissolution Interface." Journal of applied physics 81, no. 9 (1997): 6171-78.

[1.52] Thönissen, M, MG Berger, S Billat, R Arens-Fischer, M Krüger, H Lüth, W Theiss, et al. "Analysis of the Depth Homogeneity of P-Ps by Reflectance Measurements." Thin Solid Films 297, no. 1-2 (1997): 92-96.

[1.53] Lin, Victor S-Y, Kianoush Motesharei, Keiki-Pua S Dancil, Michael J Sailor, and M Reza Ghadiri. "A Porous Silicon-Based Optical Interferometric Biosensor." Science 278, no. 5339 (1997): 840-43.

[1.54] Tinsley‐Bown, AM, LT Canham, M Hollings, MH Anderson, CL Reeves, TI Cox, S Nicklin, et al. "Tuning the Pore Size and Surface Chemistry of Porous Silicon for Immunoassays." physica status solidi (a) 182, no. 1 (2000): 547-53.

[1.55] De Stefano, Luca, Paolo Arcari, Annalisa Lamberti, Carmen Sanges, Lucia Rotiroti, Ilaria Rea, and Ivo Rendina. "DNA Optical Detection Based on Porous Silicon Technology: From Biosensors to Biochips." Sensors 7, no. 2 (2007): 214-21.

[1.56] Min, Hee-Kyung, Ho-Sik Yang, and Sung M Cho. "Extremely Sensitive Optical Sensing of Ethanol Using Porous Silicon." Sensors and Actuators B: Chemical 67, no. 1 (2000): 199-202.

[1.57] Létant, S, and MJ Sailor. "Detection of HF Gas with a Porous Silicon Interferometer." Advanced Materials 12, no. 5 (2000): 355-59.

[1.58] Gao, Jun, Ting Gao, and Michael J Sailor. "Porous-Silicon Vapor Sensor Based on Laser Interferometry." Applied Physics Letters 77, no. 6 (2000): 901-03.

[1.59] Vincent, G. "Optical Properties of Porous Silicon Superlattices." Applied physics letters 64, no. 18 (1994): 2367-69.

[1.60] Snow, PA, EK Squire, P St J Russell, and LT Canham. "Vapor Sensing Using the Optical Properties of Porous Silicon Bragg Mirrors." Journal of Applied Physics 86, no. 4 (1999): 1781-84.

[1.61] Arroyo-Hernández, M, RJ Martín-Palma, V Torres-Costa, and JM Martínez Duart. "Porous Silicon Optical Filters for Biosensing Applications." Journal of non-crystalline solids 352, no. 23 (2006): 2457-60.

[1.62] Rea, Ilaria, Annalisa Lamberti, Ivo Rendina, Giuseppe Coppola, Mariano Gioffrè, Mario Iodice, Maurizio Casalino, Edoardo De Tommasi, and Luca De Stefano. "Fabrication and Characterization of a Porous Silicon Based Microarray for Label-Free Optical Monitoring of Biomolecular Interactions." Journal of Applied Physics 107, no. 1 (2010): 014513-13-4.

[1.63] Reece, PJ, G Lerondel, WH Zheng, and M Gal. "Optical Microcavities with Subnanometer Linewidths Based on Porous Silicon." Applied physics letters 81, no. 26 (2002): 4895-97.

[1.64] Ouyang, Huimin, Christopher C Striemer, and Philippe M Fauchet. "Quantitative Analysis of the Sensitivity of Porous Silicon Optical Biosensors." Applied Physics Letters 88, no. 16 (2006): 163108-08-3.

[1.65] Baratto, C, G Faglia, G Sberveglieri, Z Gaburro, L Pancheri, C Oton, and L Pavesi. "Multiparametric Porous Silicon Sensors." Sensors 2, no. 3 (2002): 121-26.

[1.66] De Stefano, Luca, and Sabato D'Auria. "Confocal Imaging of Protein Distributions in Porous Silicon Optical Structures." Journal of Physics: Condensed Matter 19, no. 39 (2007): 395009.

[1.67] Ferrand, P, and R Romestain. "Optical Losses in Porous Silicon Waveguides in the near-Infrared: Effects of Scattering." Applied Physics Letters 77, no. 22 (2000): 3535-37.

[1.68] Rong, Guoguang, Ali Najmaie, John E Sipe, and Sharon M Weiss. "Nanoscale Porous Silicon Waveguide for Label-Free DNA Sensing." Biosensors and Bioelectronics 23, no. 10 (2008): 1572-76.

[1.69] Wei, Xing, and Sharon M Weiss. "Guided Mode Biosensor Based on Grating Coupled Porous Silicon Waveguide." Opt. Express 19, no. 12 (2011): 11330-39.

[1.70] Jamois, C., Li, C., Gerelli, E., Orobtchouk, R., Benyattou, T., Belarouci, A., Chevolot, Y., Monnier, V. and Souteyrand, E. (2011). New concepts of integrated photonic biosensors based on porous silicon, Biosensors - Emerging Materials and Applications. Ed. Pier Andrea Serra, Intech, pp. 265–290.

[1.71] Guillermain, E, V Lysenko, and T Benyattou. "Surface Wave Photonic Device Based on Porous Silicon Multilayers." Journal of luminescence 121, no. 2 (2006): 319-21.

[1.72] Guillermain, E, V Lysenko, R Orobtchouk, T Benyattou, S Roux, A Pillonnet, and P Perriat. "Bragg Surface Wave Device Based on Porous Silicon and Its Application for Sensing." Applied physics letters 90, no. 24 (2007): 241116-16-3.

[1.73] Descrovi, Emiliano, Francesca Frascella, Beniamino Sciacca, Francesco Geobaldo, Lorenzo Dominici, and Francesco Michelotti. "Coupling of Surface Waves in Highly Defined One-Dimensional Porous Silicon Photonic Crystals for Gas Sensing Applications." Applied Physics Letters 91, no. 24 (2007): 241109-09-3.

[1.74] Jamois, C, C Li, R Orobtchouk, and T Benyattou. "Slow Bloch Surface Wave Devices on Porous Silicon for Sensing Applications." Photonics and Nanostructures-Fundamentals and Applications 8, no. 2 (2010): 72-77.

[1.75] Jamois, C., Li, C., Gerelli, E., Chevolot, Y., Monnier, V., Skryshevskyi, R., Orobtchouk, R., Souteyrand, E. and Benyattou, T. (2010a). Porous-silicon based planar photonic crystals for sensing applications, Proc. SPIE 7713, Conference on Photonic Crystal Materials and Devices IX, 7713OU, pp. 1–10

[1.76] N. J. Halas, “Connecting the dots: Reinventing optics for nanoscale dimensions,” PNAS 106 (10), 3643 (2009)

[1.77] L. Novotny and N. van Hulst, “Antennas for light,” Nature Photon. 5, 83 (2011)

[1.78] P. Muhlschlegel, H.-J. Eisler, O. J. F. Martin, B. Hecht, and D. W. Pohl, “Resonant optical antennas,” Science 308, 1607 (2005)

[1.79] W. L. Barnes, A. Dereux, and T. W. Ebbesen, “Surface plasmon subwavelength optics,” Nature 424, 824 (2003)

[1.80] A. Sundaramurthy, K. B. Crozier, and G. S. Kino, “Field enhancement and gap dependent resonance in a system of two opposing tip-to-tip Au nanotriangles,” Phys. Rev. B 72, 165409 (2005)

[1.81] B. Baumeier, T. A. Leskova, and A. A. Maradudin, “Cloaking from surface plasmon polaritons by a circular array of point scatters,” Phys. Rev. Lett. 103, 246803 (2009)

[1.82] T. H. Taminiau, F. D. Stefani, F. B. Segerink, and N. F. van Hulst, “Optical antennas direct single-molecule emission,” Nature Photon. 2, 234 (2008)

[1.83] A. Sundaramurthy, P. J. Schuck, N. R. Conley, D. P. Fromm, G. S. Kino, and W. E.Moerner, “Toward nanometer-scale optical photolithography: utilizing the near field of bowtie optical nanoantennas,” Nano Lett. 6 (3), 355 (2006)

[1.84] T. Xu, Y.-K. Wu, X. Luo, and L. J. Guo, “Plasmonic nanoresonators for high resolution colour filtering and spectral imaging,” Nature Comm. 1, 59 (2010)

[1.85] H. A. Atwater and A. Polman, “Plasmonics for improved photovoltaic devices,” Nature Mater. 9, 205 (2010)

[1.86] Log periodic antenna for the VHS and UHF bands (140-470 MHz) c2008 K. Krallis (www.wikipedia.com)

[1.87] TP ZHANG, Plasmonic-Photonic Hybrid Nano-device, Institut des Nanotechnologies de Lyon, Thesis defense on 22th November, 2012

[1.88] STEFAN A. MAIER, PLASMONICS: FUNDAMENTALS AND APPLICATIONS, Springer, 2007.

[1.89] Harris, R. D., and James S. Wilkinson. "Waveguide surface plasmon resonance sensors." Sensors and Actuators B: Chemical 29, no. 1 (1995): 261-267.

[1.90] Devaux, Eloise, Thomas W. Ebbesen, Jean-Claude Weeber, and Alain Dereux. "Launching and decoupling surface plasmons via micro-gratings." Applied physics letters 83, no. 24 (2003): 4936-4938

[1.91] Homola, Jiří, Sinclair S. Yee, and Günter Gauglitz. "Surface plasmon resonance sensors: review." Sensors and Actuators B: Chemical 54, no. 1 (1999): 3-15

[1.92] O'NEAL, D. Patrick, HIRSCH, Leon R., HALAS, Naomi J., et al. “Photo-thermal tumor ablation in mice using near infrared-absorbing nanoparticles”. Cancer letters, 2004, vol. 209, no 2, p. 171-176.

[1.93] P. Nordlander et al., “Plasmon Hybridization in Nanoparticle Dimers,” Nano Letters 4, no. 5 (May 1, 2004): 899–903, doi:10.1021/nl049681c.

[1.94] Isabel Romero et al., “Plasmons in Nearly Touching Metallic Nanoparticles: Singular Response in the Limit of Touching Dimers,” Optics Express 14, no. 21 (October 16, 2006): 9988–9999, doi:10.1364/OE.14.009988.

[1.95] Garnett W. Bryant, F. Javier Garcia de Abajo, and Javier Aizpurua, “Mapping the Plasmon Resonances of Metallic Nanoantennas,” Nano Letters 8, no. 2 (February 1, 2008): 631–636, doi:10.1021/nl073042v.

[1.96] Maier, Stefan A., and Harry A. Atwater. "Plasmonics: Localization and guiding of electromagnetic energy in metal/dielectric structures." Journal of Applied Physics 98, no. 1 (2005): 011101-011101.

[1.97] Nogami, Masayuki. "Synthesis and Self-Assembly of Gold Nanoparticles by Chemically Modified Polyol Methods under Experimental Control." Journal of Nanomaterials 2013 (2013).

[1.98] Julien R G Navarro, Delphine Manchon, et al., Synthesis of PEGylated gold nanostars and bipyramids for intracellular uptake, Nanotechnology 23, pp. 465602, (2012)

[1.99] Carsten S¨onnichsen, “Plasmons in metal nanostructures”, Ludwig-Maximilians-University of Munich, 20, June, 2001.

[1.100] Weihong Shi, Justin Casas, Meenakshi Venkataramasubramani, and Liang Tang, “Synthesis and Characterization of Gold Nanoparticles with Plasmon Absorbance Wave length Tunable from Visible to Near Infrared Region”, International Scholarly Research Network, ISRN Nanomaterials, Volume 2012, Article I D 659043, 9 pages doi:10.5402/2012/659043.

[1.101] Stefan Löfas, alan McWhirter, “The Art of Immobilization for SPR sensors”, Springer Ser Chem Sens Biosens 2006, 4: 117-151, DOI: 10.1007/5346_017

[1.102] Yun-Chorng Chang, Shih-Ming Wang, Hsin-Chan Chung, Chun g-Bin Tseng, Shih-Hui Chang, ‘Large-Area Bowtie Nanoantenna Arrays Fabricated with Economic Oxygen Plasma-Assisted Nanosp here Lithography’, Plasmonics (2011), Springer Science+Business Media, LLC 2011, 6:599– 604, DOI 10.1007/s11468-011-9240-5

[1.103] Haes, Amanda J., Shengli Zou, George C. Schatz, and Richard P. Van Duyne. "A nanoscale optical biosensor: the long range distance dependence of the localized surface plasmon resonance of noble metal nanoparticles." The Journal of Physical Chemistry B 108, no. 1 (2004): 109-116

[1.104] Kumar, Anil. Optical nano-antennas: Fabrication, characterization and applications. University of Illinois at Urbana Champaign, 2011

[1.105] Cubukcu, Ertugrul, Eric A Kort, Kenneth B Crozier, and Federico Capasso. "Plasmonic Laser Antenna." Applied Physics Letters 89, no. 9 (2006): 093120-20-3

[1.106] Aizpurua, Javier, Garnett W Bryant, Lee J Richter, FJ García De Abajo, Brian K Kelley, and T Mallouk. "Optical Properties of Coupled Metallic Nanorods for Field-Enhanced Spectroscopy." Physical Review B 71, no. 23 (2005): 235420

[1.107] E. Prodan, C. Radloff, N. J. Halas, and P. Nordlander, "A hybridization model for the plasmon response of complex nanostructures," Science, 302, 419-422 (2003)

[1.108] J. Aizpurua, P. Hanarp, D. S. Sutherland, M. Käll, G. W. Bryant, and F. J. García de Abajo, "Optical properties of gold nanorings," Phys. Rev. Lett. 90, 057401 (2003)

[1.109] K. G. Thomas, S. Barazzouk, B. I. Ipe, S. T. S. Joseph, and P. V. Kamat, "Uniaxial plasmon coupling through longitudinal self-assembly of gold nanorods," J. Phys. Chem. B, 108, 13066-13068 (2004)

[1.110] K. H. Su, Q. H. Wei, X. Zheng, J. J. Mock, D. R. Smith, and S. Schultz, "Interparticle coupling effects on plasmon resonances of nanogold particles," Nano Lett. 3, 1087-1090 (2003)

[1.111] T. Atay, J-H. Song, and A. V. Nurmikko, "Strong interacting plasmon nanoparticle pairs: from dipoledipole interaction to conductively coupled regime," Nano Lett. 4, 1627-1631 (2004)

[1.112] L. Gunnarsson, T. Rindzevicius, J. Prikulis, B. Kasemo, M. Käll, S. Zou, and G. C. Schatz, "Confined plasmons in nanofabricated single silver particle pairs: experimental observations of strong interparticle interactions," J. Phys. Chem. B 109, 1079-1087 (2005)

[1.113] A. Sundaramurthy, K. B. Crozier, G. S. Kino, D. P. Fromm, P. J. Schuck and W. E. Moerner, "Field enhancement and gap-dependent resonance in a system of two opposing tip-to-tip Au nanotriangles," Phys. Rev. B 72, 165409 (2005)

[1.114] Grober, Robert D, Robert J Schoelkopf, and Daniel E Prober. "Optical Antenna: Towards a Unity Efficiency near-Field Optical Probe." Applied Physics Letters 70, no. 11 (1997): 1354-56.

[1.115] Crozier, K. B., A. Sundaramurthy, G. S. Kino, and C. F. Quate. "Optical antennas: Resonators for local field enhancement." Journal of Applied Physics 94, no. 7 (2003): 4632-4642

[1.116] Farahani, J. N., D. W. Pohl, H. J. Eisler, and B. Hecht. "Single Quantum Dot Coupled to a Scanning Optical Antenna: A Tunable Superemitter." Physical Review Letters 95, no. 1 (06/28/ 2005): 017402

[1.117] Schuck, P. J., D. P. Fromm, A. Sundaramurthy, G. S. Kino, and W. E. Moerner. "Improving the mismatch between light and nanoscale objects with gold bowtie nanoantennas." Physical Review Letters 94, no. 1 (2005): 017402

[1.118] A. Sundaramurthy, P. J. Schuck, N. R. Conley, D. P. Fromm, G. S. Kino, and W. E Moerner, “Toward nanometer-scale optical photolithography: utilizing the near-field of bowtie optical nanoantennas,” Nano Lett. 6, 355-360 (2006)

[1.119] Kim, Youngjin, Robert C Johnson, and Joseph T Hupp. "Gold Nanoparticle-Based Sensing of “Spectroscopically Silent” Heavy Metal Ions." Nano Letters 1, no. 4 (2001): 165-67

[1.120] Ulijn, Rein V. "Enzyme-Responsive Materials: A New Class of Smart Biomaterials." Journal of Materials Chemistry 16, no. 23 (2006): 2217-25

[1.121] Tsai, Charng-Sheng, Ting-Bin Yu, and Chao-Tsen Chen. "Gold Nanoparticle-Based Competitive Colorimetric Assay for Detection of Protein–Protein Interactions." Chemical communications, no. 34 (2005): 4273-75

[1.122] Mayer, Kathryn M, Feng Hao, Seunghyun Lee, Peter Nordlander, and Jason H Hafner. "A Single Molecule Immunoassay by Localized Surface Plasmon Resonance." Nanotechnology 21, no. 25 (2010): 255503

[1.123] Greg Barbillon « Etude théorique et expérimentale de nanocapteurs d'espèces biochimiques à plasmons de surface localisés sur des nanoparticules métalliques », PhD thesis (2007)

[1.124] Cinel, Neval A, Serkan Bütün, and Ekmel Özbay. "Electron Beam Lithography Designed Silver Nano-Disks Used as Label Free Nano-Biosensors Based on Localized Surface Plasmon Resonance." Optics Express 20, no. 3 (2012): 2587-97

[1.125] G. Barbillon, J.-L. Bijeon, J. Plain, M. Lamy de la Chapelle, P.-M. Adam, P. Royer, "Electron beam lithography designed chemical nanosensors based on localized surface plasmon resonance." Surface Science 601.21 (2007): 5057-5061

[1.126] Acimovic, S. S., Kreuzer, M. P., Gonzalez, M. U., et al., Acimovic, Srdjan S., et al. "Plasmon near-field coupling in metal dimers as a step toward single-molecule sensing." ACS nano 3.5 (2009): 1231-1237

[1.127] He L, Musick MD, Nicewarner SR, et al., He, Lin, et al. "Colloidal Au-enhanced surface plasmon resonance for ultrasensitive detection of DNA hybridization." Journal of the American Chemical Society 122.38 (2000): 9071-9077

[1.128] Lakowicz, Joseph R. "Plasmonics in biology and plasmon-controlled fluorescence." Plasmonics 1.1 (2006): 5-33

[1.129] Jeffrey N. Anker, W. Paige Hall, Olga Lyandres, et al. "Biosensing with plasmonic nanosensors." Nature materials 7.6 (2008): 442-453

[1.130] Chen, Wenbin, Xijuan Tu, and Xiangqun Guo. "Fluorescent Gold Nanoparticles-Based Fluorescence Sensor for Cu^{2+} Ions." Chem. Commun., no. 13 (2009): 1736-38

[1.131] Roux, Stéphane, et al. "Synthesis, characterization of dihydrolipoic acid capped gold nanoparticles, and functionalization by the electroluminescent luminol." Langmuir 21.6 (2005): 2526-2536

[1.132] Kinkhabwala, Anika, Zongfu Yu, Shanhui Fan, Yuri Avlasevich, Klaus Müllen, and W. E. Moerner. "Large single-molecule fluorescence enhancements produced by a bowtie nanoantenna." Nature Photonics 3, no. 11 (2009): 654-657

[1.133] Fleischmann, M_, P. J. Hendra, and A. J. McQuillan. "Raman spectra of pyridine adsorbed at a silver electrode." Chemical Physics Letters 26.2 (1974): 163-166

[1.134] Xu, Hongxing, et al. "Electromagnetic contributions to single-molecule sensitivity in surface-enhanced Raman scattering." Physical Review E 62.3 (2000): 4318

[1.135] Cao, YunWei Charles, Rongchao Jin, and Chad A. Mirkin. "Nanoparticles with Raman spectroscopic fingerprints for DNA and RNA detection." Science297.5586 (2002): 1536-1540

[1.136] Fromm, David P., Arvind Sundaramurthy, Anika Kinkhabwala, P. James Schuck, Gordon S. Kino, and W. E. Moerner. "Exploring the chemical enhancement for surface-enhanced Raman scattering with Au bowtie nanoantennas." Journal of Chemical Physics 124, no. 6 (2006): 61101-64100

[1.137] Lu, Guowei, Bolin Cheng, Hong Shen, Yueliang Zhou, Zhenghao Chen, Guozhen Yang, Olivier Tillement, Stéphane Roux, and Pascal Perriat. "Fabry-Perot type sensor with surface plasmon resonance." Applied physics letters 89, no. 22 (2006): 223904-223904

[1.138] Ameling, Ralf, Lutz Langguth, Mario Hentschel, Martin Mesch, Paul V. Braun, and Harald Giessen. "Cavity-enhanced localized plasmon resonance sensing." Applied Physics Letters 97, no. 25 (2010): 253116-253116

[1.139] Ameling, Ralf, and Harald Giessen. "Cavity plasmonics: large normal mode splitting of electric and magnetic particle plasmons induced by a photonic microcavity." Nano letters 10, no. 11 (2010): 4394-4398

[1.140] Schmidt, Markus A., Dang Yuan Lei, Lothar Wondraczek, Virginie Nazabal, and Stefan A. Maier. "Hybrid nanoparticle - microcavity-based plasmonic nanosensors with improved detection resolution and extended remote-sensing ability." Nature communications 3 (2012): 1108

Chapter 2 Device Fabrication and Optical Characterization

2.1 INTRODUCTION 119

2.2 FABRICATION 121

2.2.1 Anodization 121

2.2.2 Fabrication of bowtie NA arrays 122

2.2.3 Description of the fabrication steps 126

2.2.4 Structural characterization by SEM 132

2.2.5 Some fabrication issues: Discussion 133

2.3 OPTICAL CHARACTERIZATION 141

2.3.1 Optical Macro-Reflectivity 141

2.3.2 Micro-Reflectivity/Transmission set-up 149

2.4 CONCLUSION 156

2.5 REFERENCES 157

2.1 Introduction

The 3 systems presented in Fig 2.1 will be compared in order to study the interaction between bowtie NAs and Fabry-Perot interferometer.

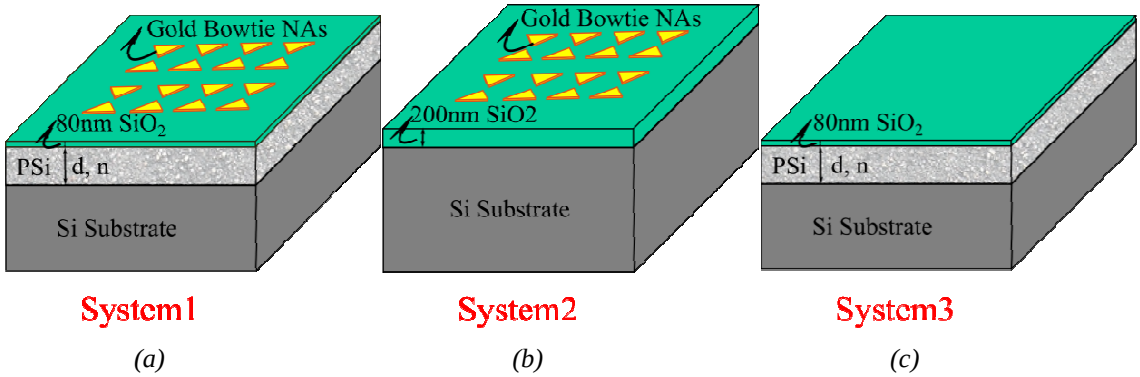

(a) *(b)* *(c)*

Fig 2.1 Schematic view of the 3 Systems: (a) System 1: Hybrid structure of Fabry-Perot (F-P) interferometer (monolayer of meso-PSi) and gold Bowtie NAs with 80nm SiO_2 as a spacer; (b) System 2: NAs alone (Same Bowtie NAs as System1, but on Si substrate with 200nm SiO_2 as a spacer); (c) System 3: F-P interferometer alone: monolayer of PSi on Si with its 80nm SiO_2 protective mask

The 3 systems are presented below:

- System 1: Hybrid structure of Fabry-Perot (F-P) interferometer and Bowtie NAs array. As shown in Fig 2.1 (*a*), gold bowtie NAs array are deposited on top of F-P interferometer, which is a monolayer of meso-PSi on Si substrate; an 80nm-thick SiO_2 spacing layer is deposited on top of the PSi surface to smoothen and protect the PSi surface during NAs fabrication. Typically, the PSi monolayer is about 5 µm thick (*d*) and its refractive index (*n*) is around 1.5 similar to the SiO_2 spacing layer refractive index.
- System 2: Bowtie NAs alone (Fig 2.1(*b*)): the same NAs arrays as System 1, fabricated on Si substrate (without PSi interferometer); a 200 nm - thick SiO_2 layer is used as a spacer between NAs and the substrate; the thickness of the spacing layer has been increased with respect to System 1 in order to make sure that the NAs do not "feel" the underlying Si substrate and have a similar environment as System 1 with a substrate refractive index of 1.5.
- System 3: Fabry-Perot interferometer alone (Fig 2.1 (*c*)). It consists of the monolayer of meso - PSi with its protective SiO_2 layer. This system corresponds to the zones outside the

NA arrays of System 1 on the same sample, allowing for a direct comparison between these two systems.

In this chapter, we will present the experimental fabrication and characterization for the 3 systems. It mainly includes:

- Fabrication
    - Anodization for PSi layer fabrication;
    - Techniques for SiO_2 layer deposition (Sputtering or PECVD);
    - NA fabrication by electron-beam lithography and lift-off;
    - Structural characterization via SEM observations;
- Optical set-up
    - Macro-Reflectivity for PSi layers characterization (determination of refractive index and thickness);
    - Micro-Reflectivity/Transmission for the study of the optical properties of the 3 systems;
    - Micro-fluidic system used for experiments in liquid environment, in particular for sensing studies.

2.2 Fabrication

2.2.1 Anodization

The anodization setup and procedure used in this work were developed and optimized for Photonics applications in Elisa Guillermain's PhD thesis. They were also used by Cheng Li to realize photonic crystals based on meso-PSi [2.1, 2.2].

2.2.1.1 Setup description

As shown in Fig 2.2.1, the electrochemical etching is carried out in a Teflon cell. A highly boron doped (p^+-type), <100> - oriented silicon substrate is placed on a copper plate at the bottom of the cell, in contact with the electrolyte. Liquid tightness between the anode and the Teflon cell is ensured by a chemically-inert rubber O-ring, leaving a contact area of exactly 1 cm^2 between the Si substrate and the electrolyte for the anodization to take place. A spirally shaped platinum wire acting as the cathode is placed in the electrolyte at the top of the cell. Platinum is chosen because it is chemically inert. The electrolyte consists of a 50% commercial aqueous hydrogen fluoride (HF) solution, diluted to 35% with ethanol. Prior to anodization, the whole cell is cooled down to -40°C in a freezer (Frima Concept CONG160 with electronic regulator BETA CB009) to minimize the interface roughness. The anodization current (I_{ano}) is supplied by Keithley 6221 generator ensuring high precision of desired anodization current and time (t_{ano}) [2.1, 2.2, 2.3].

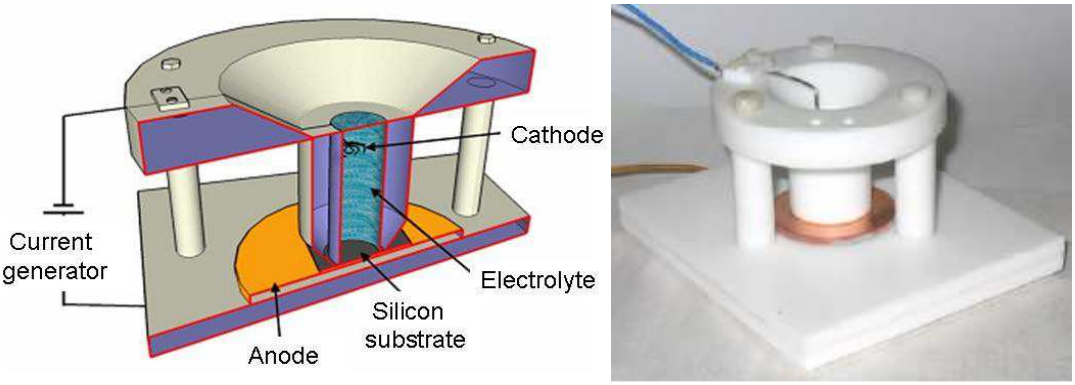

(a) *(b)*

Fig 2.2.1 (a) Schematic view of the anodization cell; (b) Photography of the assembled cell [2.1, 2.2]

2.2.1.2 Procedure

The anodization procedure can be separated into 4 steps:

1) *Preparation*: prior to etching, the Pt electrode, o-rubber ring, as well as the Teflon parts were rinsed with ethanol and the silicon substrate was rinsed successively with acetone and ethanol; then all parts were completely dried under a steam of nitrogen; the copper plate should be thoroughly cleaned with sandpaper in order to remove the natural oxide on its surface, which would prevent ohmic contact between Si and Cu plate; then the above clean parts were assembled together. Leak proof was checked with ethanol filling, before pouring the electrolyte into the cell.
2) *Cooling*: in order to perform the low temperature anodization with high thermal stability, the assembled cell is left inside the freezer for at least 2 hours to have it homogeneously cool down to -40°C;
3) *Electrochemical etching*: after temperature stabilization, the cell is connected to the current generator to start the anodization. The anodization parameters (current value and time) are set according to previous calibrations. In the case of a 5 µm-thick meso - PSi monolayer with 75% porosity – corresponding to a refractive index n = 1.5 – current density and time should be set as 30 mA / cm² and 260 s, respectively [2.1].
4) *Post-etching*: after anodization, the cell is removed from the freezer, emptied of the electrolyte and is carefully rinsed with ethanol. After disassembling the cell, the PSi sample is left to soak in ethanol for several minutes to ensure that no HF is left inside the pores. At last, the sample is dried with nitrogen flow and characterized by Macro-Reflectivity, as presented in section 2.3.1.

2.2.2 Fabrication of bowtie NA arrays

In the following, the fabrication procedure for Bowtie NAs is presented in detail. This fabrication process has been adapted from a procedure initially optimized at NanoLyon Platform in the framework of the PhD thesis of Taiping Zhang for the fabrication of isolated NAs positioned with high accuracy on top of photonic devices. [2.4]. We have adapted this procedure in order to optimize the fabrication of NA arrays on PSi and Si substrates.

2.2.2.1 Desired designs

As shown in Fig 2.2.2, we aimed at fabricating square arrays of bowtie NAs (50 µm x 50 µm) with an inter-particle distance of 800 nm in both *x* and *y* direction. The desired design of each NA consists of two isosceles triangles with 540 nm base length (labeled as A1) and 280 nm height (A2). The two triangles are placed tip to tip at 20 nm distance (Gap).

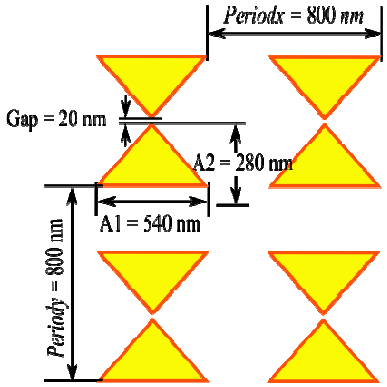

Fig 2.2.2 Desired NA designs

Due to the porous structure of PSi layer, it is necessary to deposit a spacing layer, both to protect the pores from the penetration of any materials or chemicals during the technological process, and to smoothen the surface for a more homogeneous and reproducible NA fabrication. This spacing layer should be thick enough to play its role, but it should disturb as little as possible the optical properties of the systems. A layer too thick or with a high refractive index would hinder the interaction between NAs and interferometer; hence, a silica layer with 80 nm optimal thickness has been selected.

In order to enable a good comparison between the systems, for System 2 a 200 nm - thick SiO_2 layer is chosen as a spacer between NAs and the Si substrate, to make sure that in this case the NAs have a similar dielectric environment (refractive index 1.5) as System 1.

Since System 3 corresponds to the areas outside the NA arrays of System 1, they are fabricated on the same samples. Hence, in the following we will focus on System 1 and 2 to introduce the flowchart of general process for Bowtie NAs fabrication.

2.2.2.2 General process flowchart

The general flowchart for NA fabrication is shown in Fig 2.2.3. The initial substrates for System 1 and 2 are different, as the first one is prepared by anodization and the second one is:

a commercial silicon wafer (Fig 2.2.3 (*a*)); In a second step ((Fig 2.2.3 (*b*)), the silica layers with 80 nm and 200 nm thickness, respectively, are deposited either by PECVD (plasma enhanced chemical vapor deposition) or sputtering techniques; The following steps are the same for both systems. First, a MMA/PMMA double layer of resist is deposited on the substrates by spin-coating ((Fig 2.2.3 (*c*)); next, electron-beam (e-beam) lithography (exposure and development) is performed to pattern the resist with the desired NA designs ((Fig 2.2.3 (*d*)); metal is deposited on the resist and on the revealed SiO_2 surface at the bottom of the patterns ((Fig 2.2.3 (*e*)); finally, a lift-off enables to dissolve the resist, leaving only the metal islands deposited on the SiO_2 surface.

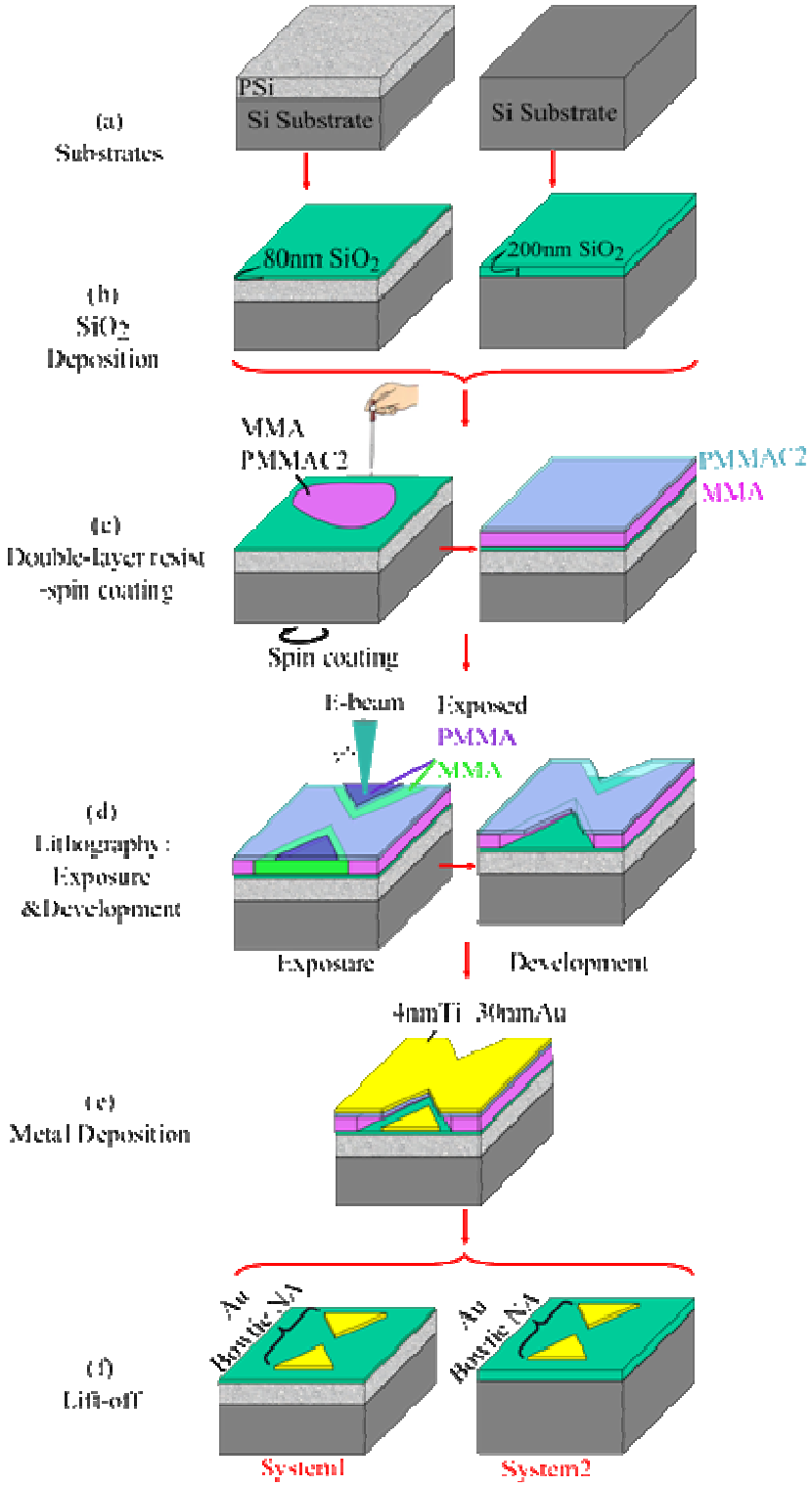

Fig 2.2.3 General process flowchart of Bowtie NA fabrication for System 1 and System 2 (a): substrates: monolayer of PSi on Si substrate (System 1) and Si Substrate (System 2); (b) SiO_2 deposition; (c) Spin-coating of resist double layer (MMA/PMMA); (d) electron-beam lithography: Exposure and development; (e) Metal deposition;(f) Lift-off

In the following, the successive fabrication steps are described in detail.

2.2.3 Description of the fabrication steps

1. Substrates preparation

In both cases, the Si substrates are highly boron-doped 500 µm-thick Si substrates. For System1, a monolayer of PSi has been etched into the Si substrate via anodization, as discussed in section 2.2.1.

2. Silica layer deposition

80 nm and 200 nm-thick SiO_2 layers, respectively, are deposited on the substrates. Four different deposition techniques have been tested at Nanolyon platform to obtain the best SiO_2 layer quality: 2 PECVD systems, an Oxford Plasmalab 80+ and an electron cyclotron resonance (ECR) assisted PECVD [2.12], as well as 2 sputtering systems, an Alliance Concept equipment (AC450) and a Materials Research Corp. (MRC) RF magnetron sputter system.

PECVD is a process to deposit thin films from a gas state to a solid state on a substrate. Here, we use the chemical reaction between the gas SiH_4 and N_2O in Ar plasma to form the SiO_2 layer, as illustrated in Fig 2.2.4 (*a*). The 2 systems tested have very different characteristics, leading to very different layer qualities. For Oxford Plasma 80+ deposition system, the deposition rate is around 40 nm/min, and the surface roughness is around 3 nm; the resulting SiO_2 has a low density, contains hydrogen and its refractive index is 1.47 (@ 532 nm). For the ECR PECVD, the deposition rate is 2-3 nm/min; the temperature is about 50°C, the refractive index is 1.46 (@ 532 nm) and the resulting layer is much denser.

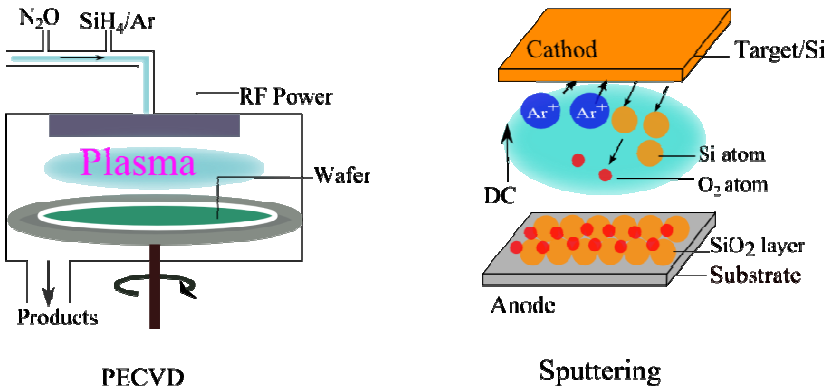

Fig 2.2.4 Schematic view of SiO_2 layer deposition techniques: (a) PECVD; (b) Sputtering

Sputtering is a physical deposition technique. As shown in Fig 2.2.4 (*b*), an Ar plasma is also used in this case, in order to accelerate Ar^+ ions towards a target of Si acting as a cathode. Under bombardment by the high-energy ions, Si atoms are removed from the target and combine with oxygen atoms present in the plasma to form a SiO_2 film on the substrate surface. In the case of both the MRC and the AC450 sputtering systems, the deposition rate is about 5 nm / min; the temperature is 250°C and refractive index is 1.45 (@ 532 nm).

3. Double layer resist preparation

Before lithography, a thin, uniform and smooth layer of e-beam sensitive resist needs to be deposited on the substrate surface by spin coating. The procedure is the following:

1) A small drop of resist is deposited onto the center of the substrate;

2) Then the substrate is spun with an adjustable high speed, in order to spread the resist on the substrate by centrifugal force. The remaining thin film of resist on the substrate surface is highly homogeneous with a thickness directly related to the rotation velocity of the spin coater.

3). Next, in order to enhance the adhesion of resist on the substrate and evaporate the remaining solvent from the resist layer, a soft baking is necessary, which is done on a hot plate.

The final film thickness depends on the nature of the resist (viscosity, drying rate, surface tension, etc.) and the parameters chosen for the spin coating (rotational speed, acceleration…) [2.5].

One of the main issues in the NA fabrication process is to obtain a strong undercut of the resist patterns profile, in order to prevent metal deposition on the resist side walls (Fig 2.2.5 (*a*)), which would hinder the access of solvents for resist dissolution during the lift - off process and / or lead to undesired presence of metal around the patterns on the substrate after lift-off [2.13, 2.14].

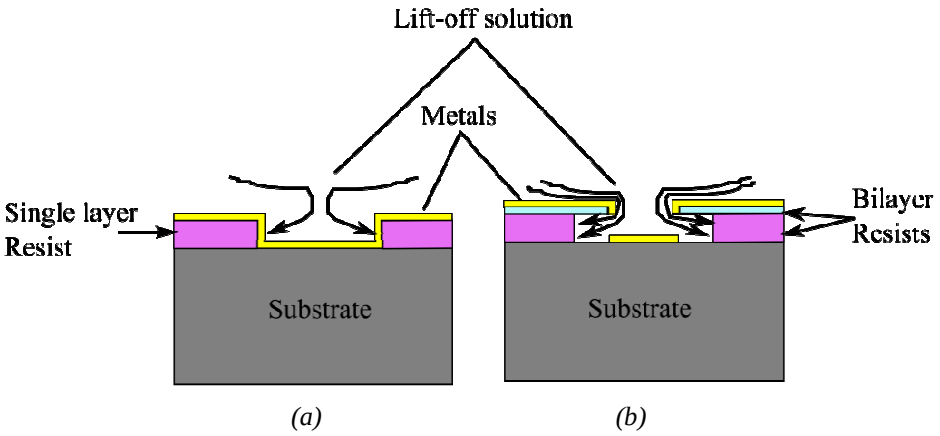

Fig 2.2.5 Schematic view of resist dissolution during lift-off for single (a) and double (b) resist layers

In order to overcome this problem, we choose to perform lithography with a double layer of resist (Fig 2.2.5 (*b*)), where the lower layer should have a higher sensitivity to the electron beam and / or development solution in order to yield larger patterns after development. This undercut profile of resists prevents sidewall deposition of metallic films. To meet this requirement, in our case the lower and upper layers consist of 495K MMA (methylmethacrylate) and 950K PMMA – C2 (poly-methylmethacrylate), respectively. The thicknesses are 170 nm for the low-weight MMA resist and 75 nm for the high-weight PMMA-C2 resist, and are obtained with rotation velocities of 3000 and 2000 tr/min, respectively. After coating of each layer, soft baking is necessary. For MMA, the temperature is 150°C and 180°C for PMMA; the baking time is 90s for both layers.

Before e-beam writing, a thin film of aluminum can also be deposited on top of the resist to enable charge dissipation under the electron beam and minimize distortion during lithography [2.6]. Al deposition is particularly useful when performing lithography on insulating substrates, which is the case of our PSi + SiO_2 systems. The metal film has to be removed by chemical etching before the development.

4. Electron beam lithography

Electron beam lithography is a widely used technique in integrated circuits manufacture and nanotechnology architectures [2.6]. By two successive steps, exposure and development (as shown in Fig 2.2.3(*d*)), we can create any critical structures in the resist with nanometer precision, that can subsequently either be transferred to the substrate material, often by etching or be used as a mask to produce nanostructures on top of the substrate, usually by lift-off.

- Exposure:

The exposure corresponds to the use of an electron beam to scan the surface covered with an electron-sensitive resist in previously user-defined areas, in order to “write” the desired patterns into the resist; the patterns and layouts are defined using a CAD software integrated in the lithography system; the exposed regions are chemically modified under the electron beam.

In this study, the lithography is carried out with an Inspect F-50 FEI scanning electron microscope (SEM) equipped with the Raith lithography software Elphy Plus; the acceleration voltage is 30 kV, the beam current I is about 10 pA and is measured using a Faraday cup integrated into the sample stage. The current fluctuations of the FEG-tip are compensated by a variation of exposure time in order to keep the nominal exposure dose constant. Here, we define the nominal dose as the total current density per unit area:

$$Dose = \frac{I \times Area\ dwell\ time}{(Area\ step\ size)^2},$$

Where “Area dwell time” is the exposure time per unit area, and “Area step size” is the lateral dimension of the unit area. The nominal exposure dose is set to 100 µAs/cm^2. The actual dose used for exposure can then be varied at will during lithography by applying a variation factor to the nominal dose.

The lithography system is also equipped with an interferometric stage, allowing for stitching, i.e., automatic alignment of the different writefields constituting the patterns. Here, we define the writefield as the area that can be scanned by the beam at fixed stage position, corresponding to a given magnification. As our NA arrays are usually a few tens of µm in size, we choose to perform the exposure with a magnification of 2300 corresponding to a writefield size of 50μm.

- Development:

The development corresponds to the selective chemical removal of resist to reveal the patterns; either the exposed (positive resist: ex. PMMA) or the non-exposed regions of the resist (negative resist) are removed.

In the case of MMA and PMMA resist, the exposed region is removed by a mixture of Methyl isobutyl ketone (MIBK) and isopropanol (IPA), 1:1 for 45 s. After, the whole sample is rinsed in IPA, dried with nitrogen gas stream, and at last baked at 100°C on a hotplate for 60 s.

5. Metal deposition by electron beam evaporation

After e-beam lithography, 4nm titanium (Ti) and 30nm gold (Au) are successively deposited on the patterned resist by electron beam heat evaporation. The Ti film is used as an adhesive layer between gold and substrate.

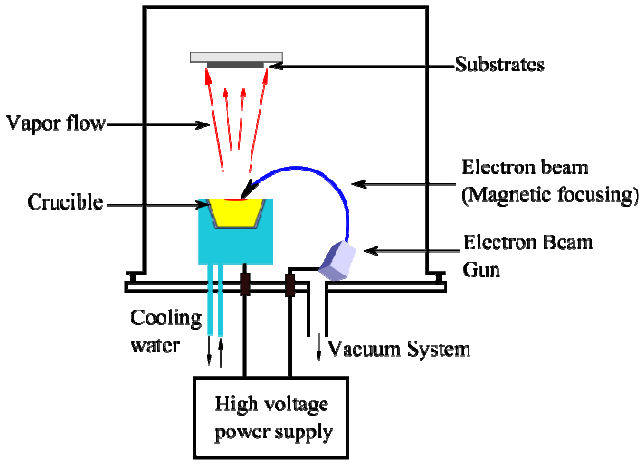

Fig 2.2.6 Electron Beam Heating Evaporation

The metal is deposited onto the substrates in a Leybold electron beam heating evaporator. This technique is based on the heat produced by high energy electron beam bombardment on the material to be deposited (here, Ti/Au). As illustrated in Fig 2.2.6, the electron beam is generated by an electron gun, and focused onto the target material, which is contained within a water-cooled, grounded crucible. The evaporated material deposits onto the substrate lying upside down above the material target. The amplitude and shape of electron beam scanning on the material target can be optimized for each material, and automatically controlled by an electro-magnetic system [2.7].

The deposition is performed under vacuum ($\sim 2\times10^{-7}$ torr), with a deposition rate of 0.5Å/s for both metals, achieved via accurate control of the emission current.

6. Lift - off

After metal deposition, the final step in the NA fabrication is a lift - off, i.e., a chemical dissolution of the resist layer and of the metal deposited on its surface, to leave only the metal islands deposited on the substrate surface at the bottom of the resist patterns. Our optimized lift-off process mainly includes 4 steps that are illustrated in Fig 2.2.7:

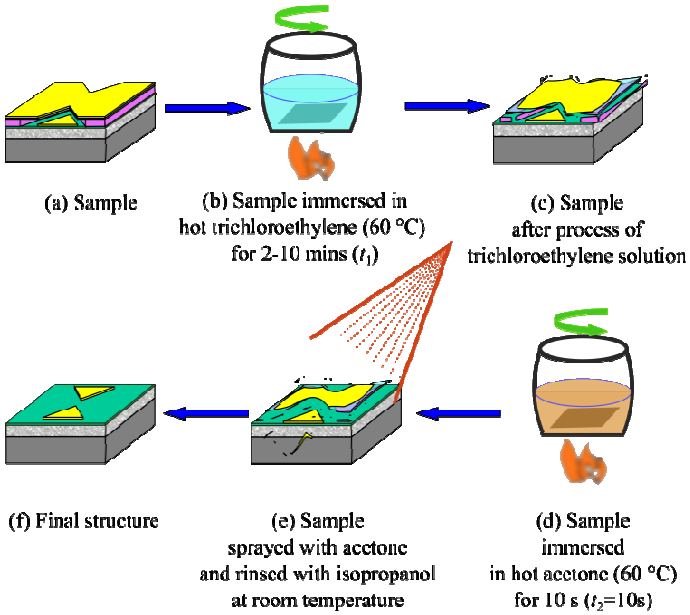

Fig 2.2.7 Schematic view of the different steps in our lift - off process

- *First dissolution in hot trichloroethylene:* the sample is immersed in 20 ml trichloroethylene solution heated at 60°C in a beaker, with some agitation to facilitate the interaction between the solution and the resists (Fig 2.2.7 (*b*)) [2.15]. After a few minutes, the gold layer exhibits some drapes visible with naked eyes (Fig 2.2.7 (*c*));
- *Second-step dissolution in hot acetone*: the sample is immersed in 20 ml hot acetone solution (60°C) about 10 seconds (Fig 2.2.7 (*d*)), which enhances dissolution of the resist under the metal films.
- *Acetone spray*: in order to eliminate the left-over of resist and metal cover on the surface, the sample is sprayed with acetone at room temperature. As a result, only the metal deposited directly on the SiO_2 substrate remains on the surface (Fig 2.2.7 (*e*)).
- *Rinsing*: finally, the whole sample is rinsed with IPA.

It is worth mentioning that the time of sample immersion in the trichloroethylene solution (t_1) is the most important factor for the whole process. However, this time is strongly dependent on the age of the solution. The newer the solution is, the shorter the time (t_1) will be.

2.2.4 Structural characterization by SEM

Scanning electron microscopy (SEM) is employed throughout this PhD work for the structural characterization of both PSi layer and bowtie NAs. The equipment used is a Tescan MIRA 3-LMH SEM. Because of the insulating substrates, we perform the observations at relatively low acceleration voltage (5kV). Two different secondary electron (SE) detectors are available on the equipment. The "standard" SE Everhart-Thornley detector is used with typically 5 mm working distance to observe the surface and profile of PSi layer; Fig 2.2.8 shows an example of such a characterization. In Fig 2.2.8 (a), the profile view of a PSi layer is observed, and a layer thickness of about 5.66 µm is measured, while Fig 2.2.8 (*b*) shows the SEM view of the PSi surface.

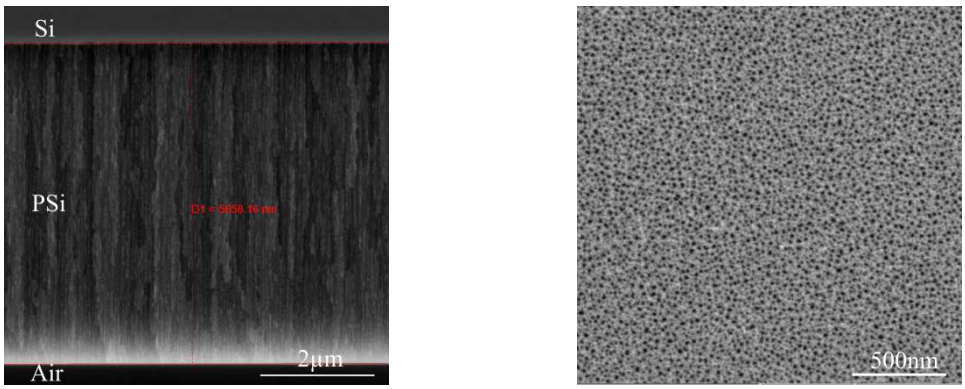

(a) *(b)*

Fig 2.2.8 SEM view PSi layer (a) Profile (b) Surface

A second SE detector placed in the column allows for high-resolution observation with smaller working distance (3.5 mm in our case) and is used for measuring NAs dimensions and checking their homogeneity. This is illustrated in Fig 2.2.9, where Fig 2.2.9 (a) shows a global view of an array of NAs that enables to check the macro-scale homogeneity and fabrication success; and Fig 2.2.9 (b) shows a higher magnification image of two NAs from which the dimensions could be measured. In order to check the micro-scale uniformity for each NAs array, 3 to 4 pairs of NAs like the ones shown in Fig 2.2.9 (b) are systematically observed to determine their average dimensions.

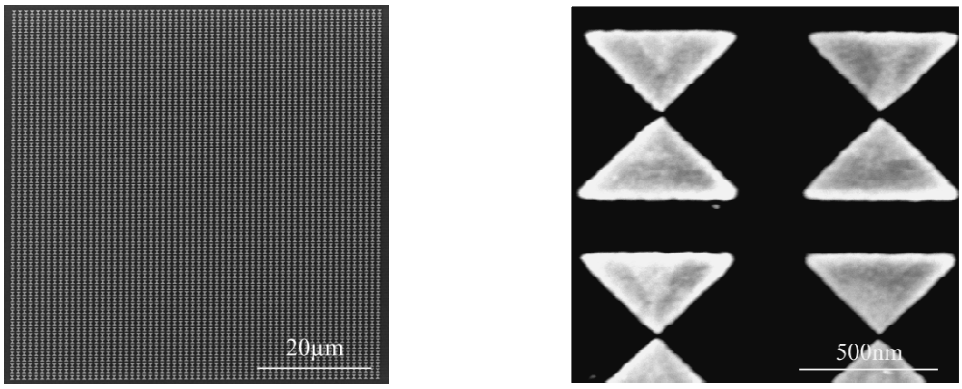

(a) *(b)*

Fig 2.2.9 SEM view NAs (a) whole array (b) detail of single NAs

During the whole fabrication optimization, several critical issues required thorough study, in particular some steps of NA realization such as silica layer preparation, e-beam lithography, and lift-off. They are discussed in more details in the following.

2.2.5 Some fabrication issues: Discussion

2.2.5.1 Effect of Silica layer quality

As mentioned above, there are 4 equipments available for SiO_2 layer deposition at our technological platform: 2 sputtering systems (MRC and AC450), and 2 PECVD (Oxford and ECR PECVD). The selection of equipment is very important, since the density and interconnectivity of grains of the silica layer is decisive for the non-accessibility of PSi pores during the fabrication process, as well as for the surface morphology of bowtie NAs, which will influence the plasmonic property of such structures.

In Fig 2.2.10, we present 80 nm-thick silica layers deposited on PSi substrates using each technique: sputtering with MRC (*a*) and AC450 (*b*), ECR PECVD (*c*) and Oxford PECVD (*d*). In each case, the left and right pictures show the silica surface before and after NA fabrication process, respectively. Comparing the surface roughness and / or aspect of grains in the different cases, the best choice is the ECR PECVD, which yields very smooth silica surface both before and after NA fabrication, as well as very smooth NA surface; the two sputtering techniques are also acceptable. Even if the MRC seems to yield smoother silica surface than the AC450, after fabrication the aspect of silica and NA surfaces look very similar and in both cases the grains are visible both on the silica and on the metal; The Oxford

PECVD is the worst choice for our application, as the very high surface roughness leads to bad NA morphology after fabrication.

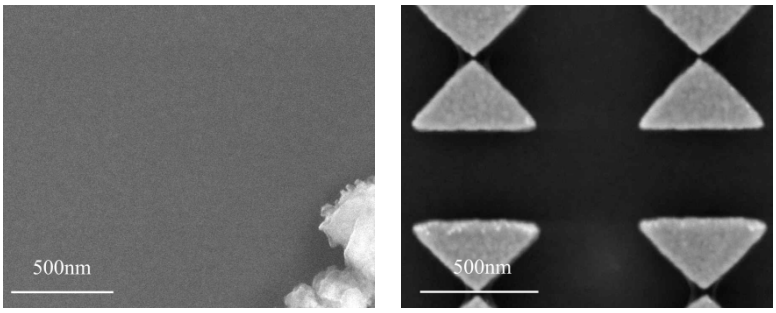

(a) MRC sputtering

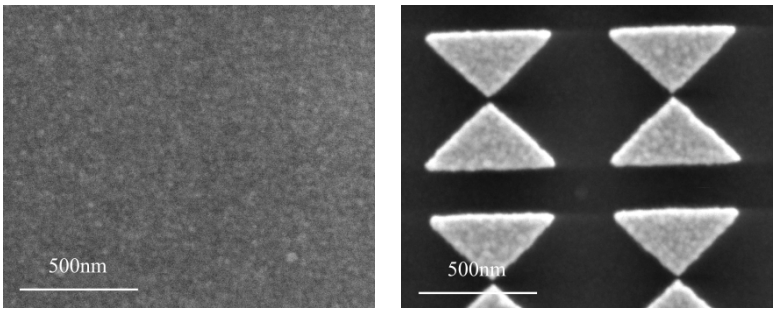

(b) AC450 sputtering

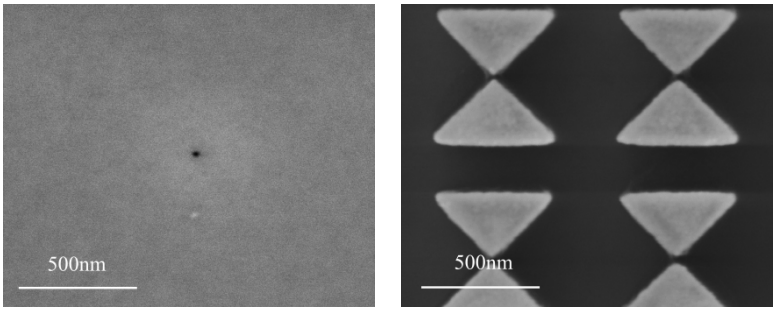

(c) ECR PECVD

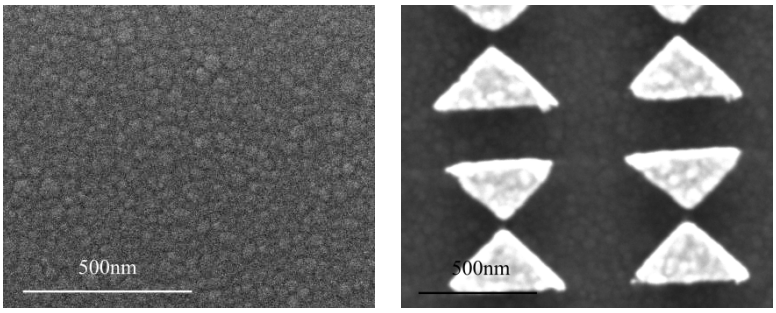

(d) Oxford PECVD

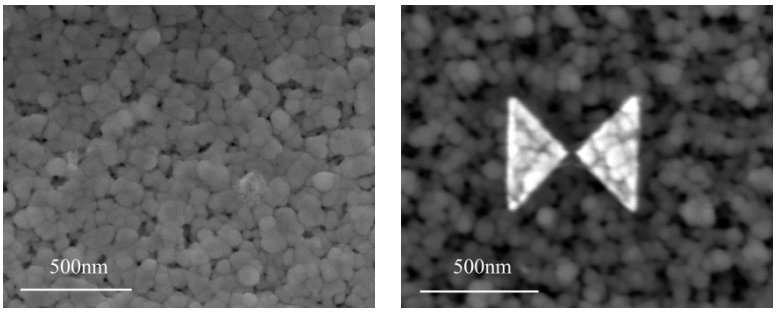

(e) Low-density silica layer

Fig 2.2.10 SEM images of the SiO_2 surface obtained with our different deposition equipment. (a) and (b) are sputtered layers using MRC and AC450 equipment, respectively, in similar conditions (250°C, 10^{-2} Torr); (c) and (d) are layers deposited with ECR PEVCD and Oxford PECVD, respectively. Fig (e) shows an example with less dense SiO_2 layer. In all cases, Left and Right pictures show the state of the surface before and after NA fabrication, respectively

In order to highlight the importance of grain density during NA fabrication, Fig 2.2.10 (*e*) shows an example of sample with lower silica density. It is very clear from these images that the chemical steps during NA fabrication lead to a size reduction of silica grains if the layer is not dense enough, resulting not only in bad NA morphologies, but also in a permeability of the silica layer enabling the penetration of vapours and solutions within the pores of the underlying PSi substrate. It has to be expected that the sputtered layers shown in Fig 2.2.10 (*a*) and (*b*) are also slightly permeable, as will be discussed later in chapter 4.

In the samples discussed later in this PhD thesis, the silica layers were either deposited by ECR PECVD or by the AC450 sputtering system.

2.2.5.2 Proximity effect in electron-beam lithography

Electron beam lithography enables to provide any critical patterns with high resolution. However, an important phenomenon, strongly influencing its final resolution and pattern accuracy, is the beam / resist / substrate interaction. Under a given acceleration voltage, the electrons will penetrate the resist, and most of them suffer many small angle, inelastic scattering events, (called *forward scattering*), whose effect is to broaden the beam diameter (see Fig 2.2.11). When they come into the substrate, the collisions with atoms of the latter will lead to large angle, elastic scattering, which is called *backscattering*. In this case, the electrons may return back through the resist at a significant distance from the incident beam, leading to additional resist exposure. These so-called proximity effects will lead to exposed patterns that are usually larger than the designed ones [2.8]. However, this deviation from the desired

dimensions strongly depends on the proximity of other exposed patterns, due to the extension of electron-substrate interaction volume (Fig 2.2.11).

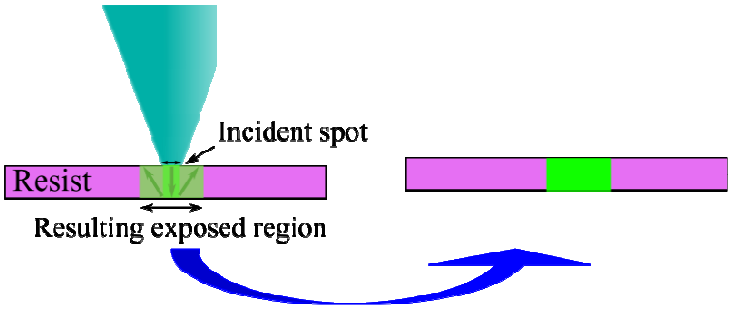

Fig 2.2.11 Schematic view of Proximity effect

In this study, we aimed at fabricating a square array of bowtie NAs (50 µm x 50 µm) with 800 nm inter-particle distance in both *x* and *y* direction. In the desired design, the 2 triangles constituting the NA should have a base length A1 of 540 nm and a height A2 of 280 nm, and are placed tip to tip with a 20 nm gap. Due to the proximity effects, the dimensions of the fabricated NAs and the gap size will usually be different from the desired design; therefore, some optimization is necessary, as presented in the following.

A. optimal dose selection

There are 2 ways to compensate the proximity effects when optimizing a pattern: tune the pattern dimensions, or tune the exposure dose.

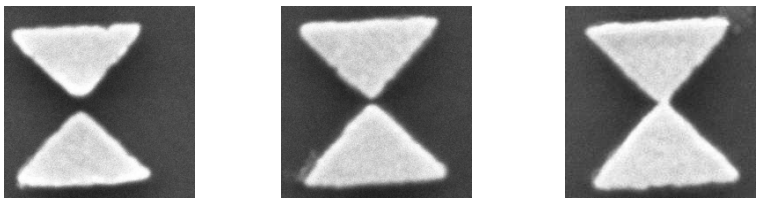

A1 = 462 nm	**A1 = 506 nm**	**A1 = 516 nm**
A2 = 266 nm	**A2 = 277 nm**	**A2 = 293 nm**
Gap = 54 nm	**Gap = 17 nm**	**Gap = 0 nm**

(a) Dose 0.8 *(b) Dose 1.0* *(c) Dose 1.2*

Fig 2.2.12 Examples of bowtie NAs realized with the desired design and different dose factors (a, b, c are for dose factors 0.8, 1.0 and 1.2, respectively)

Fig 2.2.12 shows examples of fabricated NAs when the dimensions of the desired pattern are kept and only the dose is varied: in this case (*a*), (*b*) and (*c*) are the NAs obtained using dose factors of 0.8, 1.0 and 1.2, respectively. Comparing these 3 examples, we can deduce that a good matching between the desired and fabricated dimensions cannot be obtained for all 3

dimensions A1, A2 and Gap at the same time. With the nominal dose (dose factor 1.0) the gap and A2 are close to the desired values, but A1 is too small; with higher dose (dose factor 1.2), the gap disappears. This result indicates that proximity effects are different in the *x* and *y* directions, most probably due to the high anisotropy of the design.

Hence, in order to correctly compensate for proximity effects, the dimensions of the design have to be varied as well. Fig 2.2.13 presents the variations of design dimensions selected for the fabrication of the NAs. Keeping A2 constant at 280 nm, 3 different values of A1 are designed, 580 nm, 600 nm, and 620 nm, as well as 3 different Gap sizes, 20 nm, 30 nm, and 40 nm. In total, the designed pattern consists of 9 NA arrays with slightly different NA dimensions, as shown in Fig 2.2.13.

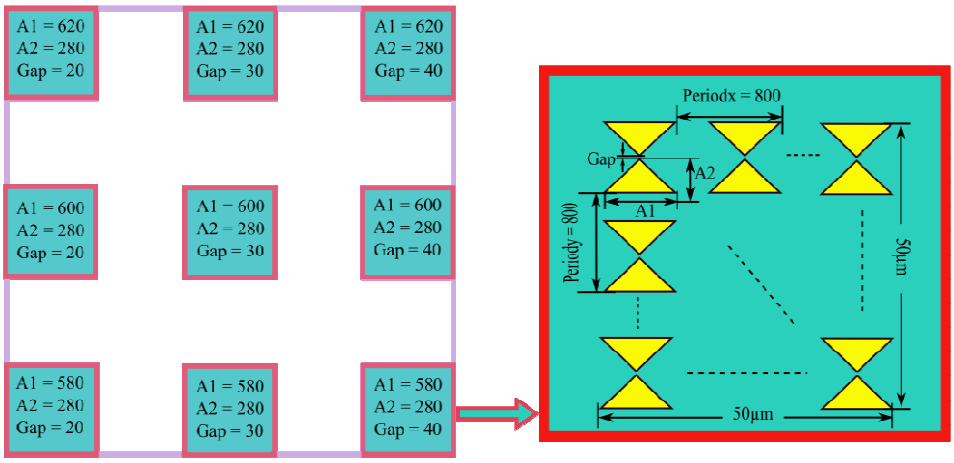

Fig 2.2.13 Pattern of designed NA arrays with varied NA dimensions (the unit for NAs sizes is nm)

With the above varied designed patterns, bowtie NAs having exactly the desired dimensions can be obtained by optimizing the exposure dose. However, since electron scattering is depending on the substrate, the optimal dose factor strongly depends on the nature of the substrate (SiO_2/PSi/Si vs. SiO_2/Si) as well as the thickness of the layers. For example, for 5 µm PSi layer thickness, the optimal dose factor is 1.2, whereas for 7 µm thickness, it is 1.0.

B. Homogeneity within a NA array

Depending on their position within the NA array, the proximity effects for the NAs are different, as shown in Fig 2.2.14. While the proximity effects are quite homogeneous in the centre, they tend to be reduced towards the edges of the arrays, due to a reduction of the

amount of neighbours for each NA. This leads to smaller dimensions and larger gaps for NAs at the edges with respect to NAs at the centre of the arrays.

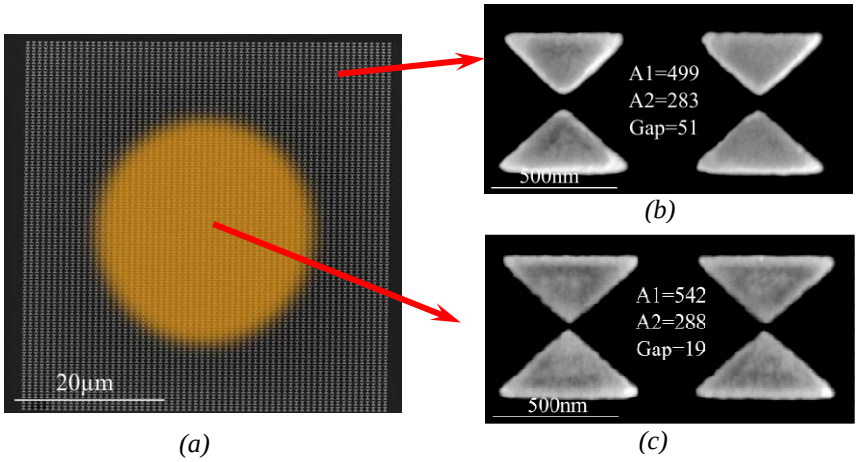

Fig 2.2.14 Homogeneity within a square (a): NAs arrays with sizes 50µm x 50µm; the orange disk shows the size of the excitation beam used in the optical setup; (b) NAs in the center of a square; (c) NAs at the corner of a square

Fig 2.2.14 shows that the difference of NA dimensions can be as large as ~30 – 40 nm from centre to corner. There are 2 ways to deal with this phenomenon: either the NA dimensions or doses should be varied on each array from centre to edge in order to compensate for the proximity effects; or the size of the excitation beam in the optical experiments should be adapted to match the zone of high homogeneity at the centre of each array. As will be presented later in this chapter, we have chosen the second option. Because the transition region with varying NA dimensions extends over several µm around the edges of each array, we have chosen a beam size of 30 µm in order to minimise the influence of NA inhomogeneity on the optical properties [2.11]. This beam size is highlighted by an orange circle in Fig 2.2.14.

It is worth mentioning that the NA dimensions discussed above are the average values over 6 to 8 individual NAs. The measurement accuracy of SEM measurement is around 5 nm, and the NA dimensions within the homogeneous zone in each array show a fluctuation < 10 nm from the average value.

2.2.5.3 Lift-off

As presented in the previous section, lift-off is the last step in NA fabrication, during which the metal layers (Ti + Au) on top of the resist are lifted off via dissolution of the resist with hot trichloroethylene. The metal patterns deposited directly on the substrate are kept and form the desired NAs.

There are 2 main issues affecting the quality of the resulting NA patterns after lift-off, as discussed in the following.

A. Age of trichloroethylene solution

The dissolution time of e-beam resist with trichloroethylene is crucial to the quality of resulting NA. However, the dissolution time is dependent on the age of the solution. The newer the solution is, the shorter the time. The challenge is to find the optimum dissolution time for each solution age, since an incomplete dissolution would lead to some metal residues on the surface, as shown in Fig 2.2.15.

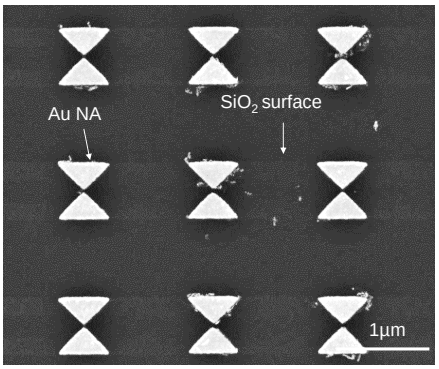

Fig 2.2.15 SEM view of NAs showing an example for bad lift-off due to incomplete resist dissolution

B. Undesired deposition of metal on resist walls

NA patterns usually exhibit systematic ultra-thin curled metal layers along particular edge directions, as well as parasitic ultra-thin metal layers in the NA gap, as shown in Fig 2.2.16 (b). This is probably due to the deposition of metal on resist walls and/or on the surface underneath the top resist layer during metal evaporation, as schematically illustrated in Fig 2.2.16 (*a*). Indeed, the evaporated metal atoms have isotropic trajectories and it is probable that some of them reach the resist walls or the substrate surface underneath the top resist layer, leading to the formation of an ultrathin but continuous metal layer connecting the

bottom patterns to the layer on top of the resist. This ultrathin layer is permeable to the solvents, hence not preventing the resist dissolution. The lift-off of the metal top layer most probably breaks the ultrathin metal layer, whose remaining end curls along the edge of the NA pattern. As the lift-off process is usually starting at one end of the sample and propagates in one direction throughout the sample, the curled edge is the same on each NA, resulting in a systematic feature throughout each whole sample and indicating the particular direction of the lift-off (Fig 2.2.16 (*a* - *c*)).

The deposition of ultrathin metal layer on the substrate around the gap of each NA demonstrates that the 2 triangles constituting the NA are interconnected in the underlying MMA resist pattern, while the top PMMA resist forms a bridge between the 2 triangles, resulting in the small NA gap (Fig 2.2.16 (*d*)).

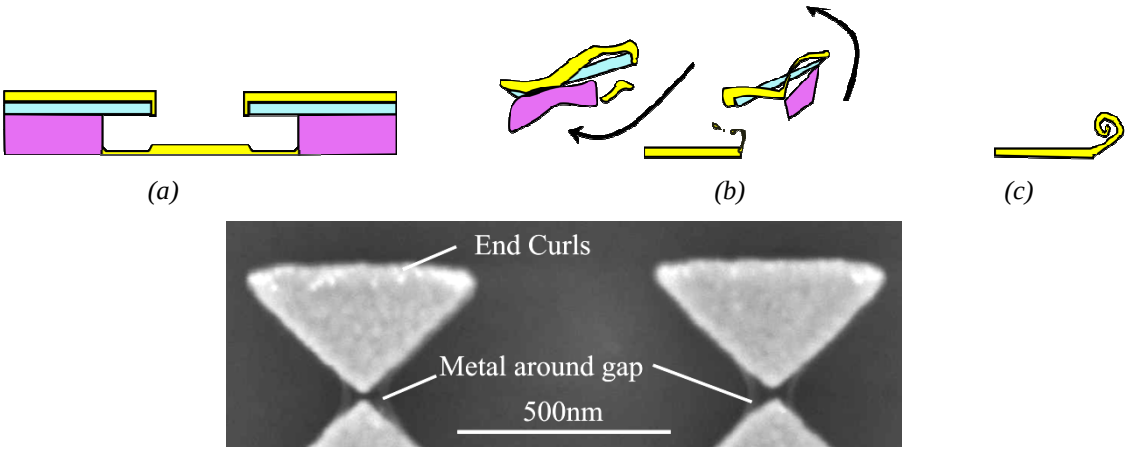

Fig 2.2.16 (a-c) Suggested explanation for undesired metal deposition; (d) SEM view of NAs showing the results of undesired metal deposition

2.3 Optical Characterization

In this section, the optical set-ups used for sample characterization will be introduced, and the methods for data analysis will be discussed. There are mainly two different types of optical characterization used in this work: macro-reflectivity for determination of macroscopic properties such as thickness and refractive index of the PSi layers; and micro-reflectivity / transmission for measurements of optical properties of the devices at a micro-scale, such as the response of NA arrays.

2.3.1 Optical Macro-Reflectivity

After anodization, the freshly fabricated PSi layer should be quickly characterized in order to determine its thickness and refractive index, since the fresh layer oxidizes when exposed at ambient atmosphere. Here we use macro-reflectivity (Macro-R) in the 900 – 1700 nm infrared range to characterize the PSi layer properties.

2.3.1.1 Principle of the Macro-R measurement

The principle of the macro-R measurement is shown in Fig 2.3.1 (*a*). When a plane wave is normally incident on the substrate surface, a part of it is reflected at the upper interface (Interface2), while the other part is transmitted. When the transmitted beam reaches the lower (Interface1) interface of the thin film, a part of the beam is transmitted and the other part is reflected back towards the upper interface (green beam on Fig 2.3.1). At interface 2, the beam component directly reflected (orange beam) interferes with the ones that have travelled through the thin film (green beam) to build up the reflectivity response of the film. The phase difference between the interfering beams is directly related to the optical path in the thin film according to the following equations:

$$\text{Constructive interference: } \Delta\varphi = 2m\pi \quad \rightarrow \quad \frac{4nd}{\lambda} = 2m\pi \qquad \text{(EQ-2-1-1)}$$

$$\text{Destructive interference: } \Delta\varphi = (2m \pm 1)\pi \quad \rightarrow \quad \frac{4nd}{\lambda} = (2m \pm 1)\pi \qquad \text{(EQ-2-1-2)}$$

where $\Delta\varphi$ is the phase difference, m is an integer, n and d are the refractive index and thickness of the film, respectively, and λ is the wavelength.

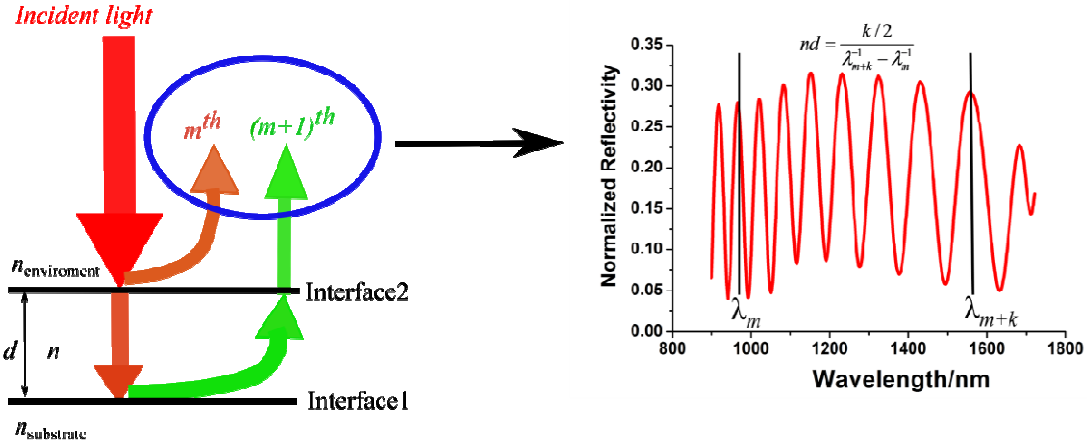

(a) *(b)*

Fig 2.3.1 Schematic illustration of PSi interference layer with thickness d and refractive index n; (b): Reflectivity of PSi monolayer on its Si substrate normalised by reflectivity signal from Silver mirror

In the case of a spectral measurement, the reflectivity response exhibits intensity oscillations with maxima and minima corresponding to the constructive and destructive interferences, respectively, as shown in Fig 2.3.1 (*b*). It can be shown that the positions of maxima of the m^{th} order λ_m and of the $(m+k)^{th}$ order λ_{m+k} are related to the optical path nd by the following equation:

$$nd = \frac{k/2}{\lambda_{m+k}^{-1} - \lambda_m^{-1}} \quad (k<0) \qquad \text{(EQ-2-2)}$$

More details are discussed in Appendix A.

It should be noted that the experimental configuration discussed in Fig 2.3.1 (*b*), where the PSi layer is on top of its Si substrate, is not strictly speaking a monolayer configuration as the substrate is backside polished, hence leading to back-reflections. Due to the high doping and large thickness of the substrate, the influence of such back-reflections is almost negligible. However, the strong decrease of absorption in the Si substrate above 1100 nm should result in an increase of back-reflected signal, and explains the sudden shift of the fringes towards higher reflectivity that can be observed on the spectrum at this specific wavelength.

2.3.1.2 Set-up

The set-up used for macro-R measurements is shown in Fig 2.3.2. A tungsten white light source (Avalight-Hal-Tungsten halogen light source) is connected to the source branch of a Y-junction fiber; light reaches the sample surface at normal incidence with spot size ~ 1 mm; The response of the sample is reflected back into the fiber towards a 512-elements InGaAs array (NIRQuest512) spectrometer suitable for the 900 – 1700 nm wavelength range. The reflectivity spectra are recorded via the SpectraSuite software by Ocean Optics.

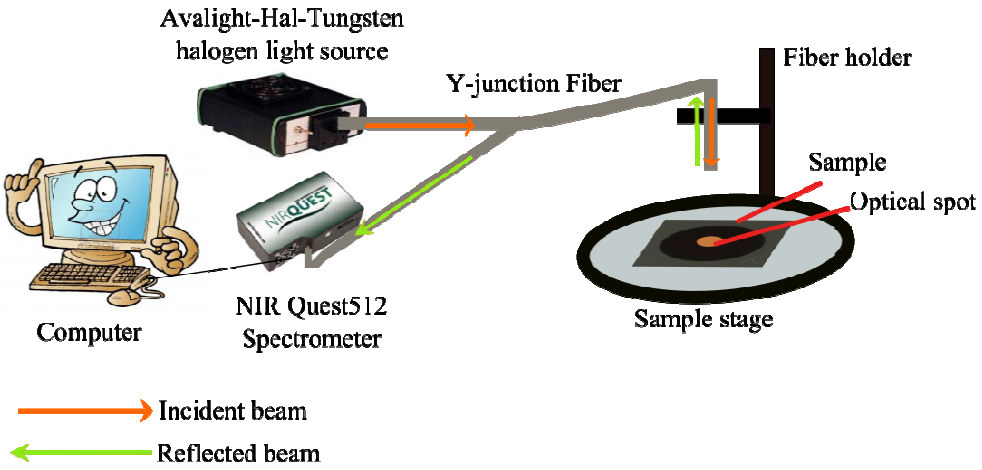

Fig 2.3.2 Schematic view of Macro-Reflectivity Optical setup

The reflectivity spectrum of the sample is normalized by the high reflectivity of a silver mirror, and dark signal is also subtracted from the measured signal, according to EQ-2-3:

$$R = \frac{R_{Signal-PSi} - R_{Dark}}{R_{Mirror} - R_{Dark}} \qquad \text{(EQ-2-3)}$$

2.3.1.3 Analysis

The optical thickness of the layer (*nd*) can be directly deduced from the reflectivity spectrum since it is related to the positions of maxima and minima of reflectivity by (EQ-2-2) ($nd = \frac{k/2}{\lambda_{m+k}^{-1} - \lambda_m^{-1}}$ with k<0). In order to separately determine the 2 parameters *n* and *d*, 2 methods can be used:

- Destructive method: the thickness value *d* is measured from SEM profile observation; the refractive index value is then deduced from the optical path *nd*.

- Non-destructive method: we use a home-built Matlab code to fit the measured reflected spectrum and deduce the parameters. In order to separately determine *n* and *d*, this fit takes into account not only the position of maxima but also their amplitude – related to the index contrast between the film and its surrounding – as well as the variation of refractive index with the wavelength More details are discussed in Appendix B.

As presented in chapter 1, we use the LLL effective medium approximation by to relate the porosity to the refractive index of our mesoporous layers, which in the case of freshly prepared porous silicon is:

$$n_{eff-fresh}^{2/3} = n_{Si}^{2/3}(1 - P_{air-fresh}) + P_{air-fresh} \qquad \text{(EQ-2-4)}$$

Fig 2.3.3 shows an example of macro-R experimental spectrum of a fresh PSi monolayer (black curve) as well as the Matlab fit (red curve) and corresponding analysis yielding the value of refractive index (blue curve). For this particular sample, the results of the fit are a thickness about 5.64 µm and a porosity of 75%, corresponding to a refractive index of 1.52 at 1.5 µm wavelength.

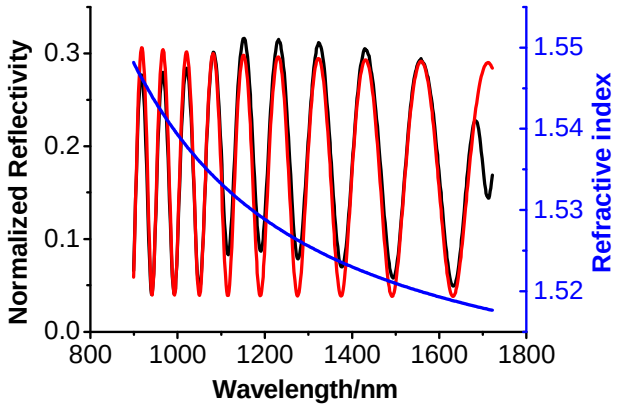

Fig 2.3.3 Reflectivity and refractive index of a mono-PSi layer (Black curve: experimental spectra; red curve: fit; blue curve: refractive index deduced from fit)

In order to verify the accuracy of such a fit, the thickness of the PSi layer was also measured with SEM, and was found to be about 5.66 µm, which is in perfect agreement with the fit result (taking into account the accuracy of SEM measurements). Selecting two fringe maxima quite far apart (large *k*) on the experimental spectrum and injecting the wavelength of these maxima as well as the SEM thickness into EQ-2-2, a refractive index value *n* about 1.57 could be deduced, corresponding to a porosity of 73%.

Both methods show a slight discrepancy between the deduced index values (3% variation), which is mostly due to inaccuracies introduced by the experimental setups, the manual reading of the reflectivity maxima and by the assumption that the refractive index is constant over the whole measured wavelength range in the manual method, whereas the fit takes into account the wavelength variation of refractive index and neglects any experimental imperfection or inaccuracy.

2.3.1.4 Discussion

Homogeneity of PSi layers

As discussed in the literature [2.7, 2.9], fluctuations in etching velocity and anodization conditions throughout a whole PSi sample lead to fluctuations of optical constants and layer thickness within the porous silicon layers. This usually results in a deterioration of the optical quality of the samples. In our case, the main factors influencing homogeneity at millimeter scale are gradients of Si substrate doping within the samples and inaccuracy in the control of the platinum electrode position (electrode not perfectly centered and/or slightly tilted).

In the present work, it is crucial that PSi layers yield high homogeneity to make sure that their optical behavior remains the same from one position to another on each sample, in order to enable a direct comparison of the response of the different NA arrays fabricated on the sample, as well as a comparison between the hybrid structures with NAs and the surrounding substrate (interferometer without NAs). Indeed, if NA arrays with different parameters are fabricated on two positions of a PSi sample yielding different optical response, it can be very hard to discriminate the contributions of these two factors in order to compare the optical response of the hybrid structures.

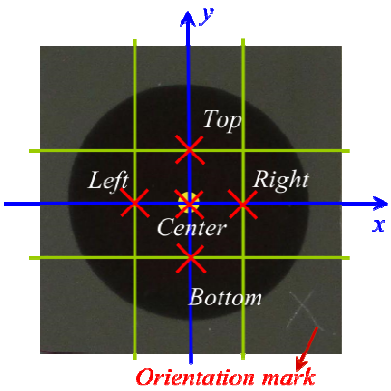

Fig 2.3.4 Schematic view of the five points on PSi systematically measured to check the homogeneity (the yellow point at the center represents the position of the light spot). The left, right, top and bottom points are half-way between the center and the edge of PSi region.

In order to verify the good homogeneity of the PSi layers, the reflectivity was systematically measured at different positions on each sample as shown in Fig 2.3.4. The orientation of each sample is marked with a cross in its right-bottom corner. 5 measurements points are chosen, the first one at the center of the PSi disk and the other points half-way between the center and the edge in each direction: ‘left’, ‘right’, ‘top’ and ‘bottom’.

Fig 2.3.5 illustrates 2 examples of PSi layers, the first one with bad homogeneity, and the second one with good homogeneity. For both samples, the spectra at each position have been fitted in order to determine the layer thickness and refractive index listed in the tables. In the case of the layer with bad homogeneity (Fig 2.3.5 (*a*)), the reflectivity spectra at the different positions do not overlap; the fits indicate differences of optical thickness Δnd up to 0.2 µm. In the case of the layer with good homogeneity (Fig 2.3.5 (*b*)), all 5 spectra are overlapping and the variation of optical thickness is only about 0.01 µm.

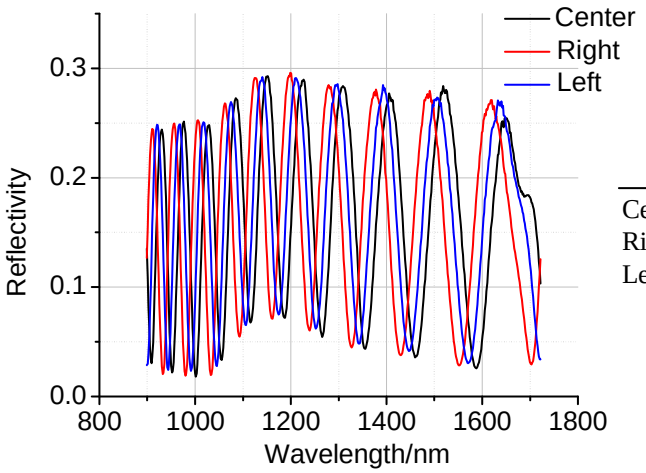

	$d/\mu m$	n	$P/\%$	$nd/\mu m$	$(\Delta nd)_{max}/\mu m$
Center	5.71	1.6	72	9.14	
Right	5.66	1.58	73	8.94	0.2
Left	5.73	1.58	73	9.05	

(a) Bad homogeneity

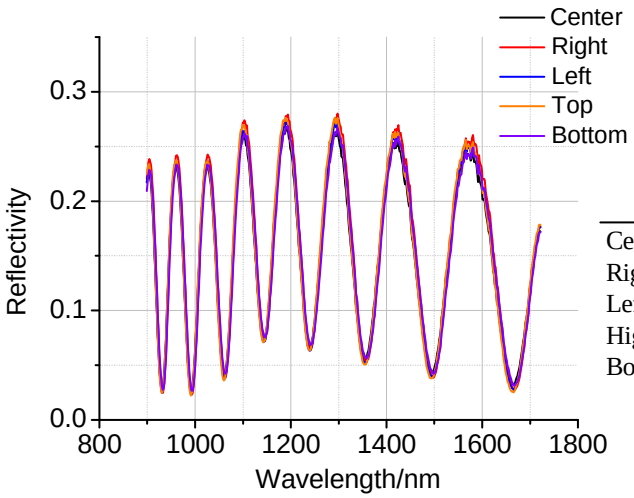

	$d/\mu m$	n	$P/\%$	$nd/\mu m$	$(\Delta nd)_{max}/\mu m$
Center	4.53	1.57	73	7.09	
Right	4.55	1.56	73	7.10	
Left	4.54	1.56	73	7.09	0.01
High	4.53	1.57	73	7.09	
Bottom	4.55	1.56	73	7.10	

(b) Good homogeneity

Fig 2.3.5 (a) Reflectivity of a PSi layer with bad homogeneity, and corresponding fit results for the 3 positions shown in the spectrum (the value of refractive index n is given at λ = 1.5 µm). The sample was anodized with 30 mA/cm² current density during 260 s; (b) Reflectivity of a PSi layer with good homogeneity, and corresponding fit results for all 5 positions shown in the spectrum. The sample was anodized with 37 mA/cm² current density during 200 s.

The PSi samples selected in this thesis and discussed in the following chapters are only samples yielding high homogeneity such as the example shown in Fig 2.3.5 (b).

Aging of PSi layers

It is well-known that a fresh PSi layer gets slightly oxidized after being exposed in ambient atmosphere for some time [2.10]. The formation of the native oxide film on the pore walls modifies the average refractive index of the PSi layer, resulting in a modification of the

optical response. This is illustrated in Fig. 2.23, which shows the comparison between the macro-reflectivity spectra of a freshly-anodized PSi layer (blue curve), and of the same layer 10 months later, stored at ambient atmosphere (red curve). The inter-fringe distance for the aged sample is clearly larger than for the freshly prepared one, indicating a decrease of optical path and of refractive index.

In order to quantify the effect of sample aging, the proportion of oxide has been evaluated by taking into account the presence of silica in the LLL model used in the fit algorism of the reflectivity spectra, as well as the volume expansion of silica with respect to the consumed silicon:

$$n_{eff-oxi}^{2/3} = n_{Si}^{2/3}(1 - P_{air-oxi} - P_{Si-oxi}) + P_{air-oxi} + n_{SiO_2}^{2/3} P_{SiO_2} \qquad \text{(EQ-2-4-1)}$$

$$P_{Si-oxi} = 0.44 P_{SiO_2} \qquad \text{(EQ-2-4-2)}$$

$$P_{air-oxi} = P_{air-fresh} - 0.56 P_{SiO_2} \qquad \text{(EQ-2-4-3)}$$

$$n_{eff-oxi}^{2/3} = n_{eff-fresh}^{2/3} + (n_{SiO_2}^{2/3} - 0.44 n_{Si}^{2/3} - 0.56) P_{SiO_2} \qquad \text{(EQ-2-4-4)}$$

where $n_{eff\text{-}fresh}$ and $n_{eff\text{-}oxi}$ are the effective refractive index of PSi layer in fresh and oxidized state, respectively; n_{Si} and n_{SiO2} are the refractive index of Si and SiO_2, respectively. $P_{Air\text{-}fresh}$, $P_{Air\text{-}oxi}$, and P_{SiO2} are respectively the porosity in fresh and oxidized state, as well as the proportion of SiO_2 in the PSi layer.

In the case of the sample presented in Fig 2.3.6, the layer thickness is about 7.98µm, and the initial effective refractive index $n_{\text{eff-fresh}}$ is 1.55, corresponding to a porosity of 74%; 10 months later the refractive index $n_{\text{eff-oxi}}$ has decreased to 1.43, corresponding to a porosity of 66%, and a percentage of SiO_2 of 15%. In order to evaluate the thickness of oxide film d_{SiO2}, we consider the specific surface S corresponding to the initial porosity and make the approximation of a planar surface [2.2]:

$$d_{SiO_2} = P_{SiO_2} / S \qquad \text{(EQ-2-4-5)}$$

The approximate thickness of oxide film is 1.5 nm, for a specific surface around 100 m^2/cm^3.

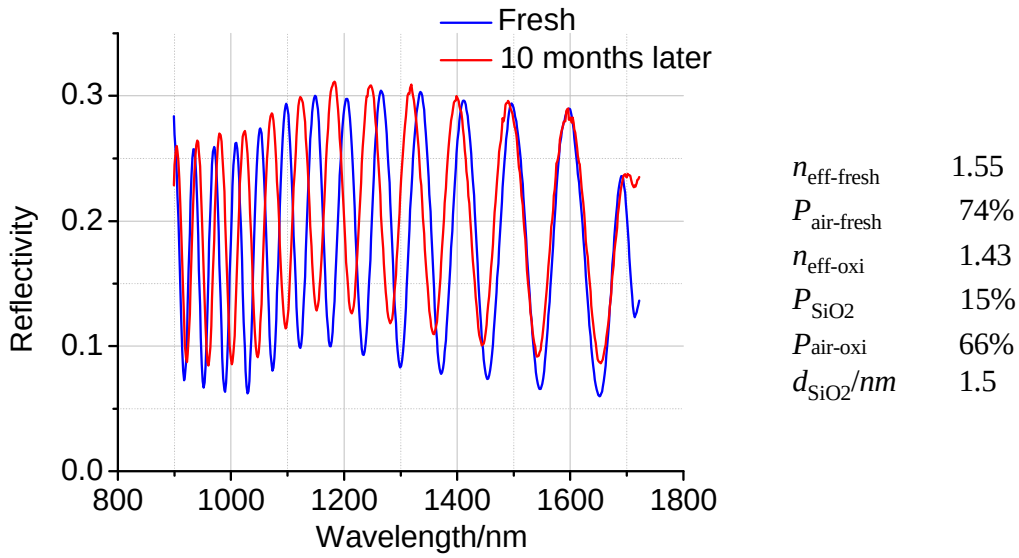

Fig 2.3.6 Reflectivity of a freshly-anodized PSi layer (Blue curve) and 10 months later (Red curve) after aging at ambient atmosphere; the analysis of optical characterizations is summarized in the table.

The discussion above highlights how sample aging can be crucial for the optical properties of the devices, and how we can quantify this phenomenon by macro-R measurements. Therefore, the PSi samples discussed later in this PhD thesis have been systematically characterized by macro-R directly after anodization, in order to determine the initial thickness and porosity prior to any oxidation.

2.3.2 Micro-Reflectivity/Transmission set-up

The micro-reflectivity/transmission (micro-R/T) set-up is dedicated to optical far-field spectral characterization of reflected and transmitted light for structures with micrometer dimensions, such as the NA arrays. The set-up has also been implemented to enable sensing experiments.

As discussed in the previous section, a thin layer of PSi on Si substrate behaves as an interferometer when illuminated with white light at normal incidence. In the case of our hybrid system, NA arrays are added on top of the interferometer. If the localized surface plasmon resonances in NAs interact with the underlying interferometer, the optical response of interferometer should be influenced by the presence of the NAs and in turn, the plasmonic response of the NAs should be influenced by the presence of the interferometer. The micro-R/T set-up will enable to study how the two systems interact with each other.

2.3.2.1 Set-up description

The micro-R/T set-up is based on an inverted microscope configuration and is presented in Fig 2.3.7. The set-up uses the same white light source and spectrometer than the macro-R setup, and can be divided into different branches:

- Incident beam: Light emitted by the source is first injected into a multimode fiber with N.A.0.22 and 105 µm-core diameter. The fiber is connected to a lens with f = 30 mm, which is collimating the light beam. A polarizor with 1200 – 1600 nm effective wavelength is used to control light polarization. Unless specified otherwise, all the results discussed in the present PhD work have been obtained for a polarization of the incident beam parallel to the bowtie NA axis '$E_{||}$' – see inset in Fig. 2.24. Then the beam is focused onto the sample surface at normal incidence via a Mitutoyo objective (NIR 20x NA0.4), into a small spot with ~33 µm waist – see inset on Fig 2.3.7.
- Detected beams: The signal collection is almost symmetrical for both reflected and transmitted light beams. The reflected beam goes back through the microscope objective onto a beam splitter that separates the reflected light from the incident one, and is then focused into a multimode fiber with 200 µm diameter through a lens identical to the one mentioned above, before being collected by the NIRQuest512 spectrometer. The transmitted beam goes through a second identical x20 objective, then through identical lens and multimode fiber towards the spectrometer.
- Visualization: For visualization the visible part of the white light spectrum is used. The visualization branch is inserted on the reflected beam via a beam splitter that sends part of the signal into a visible camera (Andor's Neo sCMOS camera) with ultra sensitive imaging ability and low read noise ($1e^-$). The camera enables to monitor the accurate micro-positioning of the devices.
- Sample positioning: Accurate device micro-positioning is achieved via an XYZ piezoelectric table. The sample holder is opened at its center to allow for detection of the transmitted signal.

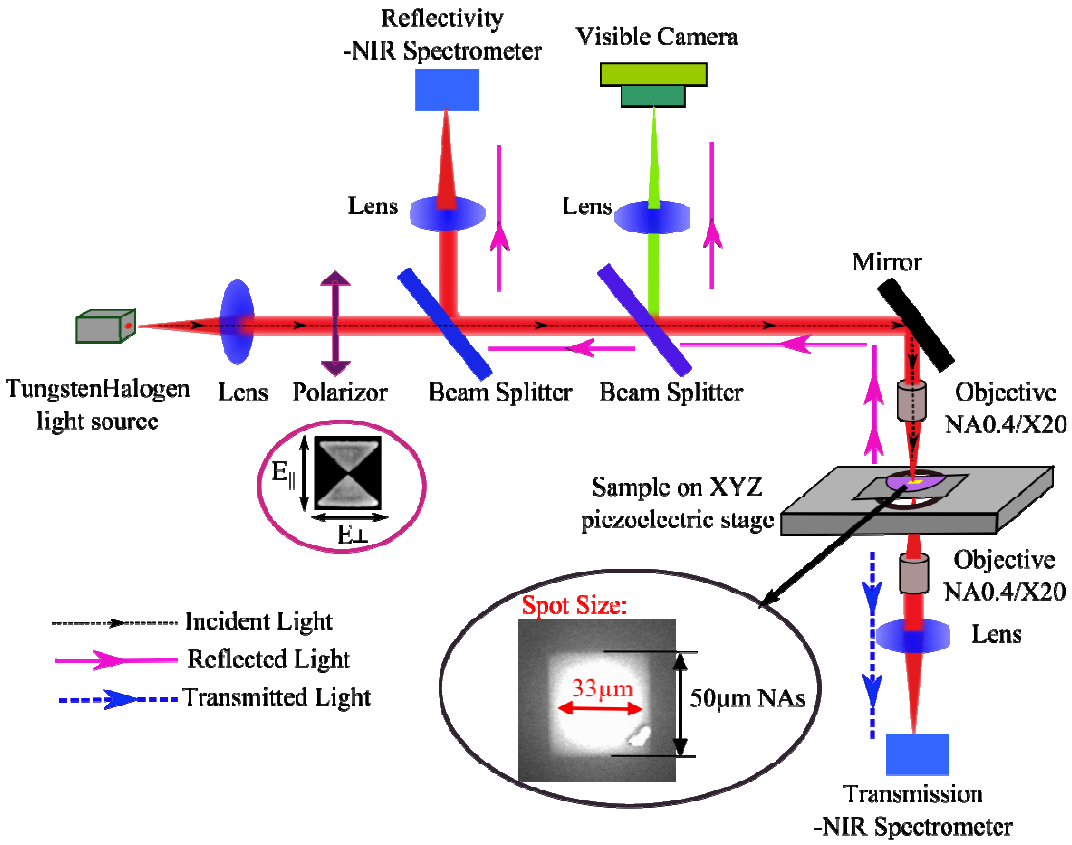

Fig 2.3.7 Micro-R/T setup for NA characterization

2.3.2.2 Fluidic cell

The sensing experiments performed during this PhD work require the use of an opto-fluidic cell enabling to monitor small variations of environment. This fluidic cell is presented in Fig 2.3.8 and has been designed and fabricated by Abdelmounaim Harouri [2.16] with the help of Cécile JAMOIS, Mohsen EROUEL and Robert PERRIN.

In this case, the sample is fixed onto a micro-glass slide using a polymer, such as PMMA resist or PDMS. The glass slide is inserted in a groove made in an aluminium alloy slide as shown in Fig 2.3.8 (c), and constitutes the bottom of the fluidic cell. Aluminium has been chosen to ensure rigidity and stability while keeping the whole cell light enough for the piezo stage of the micro-R set-up. A similar aluminium frame holding another glass slide constitutes the top of the cell. 2 holes are pierced through the top glass slide to insert the capillary tubes necessary for the circulation of fluids, which are fixed by Silicon gel. The 2 cell parts are assembled using 4 screws and with a rubber ring acting as a water-proof spacer between them. The space between the glass slides inside the rubber ring forms a semi-closed chamber communicating with the outside via the 2 capillary tubes (See Fig 2.3.8 (a)). In order to

perform the sensing experiments in liquid environment, water/ethanol mixtures are injected into the fluidic cell, since the variation of refractive index of such mixtures is known [2.11]. A syringe is used to inject the liquid into the chamber through the tubes. Then the cell is placed on the sample stage of the micro-R/T set-up for the optical characterization.

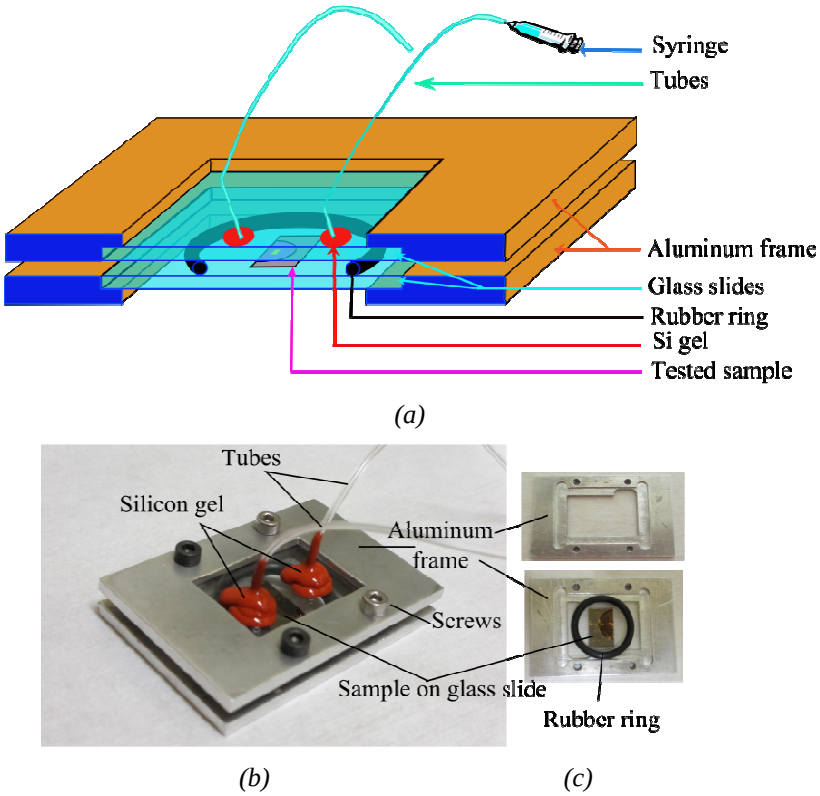

Fig 2.3.8 (a) Schematic view of the fluidic cell; (b) Photograph of the assembled cell; (c) photographs of parts of the cell

2.3.2.3 Reference measurements for reflectivity and transmission

1. Reference signals

Since each element in the micro-R / T set-up has its own wavelength-dependent optical response, which is embedded in the resultant optical 'raw' signal detected by the spectrometer, a proper reference measurement is crucial to separate the contribution of the studied structures.

In the case of reflectivity, the reference signal is performed with a silver mirror. However, there is a discrepancy between the height of the sample fixed on the glass slide and the height of the mirror, which prevents from a perfect normalization. An alternative to the silver mirror would be normalization with respect to the Si substrate directly on the samples – i.e., the non-

porous regions at the edges of the samples, corresponding to Si substrate + 80 *nm* SiO_2 layer. This alternative presents the advantage of exactly the same height for both the reference surface and the excited structures, which yields a better reference from the point of view of the setup contribution. As shown in Fig 2.3.9 (*a*), although the substrate reference yields lower signal intensity with respect to the mirror, the ratio between both signals only shows a very slight monotonic increase over the transparency range of the substrate materials, which should not alter further analysis of the measurement results. The feature observed at 1.4µm in all 3 spectra is attributed to attenuation in the fibers (See Appendix C).

In the case of transmission measurements, the sample is fixed on the glass slide using optical gel in order to avoid any interferometric effect due to an air slit between the sample and the glass. In this case, the reference signal is measured through the glass slide in order to approximately keep the same focal plane as for the devices while taking into account the contribution of the glass. Similar to reflectivity measurements, a reference with respect to the sample substrate is a possible alternative, since the ratio between both signals only shows a slight monotonic decrease for $\lambda > 1100$ nm due to absorption in the highly-doped silicon substrate, as shown in Fig 2.3.9 (*b*).

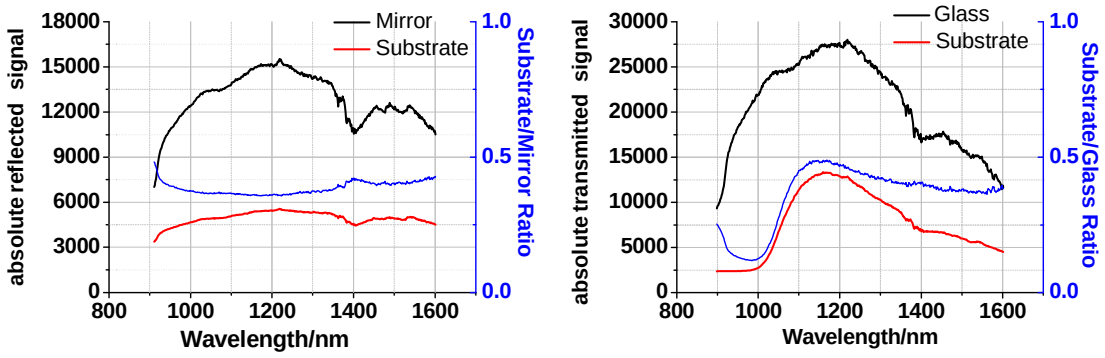

(*a*) (*b*)

Fig 2.3.9 Reflected (a) and transmitted (b) reference signals: "standard" references from silver mirror and glass slide, respectively (black curves), "substrate" references from the 80nm SiO_2/Si substrate (red curves) and ratio between the substrate and standard references (blue curves).

2. Comparison between normalizations

Fig 2.3.10 presents the comparison between the 2 alternative normalizations on 2 different samples, the first one with a NA array (system 2) and the other one with an interferometer

(system 3). In both cases, the spectra are shown both when the sample is in air environment (Fig 2.3.10 (*a* - *d*)), and when it is in the opto-fluidic cell in water environment (Fig 2.3.10 (*e* - *f*)). The black spectra are normalized by the "standard" reference signals (silver mirror and glass slide for reflection and transmission, respectively); the red spectra are normalized by the substrate.

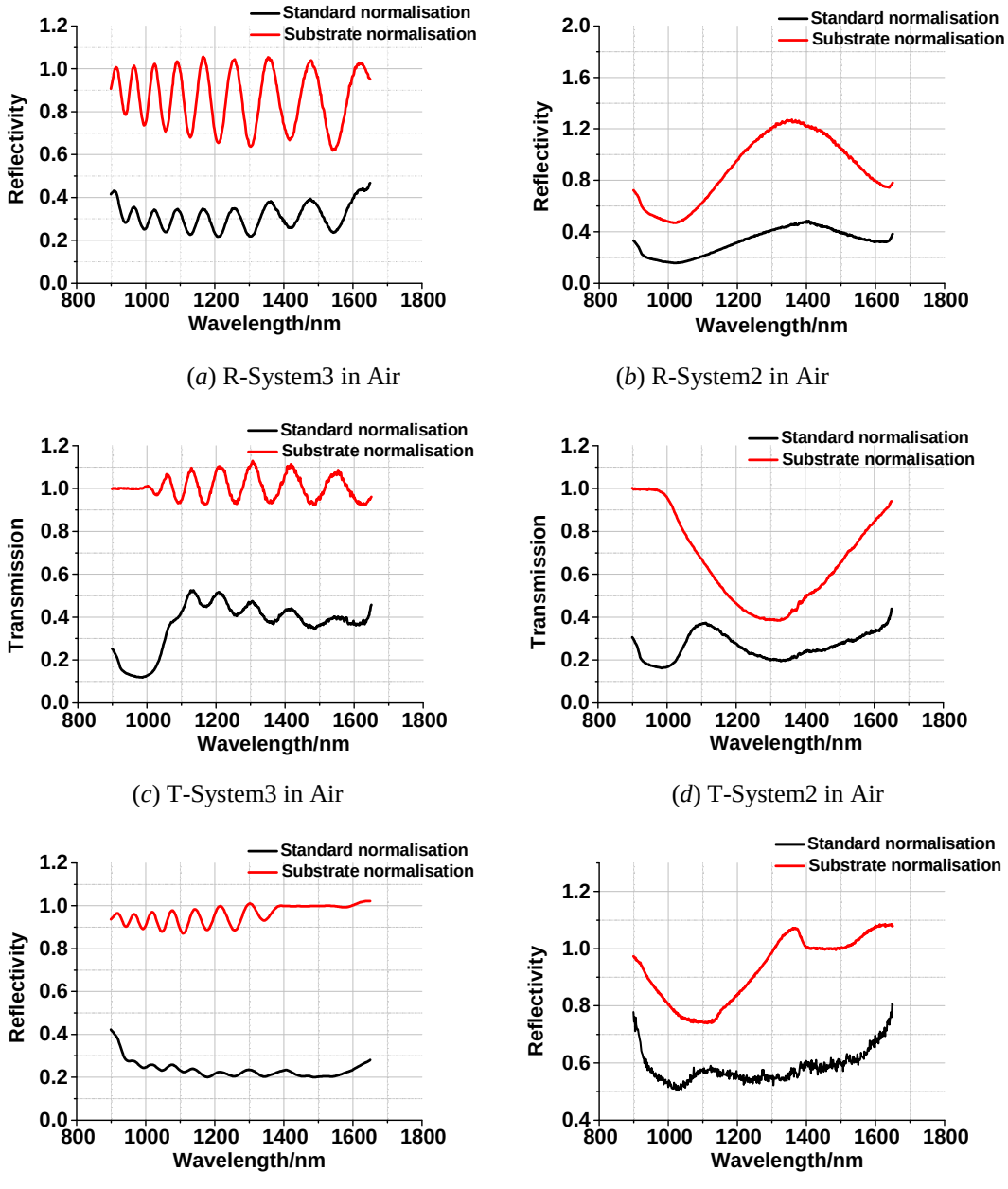

(*a*) R-System3 in Air

(*b*) R-System2 in Air

(*c*) T-System3 in Air

(*d*) T-System2 in Air

(e) R-System3 in water

(f) R-System2 in water

Fig 2.3.10 Comparison between normalization with standard reference (black curves) and substrate reference (red curves): (a) Reflected spectra of System3 in Air; (b) Reflected spectra of System2 in Air; (c) Transmitted spectra of System3 in Air; (d) Transmitted spectra of System2 in Air; (e) Reflected spectra of System3 in Water; (f) Reflected spectra of System2 in Water

The comparison between the spectra shown in Fig 2.3.10 leads to 2 main observations:

- The reference by the substrate yields normalized signals that can be larger than 1. However, it also yields much larger signal amplitude. Enhancement of the signal amplitude by a factor of 2 or higher can be observed comparing with the "standard" normalizations. This is even more obvious in the case of water environment (Fig 2.3.10 (*e*) and (*f*)).
- The feature around 1.4µm, attributed to absorption in the optical fibers, is strongly reduced in the case of substrate normalization with respect to standard normalization. This is particularly clear for System2. This demonstrates that normalization by the substrate is better to eliminate the contributions from the optical setup, allowing for a better analysis of the results.

Hence, substrate normalization will be preferred in the results presented in the following chapters, especially in chapter 4 for the discussion about the sensing potential of our device.

2.4 Conclusion

In this chapter, we presented the experimental fabrication procedures and techniques for the 3 systems that will be realized and compared in this work. We also presented the optical set-ups of macro-R and micro-R/T used for characterizing the PSi layers and the micro-devices, respectively. The fluidic cell used for the sensing experiments has also been described. Combining all these experimental techniques will enable the successful study and analysis of the interaction between PSi interferometer and NAs, which will be discussed in the next chapter.

2.5 References

[2.1] Li C, Nouvelle filière nanotechnologique sur silicium poreux : Application à des dispositifs photoniques, Institut des Nanotechnologies de Lyon, Thesis defense on 25th May, 2010

[2.2] Guillermain, E., Dispositifs nanophotoniques à ondes de surface en silicium poreux : Technologie et application à la bio-détection. Institut des Nanotechnologies de Lyon, Thesis defense on 19th November, 2007.

[2.3] E. Guillermain, V. Lysenko, et al, Bragg surface wave device based on porous silicon and its application for sensing, APPLIED PHYSICS LETTERS, 90, 241116, 2007.

[2.4] TP ZHANG, Plasmonic-Photonic Hybrid Nano-device, Institut des Nanotechnologies de Lyon, Thesis defense on 22th November, 2012.

[2.5] http://www.clean.cise.columbia.edu/process/spintheory.pdf

[2.6] SPIE Handbook of Microlithography, Micromachining and Microfabrication.

[2.7] http://www.thermionics.com/en-us/Desktop/Knowledge/View/Articles/8f9d3d35-2727-4a64-93b6-373dd1fdf075/6e0d9ffc-e147-40a0-b7a7-ec14982ba1f9/

[2.8] Roger Newman, Fine line lithography, North-Holland Publishing Company, 1980 - Art - 481 pages.

[2.9] Electron Beam Lithography patterning of superconducting and magnetic nanostructures for novel optical and spintronic devices, Vito Pagliarulo, UNIVERSITA' DEGLI STUDI DI NAPOLI 2010.

[2.10] C. Jamois, New concepts of integrated photonic biosensors based on porous silicon, Biosensors – Emerging Materials and Applications, 2011.

[2.11] Nowakowska, Janina, "The Refractive Indices of Ethyl Alcohol and Water Mixtures" (1939). Master Thesis. Paper 668.

[2.12] C. Martinet, V. Paillard, A. Gagnaire, J. Joseph, Deposition of SiO2 and TiO2 thin films by plasma enhanced chemical vapor deposition for antireflection coating, J. Non-Cryst. Solids, v216, pp77-82.

[2.13] http://snf.stanford.edu/Process/Lithography/liftoff.html

[2.14] D. R. S. Cumming, S. Thoms, S. P. Beaumont, and J. M. R. Weaver; “Fabrication of 3 nm wires using 100 keV electron beam lithography and poly(methyl methacrylate) resist”; Appl. Phys. Lett. 68, 322 (1996); http://dx.doi.org/10.1063/1.116073

[2.15] http://www.epa.gov/oppt/existingchemicals/pubs/TSCA_Workplan_Chemical_Risk_Assessment_of_TCE.pdf

[2.16] Abdelmounaim Harouri, Biocapteurs photoniques : Réalisation d’une cellule fluidique pour une détection in-situ, Master thesis, INSA-Lyon (2011).

Chapter 3 Investigation of Optical Interaction between F-P interferometer and Bowtie NAs

3.1 INTRODUCTION 161

3.2 STUDY OF BOWTIE NA RESONANCE 163

3.2.1 Influence of inter-particle distance 164

3.2.2 Influence of triangle tip angle 165

3.3 HYBRID DEVICE: INTERFEROMETER APPROACH 168

3.3.1 Single layer interferometer 168

3.3.2 Two - layer interferometer 170

3.3.3 Interferometer with homogeneous gold layer 174

3.3.4 Equivalent layer of Bowtie NAs array 178

3.4 HYBRID DEVICE: RESONATOR APPROACH 199

3.4.1 Principle of coupled mode theory 199

3.4.2 Study of the influence of Q and Q_c/Q_0 201

3.4.3 Study of the influence of ω_0 206

3.5 CONCLUSION 209

3.6 REFERENCES 211

3.1 Introduction

As we mentioned in the previous chapters, this work aims at investigating bio-chemical detection potential and sensitivity of the proposed hybrid device consisting of bowtie NAs and PSi layer interferometer. Before doing so, it is crucial to completely understand the different interactions between the 2 structures:

What is the influence of the interferometer on the response of the NA array?

How is the behavior of the interferometer influenced by the presence of the NA array and its tunable plasmonic resonance?

Hence, in this chapter, we will study the coupling mechanisms from the 3 following aspects:

- 1. Study of bowtie NA resonance

This first part is dedicated to the basic investigation of coupling mechanisms between the 2 triangle-shaped gold particles constituting a bowtie NA, in order to gain a better understanding of the NA resonance behavior. This study is performed on System 2 – NA array directly deposited on Si substrate with 200 nm SiO_2 spacing layer. By adjusting the triangle dimensions and the inter-particles distance, the tunability of resonance can be studied.

- 2. Interferometer approach

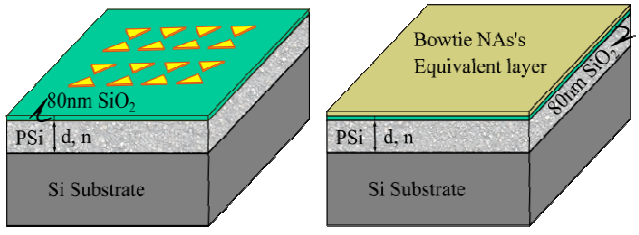

Fig 3.1.1 Representation of the model proposed in the interferometer approach: the NA array of the hybrid device (a) is modelled by an equivalent layer placed on top of the interferometer (b)

According to the principle of thin film interference, a phase matching model for multi-layer interferences is proposed. In this model, the bowtie NA array is supposed to be equivalent to an extra layer which is placed on top of the interferometer – i.e., the monolayer of PSi with its 80 nm SiO_2 spacing layer – as shown in Fig 3.1.1. The effective dielectric function of the

equivalent layer is determined using the Drude model and the effect of such an equivalent layer on the behavior of the hybrid structure is studied and compared to experimental results.

- 3. Resonator approach

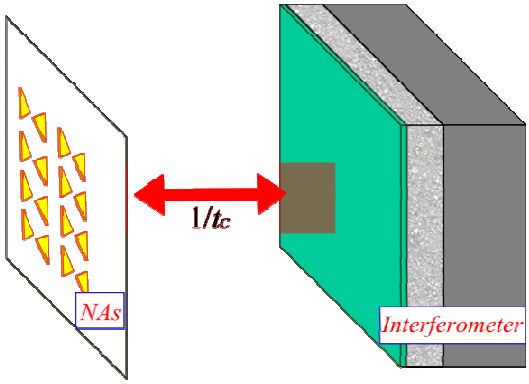

Fig 3.1.2 Representation of the resonator approach: the hybrid device is viewed as a harmonic oscillator (NA array) coupled to the interferometer

The plasmon resonance of the bowtie NA array can be viewed as a harmonic oscillator (Fig 3.1.2). The coupling between NAs and interferometer is investigated with coupled mode theory, which describes the global temporal-spectral characteristics of the optical power transfer and storage within the hybrid device. This approach will allow for complementary analysis of the interferometer-NA interaction at resonance.

3.2 Study of bowtie NA resonance

As discussed in Chapter 1, the resonance peak wavelength and line shape of a nanoparticle are not only dependent on its size, shape, composition and orientation, but also related to its local dielectric environment. Hence, before the investigation of coupling between bowtie NAs and interferometer, it is important to investigate the coupling mechanisms leading to resonance of bowtie NAs.

The structure considered in this section is a NA array deposited on Si substrate with 200nm SiO_2 spacing layer (Fig 3.2.1), and will be nominated as "System 2". The role of SiO_2 spacing layer is to keep NAs in the same environment (refractive index is 1.5) as our designed hybrid device. The 200 nm thickness has been chosen in order to exclude the layer interferometric effect within the wavelength range of interest.

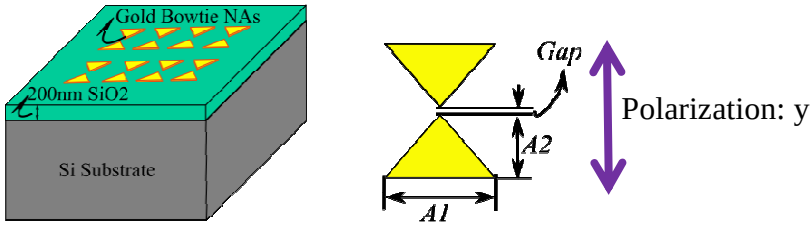

Fig 3.2.1 The structure considered in this section: "System 2"is consisting of a NA array on Si substrate with 200nm SiO_2 spacing layer.

By adjusting the dimensions of triangles constituting each NA and the inter-particle distance, the tunability of NA resonance is studied via far-field micro-reflectivity measurements using the optical set-up presented in chapter 2. Both FDTD simulation and experimental results are discussed below. For the experimental results, there are two points worth noting:

- First, the reference signal is from the SiO_2/Si substrate, unless mentioned otherwise;
- Second, in order to eliminate the noise and have a more accurate reading of the wavelength position of maxima, some smoothening of the spectra could be performed when analyzing the data with Matlab.

For the following experimental results, we keep the same condition as above, unless there is special illustration.

3.2.1 Influence of inter-particle distance

The first study concerns the influence of the inter-particle distance – called "Gap" in the following – on the resonance wavelength of the bowtie NAs. The shape and dimension of the triangles are kept constant with A1 = 510 nm and A2 = 280 nm, while the value of the Gap is varied between 20 nm, 40 nm and 60 nm. The reflectivity spectra are shown in Fig 3.2.2, both for FDTD simulations and experimental results.

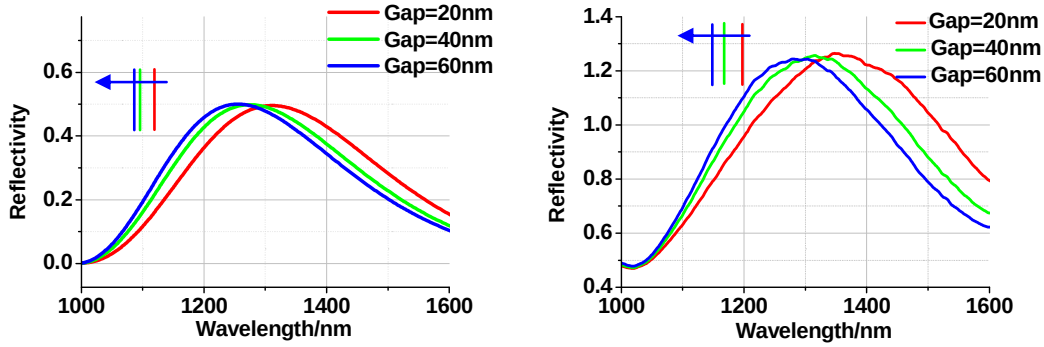

(a) *(b)*

Fig 3.2.2 Reflectivity spectra of NAs with varying gap value (a) FDTD Simulation; (b) Experimental results. The bowtie NAs have dimensions A1 = 510 nm and A2 = 280 nm.

In Fig 3.2.2, it is obvious that the plasmon resonance experiences a blue shift as the gap size increases. This is illustrated in Fig 3.2.3, which shows the position of the resonance depending on the inter-particle distance.

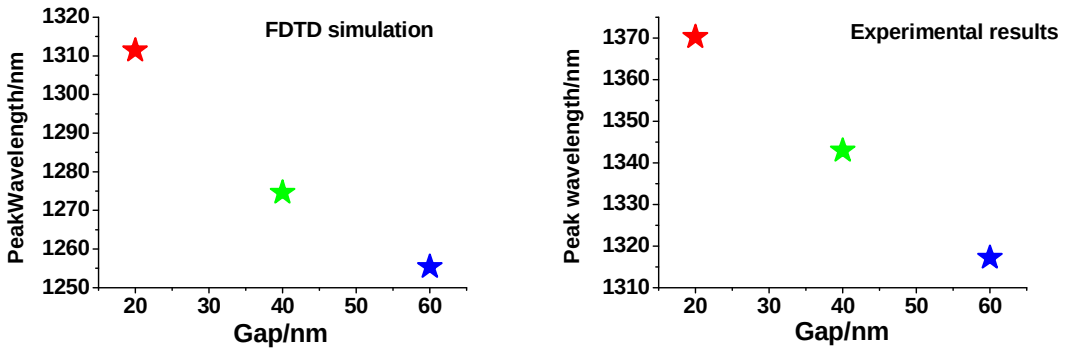

(a) *(b)*

Fig 3.2.3 Resonance wavelength vs. Gap for the spectra shown in Fig 3.2.2. (a) FDTD simulation; (b) experimental results

The red shift of the resonance with decreasing gap size is a well-known phenomenon that can be directly related to the coupling strength between the two particles constituting the nano-

antenna. For coupled dimers, there are three regimes of particle separation, illustrated in Fig 3.2.4, that reveal different behaviors [3.1]. For large distances, they behave independently like single particles. As the particle gap is reduced, the dipolar response redshifts. Initially, the far-field response weakens because the effective dipole of the coupled dimer is reduced. For even smaller separations, the modes continue to redshift, there is a strong buildup of charges at the gap, near-fields in the gap are enhanced, and the far-field scattering begins to increase again [3.1].

It should be pointed out that the slight discrepancy of resonance wavelengths between the experimental results and the FDTD simulations can be explained by the imperfection and fluctuations of the NA shapes after fabrication [3.6], as discussed in Chapter 2, whereas the simulation considers perfect structures.

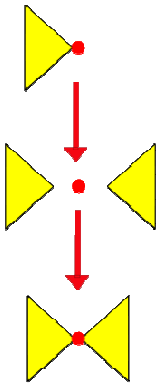

Fig 3.2.4 Geometric illustration of the 3 coupling regimes with decreasing gap size

3.2.2 Influence of triangle tip angle

The next parameter to investigate is the angle of the triangle tip, corresponding to A1/A2 ratio. Here A2 is kept constant at 280 nm, as well as the Gap at 20 nm, and the value of A1 is varied. The reflectivity spectra are shown in Fig 3.2.5 both for FDTD simulation and experiments.

In Fig 3.2.5 the resonance wavelength shows a small red shift with increasing A1, i.e., increasing triangle tip angle. For clarity, the resonance wavelengths are plotted again in Fig 3.2.6 (*a*) and (*b*), respectively, for the FDTD and the experimental results. Very good agreement is found between simulations and experiments in the variation of the resonance wavelength with increasing A1.

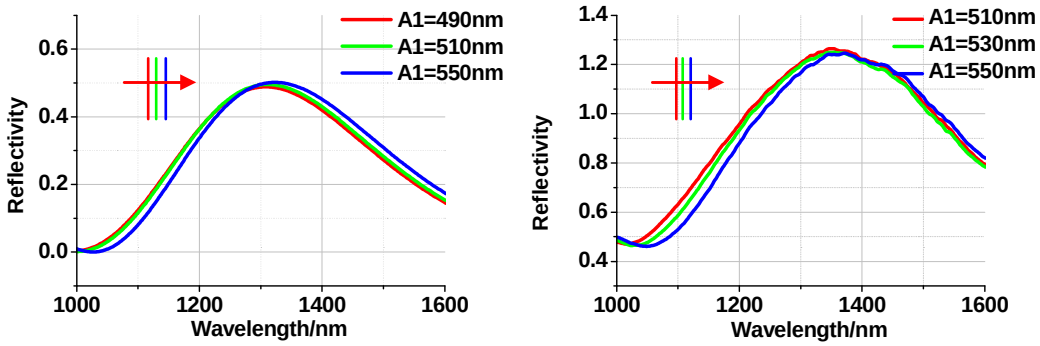

(a) *(b)*

Fig 3.2.5 Reflectivity spectra of NAs with varying A1 value while keeping A2 = 280 nm and Gap = 20 nm. (a) FDTD Simulation for 490 nm (red), 510 nm (blue) and 550 nm(green); (b) Experimental results for 510 nm (red), 530 nm (blue) and 550 nm(green)

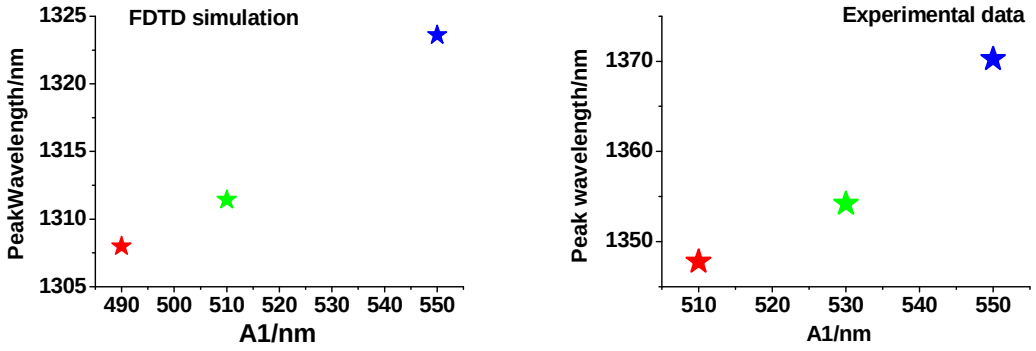

(a) *(b)*

Fig 3.2.6 Resonance wavelength vs. A1for the spectra shown in Fig 3.2.5: (a) FDTD simulation; (b) experimental results

The result shown in Fig 3.2.6 is in good agreement with Wei Ding's work [3.2]. According to their investigation, there are 2 different mechanisms for plasmon resonances in bowtie NAs depending on the bow angle:

- For small angle, under plane wave illumination with parallel polarization there is one standing surface plasmon polariton (SPP) along the antenna axis, as shown in Fig 3.2.7 (a). In this case, the plasmon resonance is determined by the antenna length, L and the effective index of the SPP, $n_{eff}(x)$:

$$\lambda_0 \approx 2\int_{-L/2}^{L/2} n_{eff}(x)dx + \delta,$$

When the angle increases, the SPP "sees" more metal leading to a decrease of n_{eff}, which leads to a blue shift;

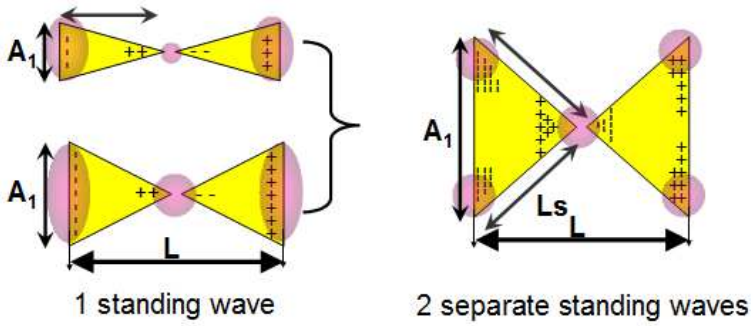

(a) Small angle *(b) big angle*

Fig 3.2.7 Schematic illustration of the 2 cases for NA resonance depending on the triangle bow angle

- For bow angles larger than 80°, the above equation is invalid. In this case, there exist 2 standing SPP waves along the 2 sloping sides of each triangle, as illustrated in Fig 3.2.7 (b). As the resonance wavelength is varying with the length – in this case, the length of sloping side Ls – an increase of A1 induces a larger Ls, which leads to a red shift of the plasmon resonance.

As the bow angle in our design is around 80° to 90°, we are in the case of the 2 separate standing waves, which yields a red shift of the resonance with increasing angle – or increasing A1. However, the observed shift is not very sensitive to A1 variations. According to FDTD simulations, the shift is less than 20 nm (1.5%) for 60 nm A1 variation (11%); in the case of the experimental results, the variation is slightly larger – 22 nm red shift (1.5%) for 40 nm A1 variation (7.5%).

3.3 Hybrid device: Interferometer approach

3.3.1 Single layer interferometer

3.3.1.1 Phase matching condition

As discussed in Chapter 2, when a white light beam is normally incident on a thin film, like the monolayer of PSi (n_{PSi}, d_{PSi}) on Si substrate (n_{Si}) and air environment (n_{air} = 1) shown in Fig 2.3.1 (a), the reflected light from both PSi/air and PSi/Si interfaces interfere with each other. Depending on the phase conditions constructive or destructive interferences occur, leading to Fabry-Perot (F-P) interference fringes in the reflected spectrum.

The phase difference$\Delta\varphi_1$ between the reflected light beams at the 2 interfaces is:

$$\Delta\varphi_1 = \frac{4\pi}{\lambda} n_2 d \qquad \text{(EQ-3-3-1)}$$

where n_2 and d are the effective refractive index and thickness of the thin film, respectively. If $n_2 = n_{PSi}$, with $1 < n_{PSi} < n_{Si}$, we have:

$$R = R_{max,}\ \Delta\varphi_1 = 2m\pi,\ m = 0, \pm 1, \pm 2, \cdots \qquad \text{(EQ-3-3-2)}$$

$$\text{with } \lambda_{max\,1} = \frac{4n_{PSi}d}{2m} \qquad \text{(EQ-3-3-3)}$$

where R is the reflectivity of the device, R_{max} is its maximal value, λ_{max1} is the wavelength value when $R = R_{max}$ and m is the fringe order. The equations above are called Phase matching condition for thin film interference [3.3].

From this condition it is obvious that the optical path – the product of refractive index and thickness of the thin film – is one of the most important parameters influencing the fringe distribution with wavelength, because it sets the wavelength values for the maxima or minima of reflectivity (peak or dip) as well as the spacing $\Delta\lambda$ between the positions of two adjacent fringes, as was shown in EQ-3-3-3. Besides, the refractive index contrast at each interface thin film/environment and thin film/substrate determines the values of R_{max} as well as R_{min} (minimum of reflectivity).

3.3.1.2 Application to experimental structures

The phase matching condition for single layer interferometer presented above can be verified with the reflectivity spectrum of a PSi monolayer on Si substrate shown in Fig 3.3.1 (labeled as “PSi/Si”). Such a spectrum can be simulated, e.g. using the transfer matrix method (TMM), which is an effective method to analyze the propagation of electromagnetic waves through a layered medium on basis of their boundary conditions [3.4].

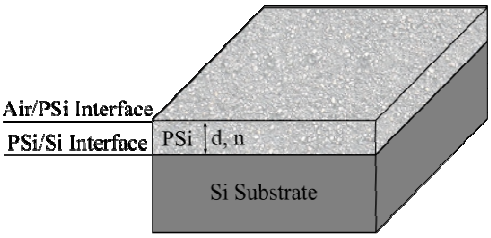

Fig 3.3.1 Schematic view of monolayer of PSi on Si substrate (PSi/Si)

As an illustration, a 4.85 µm-thick PSi layer anodized on Si substrate was fabricated by anodization and characterized by macro-reflectivity. The variation of the PSi refractive index with wavelength was determined from the fit of the reflectivity spectrum yielding a porosity of air ($P_{\text{air-oxi}}$) - 53% and percentage of SiO_2 (P_{SiO2}) - 19% attributed to natural oxidation, considering that in the transparency domain of Si, the refractive index of the material can be deduced from a Cauchy law [3.5]. The variations of the refractive index with wavelength are shown in Fig 3.3.2 (*a*) and Fig 3.3.2 (*b*)) for PSi and Si, respectively. The experimental macro-R spectrum is plotted in Fig 3.3.3 (*a*) (blue curve).

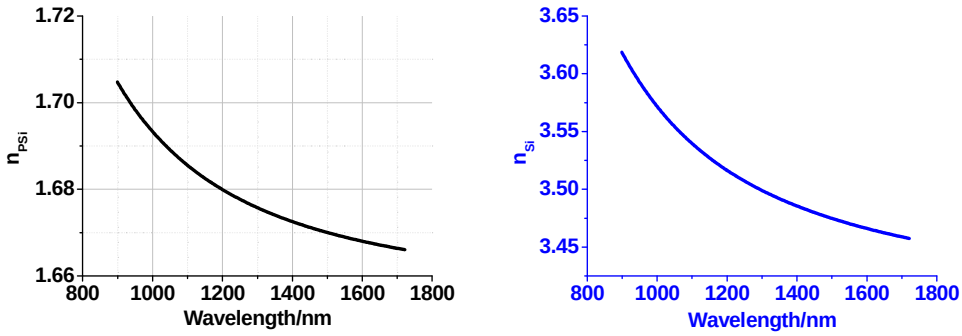

(a) *(b)*

Fig 3.3.2 Refractive index of (a) PSi, (b) Si

The parameters deduced from the experimental data ($d_{\text{PSi}} = 4.85$ µm, n_{PSi} shown in Fig 3.3.2 (*a*)) were then used in TMM simulation. Such a simulation considers that the

materials below and above the PSi layer – the Si substrate and air, respectively – have thicknesses set to 0. The simulated reflectivity spectrum is plotted in Fig 3.2.3 (*a*) (red curve).

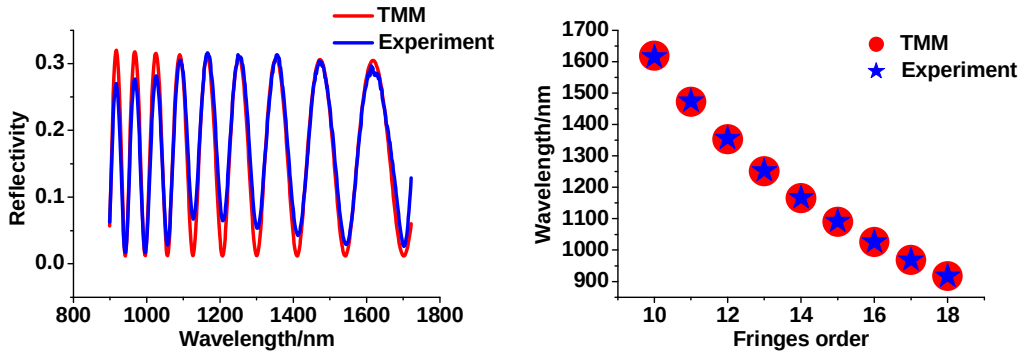

(a) *(b)*

Fig 3.3.3 (a) Reflectivity of PSi/Si (red curve for TMM simulation, blue curve for experimental results); (b) Wavelength vs. Fringe order for the spectrum shown in (a): red dots are for TMM simulation and blue stars for experimental results

Comparing the 2 spectra shown in Fig 3.3.3 (*a*), there seems to be a good matching between experimental and simulated results. In order to verify this, each fringe order *m* was calculated following the equation: $m = \frac{2n_{PSi}d_{PSi}}{\lambda_{1\max}}$ deduced from EQ-3-3-3, both for experimental results and TMM simulation. The wavelength positions of fringe maxima ($\lambda_{1\max}$) depending on the order *m* are plotted in Fig 3.3.3 (*b*). The perfect agreement between experimental positions (blue solid stars) and simulated ones (red solid circles) demonstrates the validity of both the fit of experimental reflectivity spectrum and of the TMM simulation for the case of single layer PSi interferometer.

3.3.2 Two - layer interferometer

When one or several extra thin films are placed on top of the single layer interferometer, the phase matching condition becomes difficult for analytical description. The exact expression of the phase matching model for this case is described in Appendix A. Here, we will concentrate on the particular case where the extra film is much thinner than the main interferometer layer, and build a simpler approximation of the phase matching condition.

3.3.2.1 Phase matching model

Compared to air, an extra thin layer of another material will modify the phase difference between the reflected beams from the 2 external interfaces (i.e., PSi/Si interface and extra layer/air interface, as shown in Fig 3.3.4). According to the analysis presented in the previous section and boundary condition at the interface, for an extra thin layer on top of PSi / Si the phase matching condition could be modified as:

$$\Delta\varphi_2 = \Delta\varphi_{prop} + \Delta\varphi_{\text{int}\,erface} = 2m\pi \qquad \text{(EQ-3-3-4)}$$

$$\Delta\varphi_{prop} = \frac{4\pi}{\lambda}\left(n_{PSi}d_{PSi} + n_e d_e\right) \qquad \text{(EQ-3-3-5)}$$

where $\Delta\varphi_2$ is the total phase shift introduced by the extra layer, $\Delta\varphi_{prop}$ represents the total phase difference due to the propagation of the wave through all layers, which is the sum of the phase differences gained from the optical path in each layer. Here, n_e and d_e are the refractive index and thickness of the extra layer, respectively, and $\Delta\varphi_{interface}$ is the phase shift upon reflection at each interface, which depends on the value of refractive index of the 2 adjacent media. When the index of extra layer n_e is close to n_2, the effect of the "Extra layer / PSi interface" can be negligible and

$$\Delta\varphi_{\text{int}\,erface} = 0 \qquad \text{(EQ-3-3-6)}$$

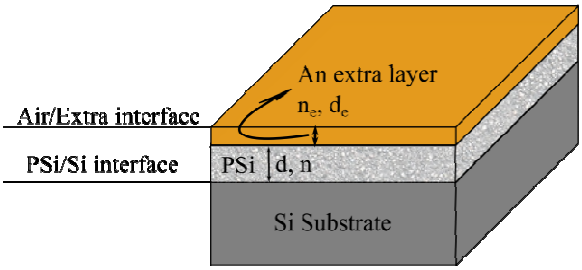

Fig 3.3.4 Model used for the phase matching approximation in the 2-layers interferometer where the extra layer placed on top of the interferometer has a thickness de and a refractive index ne.

Considering that the above condition for $\Delta\varphi_{\text{int}\,erface} = 0$ applies, and comparing the phase matching condition to the case of the one – layer interferometer PSi/Si described in (EQ-3-3-2) and (EQ-3-3-3), the wavelengths corresponding to the maxima of reflected signal for the 2 – layers system should be:

$$\lambda_{\max 2} = \frac{4}{2m}\left(n_{PSi} d_{PSi} + n_e d_e\right) \qquad \text{(EQ-3-3-7)}$$

If we consider the case where the extra layer consists of a low-absorption material such as silica, we have:

$$\lambda_{2\max} > \lambda_{1\max} \qquad \text{(EQ-3-3-8)}$$

It means, for a given order *m*, the introduction of the extra material will lead to a red shift of the fringes compared to the case of the initial single-layer interferometer.

3.3.2.2 Application to experimental structures

The experimental 2-layer system that is considered is the PSi/Si interferometer with the 80 nm-thick SiO_2 layer on top. This 2-layer-device is labeled as "SiO_2/PSi/Si" and illustrated again in Fig 3.3.5 (*a*).

In order to describe the refractive index of silica, we use again a Cauchy law, considering that the material is in its transparency domain [3.5]. The variations of silica refractive index n_{SiO2} depending on the wavelength are plotted in Fig 3.3.5 (*b*). Comparing to Fig 3.3.2 (*a*), we can see that the value of n_{SiO2} over the whole wavelength range is close to that of n_{PSi}; hence, a red shift of the interference fringes can be expected with respect to the PSi/Si system without silica, according to (EQ-3-3-8).

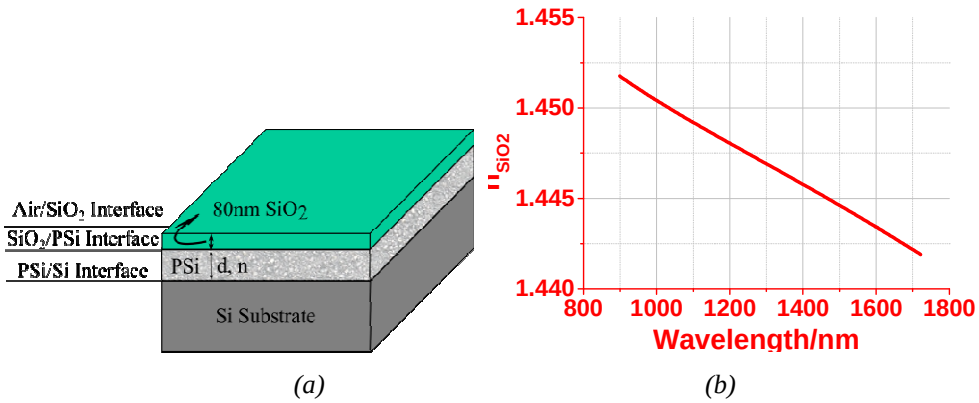

(a) *(b)*

Fig 3.3.5 (a) Schematic view of the SiO_2/PSi/Si system constituted of a 80nm-thick SiO_2 layer on PSi interferometer; (b) refractive index of silica vs. wavelength (deduced from Cauchy equation)

For the particular SiO_2/PSi/Si system, the phase matching model becomes:

$$\frac{4\pi\left(n_{PSi}d_{PSi}+n_{SiO_2}d_{SiO_2}\right)}{\lambda_{2\max}}=2m\pi \qquad \text{(EQ-3-3-9)}$$

$$m=\frac{2\left(n_{PSi}d_{PSi}+n_{SiO_2}d_{SiO_2}\right)}{\lambda_{2\max}} \qquad \text{(EQ-3-3-10)}$$

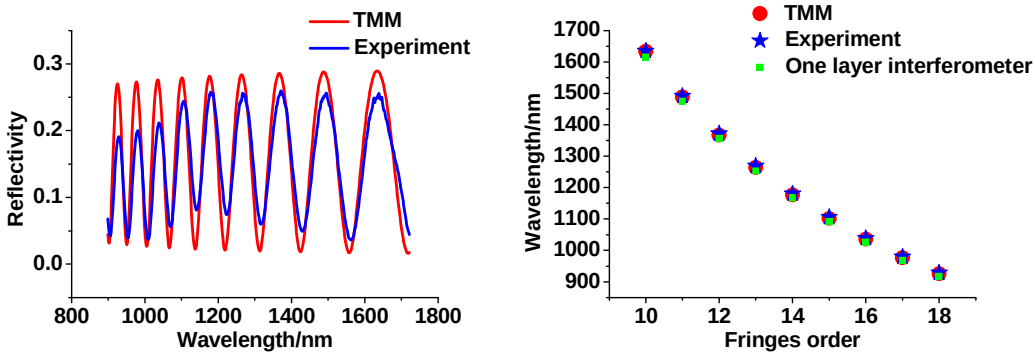

(a) *(b)*

Fig 3.3.6 (a) Reflectivity spectra of SiO_2/PSi/Si for TMM simulation (red curve) and experimental results (blue curve); (b) Wavelength vs. Fringes order deduced from the reflectivity spectra (red dots are for TMM simulation and blue stars for experimental results)

Experimentally, the same sample presented in section 3.3.1.2 is used, and is immediately characterized in macro-reflectivity after silica layer deposition. The experimental spectrum is plotted as the blue curve in Fig 3.3.6 (*a*). TMM simulations are also performed, using the same parameters discussed previously in section 3.3.1.2 and the variations shown in Fig 3.3.5 (*b*), leading to the red spectrum shown in Fig 3.3.6 (*a*). As before, in order to check for the good matching between the experimental and the simulated maxima, the wavelength values corresponding to R_{max} for each order are plotted in Fig 3.3.6 (*b*). The positions of the initial one-layer interferometer are also plotted, in order to demonstrate the observation of the red shift.

In order to validate the phase matching model proposed for the 2-layer structure, it is important to verify if the wavelength positions deduced in Fig 3.3.6 are in good agreement with (EQ-3-3-9). The discrepancy between the results presented above and the model is labeled as δ_2:

$$\delta_2=2m\pi-\frac{4\pi\left(n_{PSi}d_{PSi}+n_{SiO_2}d_{SiO_2}\right)}{\lambda_{2\max}} \qquad \text{(EQ-3-3-11)}$$

The value of δ_2 for each fringes order *m* is plotted in Fig 3.3.7, both for the experimental case and the TMM simulation. As can be seen, the absolute value of δ_2 for experimental result is smaller than 0.05π, while it is slightly larger for TMM simulation but still smaller than 0.15π. As the calculation of δ_2 also takes into account any discrepancies in the values of thickness and refractive index of the layers, as well as rounding errors and inaccuracies for the reading of the λ_{2max} values on the reflectivity spectra, we can conclude that δ_2 is negligible, which validates the phase matching model for the 2-layer system.

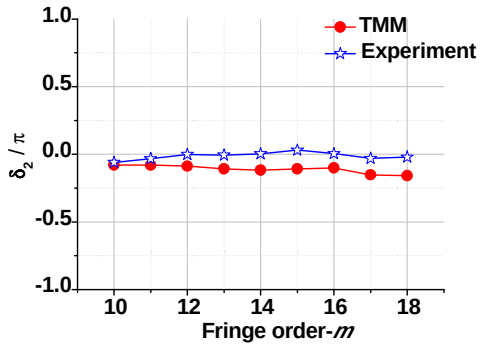

Fig 3.3.7 Discrepancy between the values deduced from reflectivity results and the phase matching model (δ_2) for the system SiO_2/PSi/Si

3.3.3 Interferometer with homogeneous gold layer

3.3.3.1 Phase matching model

The next step in our development of phase matching model is to consider the case of a 3 - layer structure consisting of the 2 - layer SiO_2/PSi/Si device discussed in the previous section, with an additional homogeneous gold layer on top. The homogeneous gold layer is interesting for the desired study of the hybrid structure consisting of the interferometer with NA array, as it constitutes a limit case for the NA array outside plasmon resonance. Again, the detailed description of the phase-matching model for this case is presented in Appendix A.

Here, we propose a simpler approach enabling direct explanation of the fringe behavior.

The 3 - layer structure is labeled as "Au/SiO_2/PSi/Si". As shown in Fig 3.3.8 (*a*), the gold layer is 30 nm thick, which is equivalent to the thickness of the fabricated NAs. The real part and imaginary part of the gold refractive index are shown in Fig 3.3.8 (*c*) and (*d*), respectively, where the dots are values from literature [3.7] and the red lines are linear fits

used in the following. The interferometer consists of a PSi layer with 5.66 µm thickness and with the refractive index shown in Fig 3.3.8 (*b*), which is deduced from experimental micro - R spectrum. As before, the silica layer is 80 nm - thick and it has the refractive index presented previously in Fig 3.3.5.

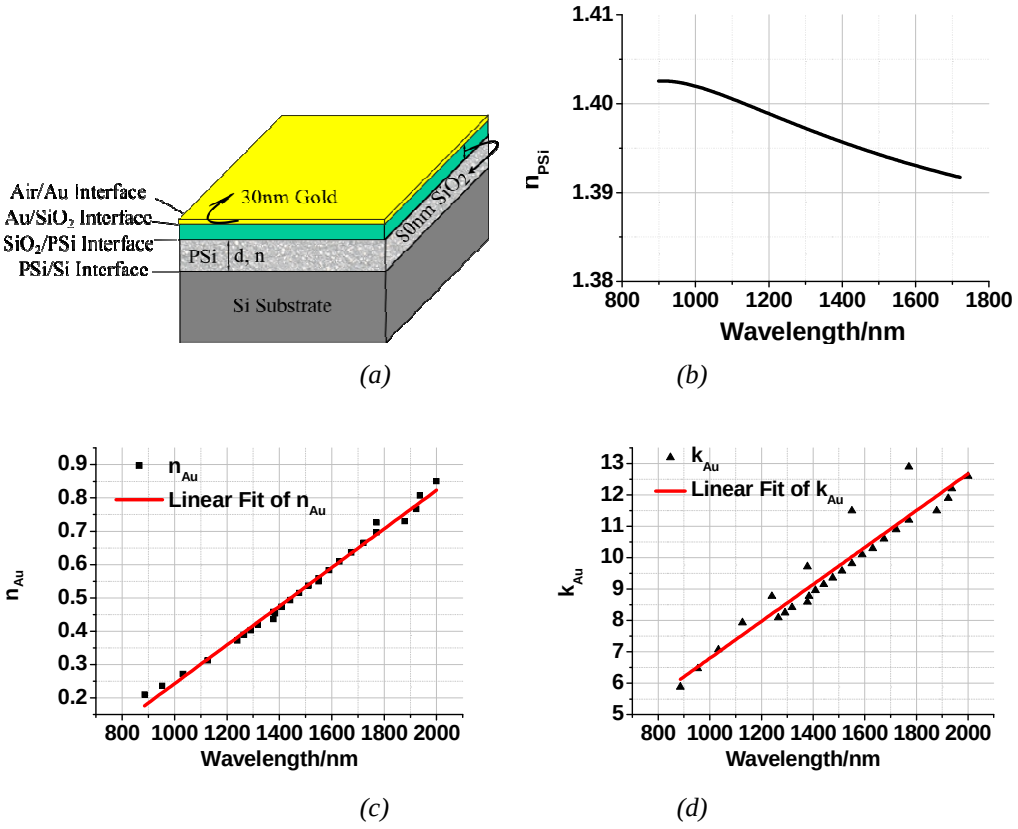

Fig 3.3.8 (a) Schematic view of the 3 - layer system Au/SiO₂/PSi/Si; (b) Refractive index of PSi; (c) Real part Re(nAu) and (d) imaginary part Im(nAu) of Au refractive index from Palik model

In the case of the gold layer, the real part Re (n_{Au}) is still responsible for variations of the optical path, whereas the non-negligible imaginary part of refractive index will induce additional absorption, which introduces an extra phase shift at the interface, i.e. $\Delta\varphi_{\mathrm{int}\,erface} \neq 0$. The value of $\Delta\varphi_{tot}$ varies with that of the real part and imaginary parts of the refractive index, with $-\pi < \Delta\varphi_{tot} < 0$ (See Appendix A). In order to develop the 3 - layer model, we follow the same principle as presented in section 3.3.2. Here, the model becomes:

$$\frac{4\pi\left(n_{PSi}d_{PSi}+n_{SiO_2}d_{SiO_2}\right)}{\lambda_{3\max}}+\Delta\varphi_{tot}=2m\pi \qquad \text{(EQ-3-3-12)}$$

$$\Delta\varphi_{tot} = 4\pi \frac{\mathrm{Re}(n_{Au})}{\lambda_3} d_{Au} + \Delta\varphi_{\mathrm{int}\,erface} \qquad \text{(EQ-3-3-13)}$$

where λ_{3max} is the wavelength corresponding to the maximum of reflectivity $R = R_{max}$ for each order m. Comparing to the model for the 2 - layer system SiO_2/PSi/Si that was given in (EQ-3-3-9):

$$\frac{4\pi(n_{PSi} d_{PSi} + n_{SiO_2} d_{SiO_2})}{\lambda_{2\,max}} = 2m\pi$$

For each fringe order m, we have:

$$\frac{n_{PSi} d_{PSi} + n_{SiO_2} d_{SiO_2}}{\lambda_{2\,max}} = \frac{n_{PSi} d_{PSi} + n_{SiO_2} d_{SiO_2}}{\lambda_{3\,max}} + \frac{\Delta\varphi_{tot}}{4\pi} \qquad \text{(EQ-3-3-14)}$$

As discussed in details in Appendix A, we have $\Delta\varphi_{tot} < 0$, which leads to:

$$\lambda_{3\,max} < \lambda_{2\,max}$$

Hence, the fringes should experience a blue shift upon addition of the homogeneous gold layer on top of the interferometer.

3.3.3.2 Application to experimental structures

Experimentally, the presence of the gold layer makes the optical characterization more difficult due to the 'Mirror effect' of gold. As a result, the interferometric properties of the underlying two - layer device are less visible on the reflectivity spectrum. As the micro - R spectra showed more pronounced fringes than the macro - R ones, in this particular case we chose to perform the analysis using the experimental micro - R spectrum shown in Fig 3.3.9. However, we have to keep in mind that this might lead to some discrepancies in the position of the fringes due to the smaller spot and the large span of incidence angles induced by the objective. Both experimental (blue curve in Fig 3.3.9 (*a*)) and TMM simulation spectra (red curve) show interferometric oscillations on the high-reflectivity signal induced by the 'Mirror effect'. In spite of the smaller fringe amplitude observed in the experimental spectrum, the wavelength positions of the reflectivity maxima still show a good agreement between

experiment and simulation, as depicted in Fig 3.3.9 (b). The positions of the initial 2 - layer interferometer are also plotted, in order to demonstrate the observation of the blue shift.

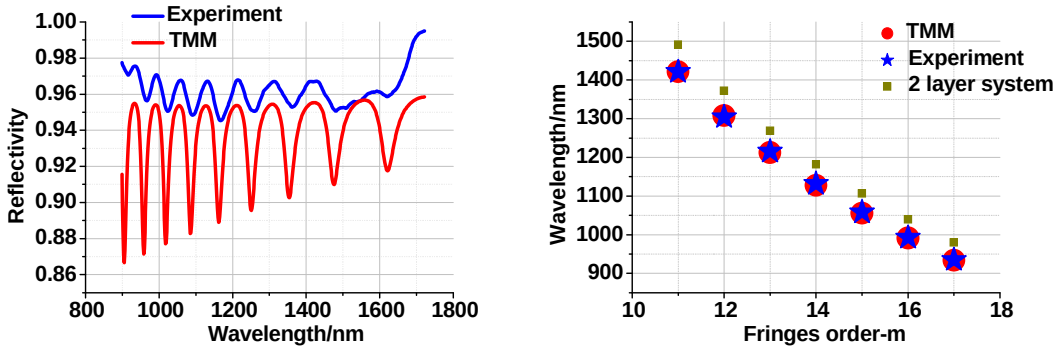

(a) *(b)*

Fig 3.3.9 (a) Reflectivity of Au/SiO2/PSi/Si; (b) Wavelength vs. Fringes order deduced from the reflectivity spectra

If we consider that there is a good agreement between the phase matching model and the values deduced from the reflectivity spectra, as was demonstrated in the case of the 2 - layer system, we can determine the total phase shift at the interface $\Delta\varphi_{tot}$ by inserting the values deduced from the reflectivity spectra into the expression given in (EQ-3-3-12):

$$\Delta\varphi_{tot} = 2m\pi - \frac{4\pi(n_{PSi}d_{PSi} + n_{SiO_2}d_{SiO_2})}{\lambda_{3\max}} \qquad \text{(EQ-3-3-15)}$$

The values of $\Delta\varphi_{tot}$ are presented in Fig 3.3.10 for both TMM simulation and experimental results.

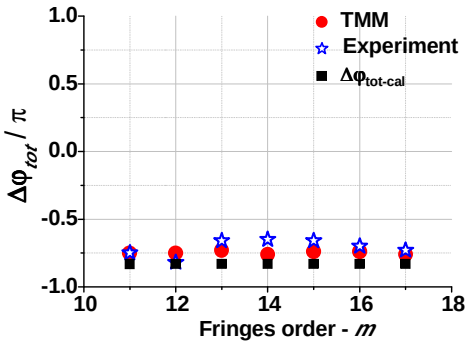

Fig 3.3.10 Phase shift induced by the metal absorption, calculated from the values deduced from reflectivity results and the phase matching model for the system Au/SiO2/PSi/Si For comparison, the values of the phase shift extracted from the exact model presented in Appendix A have been reported, considering the wavelengths corresponding to the fringe orders.

In spite of the small discrepancies between TMM and experimental results, Fig 3.3.10 shows that in both cases the value of $\Delta\varphi_{tot}$ is almost constant and about -0.75π over the whole wavelength range of interest. This result is in very good agreement with the calculation deduced from Fresnel equations in the Appendix, also shown in Fig 3.3.10 for comparison.

3.3.4 Equivalent layer of Bowtie NAs array

From a geometric point of view, the bowtie NA array can be viewed as a layer consisting of air containing gold structures, as depicted in Fig 3.3.11. Such a layer can be equivalent to an extra thin film placed on top of SiO_2/PSi/Si, building a new 3 - layer device, which is labeled as "NAs/SiO_2/PSi/Si" (System 1). In order to study the influence of such a layer using the phase matching model, it is crucial to determine the effective optical properties of this equivalent layer.

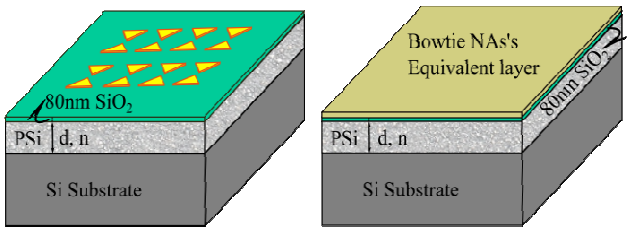

Fig 3.3.11 Schematic view of the hybrid device corresponding to System 1. This structure can be viewed as a 3 - layer system where the NA array is supposed to be equivalent to a homogeneous layer with same properties.

Similarly, the structure consisting of NA array on SiO_2/Si substrate (System 2), which has been discussed at the beginning of this chapter, can also be seen as system constituted of a single layer of SiO_2 with an equivalent layer corresponding to the NA array placed on top. Such a system, labeled as "NAs/SiO_2/Si", is of high interest for a simpler study of the behavior of the NA array. It is illustrated in Fig 3.3.12.

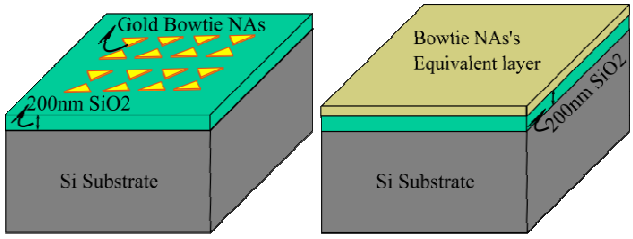

Fig 3.3.12 Schematic view of the NAs/SiO_2/Si system, corresponding to System 2

The first step in the study presented in the following is the determination of the refractive index variations of the NAs equivalent layer, considering the case of System 2 shown in Fig 3.3.12.

3.3.4.1 Dielectric function of Bowtie NA array

The Drude model

The optical properties of metals can be described by a complex dielectric constant ε_{metal} that depends on the frequency of the light.

$$\varepsilon_{metal} = \mathrm{Re}(\varepsilon_{metal}) + i\,\mathrm{Im}(\varepsilon_{metal}) \qquad \text{(EQ-3-3-16)}$$

$$n^2 = \varepsilon_{metal}; \qquad n = \mathrm{Re}(n) + i\,\mathrm{Im}(n) \qquad \text{(EQ-3-3-17)}$$

where n is the effective refractive index of the metal. According to the simple Drude model [3.8, 3.9], the interaction of metals with electromagnetic radiation is largely dominated by the free conduction electrons moving within the bulk of material. The Drude-Sommerfeld model [3.9] gives quite accurate results for dielectric constants of gold in the infrared regime, as expressed in (EQ-3-3-18):

$$\varepsilon(\omega) = 1 - \frac{\omega_p^2}{\omega^2 + i\Gamma\omega} \qquad \text{(EQ-3-3-18)}$$

where $\omega_p^2 = \dfrac{ne^2}{m_e\varepsilon_0}$ is the volume plasma frequency, m_e and e are the effective mass and charge of the free electrons, respectively, ω is the frequency of the applied electric field, ε_0 is the permittivity of vacuum. $\Gamma = v_F / l$ is related to the damping term, v_F is the Fermi velocity, and l is the mean free path of electrons between scattering events. In the case of gold, the value of ω_p is $1.38*10^{16}$/s, and Γ is $1.075*10^{14}$/s [3.11, 3.12].

In the visible range, the optical properties of metals mainly depend on the interband transition of bound electrons from lower bands into the conduction band. This contribution can be described as [3.9]

$$\varepsilon(\omega) = \varepsilon_\infty + \frac{\tilde{\omega}_p^2}{\omega_0^2 - \omega^2 - i\gamma\omega}; \ \mu = 1 \qquad \text{(EQ-3-3-19)}$$

where ε_∞ is the high-energy dielectric constant, γ is the damping constant describing radiative damping in the case of bound electrons; $\tilde{\omega}_p$ is introduced as a plasma frequency in analogy to the Drude model but with: $\tilde{\omega}_p = \sqrt{\tilde{n}e^2 / m\varepsilon_0}$, with $\tilde{n}$ the density and m the effective mass of bound electrons, respectively; $\omega_0 = \sqrt{\alpha / m}$ with α the spring constant [3.9].

Fig 3.3.13 shows the contribution to the dielectric constant of gold that derives from its bound electrons when one interband transition is taken into account, according to literature [3.9]. For its real part, a dispersion-like behavior is observed; for its imaginary part, a clear resonant behavior is observed, which is very similar to that resulting from the interaction of metal nanostructures with light. As we will discuss in the next paragraph, this observation allows us to model the NAs array by a homogeneous metallic layer using equation 3-3-19 with specific values for ε_∞, $\tilde{\omega}_p$, γ *and* ω_0

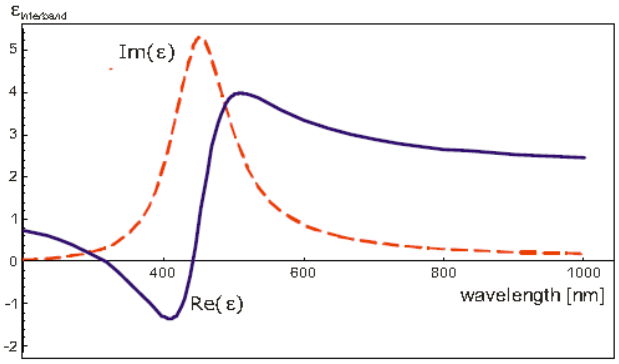

Fig 3.3.13: Dielectric function of gold attributed to bound electrons. The parameters used are $\omega_p = 4.5\times10^{14}\,/\,s$, $\gamma = 8.35\times10^{16}\,/\,s$, *and* $\omega_0 = 2\pi c/\lambda$, *with* λ*=450 nm. The solid blue line is the real part; the dashed red curve is the imaginary part of the dielectric function due to bound electrons. Extracted from [3.9]*

Dielectric function of NA array

As discussed in Chapter 1, when considering metal particles under the excitation of external electromagnetic field, the electron gas confined in three sub-wavelength dimensions shifts from its original site. The overall displacement of the electrons with respect to the positively charged lattice leads to a restoring force, which in turn gives rise to specific plasmon resonances that are depending on the geometry of the particle and local environment. For

particles of suitable shape, extreme charge accumulations can locally occur, which are accompanied by strongly enhanced optical field.

In the case of bowtie NAs, Sundaramurthy A. et al. [3.10] have built a physical model based on current distribution in the NAs to investigate the variation of the resonant wavelength depending on the gap under special polarization and explain the basis for the field enhancement. According to their analysis, when the gap is small, there is a strong displacement current flowing in the air gap between the 2 triangles. This model leads to the interpretation that the electron displacements between the 2 nano-triangles realize, to some extent, "electron transitions" between the particles. Therefore, to simulate the optical properties of bowtie NAs it is possible to adapt the model for metal dielectric constant with interband transition of bound electrons that was given in (EQ-3-3-19).

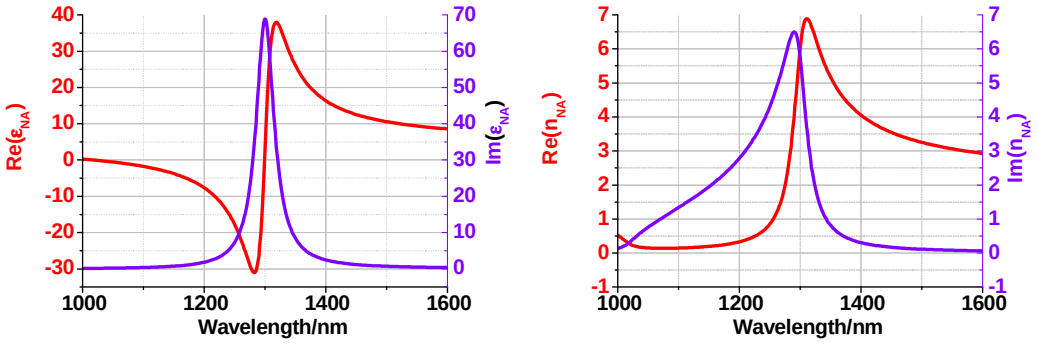

(a) *(b)*

Fig 3.3.14 (a) Effective dielectric constant of NAs: real part (red line – left y-axis) and imaginary part (purple line – right y-axis); (b) refractive index of NAs: real part (red line – left y-axis) and imaginary part (purple line – right y-axis).

In order to determine the parameters ε_∞, ω_p and γ entering the model for NA dielectric function, a fit of these 3 parameters was performed by confronting experimental spectra with results obtained from TMM simulations using the dielectric function deduced from the model. The best fit was found for the following parameters: $\varepsilon_\infty = 3$ [3.8], $\omega_p = 2\times10^{15}/s$, $\gamma = 4\times10^{13}/s$ and a resonant wavelength $\lambda_0 = 1300\ nm$ (corresponding to $\omega_0 = 1.43\times10^{15}/s$). The variations of ε and n for the resulting NA dielectric function are shown in Fig 3.3.14. They show very similar behavior to the dielectric function for metal presented in Fig 3.3.13, with giant variations around the resonant wavelength at 1300 nm both for the real part (red curves) and the imaginary part (purple curves) of the dielectric constant and refractive index.

Hence, according to the phase matching model analysis presented in the previous sections, we can expect very interesting behavior of the fringe positions upon addition of an equivalent layer with such optical property on top of the interferometer, depending on the wavelength and the corresponding value of refractive index.

Effect of silica thickness in NAs/SiO_2/Si system

The study of the interaction between the NA array and the SiO_2/PSi/Si interferometer will be performed using a comparison with the "unperturbed" system (system 2) consisting of an array of NAs with similar refractive index environment but without interferometer. Hence, it is important to demonstrate that the SiO_2 layer of the NAs/SiO_2/Si structure is only providing the desired refractive index environment without yielding any undesired interference effect that would influence the optical properties of the NA array.

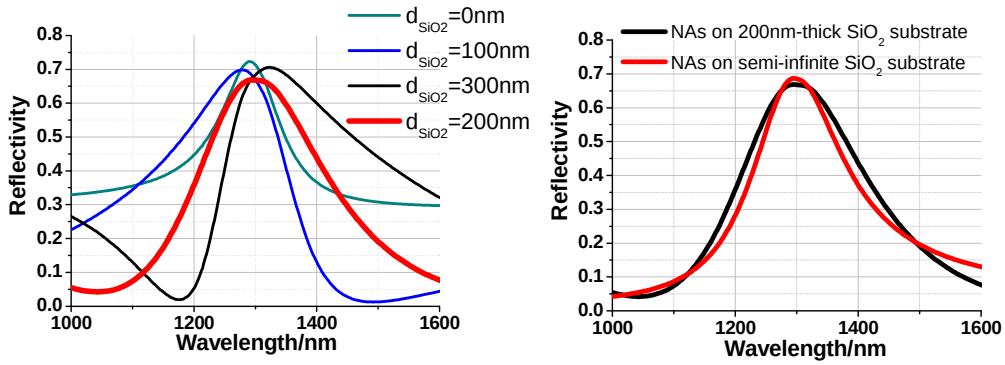

(a) *(b)*

Fig 3.3.15 (a) Reflectivity spectrum of NAs/SiO_2/Si with varying thickness of silica layer; (b) Comparison between the reflectivity of NAs/SiO_2/Si with 200 nm SiO_2 (black curve) and of NAs on semi-infinite SiO_2 substrate (red curve)

Using the parameters deduced above for the NA equivalent layer, which were shown in Fig 3.3.14, the reflectivity spectrum of NAs/SiO_2/Si was computed for a large range of layer thicknesses. As illustrated in Fig 3.3.15 (*a*), the NA resonance line shape is strongly varying with the SiO_2 thickness, showing the influence of the SiO_2 layer. As expected, the desired Lorentz shape with central symmetry is observed for 0 nm thickness, however, the refractive index environment in this case is different from the interferometer system. With increasing SiO_2 thickness, the resonance shape becomes highly asymmetrical, until a symmetrical shape is observed again for a thickness of 200 nm. For larger thicknesses, the resonance shape is again asymmetrical. Hence, a SiO_2 thickness around 200 nm seems to be the best choice to minimize the influence of the finite SiO_2 layer on the properties of the NA array. This is

demonstrated in Fig 3.3.15 (*b*), where the spectrum for 200 nm SiO_2 thickness (black curve) shows good agreement with the unperturbed resonance of the same bowtie NAs on semi-infinite SiO_2 substrate (red curve).

3.3.4.2 Multi-layer interference model for NAs/SiO_2/PSi/Si

We now have all the elements to investigate the hybrid device NAs/SiO_2/PSi/Si (System 1), which is presented in the following. The properties determined for this system will be the object of a double comparison: on one hand with the SiO_2/PSi/Si 2 - layer system (System 3) and on the other hand with the NAs/SiO_2/Si (System 2).

Phase matching condition

The exact description of phase matching condition for the NAs/SiO2/PSi/Si is presented in Appendix A. Here, we will follow the same simplified approach as in the case of the homogeneous gold layer discussed previously.

Since the dielectric functions and thicknesses have been determined for each layer of the NAs/SiO_2/PSi/Si system, it is possible to write the phase matching model for this system as was discussed in section 3.3.3.

$$\frac{4\pi\left[n_{PSi}d_{PSi}+n_{SiO_2}d_{SiO_2}+\mathrm{Re}(n_{NA})d_{NA}\right]}{\lambda_{3\max}}+\Delta\varphi_{\mathrm{int}\,erface}=2m\pi \quad \text{(EQ-3-3-20)}$$

In order to investigate the behavior of the fringes, we compare again to the model for the 2-layer system SiO_2/PSi/Si that was given in (EQ-3-3-10):

$$\frac{4\pi\left(n_{PSi}d_{PSi}+n_{SiO_2}d_{SiO_2}\right)}{\lambda_{2\max}}=2m\pi$$

This leads to the following relation:

$$4\pi\left(n_{PSi}d_{PSi}+n_{SiO_2}d_{SiO_2}\right)\left(\frac{1}{\lambda_2}-\frac{1}{\lambda_3}\right)=\Delta\varphi_{tot} \qquad \text{(EQ-3-3-21)}$$

with, $\Delta\varphi_{tot}=4\pi\dfrac{\mathrm{Re}(n_{NA})}{\lambda_3}d_{NA}+\Delta\varphi_{\mathrm{int}\,erface}$

From (EQ-3-3-21) we can deduce the following behavior:

- There is a blue shift when $\lambda_3 < \lambda_2$, i.e. $\Delta\varphi_{tot} < 0$.
- There is a red shift when$\lambda_3 > \lambda_2$, i.e. when $\Delta\varphi_{tot} > 0$.

Hence, the behavior of the fringes is strongly depending on the respective values of $\Delta\varphi_{\text{int}\,erface}$ and Re(n_{NA}). The strong variation of dielectric function of NA equivalent layer over the wavelength range of interest induces a strong variation of the value of $\Delta\varphi_{\text{int}\,erface}$. As described in Appendix A, the total value of $\Delta\varphi_{tot}$ can be determined from the NA dielectric function using Fresnel equations. The corresponding variations are shown in Fig 3.3.16.

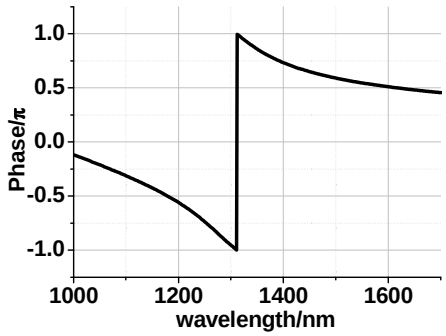

Fig 3.3.16 Variations of $\Delta\varphi_{tot} = 4\pi\dfrac{\text{Re}(n_{NA})}{\lambda_3}d_{NA} + \Delta\varphi_{\text{int}\,erface}$ *deduced from the dielectric function of the NA equivalent layer presented in Fig 3.3.14.*

The variations shown in Fig 3.3.16 induce different behaviors depending on the wavelength range:

- Below resonance (for $\lambda < 1300$ nm): $\Delta\varphi_{tot} < 0$. In this region, a blue shift of the fringes is expected.
- At resonance (for $\lambda \approx 1300$ nm), $\Delta\varphi_{tot}$ abruptly varies from $-\pi$ to $+\pi$;
- Above resonance (for $\lambda > 1300$ nm): $\Delta\varphi_{tot} > 0$. In this region, a red shift of the fringes is expected.

Simulation of the reflectivity spectrum of the hybrid structure

The behavior predicted above has been compared to TMM simulations of the reflectivity spectrum of the NAs/SiO_2/PSi/Si structure, considering the variations of effective refractive index shown in Fig 3.3.14 (*b*) for the NAs equivalent layer. The thickness of this layer is 30 nm. The underlying SiO_2/PSi/Si system has the same parameters as the one discussed in section 3.3.3, with the refractive index shown in Fig 3.3.8 (*b*) and a thickness of 5.66 µm for the PSi layer, and the same parameters as in the previous investigations for SiO_2 and Si.

The reflectivity spectrum of the hybrid structure is shown in Fig 3.3.17. For comparison, the reflectivity spectra of the SiO_2/PSi/Si 2-layer device (black curve) and of the NAs/SiO_2/Si system (blue curve) have been simulated as well. We can see that the NAs/SiO_2/PSi/Si hybrid device (red curve) exhibits both the interferometric oscillation of SiO_2/PSi/Si and the plasmonic resonance behavior of NAs/SiO_2/Si.

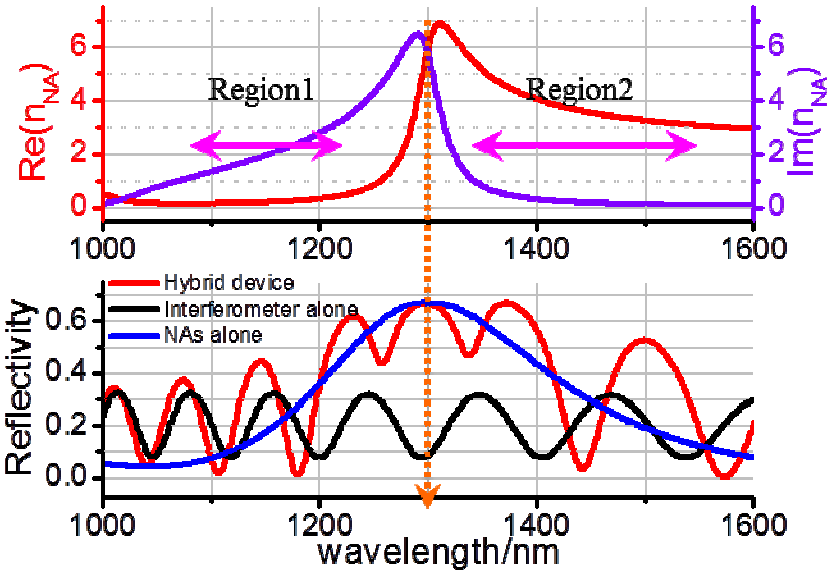

Fig 3.3.17 (a) Refractive index of the NA equivalent layer and (b) Reflectivity of NAs/SiO_2/PSi/Si (red curve), SiO_2/PSi/Si (black) and NAs/SiO_2/Si (blue)

Looking in more details at the spectra of Fig 3.3.17, we can make the following observations:

- At resonance – within the half-width wavelength range of NAs resonance – the fringes of the hybrid structure are lifted up to higher values, which is attributed to the field enhancement effect of NAs.

- Outside resonance: the fringe contrast is higher than in the case of the 2 - layer device alone. This can be related to the value of effective refractive index of NAs comparing to n_{air} and n_{PSi}.
- Over the whole spectral range, the fringes are shifted with respect to the interferometer spectrum, due to the existence of the NA equivalent layer. In region 1 of the spectrum (below resonance), a clear blue shift can be observed, whereas far above the resonance in region 2 of the spectrum, the fringes are red shifted. This is in agreement with the above predictions deduced from Fig 3.3.16. However, around the resonance, the fringe pattern seems to indicate the appearance of an extra fringe. In order to investigate this additional feature, a further analysis of the fringe orders has been performed and is presented in the following.

Analysis: Observation of a "fringe splitting" at resonance

The fringe orders on the reflectivity spectra for the interferometer have been calculated using (EQ-3-3-10). Then, in order to determine the fringe orders and $\Delta\varphi_{tot}$ for the hybrid structure, (EQ-3-3-20) has been used, considering that the absolute phase shift should be smaller than π. The orders could be easily identified and are reported with red color in Fig 3.3.17 (*b*). The results are summarized in Table 3.1, which gives a comparison of the fringe positions for the hybrid structure and the interferometer alone, for each order *m*.

λ_{2max} / nm	m	λ_{3max} / nm	$\Delta\varphi_{tot}$ / π	Δλ / nm	
1014.45	16	1011.16	-0.064	-3.29	Region 1
1081.72	15	1073.53	-0.184	-8.19	
1156.83	14	1145.43	-0.267	-11.4	
1244.53	13	1231.57	-0.263	-12.96	
1347.77	12	1296.24	0.065	-51.53	
		1371.86	0.460	24.09	Region 2
1467.79	11	1499.61	0.493	31.82	
1613.54	10	1646.58	0.438	33.04	

Table 3.1 Comparison between the fringe positions for the interferometer and the hybrid device, deduced from the PMM model. The orange line indicates the position of the NA resonance..

From Table 3.1, we can draw the following conclusions:

- Two spectral regions can be identified :
  - In Region 1 of the spectrum ($\lambda < \lambda_{NA}$), where Im (n_{NA}) > Re (n_{NA}) with Im (n_{NA}) strongly increasing and Re (n_{NA}) almost constant (Re(n_{NA}) ~ 0), the induced value of $\Delta\varphi_{tot}$ is increasingly negative ($-\pi < \Delta\varphi_{tot} < 0$) and the fringes experience a blue shift, similarly to the case of homogenous gold layer.
  - After resonance in region 2 of the spectrum, where Im (n_{NA}) decreases almost to 0 and Re (n_{NA}) is much larger than n_{air} and n_{SiO2}, the total phase shift is positive. This induces a red shift of fringes due to the increase of total optical path.
- At resonance, we can observe an interesting phenomenon: there are 2 fringes with the same order $m = 12$. It means that the plasmonic resonance of the NA array induces a degeneration of the fringe order. This can be related to the huge simultaneous variations of Re (n_{NA}) and Im (n_{NA}): while Re (n_{NA}) suddenly increases to a maximum, on the opposite, Im (n_{NA}) suddenly decreases from maximum to minimum. Similar splitting phenomena have been observed in the literature [3.12]. In particular, Ameling *et al* demonstrated a large spectral splitting of Fabry-Perot microcavity mode induced by plasmon resonance in nanowire pairs, when positioning the nanowire pairs at the maxima of electric field within the cavity [3.12]; this phenomenon was attributed to strong coupling between the cavity mode and the plasmon resonance. In analogy to this work, we can conclude that the splitting observed in our interference spectrum is a good indication of strong coupling between the interferometer and the NA array. A complete demonstration of the strong coupling could be performed via observation of the characteristic anti-crossings between the interferometer modes and the NA resonance, and will be the subject of further studies.

Influence of the interferometer on the splitting

The splitting of fringes at resonance, which has been highlighted in the previous section, may be dependent on the relative positions of the fringes with respect to the NA resonance, i.e., on the parameters of PSi layer. In order to verify this assumption, TMM simulations have been performed with varying PSi parameters, while keeping the parameters of the other layers

constant and identical to the ones used for Fig 3.3.17. Two different comparisons have been performed:

- PSi index variation with constant layer thickness: $d_{PSi} = 5\ \mu m$ and $n_{PSi} = 1.4$, 1.5, 1.6 and 1.7;
- PSi layer thickness variation with constant refractive index: $n_{PSi} = 1.5$ and $d_{PSi} = 5$, 6 and 7 µm.

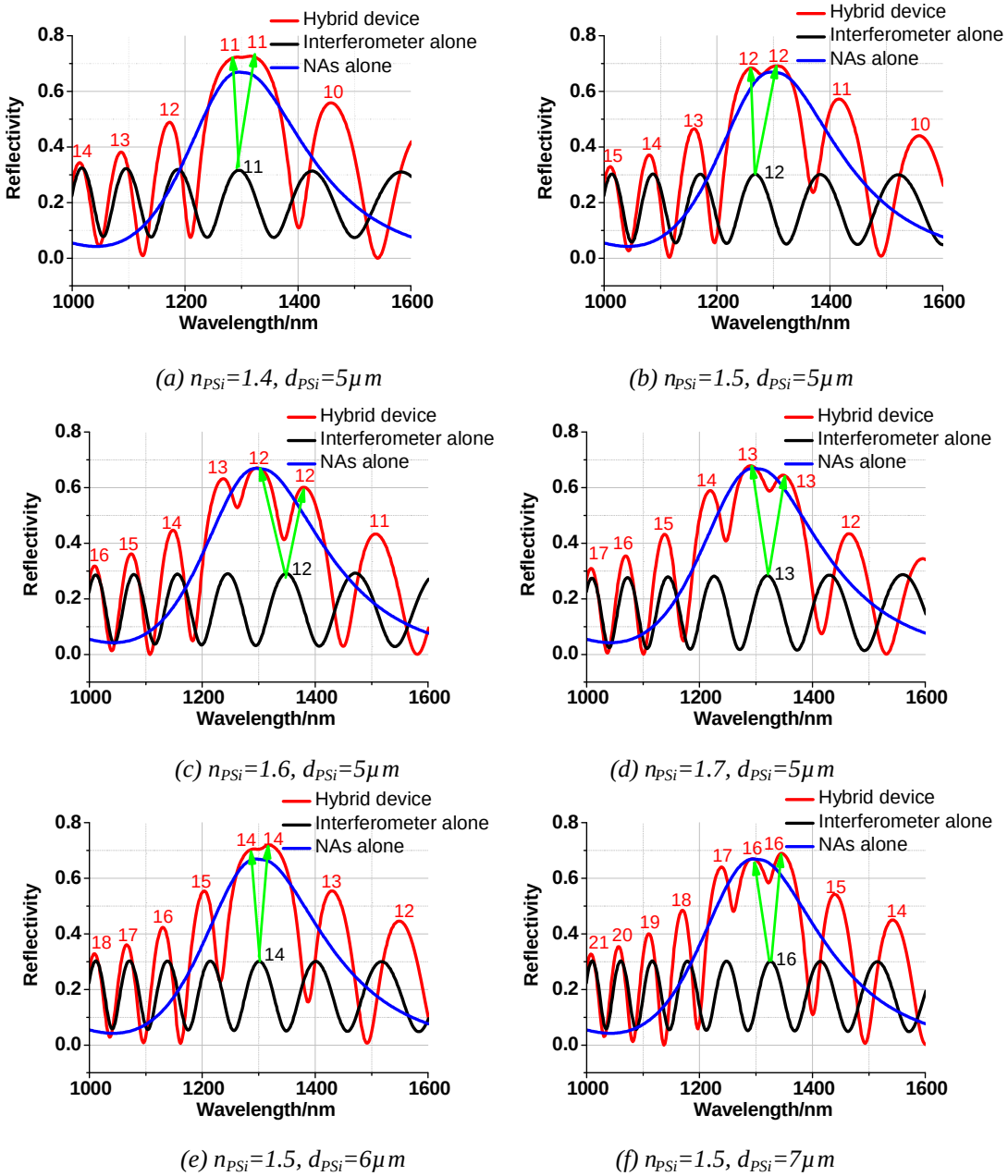

(a) n_{PSi}=1.4, d_{PSi}=5µm *(b) n_{PSi}=1.5, d_{PSi}=5µm*

(c) n_{PSi}=1.6, d_{PSi}=5µm *(d) n_{PSi}=1.7, d_{PSi}=5µm*

(e) n_{PSi}=1.5, d_{PSi}=6µm *(f) n_{PSi}=1.5, d_{PSi}=7µm*

Fig 3.3.18 Reflectivity of System 1 with varied refractive index for PSi layer (a: n_{PSi} = 1.4; b: n_{PSi} = 1.5; c: n_{PSi} = 1.6; and d: n_{PSi} = 1.7, d_{PSi} = 5 µm) and Reflectivity of hybrid device with varied thickness for PSi layer (b: d_{PSi} = 5 µm; e: d_{PSi} = 6 µm and f: d_{PSi} = 7 µm; n_{PSi} = 1.5); the one of interferometer alone (black curve) with same PSi layer with hybrid device and one of NAs alone (blue curve) are accompanied in each figure.

The reflectivity spectra for all the cases mentioned above are shown in Fig 3.3.18, where the spectra in Fig 3.3.18 (*a*), (*b*), (*c*) and (*d*) show the variation with varying refractive index, and the spectra in Fig 3.3.18 (*b*), (*e*) and (*f*) show the variation with varying thickness. The reflectivity spectra of the SiO_2/PSi/Si interferometer and of the NAs/SiO_2/Si System are drawn in black and blue, respectively, while the red curves show the spectra of the hybrid device.

Comparison between the spectra shown in Fig 3.3.18 leads to the following observations:

- In each case, there is always a fringe of interferometer – λ'_{2max} – which is split into 2 fringes – λ'_{3max} and λ''_{3max} – due to the strong coupling between NAs and the interferometer at NA resonance. The relative positions of λ'_{3max} and λ''_{3max} are on either side of λ'_{2max} and of the resonance wavelength. Here, we assume that λ'_{3max} corresponds to the smaller wavelength. The corresponding wavelength values and splitting amplitude $\Delta\lambda_3$ are summarized in Table 3.2.

- The order *m* of the split fringe depends on the optical path within the interferometer, since the split fringe is always the one closest to the NA resonance wavelength.
- The wavelength amplitude of the splitting seems to be dependent on the optical path within the interferometer.

(n_{PSi}, d_{PSi})	λ'_{2max}/nm	λ_{3max}/nm	$\Delta\lambda_3$/nm
(1.4, 5)	1294.63	1293.02	22.57
		1315.59	
(1.5, 5)	1267.18	1260.71	46.82
		1307.53	
(1.6, 5)	1244.53	1296.24	83.64
		1379.88	
(1.7, 5)	1320.42	1289.79	57.98
		1347.77	
(1.5, 6)	1301.08	1291.4	27.41
		1318.81	
(1.5, 7)	1325.25	1294.63	51.53
		1346.16	

Table 3.2 Wavelength values of split fringes for each case shown in Fig 3.3.18.

In order to perform the analysis in detail, in the following we consider the phase differences between the SiO_2/PSi/Si interferometer and the hybrid structure, choosing as a reference the

phase of λ'_{2max} on the interferometer reflectivity spectrum; this means that the relative phase of λ'_{2max} is set to zero. The 2 minima just before and after λ'_{2max}, with respective wavelength $\lambda'_{2min-(m)}$ and $\lambda'_{2min-(m-1)}$, have relative phases $-\pi$ and $+\pi$. Then, the relative phase of the NA resonance wavelength λ_{NA} with respect to λ'_{2max} has been extracted for each case shown in Fig 3.3.18, and reported on the cosine function shown in Fig 3.3.19 (*a*). The refractive index and thickness of the corresponding PSi layer are labeled on the figure as (n_{PSi}, d_{PSi}).

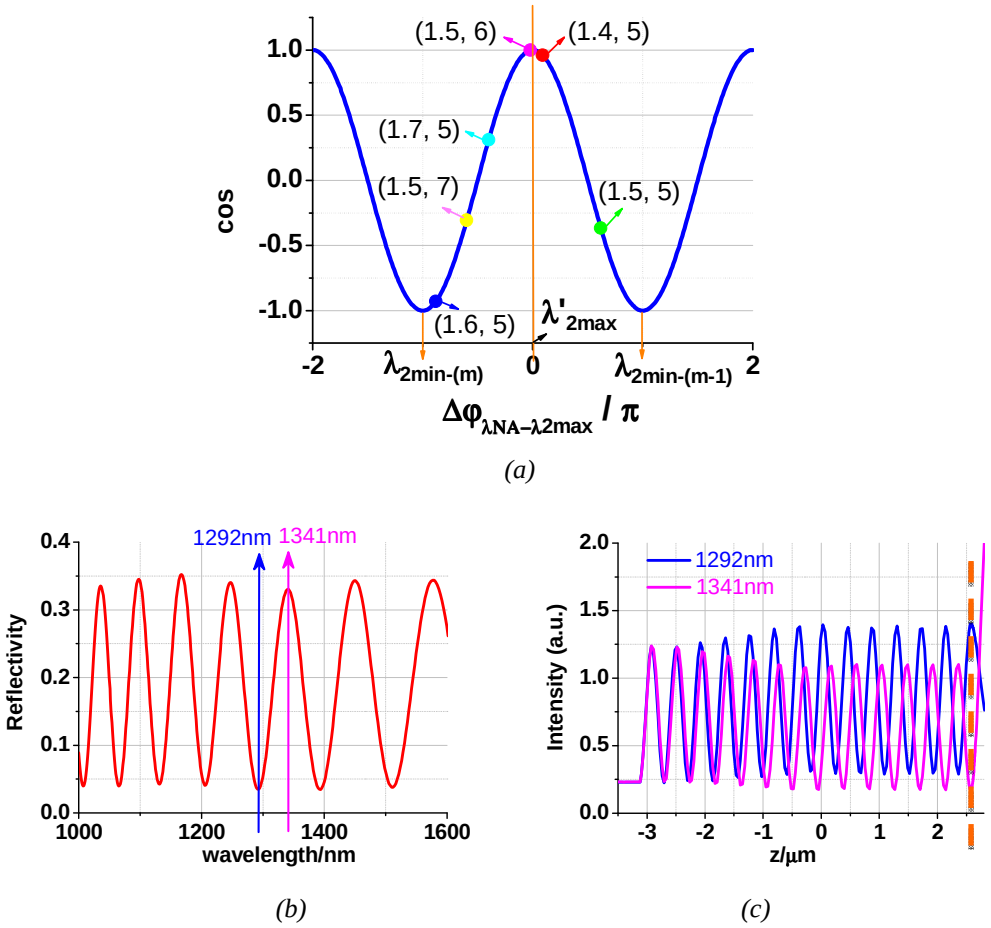

Fig 3.3.19 (a) Illustration of the relative positions of λ_{NA} to λ'_{2max} on a cosine function for the different cases shown in Fig 3.3.18; (b) Reflectivity spectrum of the interferometer with n_{PSi} = 1.52 and d_{PSi} = 5.66μm; (c) Intensity profile E^2 along z (i.e.in the structure depth) for the 2 different wavelengths 1292 nm and 1341 nm, respectively, corresponding to a minimum and a maximum of reflectivity in the spectrum shown in (b).

Fig 3.3.19 (*a*) enables to highlight the following observations:

- If the fringe position of the interferometer is such that λ_{NA} is close to λ'_{2max}, as it the case for the PSi layers with parameters (1.5, 6) or (1.4, 5), the relative phase of λ_{NA} is close to 0 and around the peak of the cosine function; In this case, the wavelength amplitude of the splitting is small, as highlighted in Table 3.2, and the

2 split fringes tend to "merge" into one broad fringe, as can be observed in Fig 3.3.18 (*a*) and (*e*);

- If the fringe position of the interferometer is such that λ_{NA} is close to a minimum λ'_{2min}, as is the case for the PSi layer with parameters (1.6, 5), the relative phase of λ_{NA} is close to $\pm\pi$ and around the dip of the cosine function; In this case, the wavelength amplitude of the splitting is large, as highlighted in Table 3.2 and Fig 3.3.18 (*c*));
- In the other cases corresponding to PSi layers with parameters (1.5, 5), (1.5, 7) or (1.7, 5), the relative phase of λ_{NA} is on the slope of the cosine function, and the wavelength amplitude of the splitting in-between the 2 former cases.

The above analysis, indicates that the largest splitting strength is observed when the fringe position of the interferometer is such that λ_{NA} is close to a minimum λ'_{2min}; on the opposite, the smallest splitting strength is observed when λ_{NA} is close to a maximum λ'_{2max}. In order to understand this point, the electric field intensity (E^2) in the interferometer depth (*z*-direction) has been calculated for 2 different wavelengths, 1292 nm and 1341 nm, corresponding to a minimum and a maximum of reflectivity, respectively. The corresponding reflectivity spectrum and electric field intensity profiles are shown in Fig 3.2.19 (*b*) and (*c*), respectively. The position of the interferometer surface is highlighted by a dashed orange line on the field profiles. It can be observed that the electric field intensity is maximum at the surface when the reflectivity is minimum (at 1292 nm), whereas the electric field intensity is minimum at the surface when the reflectivity is maximum (at 1341 nm). Considering the hybrid structure where the NA is located at the interferometer surface, this means that the NA lies at a maximum of field intensity when the reflectivity of the interferometer is minimum. As the splitting strength is directly related to the coupling strength between the interferometer and the NA, we can conclude that the splitting is the strongest when the overlap between the photonic mode and the plasmonic mode is the strongest, i.e., at a minimum of reflectivity of the interferometer. This result is in perfect agreement with the study by Ameling *et al.* presented earlier.

3.3.4.3 Experimental demonstration

Reflectivity vs. transmission studies

The optical studies performed in this work were done both in reflection and transmission for the 3 systems, as was presented in chapter 2. However, all the discussions so far have been based only on reflectivity spectra. The reason of this choice is presented in the following.

Fig 3.3.20 shows the reflectivity and transmission spectra for the 3 systems, "NAs alone" (system 2), "Interferometer alone" (system 3) and "Hybrid device" (system 1). For both systems 1 and 2, the NAs have the following average parameters: A1 = 510 nm, A2 = 280 nm, and Gap = 20 nm; For systems 1 and 3, the interferometer has the following parameters for the PSi layer: refractive index 1.52 (at λ = 1.5 µm) and thickness 5.66 µm.

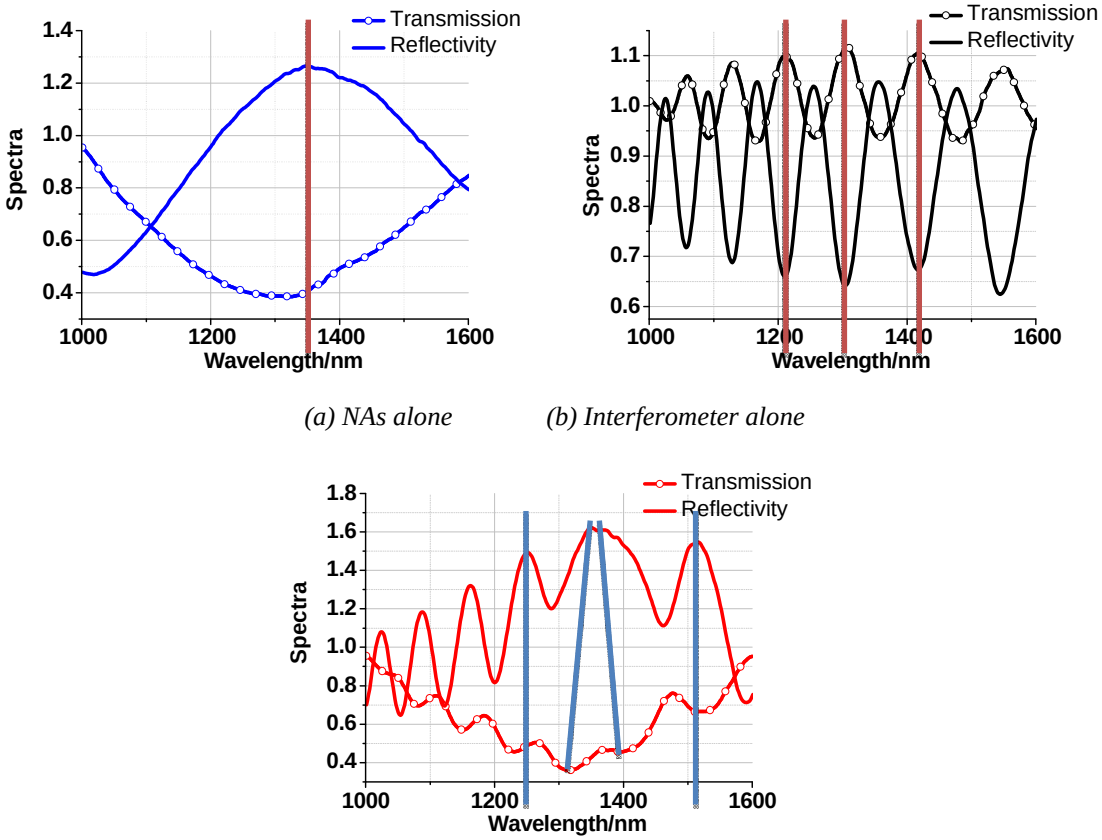

(a) NAs alone *(b) Interferometer alone*

(c) Hybrid device

Fig 3.3.20 Comparison between reflectivity and transmission spectra for the 3 systems

Fig 3.3.20 (*a*) shows the spectra for the case of the NAs alone. The transmission spectrum (blue curve with open circles) exhibits a dip at resonance due to the NAs absorption and

scattering events; the resonant wavelength is around 1300 nm, which is a bit different from the peak position in the reflectivity spectrum (blue curve). This discrepancy is attributed to the unsymmetrical environment for the upper and lower sides of NAs, air and interferometer + Si substrate, respectively. Hence, we prefer to systematically use the reflectivity spectrum to define the resonant wavelength.

Fig 3.3.20 (*b*) shows the spectra for the case of the interferometer alone. For this system, we can see that the position of maxima in the reflectivity spectrum (black curve) perfectly corresponds to the position of minima in the transmission spectrum (black curve with open circles). This agreement is the result of the phase matching condition of the interference. It can also be observed on the figure that the transmission fringes have a smaller amplitude than the reflectivity, which can be explained by the strong absorption in the highly - doped Si substrate. As both spectra provide the same information about fringes position, we prefer to systematically use the reflectivity spectrum to analyse the optical response of this system.

Fig 3.3.20 (*c*) shows the spectra for the case of the hybrid structure. Both of them exhibit the oscillations from the interferometer superimposed on the resonance peak or dip of the NAs, with a smaller fringe contrast for the transmission spectrum (red curve with open circles), similarly to the case of the interferometer alone. However, unlike the case of the interferometer alone, the fringe positions on the reflectivity spectrum (red curve) are slightly different from the positions on the transmission spectrum; the origin of this behaviour is the same as in the case of the NAs alone discussed above: the discrepancy in NA resonance wavelength between the reflectivity and transmission configurations must modify the phase matching condition between both configurations, leading to slightly different fringe positions. For the same reason, the fringe splitting also appears different: a broad peak in the reflectivity spectrum (merging of 2 split fringes), and two well - separated fringes in the transmission spectrum. However, the order of the split fringes is the same in both spectra, and no additional information can be extracted from the transmission spectrum.

Hence, according to the analysis above, the discussion presented in the following is systematically based on the reflectivity spectra.

Experimental observation of the splitting

Optical measurements were performed on several devices with varying parameters for the interferometer and the NA array. In each case, the fringe splitting was observed, with an amplitude $\Delta\lambda_3$ in agreement with the analysis presented in section 3.3.4.2. In order to highlight this behavior, two different comparisons have been selected and are presented in the following: devices with identical NAs and interferometer with different optical path, and devices with identical NAs and interferometer with different parameters but identical optical path.

1. Different optical path

Fig 3.3.21 shows the comparison between 2 hybrid devices with identical resonance λ_{NA} at 1.325 µm. The first device has an interferometer with parameters $n_{PSi} = 1.52$ and $d_{PSi} = 5.66$ µm. The second device has an interferometer with parameters $n_{PSi} = 1.31$ and $d_{PSi} = 5.9$µm. The reflectivity spectrum of each device is shown in Fig 3.3.21 (*a*) and (*b*), respectively, as well as the ones of the corresponding systems of NAs alone and interferometer alone.

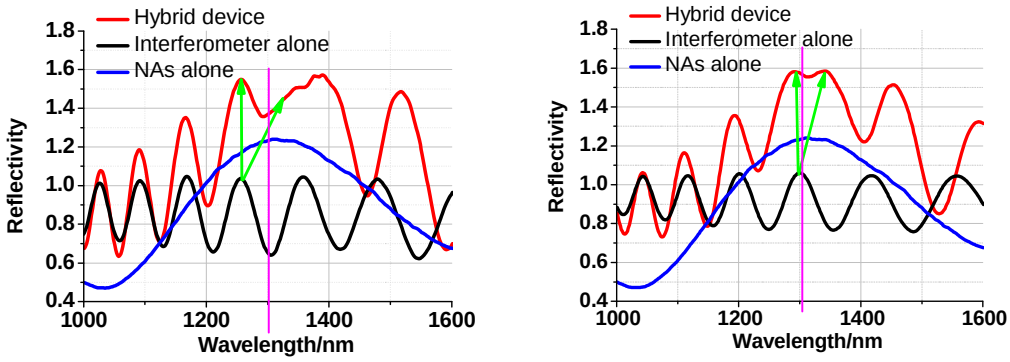

(a) n_{PSi}=1.52, d_{PSi}=5.66µm *(b) n_{PSi}=1.31, d_{PSi}=5.9µm*

Fig 3.3.21 Comparison between the reflectivity spectra (red curves) of 2 hybrid devices with identical NAs and different optical path of PSi layer, and reflectivity spectra of the other corresponding systems: interferometer alone (black) and NAs alone (blue). The pink line indicates the position of the NA resonance.

As can be observed in Fig 3.3.21 (*a*), for the first hybrid device λ_{NA} is located around a minimum of the interferometer reflectivity spectrum. The strong coupling induces a fringe splitting around $\lambda'_{2max} = 1325$ nm, leading to 2 fringes with position $\lambda'_{3max} = 1255$ nm and $\lambda''_{3max} = 1323$ nm and a wide amplitude $\Delta\lambda_3 = 68$ nm.. This is in perfect agreement with

TMM simulations, as was presented in Fig 3.3.18 (*c*). For the second hybrid device, λ_{NA} is located around the maximum of the interferometer reflectivity spectrum. In that case, the fringe splitting is leading to 2 fringes with position λ'_{3max} = 1293nm and λ''_{3max} = 1338nm and a much smaller amplitude $\Delta\lambda_3$ = 45nm. This is in perfect agreement with TMM simulations, as was presented in Fig 3.3.18 (*a*) and (*e*).

2. Same optical path

Fig 3.3.22 shows the comparison between 2 hybrid devices with identical resonance λ_{NA} at 1.38 µm. The first device has an interferometer with parameters n_{PSi} = 1.52 and d_{PSi} = 5.66 µm. The second device has an interferometer with parameters n_{PSi} = 1.78 and d_{PSi} = 4.85µm. The optical paths of the interferometers are the same in both devices. The reflectivity spectrum of each device is shown in Fig 3.3.22 (*a*) and (*b*), respectively, as well as the ones of the corresponding systems of NAs alone and interferometer alone.

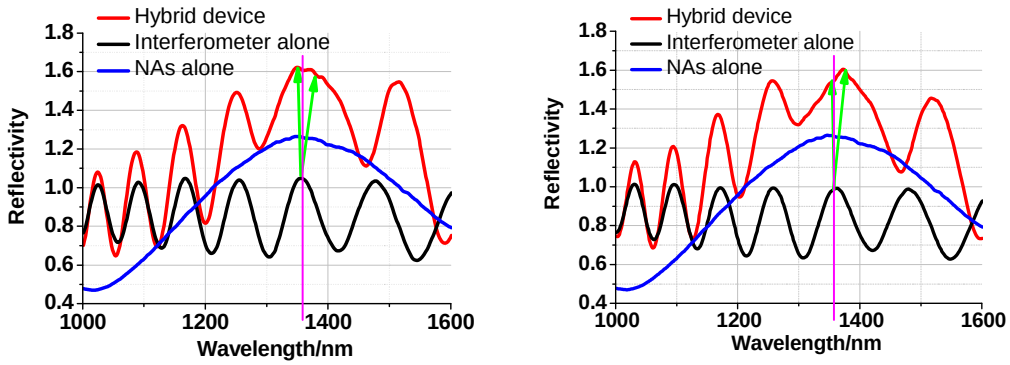

(a) n_{PSi}=1.52, d_{PSi}=5.7µm *(b) n_{PSi}=1.78, d_{PSi}=4.9µm*

Fig 3.3.22 Comparison between the reflectivity spectra (red curves) of 2hybrid devices with identical NAs and same optical path but different (n, d) parameters for the PSi layer, and reflectivity spectra of the other corresponding systems: interferometer alone (black) and NAs alone (blue). The pink line indicates the position of the NA resonance.

As can be observed in Fig 3.3.22, in both cases the fringe position of the interferometer spectrum is the same, and the resonance λ_{NA} is around a maximum of the interferometer spectrum. In both cases, the splitting appears in the form of a broad peak corresponding a very small splitting amplitude. This result demonstrates that the behavior of the split fringes is directly related to the fringe position – i.e., the optical path in the interferometer – as was assumed in the analysis presented in section 3.3.4.2.

Experimental determination of the dielectric function of NAs

The presence of interference fringes on the reflectivity spectrum of the hybrid system enables to perform an experimental approximation of the real part of the NA refractive index, using the phase matching model developed in this chapter. The refractive index can be directly deduced from (EQ-3-3-20), leading to the following expression:

$$\mathrm{Re}(n_{NA}) = \frac{(2m - \Delta\varphi_{\mathrm{int}\,erface})\lambda_{3\max}/4\pi - (n_{PSi}d_{PSi} + n_{SiO_2}d_{SiO_2})}{d_{NA}} \qquad \text{(EQ-3-3-22)}$$

As can be clearly seen in (EQ-3-3-21), the key issue is the determination of the value of $\Delta\varphi_{interface}$, as all other parameters entering this equation are known. Both $\mathrm{Re}(n_{NA})$ and $\Delta\varphi_{interface}$ could be determined by fitting the experimental reflectivity spectra of the NA array and the hybrid structure; in the present case which aims at a proof of principle, the values of $\Delta\varphi_{interface}$ will be extrapolated from a TMM simulation of the experimental structure.

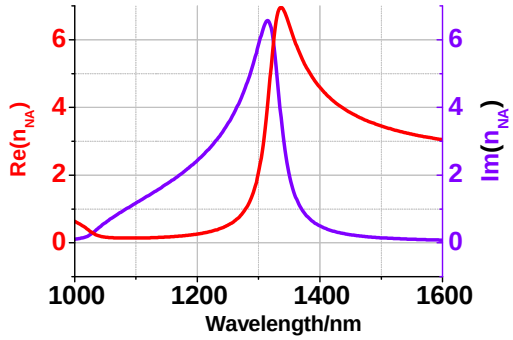

(a) Refractive index of NAs from the model

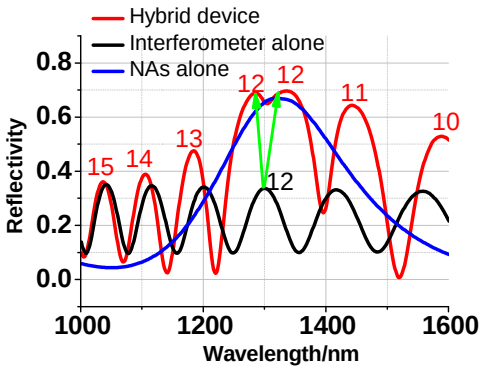

(b) Reflectivity with TMM simulation

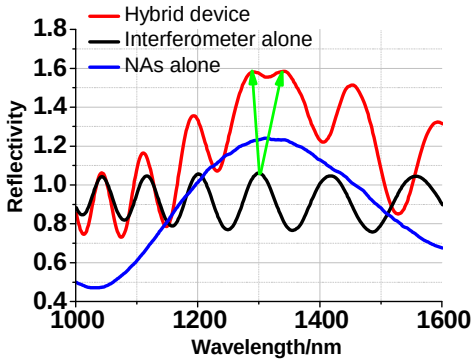

(c) Reflectivity from Experimental result

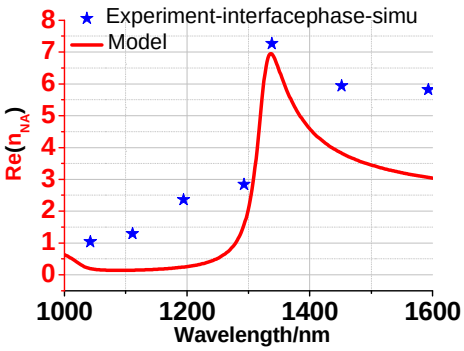

(d) Refractive index of NAs deduced from PMM

Fig 3.3.23 Experimental Determination of refractive index of NAs

The experimental system that is considered in the following has a NA resonance $\lambda_{NA} = 1325$nm, and a PSi layer with parameters $n_{PSi} = 1.31$ and $d_{PSi} = 5.9\,\mu$m. The experimental reflectivity spectra are presented in Fig 3.3.23 (*c*); the corresponding TMM simulations, presented in Fig 3.3.23 (*b*), show very good agreement, both for the NA resonance and the fringe positions, as reported in Table 3.3.

The values of $\Delta\varphi_{interface}$ have been deduced from the analysis of fringe positions on the simulated spectrum, by following the method presented in section 3.3.4.2 (see Table 3.1), and are reported in Table 3.3. Comparing to Table 3.1, we can see that the variations of $\Delta\varphi_{interface}$ are very similar in both cases. Hence, the values of $\Delta\varphi_{interface}$ extracted from the simulations have been inserted into (EQ-3-3-22) together with the data deduced from the experimental spectra, in order to determine the experimental real part of NAs refractive index. The corresponding values are plotted as blue stars in Fig 3.3.23 (*d*), and are reported in Table 3.3. Comparing to the index variations from the model used in the simulations, it can be observed that the experimental values exhibit the same tendency as the values deduced from the Drude model.

$\lambda_{2max\text{-}simu}$ / nm	m	$\lambda_{3max\text{-}simu}$ / nm	$\Delta\varphi_{interface}$ / π	$\lambda_{3max\text{-}exp}$ / nm	Re(n_{NA})
1042.38	15	1037.45	-0.166	1042.38	1.04
1116.06	14	1106.25	-0.305	1111.15	1.29
1200.75	13	1184.50	-0.380	1194.25	2.36
1299.47	12	1284.95	-0.380	1293.02	2.84
		1336.52	-0.030	1338.12	7.27
1416.71	11	1442.27	0.070	1451.85	5.94
1558.29	10	1588.31	0.080	1593.05	5.82

Table 3.3 Fringe order analysis from the simulated structures presented in Fig 3.3.23, and extrapolation of the corresponding values of $\Delta\varphi_{interface}$, used to determine the experimental values of Re(n_{NA}).

3.3.4.4 Conclusions

In this section, we used a phase matching model to investigate the interference fringes of a Fabry-Perot interferometer (PSi/Si) when an extra layer is introduced on top of it. The fringes position is strongly dependent on the dielectric constant of the materials, due to the value of phase shift at the interfaces $\Delta\varphi_{interface}$ and to the variation of total optical path.

If the extra layer is made of a non-absorbing material, like a thin SiO_2 layer, $\Delta\varphi_{\text{int}\,erface} = 0$; at the same time the increase of optical path – induced by $n_{SiO2} > 1$ – leads to a red shift of each fringe. On the opposite, if the layer is made of an absorbing material with small Re(n) and

high Im(n) such as gold, the total phase shift is strongly negative $-\pi < \Delta\varphi_{tot} < 0$; this leads to a blue shift of each fringe.

Considering an extra layer with huge refractive index variations such as a layer equivalent to a NA array, it was demonstrated that the fringe behavior can still be explained by this simple phase matching model; furthermore, a fringe splitting induced by the strong interaction between NAs and interferometer at resonance was put into evidence, with a wavelength amplitude directly related to the phase difference between interferometer and NA at resonance.

Finally, we were able to extrapolate the variations of phase shift at the interface $\Delta\varphi_{interface}$ induced by the NA array; using these values and the phase matching model, we could deduce experimental values for the dielectric constant of the NA array from experimental reflectivity measurements, which show a similar tendency as the variations deduced from the Drude model.

3.4 Hybrid device: Resonator approach

In the previous section, the bowtie NAs array was viewed as an equivalent homogeneous layer added on top of the interferometer. Its refractive index was modeled using a Lorentz function. In the interferometer view, the resonant metallic structures introduce a huge phase variation over the studied wavelength range. The interaction between NAs and interferometer can also be described using the formalism of coupled mode theory (CMT) [3.13]; this complementary approach, which models the NA array as a harmonic oscillator, can provide a faithful description of the global temporal and spectral characteristics of the optical power transfers and storages within the photonic system [3.14].

3.4.1 Principle of coupled mode theory

As already presented in chapter 1, under the stimulation of electromagnetic field the electron gas in metallic particles shifts with respect to the positively charged lattice, and the latter exerts a restoring force to the electrons, which moves them back to the original positions. When the frequency of the excitation source matches the natural frequency of surface electrons oscillating against the restoring force, localized surface plasmon occurs. This kind of electrons oscillation can simply be modeled as a harmonic oscillator, as shown in Fig 3.4.1.

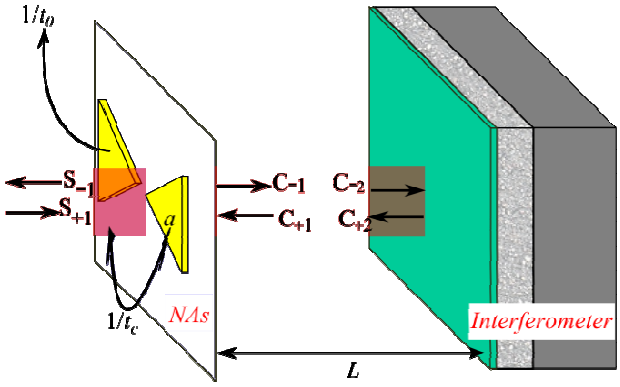

Fig 3.4.1 Schematic representation of NA on Fabry-Perot interferometer

In the present approach the bowtie NA is viewed as a monomode resonator interacting with an incident plane wave. The complex amplitude of the resonant mode is a ($|a|^2$ is the stored energy). $S_{\pm i}$ and $C_{\pm i}$ are amplitudes of propagating and counter-propagating plane waves at different positions in the system (see Fig 3.4.1). The distance between NA and interferometer

is noted as L. $\frac{1}{\tau_0}$ is the intrinsic optical loss rate of the NA (including radiation and metallic absorption) and $\frac{1}{\tau_c}$ is the coupling rate of the NA with the propagating modes.

The coupled mode theory (CMT) describes the kinetics of the NA interaction with the interferometer by the following equation:

$$\frac{da}{dt} = (j\omega_0 - 1/\tau_c - 1/\tau_0)a + KS_{+1} + KC_{+1} \qquad \text{(EQ-3-4-1)}$$

where ω_0 is the resonant pulsation of the NA, and K is the coupling coefficient between the plane waves and the resonator. According to the law of energy conservation, we have the following relations between these components:

$$S_{-1} = C_{+1} - K^* a \qquad \text{(EQ-3-4-2)}$$

$$C_{-1} = S_{+1} - K^* a \qquad \text{(EQ-3-4-3)}$$

$$K = \sqrt{\frac{1}{\tau_c}} e^{j\theta} \qquad \text{(EQ-3-4-4)}$$

According to the equations above, after Fourier Transformation it is possible to derive the transfer matrix M_r between $\begin{bmatrix} S_{+1} \\ S_{-1} \end{bmatrix}$ and $\begin{bmatrix} C_{-1} \\ C_{+1} \end{bmatrix}$:

$$M_r = \begin{bmatrix} 1 - \frac{C}{1-C} & \frac{-C}{1-C} \\ \frac{C}{1-C} & \frac{1}{1-C} \end{bmatrix} \qquad \text{(EQ-3-4-5)}$$

$$C = \frac{|K|^2}{j\omega - j\omega_0 + \frac{1}{\tau_0} + \frac{1}{\tau_c}} \qquad \text{(EQ-3-4-6)}$$

where ω is the resonant pulsation of input signal.

Finally, the matrix M_r can be inserted in our Transfer Matrix Method in order to determine the spectral characteristics of the 3 Systems. We define the quality factors Q_c and Q_0 for coupling and intrinsic loss, respectively:

$$Q_c = \omega_0 \tau_c / 2 \,,\; Q_0 = \omega_0 \tau_0 / 2$$

Then the total quality factor is: $Q = \left(Q_c^{-1} + Q_0^{-1}\right)^{-1}$

The quality factors Q_c and Q_0 and the resonance wavelength ω_0 are the 3 crucial parameters influencing the behavior of the system. To be more specific, EQ-3-4-6 can be rewritten:

$$C = \frac{1}{1 + \frac{Q_c}{Q_0}} \frac{1}{1 + j2Q\frac{\omega - \omega_0}{\omega_0}} \qquad \text{(EQ-3-4-7)}$$

In the following, the influence of these parameters is discussed in more details and compared to the experimental results. From EQ-3-4-7, we can infer that the spectral width of the resonance will be proportional to 1/Q and that the amplitude of the reflectivity spectrum will be directly related to the ratio Q_c/Q_0.

3.4.2 Study of the influence of Q and Q_c/Q_0

3.4.2.1 Influence of Q and Q_c/Q_0 on the reflectivity of NAs

Before investigating the properties of the hybrid device, it is necessary to study the plasmonic resonant behaviour of NAs alone, in order to explore the effect of key kinetics parameters Q_0 and Q_c on the coupling mechanisms of NAs with the propagating optical mode. In the present case, the NA array is represented by a resonator with the key energy transfer matrix M_r.

Considering a fixed resonant wavelength $\lambda_0 = 1325$ nm, the NA reflectivity has been computed with varying values of Q_0 and Q_c.

Fig 3.4.2 summarizes the influence of the quality factors on the reflectivity spectrum of the NAs. This study can be divided into 3 different cases:

1. Influence of Q at fixed Q_c/Q_0: this study is presented in Fig 3.4.2 (*a*) - Reflectivity spectra and (*c*) – Transmission spectra for the particular case of $Q_c/Q_0 = 0.4$, and Q varying from 1 to 10.

2. Influence of Q_c / Q_0 at fixed Q: this study is presented in Fig 3.4.2 (*b*) – Reflectivity spectra and (*d*) -Transmission spectra for the particular case of $Q = 5$, and Q_c / Q_0 varying from 0.1 to 1.

3. Particular case of $Q_c >> Q_0$: this case is presented in Fig 3.4.2 (*e*) – Reflectivity spectrum.

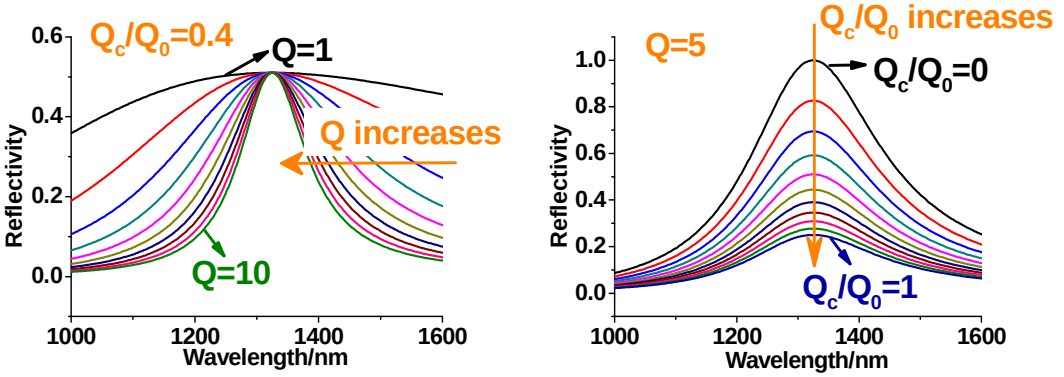

(a) Reflectivity (Fixed Q_c / Q_0, Varying Q) *(b) Reflectivity (Fixed Q, Varying $Q_1 = Q_c / Q_0$)*

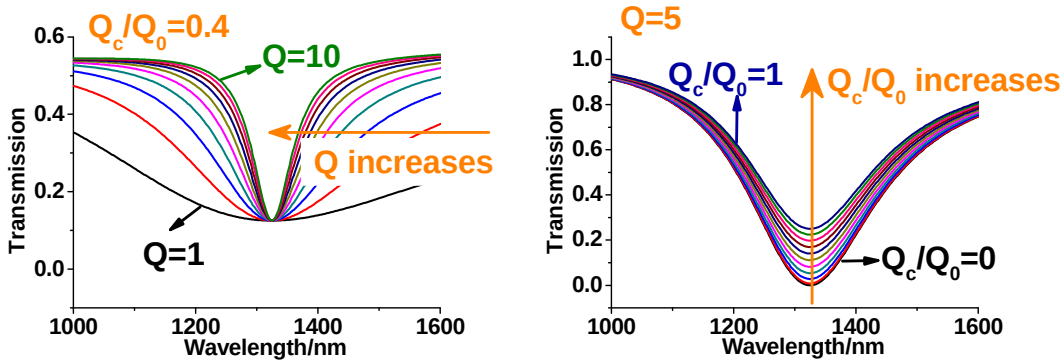

(c) Transmission (Fixed Q_c / Q_0, Varying Q) *(d) Transmission (Fixed Q, Varying $Q_1 = Q_c / Q_0$)*

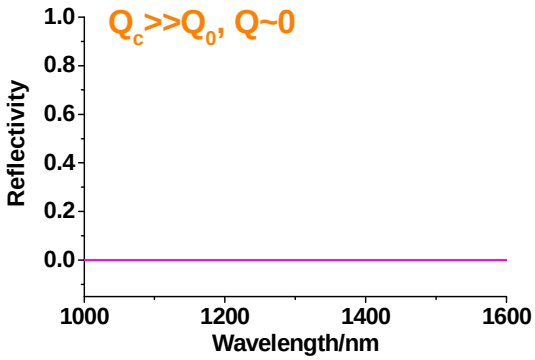

(e) Reflectivity ($Q_c >> Q_0$)

Fig 3.4.2 Influence of the quality factors on the reflectivity spectrum of NAs (λ_0=1325nm)

The different variations shown in Fig 3.4.2 lead to the following observations:

- The normalized bandwidth of the resonance is fully determined by 1/*Q*, which represents the total losses of the NA.

- At fixed Q, the amplitude of the reflectivity peak, R_{peak}, depends only on the ratio Q_c/Q_0:
    - For $Q_c << Q_0$ (over-coupling), the incident beam is fully reflected at resonance and no absorption occurs, indicating a bad coupling with the NA
    - For $Q_c = Q_0$ (critical coupling), a maximum coupling with the NAs is obtained: 25% of the incident power is reflected, another 25% is transmitted and 50% is absorbed or scattered.
- For $Q_c >> Q_0$ (under-coupling), the incident beam is fully transmitted at resonance (R tends to 0 and T tends to 1) and no absorption occurs, indicating again a bad coupling with the NA.

3.4.2.2 Determination of experimental Q values

The study presented above shows that the reflectivity spectrum of the NAs is strongly varying with the values of Q and Q_c/Q_0. Hence, the experimental Q values could be determined from a fit of the experimental spectra.

We selected the experimental 3 systems already discussed in Fig 3.3.23. The resonance is around 1300 nm for the bowtie NAs with the following parameters: triangle bases: A1 = 510 nm; distance between 2 triangles: Gap = 20 nm; and triangle height: A2 = 280 nm. The interferometer has the following parameters for the PSi layer: $n_{PSi} = 1.31$, $d_{PSi} = 5.9$ µm. The devices have been optically characterized in micro-R and the reflectivity spectrum has been normalized with the silver mirror in order to have a direct comparison with the simulations.

The experimental spectra for the 3 systems are presented in Fig 3.4.3, where the blue curve is for NAs alone – ‘System 2’, the red one is for the hybrid device – ‘System 1’ and the black one is for the interferometer alone – ‘System 3’.

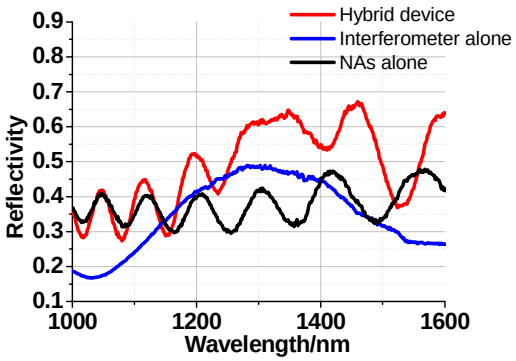

Fig 3.4.3 Experimental spectra of the 3 systems normalized with mirror

In order to determine the experimental Q values, CMT simulations with varying Q factors have been performed for all 3 devices and the simulated spectra have been compared to the experimental ones to find the best match. The resulting spectra are plot in Fig 3.4.4 for each system.

In the case of System 3 (Fig 3.4.4 (*a*)), the CMT calculation has been made for $Q_c >> Q_0$ ($Q \sim 0$), in order to prevent any excitation of the NAs; this way, the only contribution to the reflectivity spectrum comes from the interferometer. The spectrum calculated with CMT reproduces well the experimental fringe positions.

For System 2 (Fig 3.4.4 (*b*)), the best agreement between simulation and experimental spectra is found when $Q = 2.2$ and $Q_c/Q_0 = 0.42$.

For System 1 (Fig 3.4.4 (*c*)), the best agreement is found when $Q = 2.2$ and $Q_c/Q_0 = 0.3$. In particular, we can observe the same fringe splitting on the CMT spectrum as in the experimental spectrum. This is demonstrated again in Table 3.4, which gives a comparison of the wavelength positions of the split fringes in both cases; in spite of the inaccuracy on the position of the little - pronounced split fringes, very good agreement is found, with a discrepancy between the wavelength positions smaller than 1%.

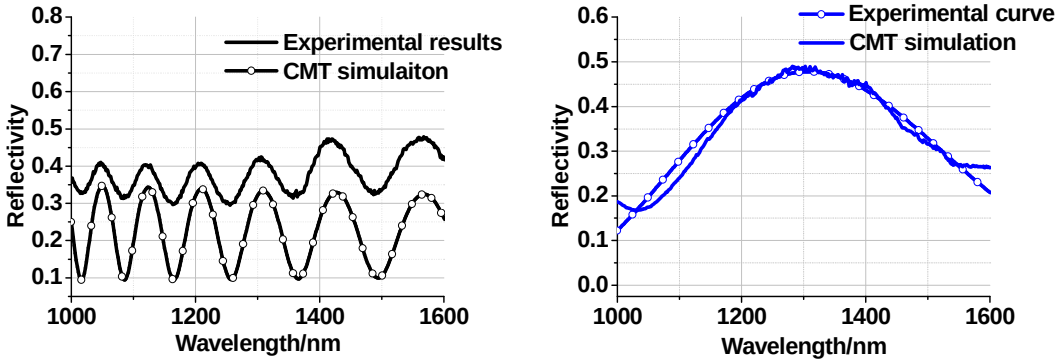

(a) Interferometer alone with Q_c >> Q_0 and Q ~ 0; (b) NAs alone with Q_c / Q_0 = 0.42, Q = 2.2;

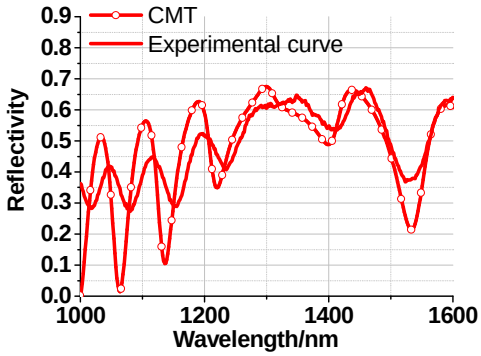

(c) Hybrid device: Q_c / Q_0 = 0.3, Q = 2.2

Fig 3.4.4 CMT simulation fit with experimental devices: (a) interferometer alone with Q_c >> Q_0 and Q ~ 0; (b) NAs alone with Q_c/Q_0 = 0.42, Q = 2.2; (c) Hybrid device with Q_c/Q_0 = 0.3, Q = 2.2. The solid lines are for experimental spectra and the lines with circles are for CMT simulation.

	λ'_{3max}/nm	λ''_{3max}/nm
Experimental results	1293	1338
CMT	1287	1346

Table 3.4 Comparison between the wavelength positions of split fringe for the hybrid device presented in Fig 3.4.4.

The optimum Q values determined for systems 1 and 2 are very close. Indeed, in the CMT simulation of the NA, the Q values should be independent on the NA environment, i.e., on the presence or absence of interferometer. However, due to experimental imperfections the experimental Q factors of the NAs might slightly vary from one NA array to the next; as illustrated by the simulations shown in Fig 3.4.5, such a slight variation of Q factor will mostly result in a slight modification of the split fringes.

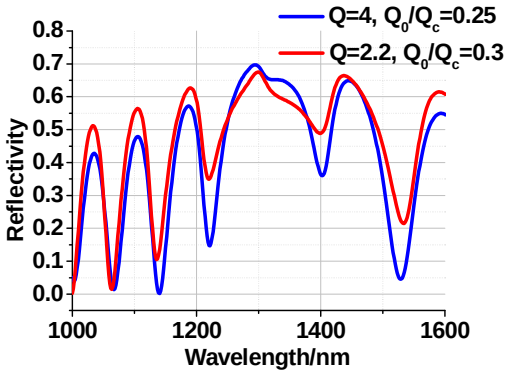

Fig 3.4.5 CMT simulations of the hybrid structure with slightly different Q factors

As the CMT theory mainly applies in the case of highly resonant systems, it is important to verify the validity of the Q values determined using this theory in the case of the low-resonance NAs. For this, we consider again the experimental spectrum for NAs alone shown in Fig 3.4.3 and 3.4.4 (*b*), and evaluate the Q factor using the following relation: $Q = \lambda_{NA} / \Delta\lambda$, where λ_{NA} is the resonance wavelength and $\Delta\lambda$ is the full width at half maximum. The resulting experimental Q factor is about 2.8, which is in good agreement with the values determined by CMT, demonstrating that the CMT approach is still valid here.

3.4.3 Study of the influence of ω_0

3.4.3.1 Influence of NA resonance wavelength on the hybrid device behaviour

We have seen above that the *Q* values used in the CMT model have a crucial influence on the shape and intensity of NA resonance, and the values of Q_0 and Q_c matching our experimental devices have been determined from a fit of the experimental spectra, both in the case of the hybrid device and NAs alone. The spectra obtained with CMT simulations reproduce well the behavior of the hybrid device, in particular the fringe splitting at resonance. The resonance wavelength λ_{NA} is also a crucial parameter, as it will influence the relative position of the resonance with respect to the fringes. Hence, tuning the resonance wavelength should lead to similar observations as the ones presented in section 3.3.3 when tuning the optical path of the interferometer. This study is presented in the following.

The values of Q_0 and Q_c used in the CMT model are the same as the ones determined in the previous section for the hybrid device, i.e., Q = 2.2 and $Q_c/Q_0 = 0.3$. To simplify the study, we choose the parameters of PSi layer as $n_{PSi} = 1.5$ and $d_{PSi} = 5\ \mu m$. The value of λ_{NA} is varied between 1260, 1290, 1310, and 1330 nm respectively. The reflectivity of the hybrid device is

shown in Fig 3.4.6 for each wavelength resonance value. As usual, the corresponding spectra of NAs alone and interferometer alone are shown as well.

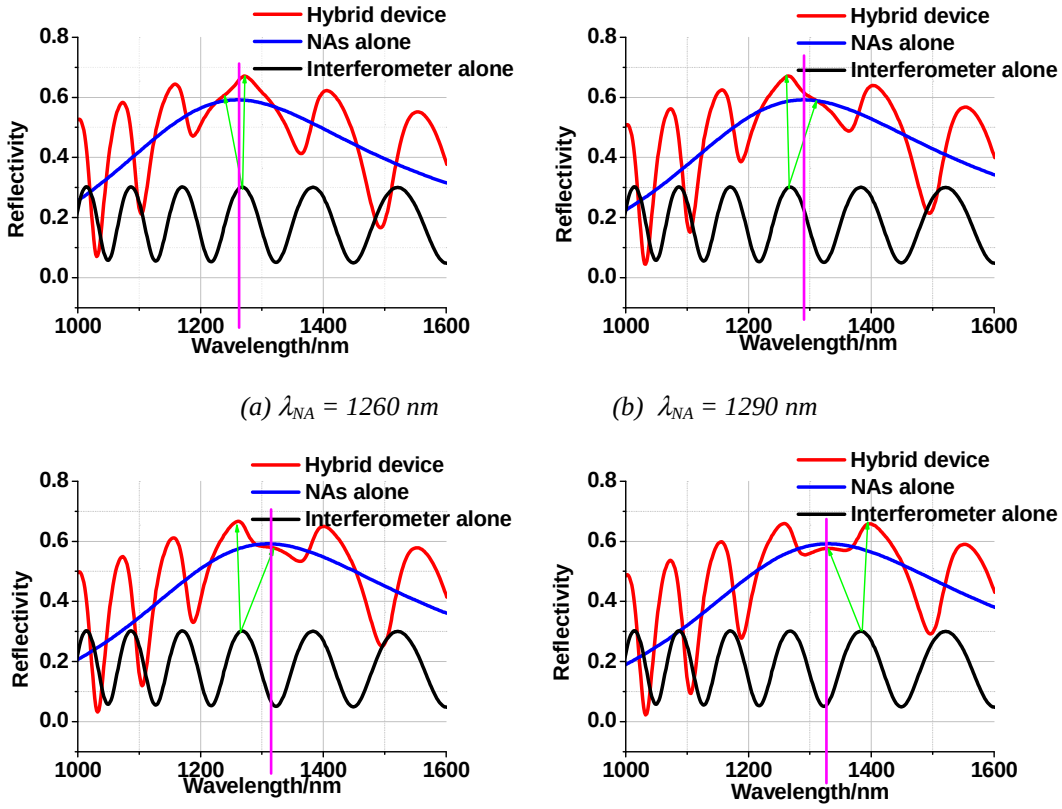

(a) λ_{NA} = 1260 nm *(b) λ_{NA} = 1290 nm*

(c) λ_{NA} = 1310 nm *(d) λ_{NA} = 1330 nm*

Fig 3.4.6 Reflectivity of hybrid device for varying resonance wavelength: (a) λ_{NA} = 1260 nm; (b) λ_{NA} = 1290 nm; (c) λ_{NA} = 1310 nm and (d) λ_{NA} = 1330 nm

As expected, the splitting behavior of the hybrid device varies depending on the resonance. This can be studied by considering the phase difference between the NA resonance and the interferometer fringe maximum. We can obtain the same conclusion as the analysis in Section 3.3.4.2.

3.4.3.2 Experimental demonstration

As discussed in section 3.3.4, for a given substrate the tunability of resonant wavelength for bowtie NAs can be obtained by adjusting the sizes and distance of triangles. As the largest variation of resonant wavelength was shown to depend on the Gap parameter, in the following we select 2 NA arrays with different gap sizes, 20 nm and 15 nm, and identical triangle parameters A1 = 510 nm and A2 = 280 nm. The underlying interferometer has parameters d_{PSi} = 5.9 µm and n_{PSi} = 1.31 for the PSi layer, and 80 nm SiO_2 spacing layer. The reflectivity

spectra of the 2 hybrid devices with different NA gaps are shown in Fig 3.4.7 (red curves), where (*a*) and (*b*) are for 20 nm and 15 nm gaps, respectively. The corresponding reflectivity spectrum of interferometer alone (black curves) and NA alone (blue curves) are also plotted.

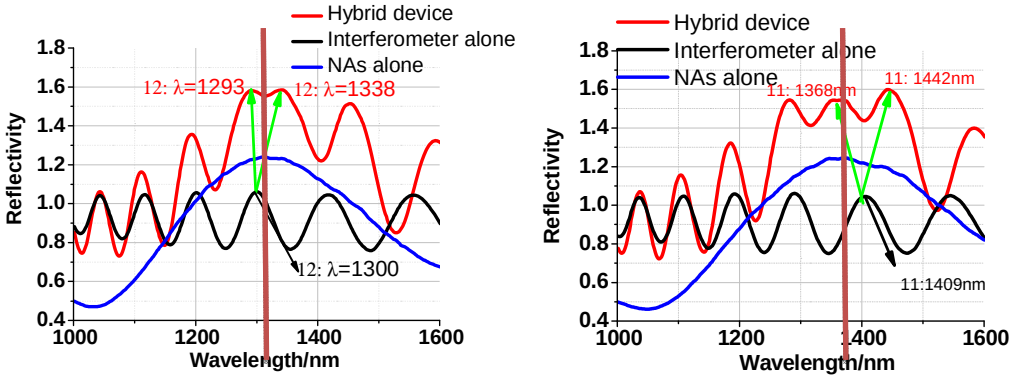

Fig 3.4.7 Reflectivity of experimental hybrid device with identical NA triangles (A1 = 510 nm, A2 = 280 nm) and different gaps: (a) Gap = 20 nm; (b) Gap = 15 nm; Red curves: Hybrid device, black curves: interferometer alone, blue curves: NAs alone.

Comparing the 2 cases shown in Fig 3.4.7, it can be verified that NAs with different gap sizes but otherwise identical parameters (A1, A2 and interferometer structure) have different resonant wavelengths: as expected, the resonance wavelength is smaller for the larger gap, with λ_c = 1325 nm and 1370 nm for 20 nm and 15 nm gaps, respectively. Therefore, the reflectivity spectrum of the hybrid device is different as well. In case (*a*), λ_c is close to the fringe maximum λ'_{2max} = 1300 nm, leading to 2 close split fringes at λ'_{3max} = 1293 nm and λ''_{3max} = 1338 nm, almost merging into one broad peak; in case (*b*), λ_c is close to the fringe minimum λ'_{2min} = 1346 nm, leading to 2 further-separated fringes at λ'_{3max} = 1368 nm and λ''_{3max} = 1442 nm. This result validates that the fringe splitting can also be controlled by tuning the resonance wavelength of the NA array.

3.5 Conclusion

In this chapter, we presented a study of the coupling mechanisms occurring within the hybrid structure consisting of an array of bowtie NAs on top of a PSi interferometer.

First, a study of the NAs alone was presented, in order to gain understanding about the influence of the different geometrical parameters of the bowtie NA, as well as the coupling mechanisms between the 2 triangle-shaped gold particles, leading to the resonance. We demonstrated that the resonance could be tuned by adjusting the triangle dimensions and the inter-particles distance.

In a second part, the influence of the NA array on the interferometer was investigated. The proposed approach was to consider the NA array to be equivalent to a homogeneous layer with same dielectric function placed on top of the interferometer. A simple phase matching model based on thin film interference was developed layer-by-layer, in order to describe the multi-layer interferences in the device and to analyze the fringe variations induced by the introduction of the equivalent layer. The plasmonic resonance behavior of the NAs was modeled using the Drude model to describe the effective dielectric constant, which exhibited giant variations around the resonant wavelength in both real part and imaginary part. The highlight of this study is the evidence of a fringe splitting induced by the NA resonance, which was demonstrated both with TMM simulations and experimental results. For a given NA resonance, we could demonstrate that the wavelength amplitude of the fringe splitting can be controlled by modifying the optical path of the interferometer. Finally, we were also able to perform an experimental mapping of the NAs dielectric constant by exploiting the fringe positions on the reflectivity measurements. The experimentally extracted values show a behavior similar to the predictions from the Drude model.

In the last part of this chapter, we used a complementary approach, which views the bowtie NA array as a harmonic oscillator. The coupling between NAs and interferometer was investigated with coupled mode theory. The behavior of NAs could be described with a specific transfer matrix M_r including 3 key parameters: the quality factors for coupling and loss, respectively, as well as the resonant wavelength. Using this approach, we could demonstrate again the fringe splitting induced by NA resonance, and we could also show that,

for a given interferometer structure, this fringe splitting can be controlled by modifying the resonant wavelength of NAs.

3.6 References

[3.1] J. Aizpurua, G. W. Bryant, L. J. Richter, F. J. García de Abajo, B. K. Kelly, and T. Mallouk, “Optical properties of coupled metallic nanorods for field-enhanced spectroscopy,” Phys. Rev. B 71, 235420 (2005).

[3.2] W. Ding, R. Bachelot, S. Kostcheev, P. Royer, and R. Espiau de Lamaestre, “Surface plasmon resonances in silver Bowtie nanoantennas with varied bow angles,” Journal of Applied Physics, vol. 108, no. 12, pp. 124314, 2010.

[3.3] M. Born and E. Wolf, “Principles of optics: electromagnetic theory of propagation, interference and diffraction of light”. Oxford, Pergamon Press, 1964.

[3.4] D. M. Topasna and G. A. Topasna, “Numerical modeling of thin film optical filters,” Education and Training in Optics and Photonics, EP5, 2009. (Conference paper)

[3.5] C. Jamois, C. Li, E. Gerelli, R. Orobtchouk, T. Benyattou, Y. Chevolot, V. Monnier and E. Souteyrand, “New Concepts of Integrated Photonic Biosensors Based on Porous Silicon,” Biosensors - Emerging Materials and Applications, Edited by Pier Andrea Serra, Publisher: InTech, 2011, ISBN 978-953-307-328-6.

[3.6] Carsten Sönnichsen, “Plasmons in metal nanostructures”, Ludwig-Maximilians-University of Munich, 20, June, 2001.

[3.7] E D. Palik, "Handbook of Optical Constants of Solids". Copyright © 1997 Elsevier Inc. ISBN: 978-0-12-544415-6.

[3.8] S. A. Maier, “Plasmonics: Fundamentals and applications”, Springer, XXV, 2007.

[3.9] L. Novotny and B. Hecht, “Principles of nano-optics”, Chapter 12, pp. 407–450, Printed in the United Kingdom at the university Press, Cambridge, 2012, ISBN 978-1-107-00546-4 Hardback-

http://www.optics.rochester.edu/workgroups/novotny/courses/OPT463/plasmonss.pdf

[3.10] A. Sundaramurthy, K. Crozier, G. Kino, D. Fromm, P. Schuck and W. Moerner, “Field enhancement and gap-dependent resonance in a system of two opposing tip-to-tip Au nanotriangles,” Physical Review B, vol. 72, no. 16, p. 165409, Oct. 2005.

[3.11] M. A. Ordal, L. L. Long, R. J. Bell, S. E. Bell, R. R. Bell, R. W. Alexander, Jr., and C. A. Ward, “Optical properties of the metals Al, Co, Cu, Au, Fe, Pb, Ni, Pd, Pt, Ag, Ti, and W in the infrared and far infrared”, Applied Optics, Vol. 22, Issue 7, pp. 1099-1119 (1983). http://dx.doi.org/10.1364/AO.22.001099.

[3.12] R. Ameling and H. Giessen, “Cavity Plasmonics: Large Normal Mode Splitting of Electric and Magnetic Particle Plasmons Induced by a Photonic Microcavity”, Nano Lett., 2010, 10 (11), pp 4394–4398. DOI: 10.1021/nl1019408

[3.13] H. A. Haus, “Waves and Fields in Optoelectronics”, Prentice Hall, Englewood Cliffs, N.J 1984.

[3.14] A. Belarouci, T. Benyattou, X. Letartre, and P. Viktorovitch, “3D light harnessing based on coupling engineering between 1D-2D Photonic Crystal membranes and metallic nano-antenna.,” Optics express, vol. 18 Suppl 3, no. May, pp. A381–94, Sep. 2010.

Chapter 4 Sensing investigation

4.1 INTRODUCTION 215
4.2 LARGE REFRACTIVE INDEX VARIATION ΔN 216
4.2.1 Validation of the sensor with PMMA layer 216
4.2.2 Sensing of liquids: Water vs. Air 224
4.3 SMALL REFRACTIVE INDEX VARIATION ΔN 226
4.3.1 Sensing of water/ethanol mixture 226
4.3.2 Detection of humidity (water vapor) 232
4.4 CONCLUSION 237
4.5 REFERENCES 238

4.1 Introduction

In chapter 3, we presented that the hybrid device constituted of a bowtie NA array and a F-P interferometer exhibits a specific spectrum showing both the NA plasmonic resonance and the oscillations of interferometer fringes: the fringes introduce a structuration on the broad NA resonant peak, leading to several peaks superimposed with the NA resonance; at the same time, coupling between the 2 device elements induces an enhancement of the fringe amplitude as well as a shift of the fringe positions and a fringe splitting at NA resonance. Hence, it would be interesting to investigate the potential of these particular optical features for sensing applications, in particular in terms of sensitivity improvement with respect to the interferometer alone and NAs alone.

The evaluation of environmental sensitivity is essential for sensing applications. In this chapter, we present sensing experiments with various device environments providing conditions for detection of large and small refractive index variations, respectively.

4.2 Large refractive index variation Δn

The first studies of the sensing potential of our hybrid device aim at investigating large variations of the refractive index of the environment. Two different cases are discussed in the following:

- Deposition of a PMMA layer on top of the device;
- Immersion of the device into water.

4.2.1 Validation of the sensor with PMMA layer

4.2.1.1 Sensitivity to the presence of PMMA layer

The purpose of this first study is the detection of a PMMA layer deposited on top of the device. Hence, this experiment compares the response of the device with PMMA layer to the device without PMMA, i.e. in air environment. In order to determine whether the hybrid device yields a gain in sensitivity with respect to the interferometer and NAs alone, the 3 devices are investigated and compared.

Description of the 3 systems:

The interferometer consists of a PSi layer with 4.85 µm thickness, which has been slightly oxidizied (d_{SiO2} ~ 1.8 nm). The refractive index is 1.66, corresponding to a porosity of 53% after oxidation. A thin (80 nm) SiO_2 layer was deposited on the PSi surface.

The NA array has the following average dimensions: A1 = 510 nm, A2 = 280 nm and Gap = 20 nm, both for the hybrid device and for the system with NAs alone. As before, the later was fabricated on top of a Si substrate with 200 nm SiO_2 spacing layer.

Optical response of the 3 systems in air:

The 3 systems were first studied in air environment. The corresponding reflectivity spectra are presented in Fig 4.2.1. We can see on these spectra that the NA resonance is positioned around 1350 nm and its linewidth is about 470 nm. On the spectrum for the hybrid structure, the splitting is observed for fringe order 12 in the form of a broader peak since the NA

resonance wavelength is close to the position of the interferometer fringe, as discussed in the previous chapter.

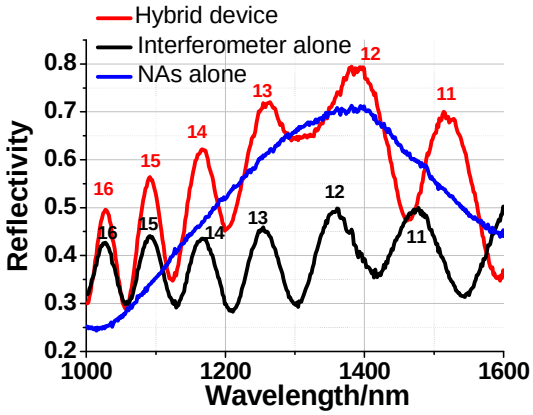

Fig 4.2.1 Reflectivity of the 3 systems in Air

Sensing experiment: Deposition of a PMMA layer on top of the systems

The sensing experiment consists in depositing a thin layer of 950 PMMA C2 on top of our 3 systems, and in observing the induced variation in the reflectivity spectra. The PMMA was deposited by spin coating and has a thickness of 240 nm. The refractive index of such PMMA resist is shown in Fig 4.2.2.

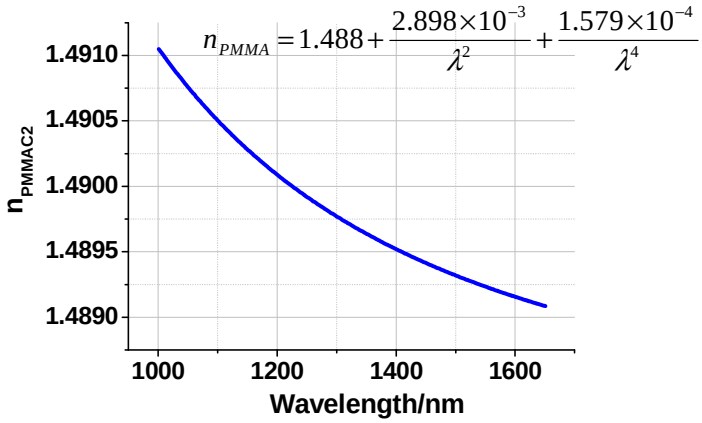

Fig 4.2.2 Refractive index of PMMA (The unit of λ in Cauchy equation is μm) [from Micro Chem resists data sheet]

The reflectivity spectra of the 3 systems with and without PMMA layer are shown in Fig 4.2.3, and lead to the following observations:

1. In the case of NAs alone (Fig 4.2.3 (*a*)), the resonance is shifted from around 1350 nm in air environment (blue curve) to 1600 nm in presence of PMMA (blue curve with open circles). This significant shift demonstrates that the plasmonic resonance of NAs is sensitive to its environment. The red shift can be explained by the refractive index variation, since $n_{PMMA}>1$.

2. In the case of the interferometer alone (Fig 4.2.3 (*b*)), the PMMA layer induces a red shift of the fringes. Considering the fringe order 12 around 1400 nm, the fringe shifts from 1370 nm in air environment (black curve) to 1410 nm in presence of PMMA (black curve with red dots). According to the model developed in the previous chapter, the PMMA layer constitutes an extra film with $n_{PMMA} > 1$ on top of the SiO_2/PSi/Si system, which explains the red shift.

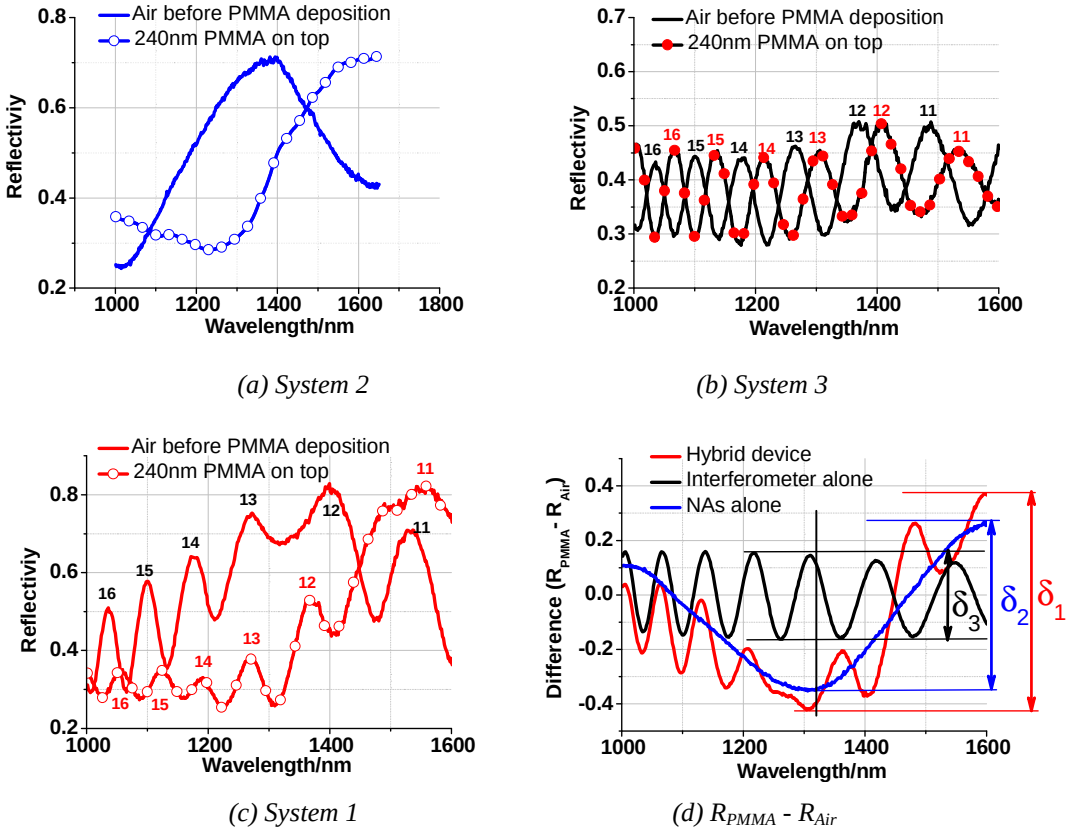

(a) System 2 *(b) System 3*

(c) System 1 *(d) R_{PMMA} - R_{Air}*

Fig 4.2.3 Optical reflectivity spectra of the 3 systems with and without PMMA layer (the curves with dots are for the devices with PMMA layer, the plain lines are for the devices without PMMA): (a) System 2 – NAs alone, (b) System 3 – interferometer alone, (c) System 1-hybrid device, and (d) Difference between the reflectivity spectra with and without PMMA for each system (red curve: hybrid device, blue: NAs alone, black: interferometer alone); here, the spectra are normalized by the silver mirror.

3. In the case of the hybrid device (Fig 4.2.3 (*c*)), the PMMA layer induces a modification of the NA environment leading to a red shift of NA resonance, as in the case of NAs alone. This resonance shift explains why the amplification of fringe amplitude observed in air environment is not observed at short wavelengths in the case with PMMA. On the other hand, the extra layer of PMMA increases the total optical path which should lead to a red shift of each fringe in view of the interferometer approach. Comparing the curves with and without PMMA layer in Fig 4.2.3 (*c*), the red shift is clearly visible for the large fringe orders before NA resonance (for m > 14); at resonance, the strong variation of NA optical constants and the strong interaction between NA and interferometer induce more complex variations, resulting in the observation of a very slight blue shift (1 nm) for m = 13, and of the fringe splitting which is initially observed for fringe order 12 around 1400 nm in air environment, and is shifted to fringe order 11 around 1600 nm in presence of the PMMA layer.

Discussion: Comparison between the sensitivities of the 3 systems

Several methods have been proposed to evaluate and compare the sensing potential of devices. One way is to consider the ratio between the wavelength shift of the peak or fringe and the refractive index variation: $S = \frac{\Delta\lambda_m}{\Delta n}$.

However, the definition above is meaningless in the case of the hybrid structure, because of the very different behaviors that could be observed in Fig 4.2.3 (c), depending on the wavelength range. As a result, for most fringes $\Delta\lambda_m$ is similar or smaller than in the case of the interferometer alone, or even impossible to define when considering the splitting.

Another way to discuss the sensitivity is to consider the difference signal, i.e. the difference between the reflectivity spectra with and without the PMMA layer:

$$\Delta R = R_{with\,PMMA} - R_{Air}$$

As this second approach is suitable for our systems, we calculated the difference signals for each system. The corresponding difference spectra are shown in Fig 4.2.3 (*d*). It is interesting to note that the difference signal for the hybrid structure shows both the oscillations and the modulation of the interferometer and the NAs difference signals, respectively. In the case of fringe order 13 where the fringe positions for the hybrid structure almost coincide, the

oscillation almost disappears in the difference signal, which becomes very similar to that of the NAs. In order to compare the sensitivity of the 3 systems, we consider 2 indicators:

- The maximum absolute value of difference signal $|\Delta R|_{max}$ – which would be a good indicator in the case of sensing measurements at fixed wavelength;
- The total amplitude of the difference signals δ, i.e. the difference between the maximum and minimum values of ΔR (ΔR_{max} and $\Delta R_{\min}$, respectively) over the whole spectral range – which would be a good indicator in the case of spectral measurements:

$$\delta = \Delta R_{\max} - \Delta R_{\min}$$

In order to quantify the sensitivity depending on refractive index variation, we introduce as well the entity δ_n:

$$\delta_n = \delta / \Delta n$$

The amplitudes δ are highlighted in Fig 4.2.3 (*d*), and are $\delta_1 \sim 0.77$ for the hybrid device, $\delta_2 \sim 0.64$ for the NAs alone, and $\delta_3 \sim 0.3$ for the interferometer alone. Using this indicator, the difference signal clearly shows a larger amplitude for the hybrid device than for the interferometer, corresponding to a sensitivity enhancement larger than 150%. The gain in sensitivity with respect to the NAs alone is smaller (20%). Considering the maximum absolute values of difference signal – $|\Delta R|_{max1} = 0.42$ for the hybrid device, $|\Delta R|_{max2} = 0.35$ for the NAs alone, and $|\Delta R|_{max3} = 0.16$ for the interferometer alone – the resulting sensitivity enhancement is very similar. As a conclusion, this comparison shows that in the case of large variations of refractive index such as the deposition of a PMMA layer, the gain in sensitivity provided by the hybrid device is relatively small with respect to a simpler device like the array of NAs on Si substrate. The corresponding sensitivity factor δ_n is 0.5.

4.2.1.2 Sensitivity to the thickness of PMMA layer

The purpose of this study is the evaluation of our devices sensitivity depending on the PMMA thickness. In this case, the experiment consists in comparing the responses of the devices when the PMMA thickness is varied.

Sensing experiment: Variation of the PMMA layer thickness

PMMA layers with different thicknesses could be deposited on the devices, via a variation of the rotation speed during spin coating: 190 nm, 220 nm and 240 nm. The corresponding reflectivity spectra for each system are shown in Fig 4.2.4, and lead to the following observations:

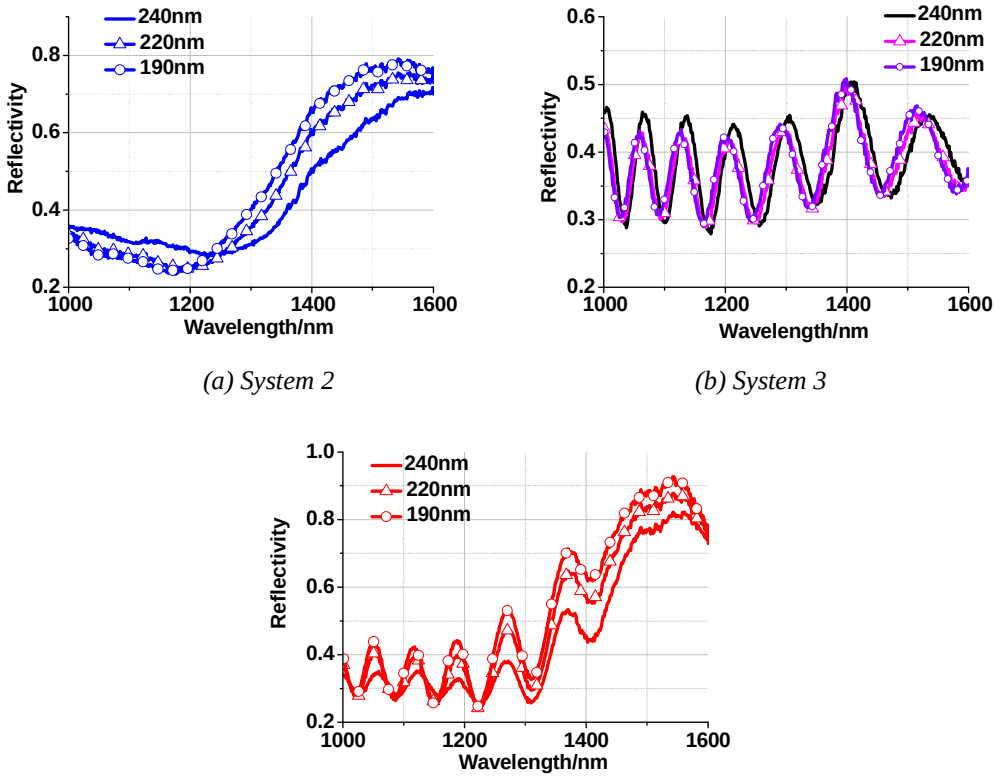

(a) System 2

(b) System 3

(c) System 1

Fig 4.2.4 Reflectivity spectra of 3 systems with different thickness of PMMA: (a) System2- NAs alone, (b) System 3 – Interferometer alone, (c) System1 – Hybrid device; The dotted curves are for 190 nm PMMA, the curves with triangles are for 220 nm PMMA, and the plain lines are for 240 nm PMMA

1. In the case of NAs alone (Fig 4.2.4 (*a*)), the increase of PMMA thickness induces a red shift of NA resonance, from λ_{190} ~ 1530 nm to λ_{220} ~ 1550 nm and λ_{240} ~ 1600 nm for 190 nm, 220 nm and 240 nm thickness, respectively. As the PMMA refractive index is the same in all 3 layers, this red shift indicates that the NA resonance is sensitive to the PMMA layer thickness, and "feels" more PMMA (and less air) as the thickness increases. Moreover, we can conclude that the NA sensing depth is larger than 240 nm. At the same time, the

maximum value of reflectivity at resonance is decreasing as the PMMA thickness increases. This shows that the enhancement of field intensity depends on the surrounding medium and its thickness.

2. In the case of the interferometer (Fig 4.2.4 (*b*)), there is a red shift of each fringe as the PMMA thickness increases, which is explained by the increase of total optical path according to our phase matching model discussed in Chapter 3. When increasing the PMMA thickness by 20 nm from 220 to 240 nm, the resulting shift is about 6 nm at 1100 nm wavelength, and similar at 1400 nm wavelength.

3. In the case of the hybrid device (Fig 4.2.4 (*c*)), there is first a red shift with increasing thickness at short wavelengths outside resonance ($\lambda < 1200$ nm) nm, which is about 4 nm at 1100 nm wavelength. With increasing wavelength, in particular for $\lambda > 1200$ nm, the fringe positions are similar for the 3 thicknesses. This means that the expected red shift of the fringes is compensated by an opposite blue shift, most probably due to a variation of dielectric function of the NA induced by the large shift of resonance depending on PMMA thickness. As observed in the case of the NAs alone, the intensity of reflected signal is decreasing with increasing PMMA thickness.

Discussion: Comparison between the sensitivities of the 3 systems

We calculated the difference between the reflectivity spectra with and without PMMA layer for each PMMA thickness. The spectra are shown in Fig 4.2.5 (*a*), (*b*) and (*c*), respectively, for the NAs alone, the interferometer and the hybrid structure. We extracted the difference δ between ΔR_{max} and ΔR_{min} for each spectrum, as well as the value of $|\Delta R|_{max}$. The corresponding values are reported in Table 4.1.

According to Table 4.1, the sensitivities of the hybrid device and the NA array do not depend much on the PMMA thickness; this might be due to the fact that the NA resonance shift induced by the presence of PMMA is of the same order of magnitude as the half-width of the resonance, which means that the amplitude of the difference signal does not vary much with these small PMMA thickness variations. On the opposite, although the interferometer has a lower sensitivity to the presence of PMMA, its sensitivity strongly varies (50%) with the PMMA thickness; in the case of the interferometer, the sensitivity comes from the phase shift at its interface induced by the optical path difference through the PMMA layer, which varies

depending on PMMA thickness. Comparing the spectra for different PMMA thicknesses for each system, we can observe that the largest variations between the spectra are not found for the wavelengths corresponding to $|\Delta R|_{max}$; this means that the sensitivity to the *presence* of PMMA is not optimum at the same wavelength as the sensitivity to a *variation* of PMMA thickness. Hence, in the case of a sensing experiment at fixed wavelength, the working wavelength has to be carefully chosen depending on the sensing event. Considering PMMA thickness variations, the best sensitivity for the hybrid structure is 0.185 at 1390 nm, while it is 0.160 at 1435 nm for the NA array and 0.065 at 1145 nm for the interferometer. In this respect, the hybrid structure is still the device showing the best sensitivity, although the gain compared to the NA array is quite small.

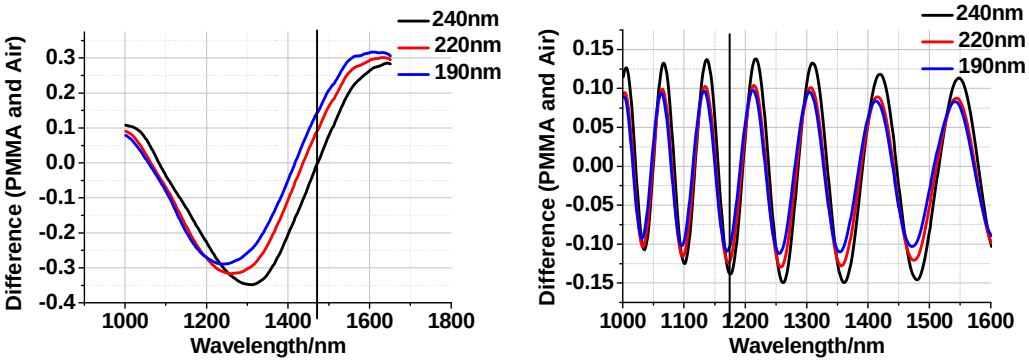

(a) System 2 *(b) System 3*

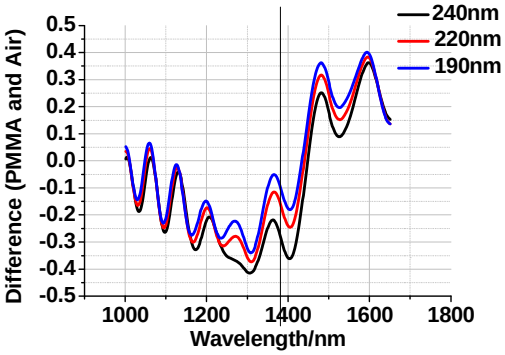

(c) System 1

Fig 4.2.5 Difference between reflectivity spectra with and without PMMA for different PMMA thicknesses: (a) System 2; (b) System 3; (c) System 1

	System2		System3		System1	
	$\|\Delta R\|_{max}$	δ	$\|\Delta R\|_{max}$	δ	$\|\Delta R\|_{max}$	δ
d_{PMMA} = 190nm	0.32	0.61	0.1	0.2	0.4	0.74
d_{PMMA} = 220nm	0.32	0.62	0.13	0.22	0.37	0.75
d_{PMMA} = 240nm	0.35	0.64	0.15	0.3	0.42	0.77
Difference 240nm - 190nm	0.03	0.03	0.05	0.1	0.02	0.03
Maximum signal variation with thickness	0.160 (1435nm)		0.065 (1145nm)		0.185 (1390nm)	

Table 4.1 Comparisons between the amplitudes of difference signals for each system with varying thickness of PMMA layer

4.2.2 Sensing of liquids: Water vs. Air

In the previous section, sensing of a PMMA layer deposited on our hybrid device surface was demonstrated and compared to the other 2 systems, considering the sensitivity deduced from the difference signals. In this particular example of large refractive index variation (air vs. PMMA) or PMMA thickness variation, the sensitivity enhancement provided by the hybrid structure is relatively small with respect to the system with NAs alone. In this section, we apply the device to liquid sensing, and present the particular example of air vs. water environment (n_{water} = 1.333).

Description of the 3 systems:

The NA array has the following average dimensions: A1 = 510 nm, A2 = 280 nm and Gap = 20 nm. The interferometer consists of a slightly-oxidized PSi layer with thickness 5.66 µm and refractive index 1.4, corresponding to a porosity of 61% after oxidation (2.5 nm SiO_2).

Sensing experiment:

After characterization of the 3 systems in air inside the empty fluidic cell, deionized water was injected inside the fluidic cell by a syringe tube, and the systems characterized again in water environment.

The spectra of 3 systems in both air and water are shown in Fig 4.2.6 (*a*) (*b*) and (*c*), respectively, with dotted curves for water environment and plain lines for air. For wavelengths larger than 1350 nm, the absorption of water is strongly increasing and the

spectra are meaningless. This will reduce the sensitivity of devices having their resonance wavelength above 1350 nm. Below 1350 nm, the spectra show a similar behavior as in the case of PMMA.

The difference between reflectivity spectra in water and air are plotted in Fig 4.2.6 (*d*) for all 3 systems. From these spectra, the values δ of total difference amplitude between ΔR_{max} and ΔR_{min} have been extracted (over the wavelength range below 1350 nm), and reach 0.70 for the hybrid device, 0.64 for the NAs alone, and 0.4 for the interferometer alone. As in the case of the PMMA layer, for the large refractive index variation considered here, the gain of sensitivity of the hybrid device is small compared to NAs alone. The corresponding sensitivity factor δ_n is 2.1.

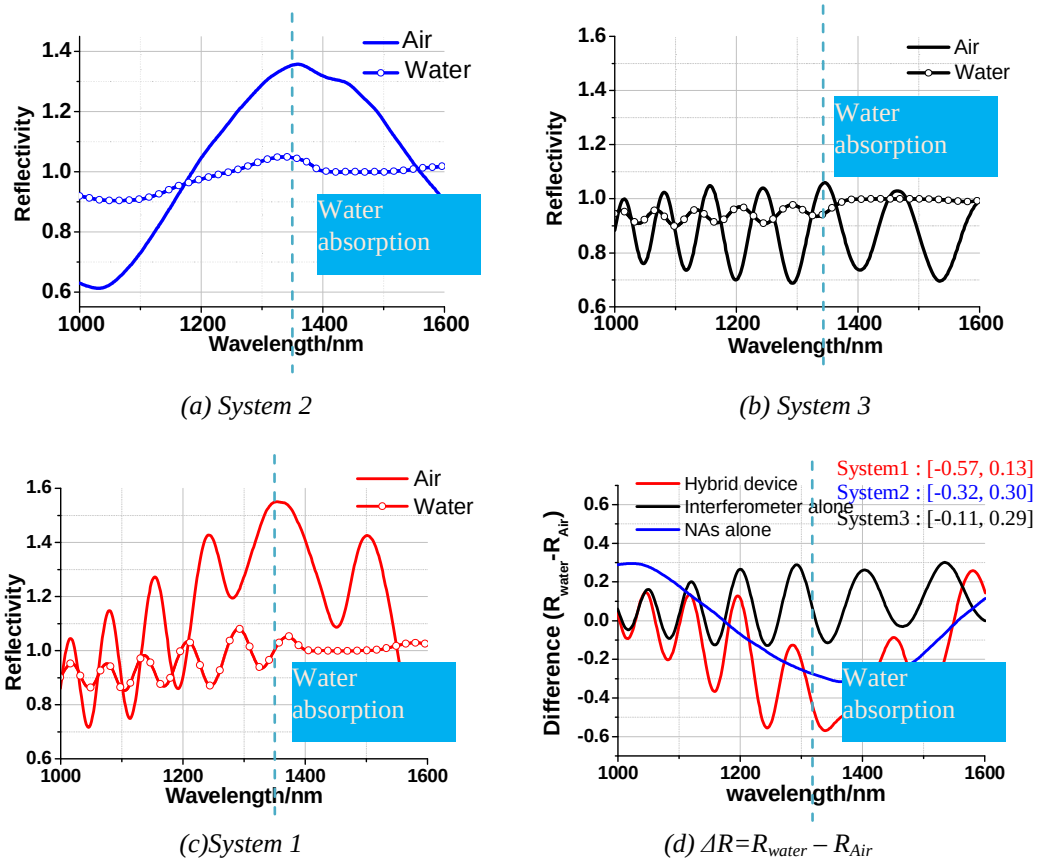

(a) System 2 *(b) System 3*

(c)System 1 *(d) $\Delta R=R_{water}-R_{Air}$*

Fig 4.2.6 Reflectivity spectra of 3 systems in air and water: (a) NAs alone; (b) Interferometer alone; (c) Hybrid device; (d) Difference signals

4.3 Small refractive index variation Δn

As sensitivity to small variation in the environment is highly interesting, in this second part we explore the potential of our hybrid device for the detection such small environment variations. Two different cases are discussed in the following:

- Variation of the percentage of ethanol in a water/ethanol mixture
- Sensing of humidity (water vapor in air)

4.3.1 Sensing of water/ethanol mixture

The refractive index of water /ethanol mixture is known [4.2] and varies between 1.333 and 1.365 depending on the percentage of ethanol in the mixture, as shown in Fig 4.3.1. Hence, by varying the water/ethanol ratio we can investigate the sensitivity of our device to small refractive index variations. In the following, we will first present this study performed with FDTD simulations, where we can neglect the liquid absorption and use a wider wavelength range. We will then discuss the experimental results.

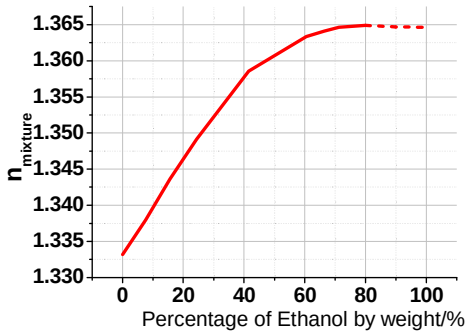

Fig 4.3.1 Refractive index of the mixture of water/ethanol vs. the percentage of ethanol by weight [4.2]. The values between 80 and 100% ethanol are an extrapolation.

4.3.1.1 FDTD simulation

The far-field reflectivity spectra of our 3 systems were calculated with FDTD simulation, first in air environment, and next in media with varying refractive index corresponding to water/ethanol mixture. In the simulations, the interferometer has a refractive index of 1.4 and its thickness is 5.66 µm; the NAs have the following dimensions: A1 = 510 nm, A2 = 280 nm and Gap = 20 nm. The reflectivity spectra of the 3 systems in air environment are presented in

Fig 4.3.2, and show an initial NA resonance wavelength around 1300 nm. For the simulations in liquid environment, the initial state is a medium with a refractive index of 1.333, corresponding to pure water – without absorption. The refractive index is varied to 1.338, 1.344 and 1.349, to simulate different ethanol ratio, respectively 10%, 20% and 30%.

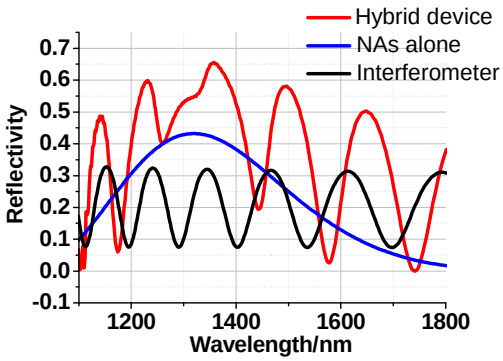

Fig 4.3.2 Reflectivity of the 3 systems in Air (FDTD simulation)

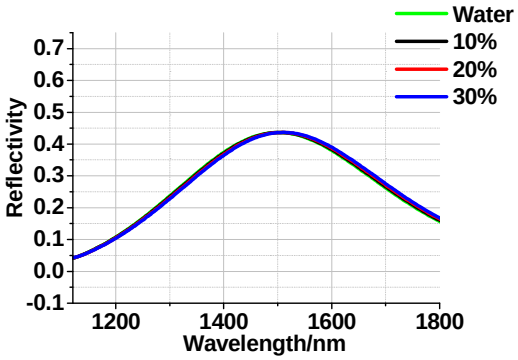

(a) System 2

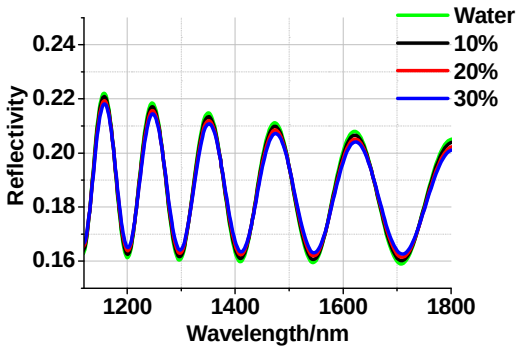

(b) System 3

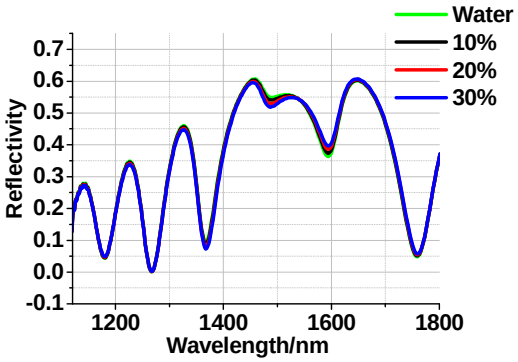

(c) System 1

Fig 4.3.3 Reflectivity of the 3 systems with varying environment refractive index: (a) NAs alone, (b) Interferometer alone, (c) hybrid device; in each figure, the green curve is for n=1.333 (pure water), the black curve is for n=1.338, the red one for n=1.344 and the blue one for n=1.349 (FDTD simulation).

The variation of reflectivity spectra with refractive index are shown in Fig 4.3.3 (*a*), (*b*) and (*c*), respectively, for the NAs alone, the interferometer alone and the hybrid device. Since the

absorption of water is not considered during the simulation, the whole NA resonance can be observed in Fig 4.3.3. The resonance peak is around 1500 nm, corresponding to a red shift of 200 nm compared to air environment. This is similar to the variation observed when depositing a PMMA layer.

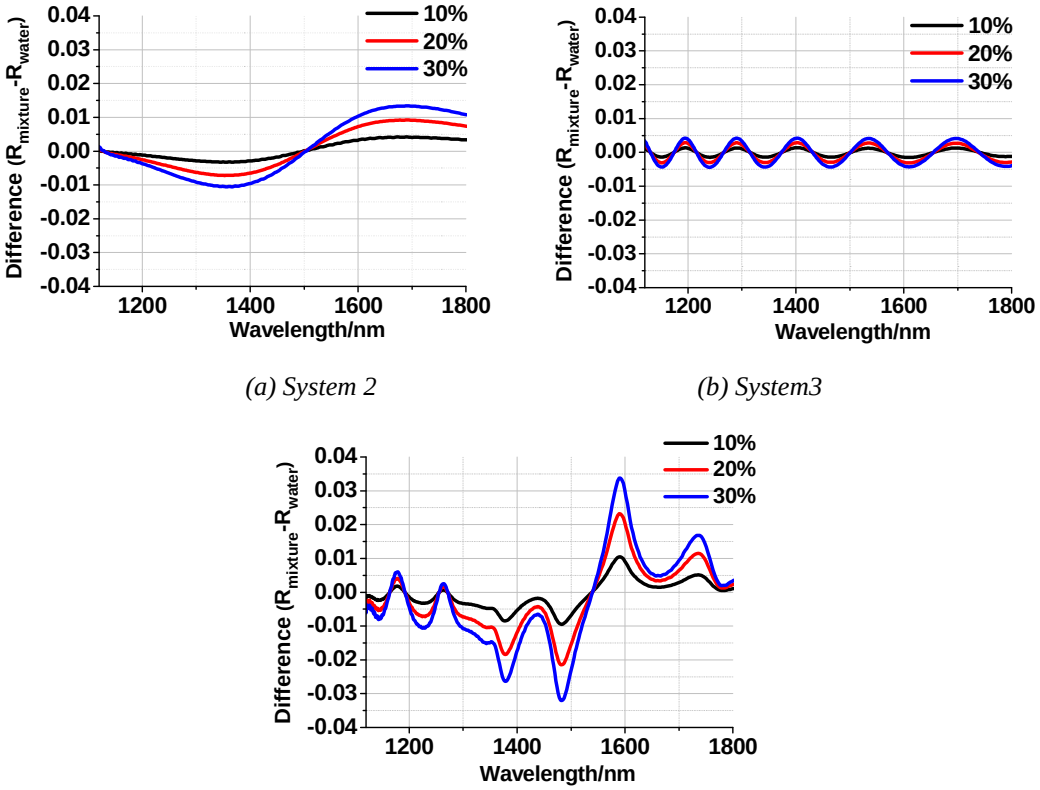

(a) System 2

(b) System3

(c) System 1

Fig 4.3.4 Difference signals $\Delta R=R_{mixture}$ - R_{water} for the 3 systems: (a) NAs alone, (b) Interferometer alone, (c) hybrid device; in each figure, the colors are the same as the ones in Fig 4.3.3

In order to evaluate the sensitivity of the devices to such small environment variations, the difference spectra were calculated with respect to pure water, and are shown in Fig 4.3.4 (*a*), (*b*) and (*c*), respectively, for each system. Comparing the 3 systems, it is clear that the variations of optical response of the hybrid device are strongly amplified at NA resonance, leading to a large difference signal.

In order to quantify the gain in sensitivity of the hybrid device, the amplitude of difference signal ($\delta = \Delta R_{max} - \Delta R_{min}$) was determined in each case, as well as the maximum absolute values of difference signal $|\Delta R|_{max}$. These values are summarized in Table 4.2. Both indicators yield a large enhancement of sensitivity for the hybrid device with respect to the NA array, by

a factor 2.5 or more for both δ and $|\Delta R|_{max}$. Compared to the interferometer alone, the sensitivity of the hybrid device is about 8 to 10 times larger. The corresponding sensitivity factor δ_n is around 4.

	System 2		System 3		System 1	
	$\|\Delta R\|_{max}$	δ	$\|\Delta R\|_{max}$	δ	$\|\Delta R\|_{max}$	δ
n=1.338	0.0042	0.0074	0.001	0.002	0.011	0.020
n=1.344	0.0091	0.0165	0.0028	0.0056	0.023	0.045
n=1.349	0.014	0.0250	0.004	0.008	0.034	0.066

Table 4.2 Amplitude of difference signal δ and maximum absolute values of difference signal $|\Delta R|_{max}$ for each system with varying environment

4.3.1.2 Experimental demonstration

Different water/ethanol mixtures with increasing ethanol volume ratio were prepared. In the following, the results obtained for large percentages of ethanol in water/ethanol mixtures (> 80% ethanol), are presented and compared to the cases of pure ethanol (100%) and pure water (0%). Table 4.3 summarizes the mixture compositions and the corresponding refractive indices.

Percentage in volume	Refractive index
0%	1.333
80%	1.3647
90%	1.3645
100%	1.3643

Table 4.3 mixture compositions (percentage of ethanol in volume) and corresponding refractive indices extrapolated from figure 4.2.1.

The devices investigated here are the same as the ones discussed in section 4.2.2. The reflectivity spectra of the 3 systems with varying environment are shown in Fig 4.3.5. Similarly to the results discussed in section 4.2.2, the spectra are flattened for large wavelengths (> 1350 nm) due to liquid absorption. Hence, the spectrum analysis will be performed only for wavelengths below 1350 nm.

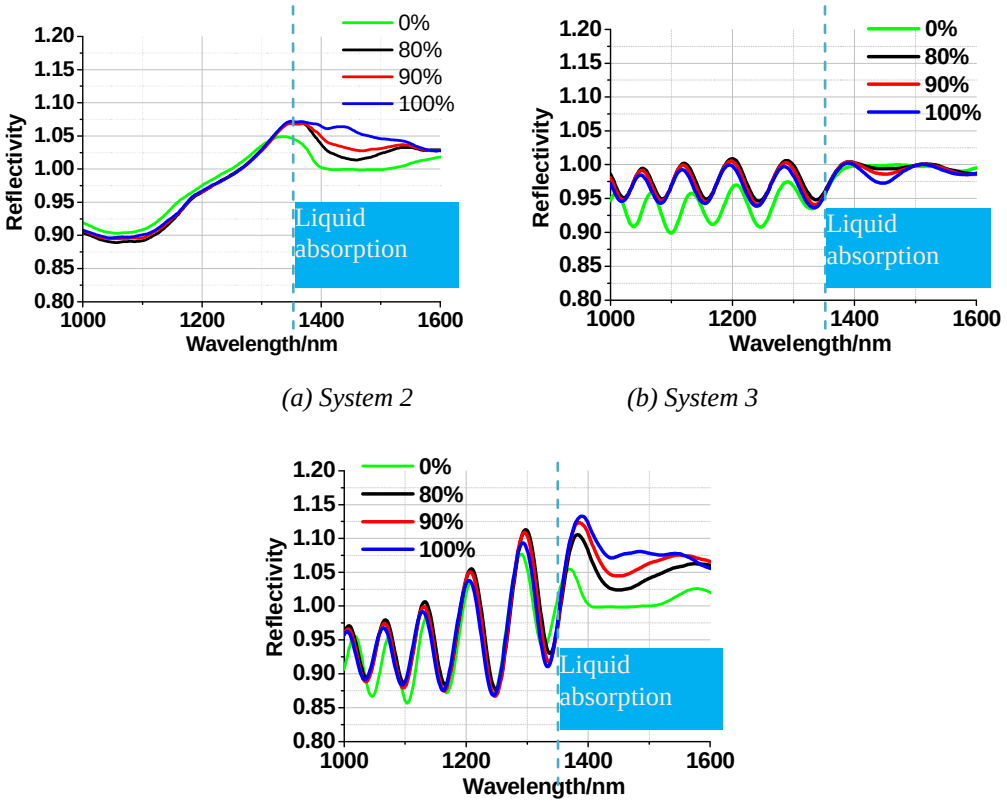

(a) System 2 *(b) System 3*

(c) System 1

Fig 4.3.5 Reflectivity of the 3 systems immersed in different water/ethanol mixtures: (a) NAs alone, (b) Interferometer alone, (c) hybrid device; in each figure, the green curve is for pure water, the black curve is for $P_{ethanol}$ *= 80%, the red one for* $P_{ethanol}$ *=90% and the blue one for* $P_{ethanol}$ *= 100%.*

For each mixture, the difference spectra with respect to pure ethanol and pure water were calculated and are shown in Fig 4.3.6. Similarly to the FDTD simulations, we can observe an enhancement of the difference signal for the hybrid structure close to the NA resonance – before the cut-off induced by liquid absorption.

The 2 sensitivity indicators δ and $|\Delta R|_{max}$ with respect to pure water and pure ethanol have been extracted in each case and are reported in Table 4.4 (*a*) and (*b*), respectively. In spite of the strong absorption of the liquid at NA resonance, we can still observe the sensitivity enhancement provided by the hybrid structure. In the case of the mixture with 90% ethanol, the difference signals with respect to pure water show a sensitivity for the hybrid device more than 3 times larger compared to the NAs alone, and 1.5 times larger compared to the interferometer. With respect to pure ethanol, the sensitivity for the hybrid device is more than 8 times larger compared to the NAs alone, and more than 5 times larger compared to the

interferometer. The corresponding sensitivity factor for the hybrid structure is $\delta_n > 3$ with respect to water ($\Delta n \sim 3.10^{-2}$) and $\delta_n > 200$ with respect to ethanol ($\Delta n \sim 2.10^{-4}$).

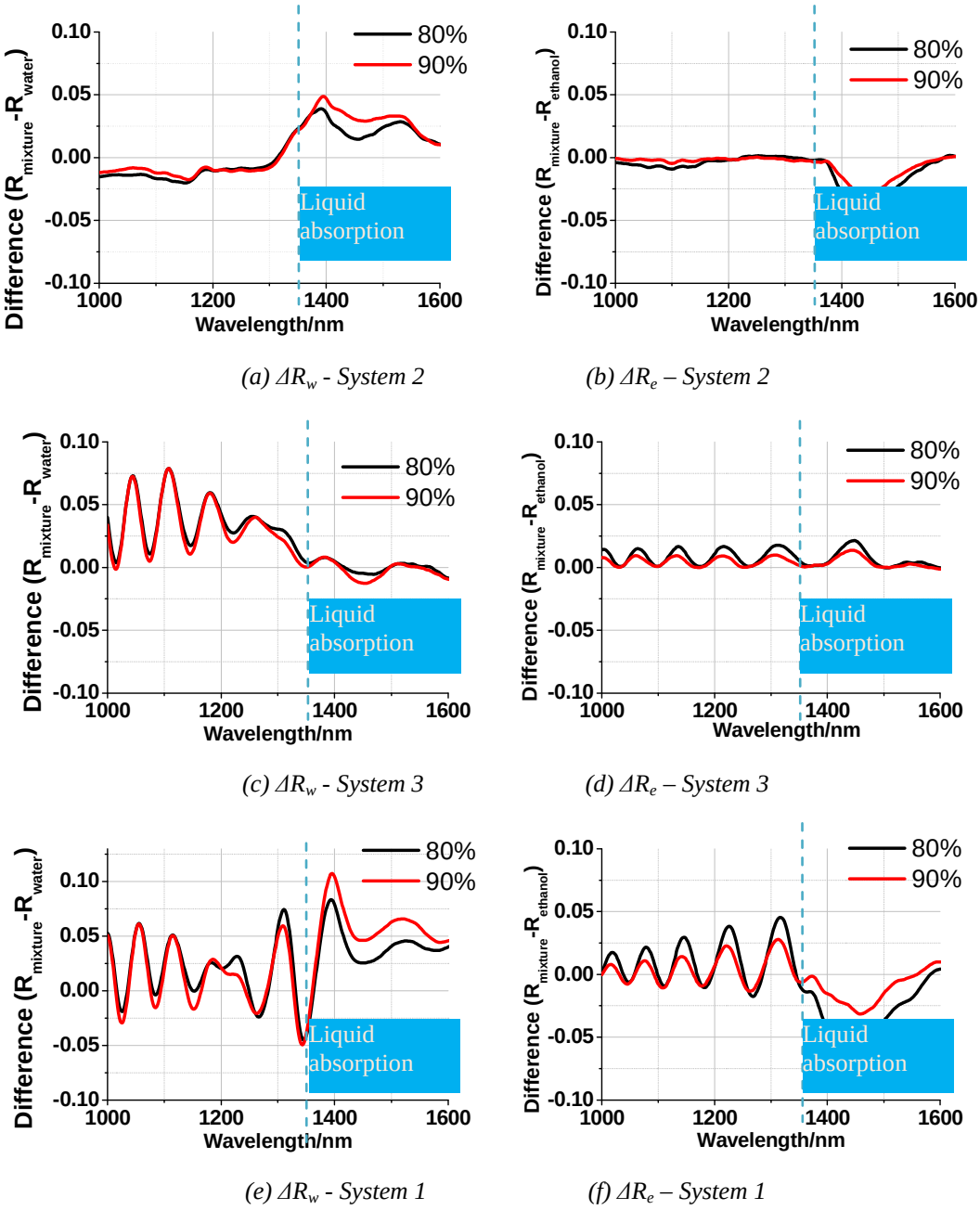

(a) ΔR_w - System 2 *(b) ΔR_e – System 2*

(c) ΔR_w - System 3 *(d) ΔR_e – System 3*

(e) ΔR_w - System 1 *(f) ΔR_e – System 1*

Fig 4.2.6 Difference signals of the 80% (black) and 90% (red) ethanol mixtures, with respect to pure water ($\Delta R_w = R_{mixture} - R_{water}$) and pure ethanol ($\Delta R_e = R_{mixture} - R_{ethanol}$) for the 3 systems: NAs alone: (a) ΔR_w, (b) ΔR_e; Interferometer alone: (c) ΔR_w, (d) ΔR_e; Hybrid device: (e) ΔR_w, (f) ΔR_e.

The influence of the liquid environment induces some slight deterioration of the quality of measurements, which is visible in the asymmetry of the difference signals; this means that accurate quantitative analysis has to be made with caution; however, the results clearly

demonstrate that the enhancement of sensitivity provided by the hybrid device with respect to the other 2 systems becomes much larger when the refractive index variations in the environment are smaller. For a very small refractive index variation such as the one induced by a change of 10% ethanol concentration ($\Delta n \sim 10^{-4}$), a 5-10-fold enhancement can be evaluated.

	System 2		System 3		System 1	
	$\lvert\Delta R_w\rvert_{max}$	δ	$\lvert\Delta R_w\rvert_{max}$	δ	$\lvert\Delta R_w\rvert_{max}$	δ
n=1.3647 ($P_{ethanol}$ = 80%)	0.023	0.037	0.079	0.068	0.073	0.122
n=1.3645 ($P_{ethanol}$ = 90%)	0.022	0.030	0.079	0.079	0.059	0.108

(a)Comparison with pure water

	System 2		System 3		System 1	
	$\lvert\Delta R_e\rvert_{max}$	δ	$\lvert\Delta R_e\rvert_{max}$	δ	$\lvert\Delta R_e\rvert_{max}$	δ
n=1.3647 ($P_{ethanol}$ = 80%)	0.009	0.01	0.018	0.018	0.046	0.064
n=1.3645 ($P_{ethanol}$ = 90%)	0.005	0.005	0.008	0.008	0.028	0.041

(b) Comparison with pure ethanol

Table 4.4 Amplitude of difference signal δ and maximum absolute values of difference signal $\lvert\Delta R\rvert_{max}$ for each mixture, with respect to pure water (a) and pure ethanol (b).

4.3.2 Detection of humidity (water vapor)

The purpose of this section is to investigate another promising potential of the hybrid structure for sensing application: monitoring of a variation of refractive index of the PSi interferometer. In chapter 2, it was pointed out that the density of the SiO_2 spacing layer could be modified by choosing the appropriate deposition technique; here we consider SiO_2 layers deposited by sputtering, with densities enabling the penetration of molecules through the SiO_2 layer into the PSi pores. If such a device is put in an environment containing, e.g., water molecules, the water molecules can penetrate inside the PSi pores and condensate on the walls, leading to a variation of refractive index of the material. This is the principle of the experiment presented in the following.

4.3.2.1 The experimental principle

The experiments for humidity sensing are performed using the fluidic cell. First, we assemble the fluidic cell containing a perfectly dry sample; next deionized water is injected into the cell with a syringe, and quickly pumped out of the cell with a second syringe to prevent any liquid

from penetrating directly into the PSi layer. Then, we hermetically close the whole circuit by connecting the 2 syringes at the end of the capillary tubes. Because of the remaining water inside the wet cell and tubes, the air in the cell becomes saturated with water vapor; some water molecules migrate through the porous SiO_2 layer and condensate onto the PSi walls.

Water condensation inside the PSi layer modifies the composition of the PSi and induces a variation of its effective refractive index, which leads to a variation of the reflectivity spectrum. Once saturation is reached, we can deduce the fraction of condensed water from LLL model:

$$n_{eff-vapor}^{2/3} = n_{si}^{2/3} P_{Si} + n_{air}^{2/3} P_{air-vapor} + n_{SiO_2}^{2/3} P_{SiO_2} + n_{water}^{2/3} f_w \qquad \text{(EQ-4-1)}$$

$$n_{eff-vapor}^{2/3} = n_{eff-oxi}^{2/3} + (n_{water}^{2/3} - 1) f_w \qquad \text{(EQ-4-2)}$$

Where f_w is the fraction of water, and $n_{\text{eff-vapor}}$ and $n_{\text{eff-oxi}}$ are the effective refractive indices of the PSi layer containing water and dry, respectively. After determining f_w, we can evaluate the corresponding thickness of condensed water by the following approximation:

$$d_{ew} = f_w / S \qquad \text{(EQ-4-3)}$$

Here, S is the specific surface of PSi, and d_{ew} is the effective thickness of water.

4.3.2.2 Experimental result and TMM simulation

The interferometer used for the vapor sensing experiment consists of a PSi layer with 4.85 µm thickness, which has been slightly oxidizied ($d_{SiO2} \sim 1.8$ nm). The refractive index is 1.66, corresponding to a porosity of 53% after oxidation. The NA array has the following average dimensions: A1 = 510 nm, A2 = 280 nm and Gap = 20 nm. The SiO_2 spacing layer was deposited with the AC450 sputtering system.

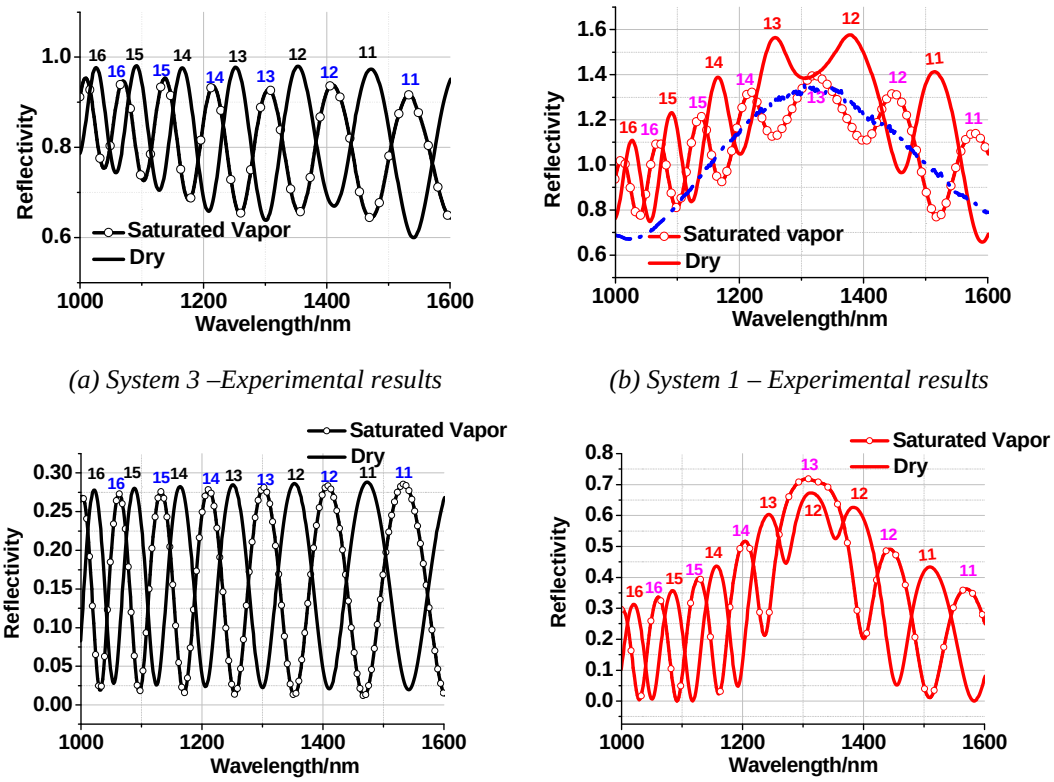

(a) System 3 –Experimental results

(b) System 1 – Experimental results

(c) System 3 – TMM simulation

(d) System 1 - TMM simulation

Fig 4.3.7 Reflectivity spectra of System 3: (a) and (c) for experimental results and TMM simulation respectively; Reflectivity spectra of System 1: (b) and (d) for experimental results and TMM simulation respectively. The curves with dots are for the structures after vapor saturation (60 min) and the ones without dots are for dry sample. The experimental spectrum of the NA alone is plotted in (b) as an indication.

During the whole experimental procedure of water condensation inside the PSi layer, the reflectivity spectra of both systems were monitored and recorded until the adsorption reached saturation. After saturation, dry air was injected into the wet cell through the syringes to dry the cell and the sample. During the drying process, a blue shift of the fringes was observed on the reflectivity spectra of both devices, until it overlapped with the initial spectrum after the PSi layer was completely dry. This means that the process is reversible.

The spectra of the structures in both initial (dry) and saturated states are presented in Fig 4.3.7 (*a*) and (b) for the interferometer alone and the hybrid device, respectively. The spectrum for the corresponding NA array alone is shown in Fig 4.3.7 (b) for comparison. No variation of resonance was observed for this system, indicating that the measured variations for the other 2 systems are only due to condensation within the PSi pores, and not at the NA surface.

These reflectivity spectra lead to the following observations:

1. In the case of the interferometer alone (Fig 4.3.7 (*a*)), there is a red shift of the fringes from the dry state (black curve) to the water-saturated state (black curve with open circles), due to the increase of the effective refractive index of PSi layer, which is attributed the adsorption of water molecules. According to equation (EQ-4-2), the effective refractive index of the water-saturated PSi layer can be estimated to $n_{\text{eff-vapor}} \sim 1.73$. The corresponding fraction of water f_w is about 21% and its effective thickness is about 1.6 nm, considering a specific surface around 100 m^2/cm^3. In order to check these values, we used these parameters to perform TMM simulations. The simulated reflectivity spectra of the interferometer in dry state (black curve) and in water-saturated state (black curve with circles) are shown in Fig 4.3.7 (*c*). Comparing it with the experimental results shown in Fig 4.3.7 (*a*), the fringe positions in both dry and saturated state fit well with each other.

2. In the case of the hybrid device (Fig 4.3.7 (*b*)), the adsorption also induces a red shift of each fringe that is highlighted by the fringe labels (order *m*) on the spectra. The adsorption of water on the PSi walls does not bring any shift of NA resonance. However, due to the shift of the fringes, the configuration of the reflectivity spectrum is modified, as was discussed in chapter 3. This can be clearly seen in Fig 4.3.7 (*b*): for the water-saturated structure, we see a broad peak at resonance (m = 13), while for the dry structure, we have a stronger splitting (m = 12), even if the first peak is not very pronounced on the experimental spectrum. This could be verified with TMM simulations, as shown in Fig 4.3.7 (*d*).

4.3.2.3 Sensitivity analysis

As before, we could expect the sensitivity to be in favor of the hybrid device, due to the contribution of the field enhancement of NA resonance. In order to verify this assumption, we consider again the reflectivity difference between the dry and water-saturated states, which is shown in Fig 4.3.8 (*a*) and (*b*), respectively, for experimental results and TMM simulations. The following sensitivity indicators can be deduced from these spectra:

- Interferometer alone:
  - experimental results: $\delta = 0.6$, $\delta_n = 7.5$
  - TMM simulation: $\delta = 0.53$, $\delta_n = 6.6$
- Hybrid device:
  - experimental results: $\delta = 1.11$, $\delta_n = 13.9$

- TMM simulation: $\delta = 0.84$, $\delta_n = 10.5$

In the case of humidity sensing, the gain in sensitivity for the hybrid device is about 2 in the experiments and 1.6 in the simulations, with respect to the interferometer alone. It has to be pointed out that this sensitivity enhancement probably depends on the configuration of the splitting at resonance, and could be optimized.

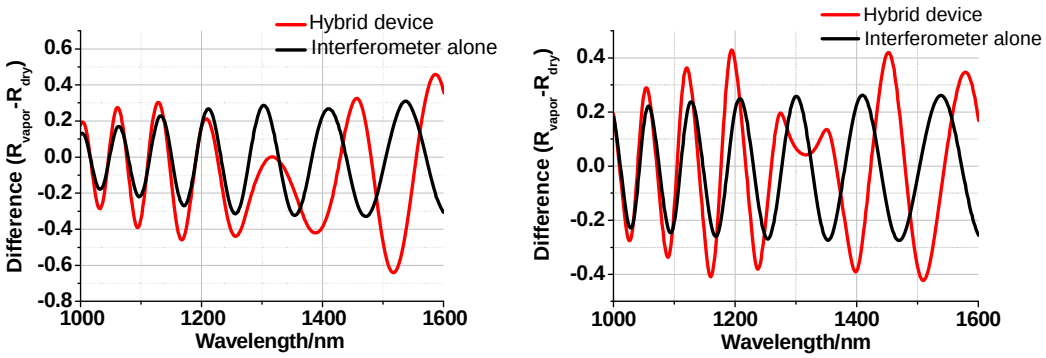

(a) Experimental results *(b) TMM simulation*

Fig 4.3.8 Difference signals of the structures between the dry and water-saturated states (red curve: hybrid device; black one: interferometer alone): (a) Experimental results; (b) TMM simulation

4.4 Conclusion

In this chapter, we explored the sensing potential of our hybrid device in different conditions. When the variation of environment is large, such as the deposition of a PMMA layer, or immersion in water, the hybrid device does not bring much gain in sensitivity compared to NAs alone. However, when the variation of refractive index is small, such as variations of ethanol percentage in a water / ethanol mixture, the sensitivity enhancement reaches a factor 5-10 compared to interferometer and NAs alone. An enhancement factor of ~2 is obtained with respect to the interferometer alone when sensing small variations of refractive index of the PSi layer, as in the case of water condensation inside the PSi. These experimental results were confirmed by simulations.

4.5 References

[4.1] http://microchem.com/pdf/PMMA_Data_Sheet.pdf

[4.2] Nowakowska, Janina, "The Refractive Indices of Ethyl Alcohol and Water Mixtures" (1939). Master's Theses. Paper 668.

Chapter 5 Conclusions and Perspectives

5.1 Conclusions

In this thesis, we realized and studied a novel hybrid photonic/plasmonic device exploiting the coupling between the surface plasmon resonance of a bowtie nano-antenna array and the photonic modes of a porous silicon interferometer. The research work included design, fabrication, characterization and investigation of the device potential for sensing applications.

The hybrid structure consists of a gold bowtie NA array on top of an interferometer, which is constituted by a monolayer of mesoporous silicon on its silicon substrate, with a silica spacing layer at its surface; throughout the whole studies presented in this thesis, the optical behavior of the hybrid structure was systematically compared to that of its two constituting elements, the NA array on one hand, and the interferometer on the other hand.

After optimization of the technological processes for the realization of the different devices, a study of the NAs alone was presented, in order to gain understanding about the influence of the different geometrical parameters of the bowtie NA, as well as the coupling mechanisms between the 2 triangle-shaped gold particles leading to the resonance. We discussed the resonance tuning obtained by adjusting the triangle dimensions and the inter-particles distance.

In a second step, the coupling mechanisms occurring within the hybrid structure were studied, following 2 different phenomenological approaches: the point of view of the interferometer and of the resonator.

- The proposed interferometer approach was to consider the NA array to be equivalent to a homogeneous layer with same dielectric function placed on top of the interferometer. A phase matching model based on thin film interference was developed layer-by-layer, in order to describe the multi-layer interferences in the device and to analyze the fringe variations induced by the introduction of the equivalent layer.
- In the resonator model, we used a complementary approach, which views the bowtie NA array as a harmonic oscillator. The coupling between NAs and interferometer was

investigated with coupled mode theory and governed by 3 key parameters: the quality factors for coupling and loss, respectively, and the resonant wavelength.

This fundamental study highlighted several highly-interesting phenomena:

- The optical response of the hybrid structure exhibits both the enhancement of NA resonance and the fringe pattern of the interferometer, with some additional features;
- A splitting of the interferometer fringes occurs at NA resonance, indicating strong coupling between the NAs and the interferometer;
- Tuning of the splitting strength can be achieved, either by modifying the optical path of the interferometer at given NA resonance, or by modifying the resonant wavelength of NAs for a given interferometer structure.

As an application of this study, we also showed that it is possible to perform an experimental mapping of the NAs dielectric constant by exploiting the fringe positions on the reflectivity measurements.

Finally, we explored the sensing potential of our hybrid device in different conditions, both with experiments and simulations. When the variation of environment is large, such as deposition of a PMMA layer, or immersion in water, the hybrid device does not bring much gain in sensitivity compared to NAs alone. However, when the variation of refractive index is small, such as variations of ethanol percentage in a water / ethanol mixture, the sensitivity enhancement reaches a factor 5-10 compared to NAs alone. An enhancement factor of ~2 is obtained with respect to the interferometer alone when sensing small variations of refractive index of the PSi layer, as in the case of water condensation inside the PSi.

5.2 Perspectives

The perspectives of this PhD work are numerous. The first one would be a direct continuity of the study presented in this thesis: a further investigation of the potential of our proposed hybrid device for sensing applications. In a second step, the 2 elements constituting the hybrid structure – the interferometer and the NA array – could be modified in order to enlarge the study to a wider family of devices with greater properties and performances.

Further investigation of the potential of our proposed hybrid device for sensing applications:

The works presented in this thesis have been mainly concerned with the detection of environment variations. Application to biosensing has not been studied yet, and would be of great interest. Such an application would rely on biomolecule immobilization at the surface of the gold NAs via thiol binding, as illustrated in Fig P-1 (a). Different standard biomolecule interactions could be investigated with varying molecule sizes, densities and configurations, in order to provide an overview on the device performances and compare with other studies: DNA hybridization, protein interaction such as biotin/avidin, or detection of virus via their interaction with sugar. Depending on molecule size and density, the response of the device will be different, as illustrated in the preliminary simulations shown in Fig P-1 (b) in the particular case of the grafting of a dense molecule layer with varying thickness.

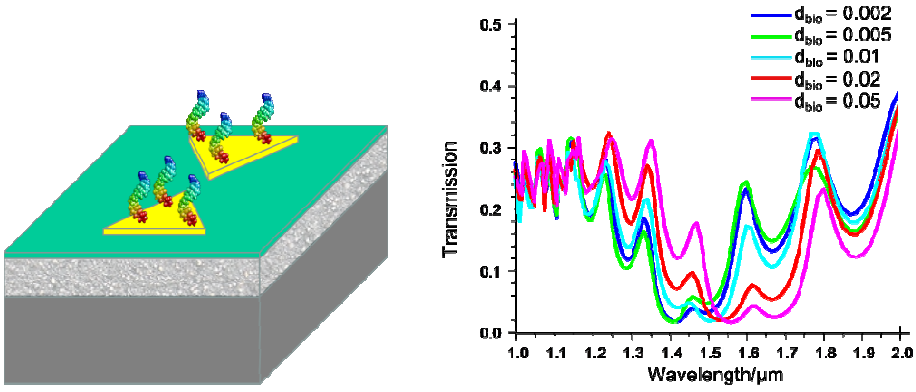

(a) *(b)*

Fig P-1 (a) Schematic view of the hybrid device used for biomolecules sensing and (b) simulation showing the optical response in the case of the sensing of a dense molecule layer with different thicknesses d_{bio} (the thicknesses are given in µm).

The whole investigation of sensing with our hybrid device has been focussing on one particular design of the NAs and the interferometer. As was shown in chapter 3, the optical response of the device can be tuned by varying the parameters of the porous silicon and NAs. Hence, an optimization of these parameters should be performed in order to obtain more interesting optical responses for sensing applications, in particular considering that the largest sensitivity of the device is around the NA resonance where the fringe patterns is strongly modified by the splitting. Furthermore, a larger optical path in the porous silicon interferometer would enable to have thinner and more numerous fringes, with probable sensitivity enhancement; similarly, a thinner NA resonance positioned at smaller wavelengths (~1200-1300 nm) would be of high interest, especially for applications in liquid environment.

Another great potential for sensing arises from the controlled porosity of the SiO_2 spacing layer. In this thesis we have presented the possibility to detect condensation of vapor onto the porous silicon walls; with specific functionalization it could also be envisaged to use the SiO_2 layer as a filter designed to let only the target species penetrate. As illustrated in Fig P-2, double sensing could also be investigated, where NAs and PSi layer would be functionalized with different targets. Indeed, the functionalization chemistries for gold and silicon are orthogonal, which means that both materials can be functionalized independently. With a very thorough understanding of the mechanisms for fringe evolution in both elements, in order to separate the different signals, simultaneous sensing of two targets could be possible.

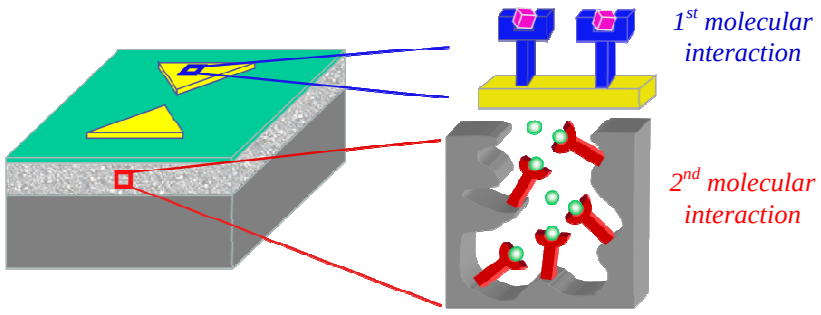

Fig P-2 Artistic view of double sensing

Finally, a further study of the fringe splitting, as well as the optimization of the structure in views of better controlling this phenomenon, might open up new routes towards sensing applications exploiting different sensing mechanisms.

Investigation of a larger variety of designs

The idea of our hybrid device can be enlarged and adapted to a large variety of new devices, in views of improving the performances. As illustrated in Fig P-3, there are two ways to achieve this. A modification of the plasmonic nanostructure, e.g., by replacing the bowtie NAs by nanorods, or different dimmers, or using a different metal, would enable to tune the NA resonance wavelength, lineshape and sensitivity. Similarly, replacing the interferometer by another photonic device, such as a microcavity or a photonic crystal yielding a photonic mode of much higher finesse, would enable strong coupling between the plasmonic resonance and the photonic mode, leading to a probable enhancement in sensitivity compared to the system with interferometer. Coupling of plasmonic nanostructures with a Fabry-Perot microcavity has already been proposed, as was presented in chapter 1 [P-1, P-2, P-3]; coupling between a photonic crystal and a bowtie NA has also been recently investigated at INL for different applications, and was highly promising [P-4]. The realization of photonic crystals in mesoporous silicon has also been successfully achieved and very promising optical performances were demonstrated [P-5]. This means that all the basic blocks are available for the investigation of new hybrid structures with a larger variety of designs.

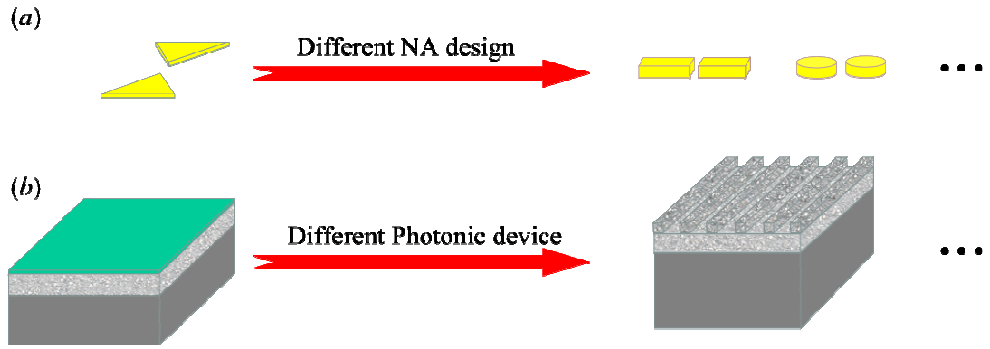

Fig P-3 Two different ways to investigate new designs of hybrid structures: (a): exploration of other plasmonic nanostructures, (b): exploration of other photonic devices

5.3 References

[P-1] Ameling, Ralf, Lutz Langguth, Mario Hentschel, Martin Mesch, Paul V. Braun, and Harald Giessen. "Cavity-enhanced localized plasmon resonance sensing." Applied Physics Letters 97, no. 25 (2010): 253116-253116.

[P-2] Ameling, Ralf, and Harald Giessen. "Cavity plasmonics: large normal mode splitting of electric and magnetic particle plasmons induced by a photonic microcavity." Nano letters 10, no. 11 (2010): 4394-4398.

[P-3] Schmidt, Markus A., Dang Yuan Lei, Lothar Wondraczek, Virginie Nazabal, and Stefan A. Maier. "Hybrid nanoparticle - microcavity-based plasmonic nanosensors with improved detection resolution and extended remote-sensing ability." Nature communications 3 (2012): 1108.

[P-4] Zhang, Taiping, Ali Belarouci, Ségolène Callard, Pedro Rojo Romeo, Xavier Letartre, and Pierre Viktorovitch. "Plasmonic-Photonic Hybrid Nanodevice."International Journal of Nanoscience 11, no. 04 (2012).

[P-5] C. Jamois, C. Li, E. Gerelli, R. Orobtchouk, T. Benyattou, Y. Chevolot, V. Monnier and E. Souteyrand, “New Concepts of Integrated Photonic Biosensors Based on Porous Silicon,” Biosensors - Emerging Materials and Applications, Edited by Pier Andrea Serra, Publisher: InTech, 2011, ISBN 978-953-307-328-6

Part III. Appendices

Appendix A: Multi-layer Thin film interference

A-1 Single layer-PSi/Si

As shown in Fig A-1-1, when a plane wave is normally incident on the substrate surface, a part of it is reflected at the upper interface (Interface 2), while the other part is transmitted. When the transmitted beam reaches the lower interface (Interface 1) of the thin film, a part of the beam is transmitted and the other part is reflected back towards the upper interface (green beam on Fig A-1-1). At interface 2, the beam component directly reflected (orange beam) interferes with the ones that have travelled through the thin film (green beam) to build up the reflectivity response of the film.

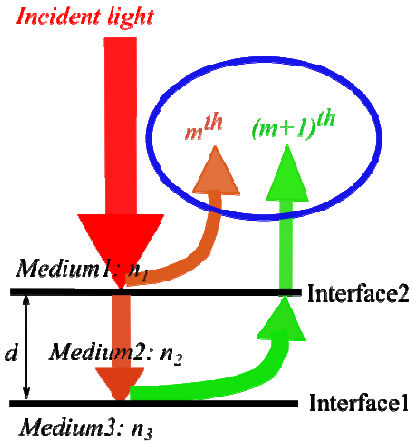

Fig A-1-1 Schematic illustration of interference of thin layer with thickness d and refractive index n_2

According to the Fresnel theory of reflection [AP-1, AP-2, AP-3], the percentage of reflected electric field – the total reflection coefficient r_{R1} – of this single-layer thin film could be expressed as:

$$r_{R1} = \frac{|r_{23}|\exp\left[i\left(\Delta\varphi_1 + \varphi_{23}\right)\right] - |r_{21}|\exp\left(i\varphi_{21}\right)}{1 - |r_{23}||r_{21}|\exp\left[i\left(\Delta\varphi_1 + \varphi_{21} + \varphi_{23}\right)\right]} = |r_{R1}|\exp\left(i\Phi_1\right) \qquad \text{(EQ-A-1-1)}$$

Where $|r_{R1}|$ and Φ_1 are the amplitude and the argument of r_{R1}, respectively; $r_{ij} = \frac{n_i - n_j}{n_i + n_j}$ is the Fresnel reflection coefficient when the light is incident from medium *i* towards medium *j* and reflected at the interface between both media (In this case, the interface will be noted as

"Medium i / Medium j interface" in the following). Here, the polarization of the incident beam is not specified, since the coefficients with *s* and *p* polarization are the same at normal incidence. φ_{ij} is the argument of r_{ij}; $\Delta\varphi_1 = \frac{4\pi}{\lambda} n_2 d$ is the phase difference due to the propagating path within the thin film between the reflected light beams at the 2 interfaces.

The total reflectivity of this single layer interferometer will be:

$$R_1 = (r_{R1} * r_{R1}^*) = |r_{R1}|^2 = \frac{|r_{23}|^2 + |r_{21}|^2 - 2|r_{23}||r_{21}|\cos(\Delta\varphi_1 + \varphi_{23} - \varphi_{21})}{1 + (|r_{23}||r_{21}|)^2 - 2|r_{23}||r_{21}|\cos(\Delta\varphi_1 + \varphi_{23} + \varphi_{21})} \quad \text{(EQ-A-1-2)}$$

The extraction for the phase matching equation is difficult from the above equation. However, according to the dielectric property of the media, specific simplification and approximation is possible.

For example, if low absorbing media are considered, their refractive index n_i and Fresnel reflection coefficient r_{ij} at the interfaces will be real. As an example, the PSi monolayer having the refractive index n_{PSi} shown in Fig 3.2.8 (*b*) and a thickness $d_{PSi} = 5.66\ \mu m$ is considered to illustrate the following investigation in the whole Appendix A.

In order to have a clear separation of Fresnel reflection coefficient at the interfaces and total reflection coefficient of each device, in the following we define new notations for them. For example, the Fresnel reflection coefficient at the PSi/Si interface in Fig A-1-1, will be noted as $r_{PSi\text{-}Si}$, and the total reflection coefficient of the monolayer interferometer will be noted as $r_{Air/PSi/Si}$.

Thus, considering $n_1 = 1$, $n_2 = n_{PSi}$, $n_3 = n_{Si}$, with $1 < n_{PSi} < n_{Si}$, we have:

$$r_{23} = r_{PSi-Si} = |r_{PSi-Si}|\exp(i\varphi_{PSi-Si}) \text{ with } |r_{PSi-Si}| < 1 \,\&\, \varphi_{PSi-Si} = \pi$$
$$r_{21} = r_{PSi-Air} = |r_{PSi-Air}|\exp(i\varphi_{PSi-Air}) \text{ with } 0 < |r_{PSi-Air}| < 1 \,\&\, \varphi_{PSi-Air} = 0$$

Hence, the total reflection coefficient r_{R1} and reflectivity R_1 could be simplified as:

$$r_{R1} = \frac{|r_{PSi-Si}|\exp[i(\Delta\varphi_1 + \pi)] - |r_{PSi-Air}|}{1 - |r_{PSi-Si}||r_{PSi-Air}|\exp[i(\Delta\varphi_1 + \pi)]} \quad \text{(EQ-A-1-3)}$$

$$R_1 = (r_R * r_R^*) = 1 + \frac{\left(|r_{PSi-Si}|^2 - 1\right)\left(1 - |r_{PSi-Air}|^2\right)}{1 + \left(|r_{PSi-Si}||r_{PSi-Air}|\right)^2 + 2|r_{PSi-Si}||r_{PSi-Air}|\cos(\Delta\varphi_1)} \qquad \text{(EQ-A-1-4)}$$

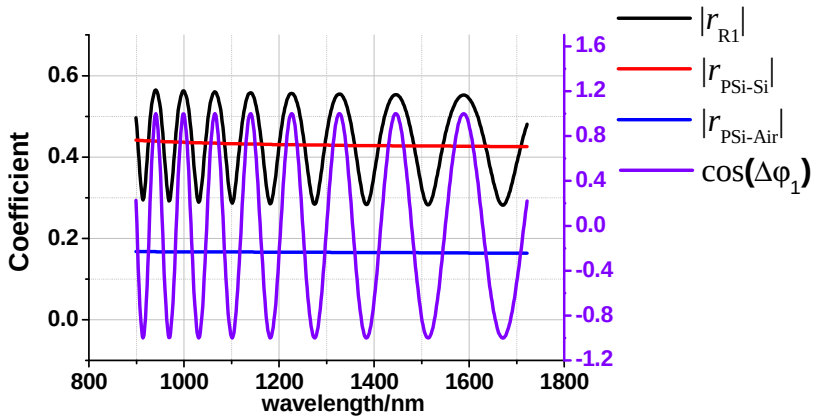

(a)

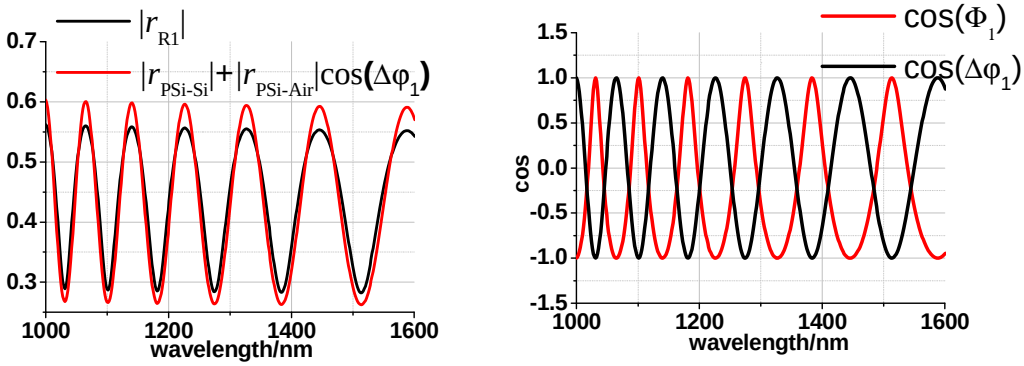

(b) *(c)*

Fig A-1-2 (a) amplitude of r_{PSi-Si}, $r_{PSi-Air}$ and r_{R1} vs. λ (left axis) and cos(Δφ₁) vs. λ (right axis); (b) $|r_{R1}|$ and $|r_{PSi-Si}|+|r_{PSi-Air}|\cos(\Delta\varphi_1)$ vs. λ; (c) cos(Φ₁) and cos(Δφ₁+π) vs. λ

The amplitudes of r_{PSi-Si}, $r_{PSi-Air}$ and r_{R1} depending on wavelength are plotted in Fig A-1-2 (a) with the left axis. The cosine function of the phase $\Delta\varphi_1 = \frac{4\pi}{\lambda} n_2 d$ with the variation of wavelength is plotted in the same figure as well with the right purple axis. From it, we can see that the amplitude $|r_{R1}|$ is modulated by the amplitude of r_{PSi-Si} and $r_{PSi-Air}$; as shown in Fig A-1-2 (b), it could be fitted with the simple following function:

$$|r_{R1}| \approx |r_{PSi-Si}| + |r_{PSi-Air}|\cos(\Delta\varphi_1) \qquad \text{(EQ-A-1-5)}$$

In order to extract an analytical expression for argument of r_{R1} (Φ_1) and confirm the phase matching model in the thesis, Φ_1 is compared to the value of $\Delta\varphi_1$. The cosine values of these 2

arguments are shown in Fig A-1-2 (c), leading to the following observation:

$$\cos(\Delta\varphi_1 + \pi) \approx \cos(\Phi_1) \qquad \text{(EQ-A-1-6)}$$

Hence,

$$\Delta\varphi_1 = (2m-1)\pi + \Phi_1 \quad m = 0, \pm 1, \pm 2, \cdots \qquad \text{(EQ-A-1-7)}$$

The phase matching model for single layer thin film can be extracted as:

$$R_1 = R_{1\max} \text{ if } \Delta\varphi_1 = 2m\pi, \quad m = 0,1,2,\ldots, \text{ or } \quad \cos(\Phi_1) = -1$$

$$\text{with } \lambda_{\max} = \frac{4n_{PSi}d_{PSi}}{2m} \qquad \text{(EQ-A-1-8)}$$

In the following, the phase matching model for the multilayer systems will be determined based on the above analysis.

A-2 Two-layer interferometer - SiO_2/PSi/Si

An extra layer is put on top of the previous mono-layer interferometer, in order to form a 2-layer system. As an example, we consider a 80 nm thick SiO_2 layer on top of the previous PSi layer. Here, we have 4 media, which are: medium 1: semi-infinite Air environment, medium 2: SiO_2 with refractive index n_{SiO2} and thickness d_{SiO2}, medium 3: PSi with refractive index n_{PSi} and thickness d_{PSi} and medium 4: semi-infinite Si substrate, as sketched in Fig A-2-1.

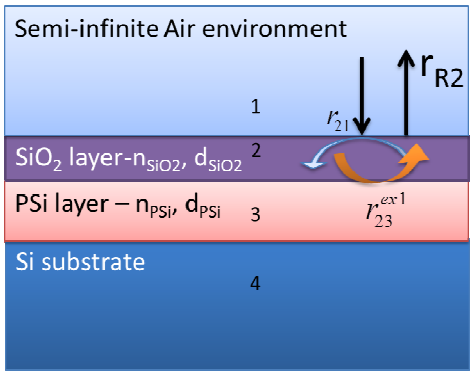

Fig A-2-1 Schematic view of an extra thin SiO_2 layer on top of the PSi/Si system

When a plane wave is normally incident on the system, it could be assumed, for simplicity, that the incident beam experiences multiple reflections/transmissions at each of the 2 new interfaces: Air/SiO_2 interface and SiO_2/PSi interface. The PSi/Si layers could be viewed as a medium associated to a specific refractive index and the Fresnel coefficient at the SiO_2/PSi interface, noted as r_{23}^{ex1}. Thus, the total reflection coefficient of this 2-layer system r_{R2} could be simply written as:

$$r_{R2} = \frac{r_{23}^{ex1}\exp(i\Delta\varphi_1^{ex1}) - r_{SiO_2-Air}}{1 - r_{23}^{ex1} r_{SiO_2-Air}\exp(i\Delta\varphi_1^{ex1})} \qquad \text{(EQ-A-2-1)}$$

where $\Delta\varphi_1^{ex1} = \frac{4\pi}{\lambda} n_{SiO2} d_{SiO2}$, $r_{\text{SiO2-Air}}$ is the Fresnel reflection coefficient at the SiO_2/Air interface.

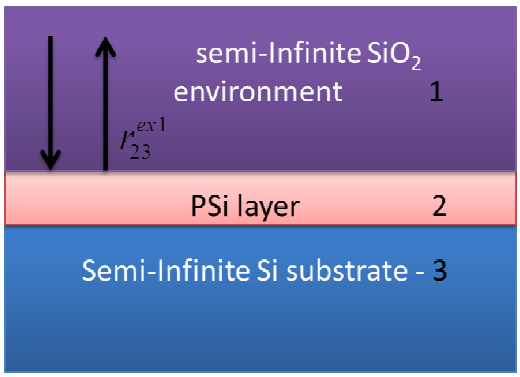

Fig A-2-2 Schematic view of single layer PSi/Si system in semi-infinite SiO_2 environment

To calculate r_{23}^{ex1}, a new single layer interferometer is built and illustrated in Fig A-2-2. It is composed of the thin PSi layer (medium 2) sandwiched between semi-infinite SiO_2 environment (medium 1) and semi-infinite Si substrate (medium 3). Hence, r_{23}^{ex1} is $r_{SiO2/PSi/Si}$.

By following the equation A-1-1, we have:

$$r_{SiO_2/PSi/Si} = \frac{r_{PSi-Si}\exp(i\Delta\varphi_1) - r_{PSi-SiO_2}}{1 - r_{PSi-Si}r_{PSi-SiO_2}\exp(i\Delta\varphi_1)} = \left|r_{SiO_2/PSi/Si}\right|\exp\left(i\varphi_{SiO_2/PSi/Si}\right) \quad \text{(EQ-A-2-2)}$$

where $\Delta\varphi_1 = \frac{4\pi}{\lambda} n_{PSi} d_{PSi}$. Here, $\left|r_{SiO_2/PSi/Si}\right|$ and $\varphi_{SiO_2/PSi/Si}$ are the amplitude and argument of $r_{SiO2/PSi/Si}$, respectively.

In Fig A-2-3 (a), the amplitudes of $r_{PSi-SiO_2}$, r_{PSi-Si} and $r_{SiO_2/PSi/Si}$ are plotted. From it, we can see that $\left|r_{PSi-Si}\right| >> \left|r_{PSi-SiO_2}\right|$ and the amplitude of $r_{SiO_2/PSi/Si}$ is modulated by the value of $\left|r_{PSi-Si}\right|$, $\left|r_{PSi-SiO_2}\right|$ and $\cos(\Delta\varphi_1)$. Fig A-2-3(*b*) presents the comparison between the arguments $\varphi_{SiO_2/PSi/Si}$ and $\Delta\varphi_1 + \pi$, expressed as cosine functions. We can see that both arguments are in phase. Hence, we can write:

$$\left|r_{SiO_2/PSi/Si}\right| = \left|r_{PSi-Si}\right| + \left|r_{PSi-SiO_2}\right|\cos(\Delta\varphi_1 + \pi) \quad \text{(EQ-A-2-3)}$$

$$\varphi_{SiO_2/PSi/Si} = \Delta\varphi_1 - (2m-1)\pi \quad \text{(EQ-A-2-4)}$$

The approximation expressed in equation A-2-3 is validated by the good agreement between

both terms shown in Fig A-2-3(c).

Combining (EQ-A-2-3), (EQ-A-2-4) and (EQ-A-2-1), the following equation is obtained:

$$r_{R2}=\frac{\left|r_{SiO_2/PSi/Si}\right|\exp\left[i\left(\Delta\varphi_2+\pi\right)\right]-r_{SiO_2-Air}}{1-\left|r_{SiO_2/PSi/Si}\right|r_{SiO_2-Air}\exp\left[i\left(\Delta\varphi_2+\pi\right)\right]}=\left|r_{R2}\right|\exp(\mathrm{i}\,\Phi_2) \qquad \text{(EQ-A-2-5)}$$

$$\Delta\varphi_2=\Delta\varphi_1+\Delta\varphi_1^{ex1}=\frac{4\pi}{\lambda}\left(n_{PSi}d_{PSi}+n_{SiO2}d_{SiO2}\right)$$

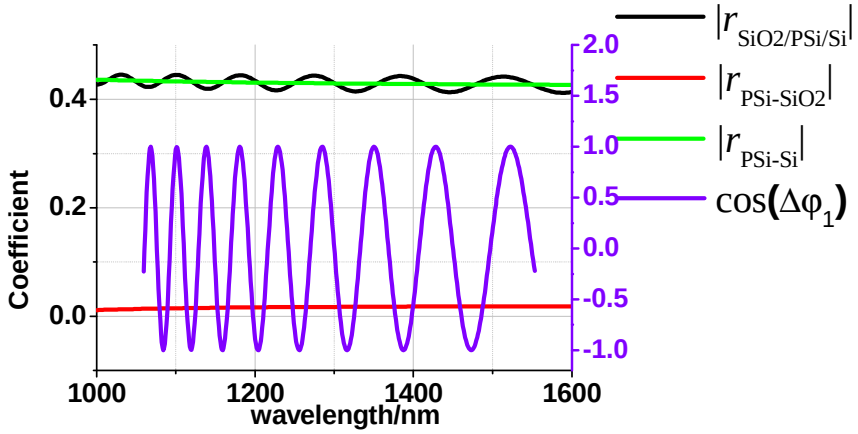

(a)

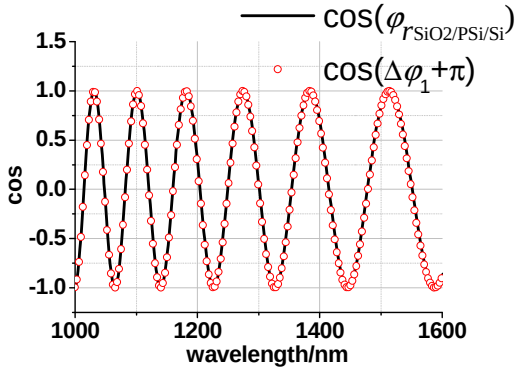

(b)

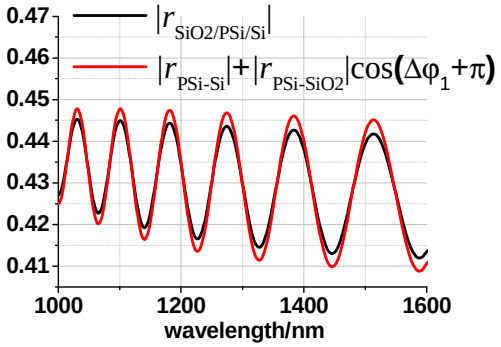

(c)

Fig A-2-3 (a) amplitude of r_{PSi-Si}, $r_{PSi-SiO_2}$ and $r_{SiO_2/PSi/Si}$ vs. λ (left axis) and cos(Δφ1) vs. λ (right axis); (b) comparison between the phases cos(Φ1) and cos(Δφ1+π) vs. λ; (c) comparison between the $\left|r_{SiO_2/PSi/Si}\right|$ and $\left|r_{PSi-Si}\right|+\left|r_{PSi-SiO_2}\right|\cos(\Delta\varphi_1+\pi)$ vs. λ

The argument of r_{R2} is labeled as Φ_2 and $\left|r_{R2}\right|$ is the amplitude. By fitting their values, we obtain:

$$|r_{R2}| \approx |r_{PSi-Si}| + \frac{|r_{PSi-Si}| + |r_{SiO_2-Air}|}{2} |r_{SiO_2/PSi/Si}| \cos(\Delta\varphi_2) \qquad \text{(EQ-A-2-6)}$$

$$\Phi_2 \approx \Delta\varphi_2 + \pi - 2m\pi \qquad \text{(EQ-A-2-7)}$$

Both approximations are validated by the good agreement between the different terms, as illustrated in Fig A-2-4 (a) and (b). Hence, the phase matching model for this 2-layer system can be expressed as:

$$\cos(\Phi_2) = -1 \text{ or } \Delta\varphi_2 = 2m\pi \qquad \text{(EQ-A-2-8)}$$

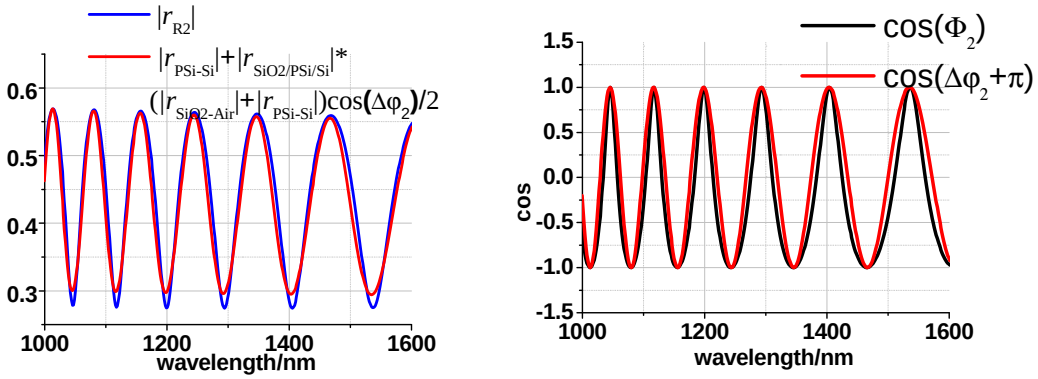

(a) *(b)*

Fig A-2-4 (a) $|r_{R2}|$ *and* $|r_{PSi-Si}| + \frac{|r_{PSi-Si}| + |r_{SiO_2-Air}|}{2} |r_{SiO_2/PSi/Si}| \cos(\Delta\varphi_2)$ *vs. λ; (b) cos(Φ₂) and cos(Δφ₂+π) vs. λ*

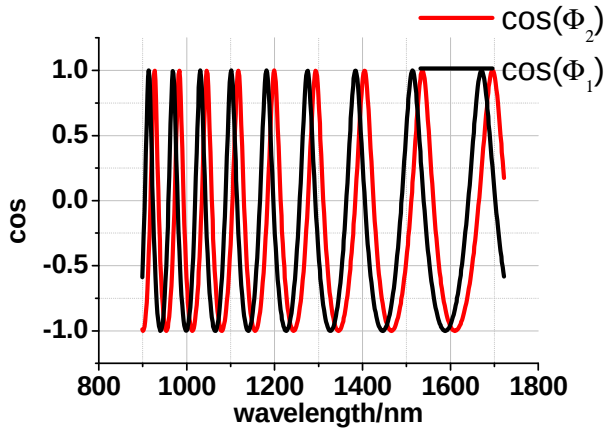

Fig A-2-5 Comparison between the arguments of the single-layer and 2-layer systems, cos (Φ₁) and cos(Φ₂)

Finally, comparing the arguments $\Phi_{1 \text{ and}} \Phi_2$ for the single-layer and 2-layer systems, a red shift is observed upon addition of the silica layer on top of the interferometer, as illustrated in Fig A-2-5.

A-3 Three-layer interferometer – Absorbing layer/SiO_2/PSi/Si

As illustrated in Fig A-3-1, an extra thin absorbing layer is added on top of the previous 2-layer system, constituting a 3-layer system. Here, we have 5 media, which are:

- Medium 1: semi-infinite Air environment,
- Medium 2: absorbing layer with a refractive index n_A and a thickness d_A (like: Au layer or the equivalent layer of NAs);
- Medium 3: SiO_2 with a refractive index n_{SiO2} and a thickness d_{SiO2};
- Medium 4: PSi with a refractive index n_{PSi} and a thickness d_{PSi};
- Medium 5: semi-infinite Si substrate.

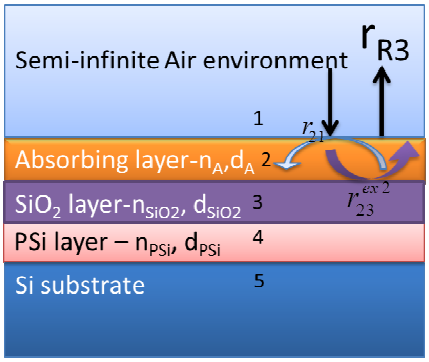

Fig A-3-1 Schematic view of an extra thin absorbing layer put on top of 2-layer SiO_2/PSi/Si system

It is worth mentioning that we consider an absorbing material with a complex refractive index: $n_A = \mathrm{Re}(n_A) + i\ \mathrm{Im}(n_A)$.

From the previous section, we can write:

$$r_{R3} = \frac{r_{23}^{ex2}\exp(i\Delta\varphi_1^{ex2}) - r_{A-Air}}{1 - r_{23}^{ex2} r_{A-Air}\exp(i\Delta\varphi_1^{ex2})} = |r_{R3}|\exp(\mathrm{i}\,\Phi_3) \qquad \text{(EQ-A-3-1)}$$

Where $\Delta\varphi_1^{ex2} = \dfrac{4\pi n_A d_A}{\lambda}$, r_{23}^{ex2} is the total reflection coefficient of 2-layer system: SiO_2/PSi/Si in the environment of the absorbing material (noted as $r_{A/SiO2/PSi/Si}$) and $r_{A\text{-}Air}$ is the Fresnel reflection coefficient at the Absorbing medium/Air interface (noted as $r_{A/Air}$).

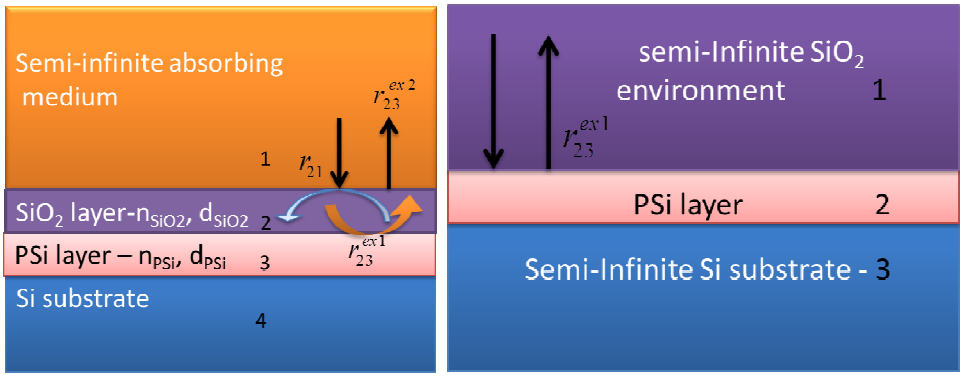

(a) r_{23}^{ex2} *(b)* r_{23}^{ex1}

Fig A-3-2 Schematic view of the formalism for the calculation of (a) $r_{23}^{ex2} = r_{A/SiO_2/PSi/Si}$ *; and (b)* $r_{23}^{ex1} = r_{SiO_2/PSi/Si}$

Similarly to the calculation of r_{23}^{ex1} in last section, r_{23}^{ex2} could be expressed as:

$$r_{23}^{ex2} = \frac{r_{SiO_2/PSi/Si}\exp(i\Delta\varphi_1^2) - r_{SiO_2-A}}{1 - r_{SiO_2/PSi/Si}\, r_{SiO_2-A}\exp(i\Delta\varphi_2^{'})} = \left|r_{A/SiO_2/PSi/Si}\right|\exp(i\,\varphi_{A/SiO_2/PSi/Si}) \quad \text{(EQ-A-3-2)}$$

Where $\left|r_{A/SiO_2/PSi/Si}\right|$ and $\varphi_{A/SiO_2/PSi/Si}$ are the amplitude and argument of r_{23}^{ex2}, respectively. We also have:

$$\left|r_{SiO_2/PSi/Si}\right| = \left|r_{PSi-Si}\right| + \left|r_{PSi-SiO_2}\right|\cos(\Delta\varphi_1) \quad \text{(EQ-A-3-3)}$$

$$\Delta\varphi_1 = \frac{4\pi}{\lambda} n_{PSi} d_{PSi} \quad \text{(EQ-A-3-4)}$$

$$\varphi_{SiO_2/PSi/Si} = \Delta\varphi_1 + \pi - 2m\pi \quad \text{(EQ-A-3-5)}$$

$$\Delta\varphi_1^{ex1} = \frac{4\pi}{\lambda} n_{SiO2} d_{SiO2} \quad \text{(EQ-A-3-6)}$$

$$\Delta\varphi_2 = \frac{4\pi}{\lambda}\left(n_{PSi} d_{PSi} + n_{SiO2} d_{SiO2}\right) \quad \text{(EQ-A-3-7)}$$

Now we consider that the absorbing material is gold, with a layer thickness d_{Au} = 30 nm, and the refractive index n_{Au} plotted in Fig 3.2.8 in chapter 3. The variations of $|r_{Au/SiO2/PSi/Si}|$ and

$\cos(\varphi_{Au/SiO2/PSi/Si})$ with the wavelength are plotted in Fig A-3-3 (*a*).

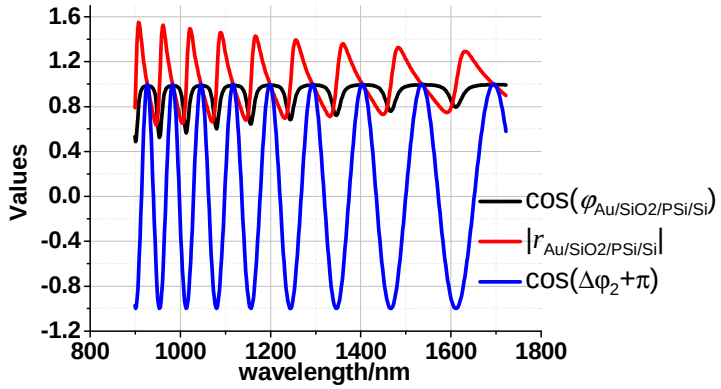

(a)

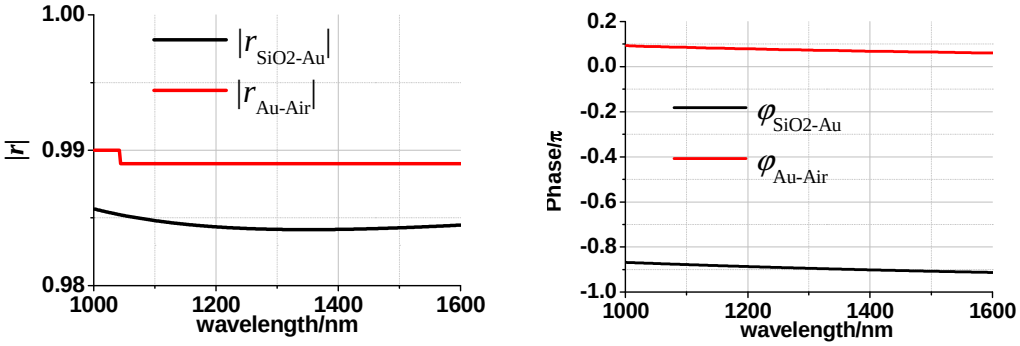

(b) *(c)*

Fig A-3-3 (a) $\cos(\varphi_{Au/SiO2/PSi/Si})$, $\cos(\Delta\varphi_2+\pi)$ and $|r_{Au/SiO2/PSi/Si}|$ vs. λ; (b) Variations of $|r_{SiO2\text{-}Au}|$, $|r_{Au\text{-}Air}|$; (c) $\varphi_{SiO2\text{-}Au}/\pi$, $\varphi_{Au\text{-}Air}/\pi$ vs. λ

From Fig A-3-3 (*a*), we can see that both amplitude and argument of $r_{23}^{ex2} = r_{Au/SiO_2/PSi/Si}$ are highly modulated and it is difficult to obtain their analytical expressions as was the case in the previous sections. Comparing to $\cos(\Phi_2)$ (i.e. $\cos(\Delta\varphi_2 + \pi)$), $|r_{Au/SiO2/PSi/Si}|$ already shows a clear blue shift. However, comparing $\cos(\Phi_2)$ and $\cos(\varphi_{Au/SiO2/PSi/Si})$, we can see that their peaks and dips are in phase.

Combining equations A-3-5, A-3-6 and A-3-1, we have:

$$r_{R3} = \frac{\left|r_{Au/SiO_2/PSi/Si}\right|\exp\left[i\left(\Delta\varphi_1^{ex2} + \varphi_{Au/SiO_2/PSi/Si}\right)\right] - \left|r_{Au-Air}\right|\exp\left(i\varphi_{Au-Air}\right)}{1 - \left|r_{Au/SiO_2/PSi/Si}\right|\left|r_{Au-Air}\right|\exp\left[i\left(\Delta\varphi_1^{ex2} + \varphi_{Au/SiO_2/PSi/Si} + \varphi_{Au-Air}\right)\right]}$$

The amplitude and cosine function of the argument for both r_{R2} and r_{R3} as a function of wavelength are plot in Fig A-3-4. By comparing the 2 arguments Φ_2 (blue line with dots) and Φ_3 (pink line), we can put into evidence an extra phase shift:

$$\Phi_3 = \Phi_2 + \Delta\varphi_{tot}$$

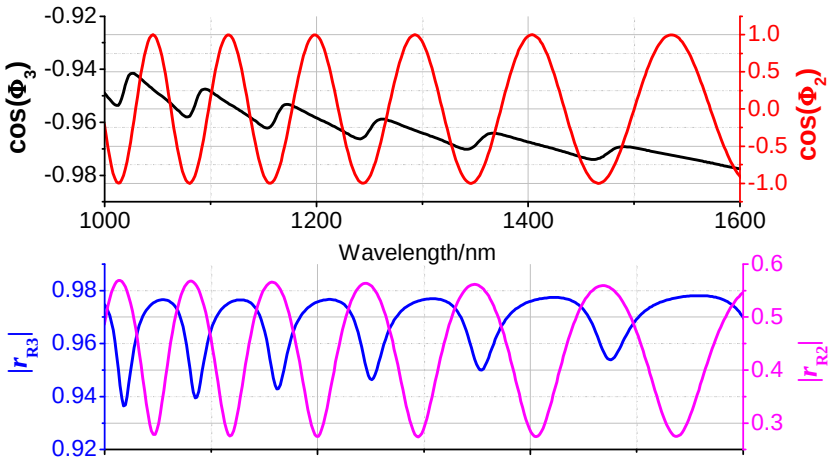

Fig A-3-4 The black curve with main left axis is for $|r_{R3}|$, the pink curve with main right axis is for $cos(\Phi_3)$ and the pure blue curve and the blue curve with circles with the insert axis are for $|r_{R2}|$ and $cos(\Phi_2)$, respectively.

In order to evaluate the value of $\Delta\varphi_{tot}$, the system shown in Fig A-3-5 is considered, where the absorbing layer is considered to be sandwich between a semi-infinite air substrate and a semi-infinite silica environment. The phase shift due to the introduction of the extra absorbing layer $\Delta\varphi_{tot}$ in the 3-layer system should be equal to the argument of the total reflection coefficient $r_{SiO2/A/Air}$ of the thin film interferometer shown in Fig A-3-5.

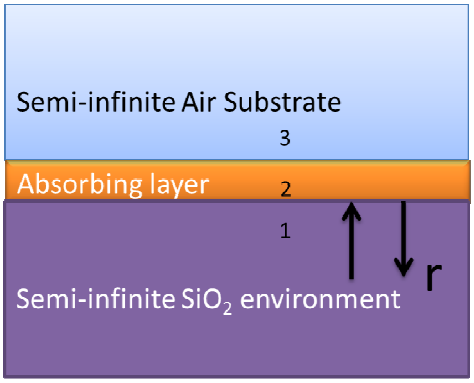

Fig A-3-5 Schematic view of the absorbing layer sandwiched between semi-infinite SiO_2 environment and Air substrate

The value of $\Delta\varphi_{tot}$ is crucial to deduce the fringes shift direction for the 3 - layer system with respect to the 2 - layer system. For a gold layer and a NA equivalent layer put on top of the previous 2 - layer system, the total phase shifts $\Delta\varphi_{tot}$ are calculated according to the equation

A-3-8 and are plotted in Fig A-3-6 (a) and (b), respectively.

$$r = \frac{r_{A-Air}\exp(i\Delta\varphi_1^{ex2}) - r_{A-SiO_2}}{1 - r_{A-Air}r_{A-SiO_2}\exp(i\Delta\varphi_1^{ex2})} = |r|\exp(\mathrm{i}\,\varphi_{tot}) \qquad \text{(EQ-A-3-8)}$$

We can see that in the case of the gold layer, the value of $\Delta\varphi_{tot}$ is close to –π over the whole wavelength range. This means that a blue shift is expected upon addition of the gold layer on top of the SiO_2/PSi/Si system. In the case of the NA equivalent layer, $\Delta\varphi_{tot}$ is first increasingly negative with a variation between 0 and –π before NA resonance, and shows an abrupt change from –π to +π at resonance, before decreasing again for larger wavelengths. This means that upon addition of the NA layer on top of the SiO_2/PSi/Si system, before resonance we should observe a blue shift of the fringes, with increasing amplitude for wavelengths closer to the resonance; after resonance we should observe a red shift.

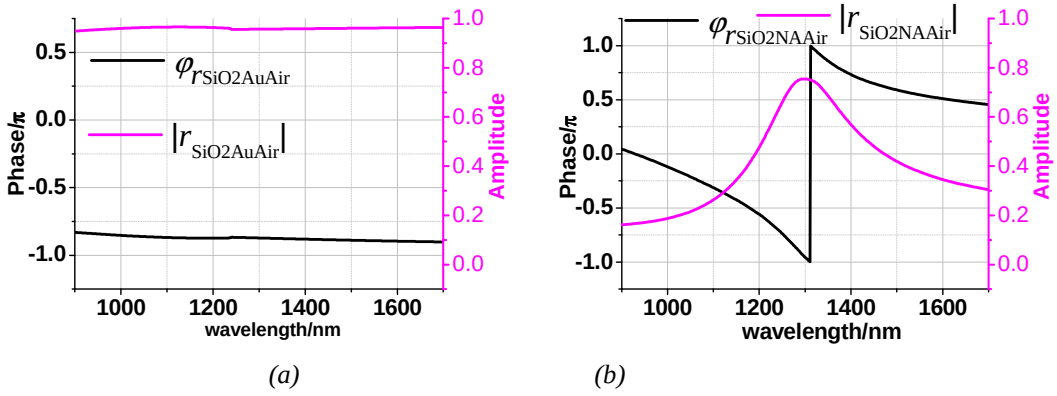

(a) *(b)*

Fig A-3-6 $\Delta\varphi_{tot}$ vs. λ (black curve) and amplitude vs. λ (pink curve) for (a) Au/SiO_2/PSi/Si; (b) NA/SiO_2/PSi/Si. The amplitude of reflection coefficient in (b) gives the position of the NA resonance.

Appendix B: Fit of macro-reflectivity spectrum for PSi layer characterization

The characterization of the PSi layer is achieved by fitting the macro-reflectivity spectrum of the PSi monolayer using a home-developed matlab code. This method enables to simultaneously obtain the thickness, effective refractive index and porosity of the PSi layer, without requiring destructive characterization like SEM measurement. The code is based on the transfer matrix method, combined with effective medium approximations (EMA), which describe the effective dielectric constant of PSi layer as a function of the host medium (Silicon) and the embedded media (air and any material coating the pores) as well as the porosity [AP-4]. Two different models have been implemented to describe the PSi dielectric function: Landau Lifshitz Looyenga (LLL) and Bruggeman models [AP-5, AP-6], expressed as follows:

$$\text{Bruggeman: } \sum_i p_i \frac{\varepsilon_i - \varepsilon_{eff}}{\varepsilon_i + 2\varepsilon_{eff}} = 0; \qquad \text{(EQ-B-1)}$$

$$\text{LLL: } \varepsilon_{eff} = \left(\sum_i \left(\varepsilon_i^{\frac{1}{3}} - \varepsilon_{si}^{\frac{1}{3}} \right) p_i + \varepsilon_{si}^{\frac{1}{3}} \right)^3, \sum_i p_i = 1 \qquad \text{(EQ-B-2)}$$

$$\varepsilon = n^2 \qquad \text{(EQ-B-3)}$$

Here, *pi* and ε*i* are the volume fraction and the complex dielectric function of the i^{th} material, respectively. Empirically, the LLL model has been shownn to be more suitable for high porosities, while for lower porosities both models converge in a similar way [AP-7].

The refractive index dispersion of the highly-doped Si is expressed according to a Cauchy law:

$$n_{Si} = 3.4227 + \frac{0.1104}{\lambda^2} + \frac{0.041}{\lambda^4} \qquad \text{(EQ-B-4)}$$

In order to determine the parameters of the PSi layer, the fit of the experimental reflectivity spectrum is performed using a Levenberg Marquardt nonlinear fitting method [AP-8].

Appendix C: Attenuation in the optical fibers at 1.4 µm

The attenuation characteristics of the optical fibers used in our micro-reflectivity setup is presented in Fig D. It shows a clear attenuation peak around 1.4 µm (highlighted by a green square). This attenuation is visible on the optical spectra as soon as there is a slight discrepancy in the light path between the reference signal and the sample signal.

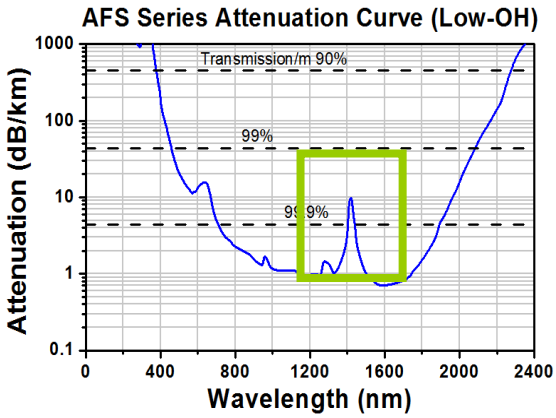

Fig D Attenuation curve of optical fibers [AP-9]

References

[AP-1] Born, M & Wolf, E “Principles of Optics”, 7th edn, Cambridge Univ. Press, 2003.

[AP-2] Kats, M. A., Blanchard, R., Genevet, P., & Capasso, F. (2012). Nanometre optical coatings based on strong interference effects in highly absorbing media.Nature materials.

[AP-3] Lekner, John. Theory of Reflection: Of Electromagnetic and Particle Waves. Vol. 3. Springer, 1987.

[AP-4] A. Wolf, B. Terheiden, and R. Brendel, Light scattering and diffuse light propagation in sintered porous silicon, J. Appl. Phys. 104, 033106, 2008

[AP-5] D.A.G. Bruggeman, "Berechnung verschiedener physikalischer Konstanten von heterogenen Substanzen", Ann. Phys. (Leipzig) 24, 636, 1935

[AP-6] H. Looyenga, "Dielectric constants of heterogeneous mixtures", Physica 31, 401, 1965

[AP-7] Theiss, W. Optical properties of porous silicon, Surface Science Reports, 29, pp. 91–192, 1997.

[AP-8] C. JAMOIS, New concepts of integrated photonic biosensors based on porous silicon, Biosensors – Emerging Materials and Applications, chap. 14, pp. 265, Intech, 2011

[AP-9] http://www.thorlabs.com/NewGroupPage9.cfm?ObjectGroup_ID=351#1509